Silica and borosilicate glass matrix composites containing carbon nanotubes

Tayyab Subhani

A thesis submitted in partial fulfilment of the requirements for the degree of

Doctor of Philosophy

September, 2012

Department of Materials

Imperial College London

London, UK

Abstract

Due to their remarkable properties and unique dimensions, carbon nanotubes (CNTs) are considered as an exciting nano-reinforcement in a variety of inorganic matrix composites. However, published data is unable to clearly define the role of CNTs on the properties of these composites, in particular, the mechanical properties including hardness, stiffness, strength and fracture toughness. This lack of knowledge is due in part to manufacturing issues, such as the dispersion of CNTs, densification of composites and microstructural changes during sintering. Moreover, interest in the electrical and thermal properties of inorganic matrix composites demands a comprehensive functional property evaluation. The still unexplored technological properties of these composites, such as thermal shock, ageing, friction and wear resistance, also deserve particular attention, in order to identify the extent of improvement that can be achieved due to CNTs. The microstructural characterisation including the nature of CNT distribution and their embedded morphology in brittle and amorphous matrices is still unclear, together with the nature of the CNT/matrix interface. Finally, the effect of different CNT aspect ratios on properties is yet to be investigated in order to choose the most suitable CNT sizes for desired composite performance.

The present study is, therefore, aimed at developing a model composite system of uniformly dispersed CNTs of different sizes and loadings in a dense, brittle and amorphous matrix, and exploring the real effect of CNTs on physical, mechanical, functional and technological properties of these composites together with their microstructural and interfacial characterisation.

Indigenously synthesised and functionalised multiwalled carbon nanotubes (MWCNTs) of four different aspect ratios (~31-65) were used as reinforcement, up to 10wt% (13.2vol%) loadings, while silica (SiO_2) glass was chosen as an inorganic matrix. Heterocoagulation upon colloidal mixing provided composite powders with homogeneously dispersed MWCNTs while pressureless sintering produced dense (96-99%) composites. The randomly oriented MWCNTs

in the glass matrix showed a mechanical MWCNT/glass interface due to the interlocking of MWCNTs with the matrix. The indentation fracture toughness was improved, by up to ~100%, but hardness and stiffness decreased by 21-38% and 20-37%, respectively. The electrical conductivity increased by >11 orders of magnitude but the thermal conductivity showed limited improvement, i.e. 41-48%.

The effect of different MWCNT sizes on the mechanical properties, such as hardness, elastic modulus and indentation fracture toughness, could not be determined due to the decrease in the densities of the composites containing higher aspect ratio MWCNTs; however, the functional properties, such as electrical and thermal conductivity, increased in proportion to the MWCNT size.

The presence of MWCNTs in the thermal shock resistant silica glass matrix did not produce thermal cracking after a single quench to 20°C from 1200°C or multiple quenches from 1000°C; however, devitrification of the glass was observed. During the thermal ageing of composites (up to 1000°C for up to 96h), no significant degradation was observed at lower temperatures (500°C) except limited surface MWCNT oxidation. However, at 750°C, considerable MWCNT oxidation was noticed, and at 1000°C, cristobalite was also formed producing surface cracking on cooling. The decarburisation depth due to MWCNT oxidation increased with time and temperature, and completely porous composites were obtained after oxidation of all of the embedded MWCNTs. The friction coefficient decreased with increase in MWCNT content, while the formation of a stable graphitic layer in composites containing 10wt% MWCNTs reversed the otherwise increasing wear rate.

Finally, the established composite processing route was applied to a commercial borosilicate glass system containing up to 10wt% (17vol%) MWCNTs. The microstructure along with the resulting mechanical and functional properties ensured the applicability of the developed model system, which is believed to serve as a guide in future for preparation of other technically relevant inorganic matrix composites containing CNTs for improved properties.

Declaration

I declare that the work presented in this thesis is my own and that all else is appropriately referenced.

Tayyab Subhani

Structure of thesis

Chapter 1 introduces the subject of the present investigation with the underlying aim to produce CNT reinforced inorganic matrix composites. Chapter 2 is a comprehensive literature review on CNT composites containing inorganic matrices, i.e. glasses and glass-ceramics. The first half of the chapter provides information on the preparation, properties, microstructure and applications of CNTs and glasses/glass-ceramics. The second half gives a brief survey on the current status of CNT-glass/glass-ceramic matrix composites. The existing composite powder preparation techniques are discussed along with the densification processes commonly used. Finally, the available mechanical and functional property data are critically reviewed. Chapter 3 clearly defines the aims and objectives of the present study in the light of the literature survey (Chapter 2), and also provides the strategy to achieve them. Chapter 4 provides an overview of the characterisation techniques used throughout the present study. Chapter 5 describes the synthesis and characterisation of MWCNTs and their suspensions, used for composite manufacture. Chapter 6 provides detailed information on the processing of a model MWCNT-SiO_2 glass composite system with emphasis on the preparation of composite powders and their densification, which is followed by physical, microstructural, mechanical, functional and technological property evaluation, together with the size effect of CNTs. Chapter 7 describes the successful development and characterisation of borosilicate glass matrix composites containing MWCNTs, as an application of the developed model composite system in Chapter 6. Finally, Chapter 8 outlines the conclusions of the present investigation in relation to the initial aims and also suggests future work.

Acknowledgements

I offer my sincere gratitude to my supervisors, Professors Aldo R Boccaccini, Milo SP Shaffer and William E Lee for their guidance throughout the PhD. It was truly an honour for me to work under these three luminaries of their fields and the experience I acquired will greatly help me to groom my professional career.

I am thankful to all of my friends in the three research groups of my supervisors for their continuous help and encouragement. I would like to recognise the special efforts of Johann Cho, whose support was outstanding to lay the foundation of my research work. Thanks are due to the faculty and students/researchers of the college for their technical support in the form of useful discussions, and staff of the college, who helped me on processing and characterising techniques. Special thanks to Vineet Bhakri, Constantin Ciurea and Ales Kratky for performing nano-indentation, TEM and wear tests, respectively, and my writing-up companions Fatemeh Pishbin and Naeem Ur-rehman. I would like to thank my examiners, Professor Shaowei Zhang and Dr. Luc Vandeperre, for becoming a part of my research work at the final stage with their valuable inputs.

My family and parents deserve a special acknowledgement for supporting my decision to opt for higher studies despite living away in the limited financial resources throughout my PhD.

Finally, I am indebted to the "Institute of Space Technology, Pakistan" for their financial support and the offer of a faculty position after the completion of my studies.

List of contents

List of Figures

List of Tables

1. Introduction

In the twenty years since carbon nanotubes (CNTs) have become an established topic, extensive research has been devoted to exploit their applications in the field of science and engineering. CNTs are one of the most intensively studied of all nanostructured materials, due to a combination of their outstanding properties and unique dimensions. As a result, the subject of nanocomposites also became broader and of greater importance after including CNTs as nanofibrous reinforcing agent to develop a new class of low density nanocomposites with enhanced properties. Research on these novel nanocomposites containing CNTs has considered a range of matrix materials including polymers, metals and ceramics. However, comparatively little attention has been paid to the use of ceramic matrices and even less to silicate glasses and partially crystalline glass-ceramics. The limited development of CNT-glass/glass-ceramic/ceramic matrix composites is due to many challenges, including good dispersion of CNTs and the densification of composites to near theoretical densities without the oxidation of CNTs after sintering. A good CNT dispersion avoids the presence of agglomerates and produces a uniform microstructure across the composite providing homogeneous properties, while the complete densification avoids porosity in composites leading to increased mechanical performance. Moreover, the involvement of high temperatures in the processing of composites encourages undesirable structural changes in the matrices, i.e. crystallisation in amorphous glasses and grain size variation in crystalline ceramics, and also promotes degradation of the CNTs.

Due to the aforementioned processing difficulties, research on CNT-glass/glass-ceramic/ceramic matrix composites is still in its infancy. The limited available data is unable to clearly describe the effect of CNTs on the properties of ceramic matrix composites (CMC) in general and specifically in glass/glass-ceramic matrix composites (GMC). Although the primary aim of incorporating CNTs in inorganic matrices is the improvement in the fracture toughness of these brittle matrices, the observed toughening improvements merge with the associated matrix microstructural changes. As a result, the solitary involvement of CNTs in toughening is difficult to isolate. Similarly, the effect of CNTs on other mechanical properties including hardness, fracture strength and elastic modulus requires further investigation, because it is still unclear whether CNTs improve these properties of the composites or otherwise. Due to the high electrical and thermal properties of CNTs, there is great interest in the functional properties of these composites. However, the improvement in inorganic matrix composites in relation to the CNT content, their percolating network and large interfacial surface area requires further investigation. The interest in these composites also demands investigation of the technological properties such as wear and thermal resistance. Moreover, the CNT structural morphology, their dispersion level and the interface type, requires to be extensively investigated in relation to composite properties. Finally, the size of reinforcement, i.e. length, diameter and aspect ratio, strongly affects the properties of composites. Hence, the effect of different CNT sizes on the properties of composites needs to be determined.

In the light of the above considerations and the comprehensive literature review (Chapter 2), the present study was performed with an aim (Chapter 3) to develop a model composite system of uniformly dispersed CNTs in an inorganic matrix, in order to explore the true effect of CNTs on the properties of composites (Chapter 6). Glass was especially chosen as a matrix material as it requires lower processing temperature and it provides an amorphous matrix, which can avoid the CNT effects on the matrix microstructural changes. As-produced composites were subsequently characterised (Chapter 4) for a wide range of physical, microstructural, mechanical, functional and technological properties together with the CNT size effects on composite properties. Finally, the processing route established for the manufacturing of the model CNT composite system was applied to a commercial borosilicate glass matrix (Chapter 7), in order to demonstrate its applicability on other technically relevant inorganic matrices.

2. Literature review

A comprehensive literature survey is presented based on CNTs, silica-based glasses/glass-ceramics, and CNT-glass/glass-ceramic matrix composites. In the first section, the structure, synthesis routes, properties and applications of CNTs are discussed, which is followed by a section on their composites briefly explaining the rationale of using CNTs as reinforcement. The third section discusses the structure, properties, types, applications and making of silica-based glasses/glass-ceramics, which is followed by a section on their composites providing motivation for their development together with the types of matrices and reinforcements, commonly used. The fifth section comprehensively reviews CNT-glass/glass-ceramic matrix composites and highlights their manufacturing and characterisation, including physical, microstructural, mechanical, functional and technological properties. A summary, at the end, outlines the critical issues and research areas related to CNT-glass/glass-ceramic matrix composites, yet to be attended and investigated.

2.1 Carbon nanotubes

For centuries, graphite, diamond and amorphous carbon have been known as the allotropes of carbon. However, recently additional forms of carbon have been recognised, i.e. spherical [1] and tubular [2-3] versions of fullerenes, and have attracted great interest. In particular, the unique structure and properties of the tubular carbon, i.e. CNTs, has drawn more attention than any other nanomaterials. As a result, in the last two decades, extensive research has centred on exploring the potential use of CNTs in a wide range of scientific and engineering fields.

2.1.1 Structure

Carbon atoms are held together by sp^3 hybrid bonds in diamond. The presence of four strong sigma covalent bonds constructs a tetrahedral structure producing hard but electrically insulating diamond. In contrast, graphite has a layered atomic structure, wherein carbon atoms in each graphene layer are linked through three sp^2 hybrid sigma bonds [4] . The out-of-plane pi bond is delocalised and distributed over the entire graphene layer making graphite conductive and highly anisotropic [5]. As a result, strong covalent bonding exists along the graphene layers and weak Van der Waals forces are present between the layers. CNTs are related to graphite because they are broadly sp^2 hybridised. However, graphene layers in CNTs are rolled up to form seamless hollow tubes; an individual atomic layer forms a single-wall carbon nanotube (SWCNT) while multiple layers rolled up concentrically constitute a multi-wall carbon nanotube (MWCNT). A structure containing pentagons or half spherical fullerenes closes the tube ends. The interlayer spacing of MWCNTs is close to that of graphite layers [6], i.e. $3.35A^o$. The diameter of the inner-most tube can be as small as 0.4nm and up to a large fraction of the outer diameter, which can reach more than 100nm [5]. SWCNTs are synthesised in bundles or ropes of up to roughly 100 tubes, arranged in a hexagonal array. They are either metallic or semiconducting depending on the chirality and diameter; armchair nanotubes are metallic, while chiral and zigzag nanotubes can be metallic or semiconducting [4]. Generally, a ratio of 1:2 is found between metallic and semiconducting SWCNTs. MWCNTs are almost always metallic [7].

2.1.2 Synthesis

CNTs are commonly produced by three techniques: (a) electric arc discharge (EAD), (b) laser ablation or evaporation (LAE) and (c) chemical vapour deposition (CVD). An even simpler classification is the high temperature (EAD and LAE) and low temperature (CVD) techniques [8].

a. Electric arc discharge

EAD was the technique used by Iijima [2], when CNTs were characterised for the first time. Typically, a voltage of 20-40V and a current of 50-100A are passed through a pair of graphite electrodes of diameter 6-12mm acting as anode and cathode, and separated by a distance of 1-4mm in an inert atmosphere, usually helium. Carbon vaporises away from the anode and arranges itself into MWCNTs, which deposit on the cathode, as a soft and dark black fibrous material [9]. Introducing transition metal catalysts into the electrodes, such as Fe, Co, Ni, Cu, Ag, Al, Pd, Pt or a combination thereof, produces SWCNTs, which deposit on the walls of the reaction chamber. SWCNTs of diameter 1-5nm and length of up to 1μm are produced as well as MWCNTs with large variation in their length and outer/inner diameter [10]. These CNTs are highly graphitised with few structural defects, and possess good electrical, thermal and mechanical properties. The yield, however, is low due to the presence of other graphitic products, particularly nanoparticles [11-12].

b. Laser ablation or evaporation

LAE was first introduced in 1995 to produce CNTs [13]. This method is quite similar to EAD except using a different heating mechanism, i.e. a high power laser to evaporate graphite, and usually a more controlled heating regime [6]. The flow of an inert gas, such as argon or helium, drives the vaporised carbon atoms away from the high temperature zone on a cold copper collector, where CNTs deposit [4]. MWCNTs can be synthesised by this technique [5], but it is more often applied for the synthesis of SWCNTs after impregnating the graphite with transition metal catalysts (1-2wt%) [6]. The processing parameters, such as the type of inert gas, hydrocarbon source, flow of inert gas, intensity of laser, and the reaction chamber temperature, influence the morphology and properties of the CNTs produced. The use of a high power laser and high purity graphite makes this technique very expensive, but it produces good quality SWCNTs at higher yields, i.e. >70% [6].

c. Chemical vapour deposition or catalytic growth process

CVD has been known for a long time as a means to deposit carbon nanofibrils [3]. However, since 1998, the method began to be optimised for the synthesis of CNTs [14-15]. In this technique, a source of carbon, usually a hydrocarbon or CO, is heated inside a quartz tube at an intermediate temperature range (500-1100°C) in the presence of a catalyst under an inert atmosphere of argon or helium gas. The molecules of the carbon source catalytically decompose to provide carbon atoms, which rearrange themselves into hexagonal networks on the metal catalyst to grow CNTs [10]. The hydrocarbon source may be a solid (camphor, naphthalene), a liquid (benzene, alcohol, hexane) or a gas (acetylene, methane, ethylene); metal catalysts including Fe, Co, Ni, Mo and other supports such as MgO, $CaCO_3$, Al_2O_3 or Si are used. Metallic catalysts can be predeposited as particles or films on a ceramic substrate or injected as colloids or organometallic vapour along the carbon feedstock. The diameter of the resulting CNTs roughly matches that of the catalyst particle, while lengths up to millimeters can be obtained [16]. CNTs grow by two different methods: (a) tip-growth and (b) base/root-growth; a weak interaction between metal and substrate allows the growth of CNTs by tip-growth, while a strong interaction favours base-growth [17]. Both horizontal and vertical furnaces are used as reaction chambers; the former is more common in a laboratory setup, whereas the latter is more often used for continuous mass production of CNTs. The advantages of the CVD-based fabrication route include the large scale production at relatively low cost together with a control of CNT growth by adjusting reaction parameters, such as temperature, time, catalyst, carbon source and gas flow rate. However, CNTs tend to be highly entangled or aligned, depending upon the parameters chosen. The application of plasma during growth is reported to enhance the alignment and straightness of CNTs at low temperatures [18].

In summary, the chosen synthesis route and the adopted processing parameters control the quality and yield of CNTs produced. Techniques using high temperature produce highly crystalline CNTs but are costly and provide low yield due to the presence of undesirable carbonaceous by-products including the other forms of fullerenes and amorphous carbon. Low temperature synthesis techniques produce cheap CNTs in large quantities but these CNTs are structurally defective.

2.1.3 Properties

CNTs possess attractive physical, mechanical and transport properties. Moreover, the tremendously increased surface area of CNTs up to 1000m^2/g [19] due to their nanosize produces novel effects. However, the properties of CNTs largely depend on their defect-free structure, which is considerably lowered by the presence of structural defects. A few of the mechanical and transport properties of CNTs in relation to the present work are discussed below.

a. Elastic modulus

Elastic modulus of CNTs has always been a controversial issue. Although, a similar elastic modulus value of CNTs is expected as that of graphite (1.06TPa) [20], and theoretical calculations [21] also predicted comparable values, the experimental results demonstrated different values (Table 9.1) ranging from 1GPa to 4150GPa [22-25]. Highly crystalline CNTs, grown by high temperature techniques, have always been the attractive choice for elastic modulus measurements and have shown higher values than CVD-grown CNTs, which show lesser values due to the presence of structural defects. For example, a decrease of an order of magnitude in the elastic modulus has been observed, i.e. from 810GPa for arc-grown MWCNTs to 27GPa for CVD-grown MWCNTs [26]. In another study, a value of 300GPa for CVD-grown MWCNTs reduced to 100GPa with the presence of defects, which further reduced to only 3GPa in highly defective MWCNTs [27]. These studies indicate that CNTs grown by the same technique but with different synthesis parameters show varied elastic modulus results. Recently, an average elastic modulus value of 130GPa was observed for CVD-grown MWCNTs of diameter >20nm [28], while a similar value (~100GPa) was obtained for MWCNTs of diameters ranging from 10-60nm [29].

MWCNTs are expected to be anisotropic in their elastic properties, as the radial elastic modulus was calculated to be about one third of that observed in the axial direction [26]. Shear modulus of CVD-grown MWCNTs and ropes of SWCNTs have also shown a very low value, i.e. 0.1-0.8 [30] and 0.7-6.5GPa [23], respectively.

Molecular dynamic simulations show that the elastic modulus of SWCNTs increases slightly with a decrease in diameter due to an increase in torsional strain [31]. A similar effect was observed experimentally in MWCNTs, where the elastic modulus decreased sharply from 1TPa to 0.1TPa when diameter increased from 8nm to 40nm [32] Similarly, the bundles of double walled CNTs (DWCNT) of diameter <5nm showed a high value of 1000GPa, which abruptly decreased to <100GPa with an increase in the size of bundles [33]. In contrast, MWCNTs are considered to have higher stiffness due to the presence of more than one nanotube arranged coaxially [5].

Techniques used to measure elastic modulus of CNTs include thermal vibration, electric field induced resonance, tensile loading inside scanning (SEM) and transmission (TEM) electron microscopy, and atomic force microscopy (AFM) [34].

b. Fracture strength

Theoretically predicted tensile strength of the CNTs is relatively high, i.e. ~135GPa [34], as compared to experimentally achieved maximum values, i.e. ≤110GPa (Table 9.2). Moreover, a large variation exists in the strength values; for example, high temperature-grown individual SWCNTs and MWCNTs showed values of 3.6-100GPa [24,35-36] and 10-110GPa [37-39], respectively. The ropes/strands of SWCNTs and low-temperature grown MWCNTs demonstrated a further decrease down to only 1.0-1.7GPa [40-42]. The compression strength values of low temperature-grown MWCNTs are similarly low, i.e. ~2GPa [28].

Nanoloading devices attached with AFM tips are generally operated inside an SEM or TEM to measure fracture strength of CNTs. A brittle fracturing mode has always been observed during tensile loading of SWCNTs, which is followed by the sword-in-sheath mechanism in the case of MWCNTs. The low experimental strength values and brittle fracture is related to the defects (Section 5.1.5) present in the CNTs [34]. A recent *in-situ* TEM test verified the breakage of the defective CNTs from the defected sites showing low fracture strength, while defect-free CNTs demonstrated values approaching that of theoretically estimated [36].

c. Fracture strains

CNTs are known to deform under tension, compression, bending and torsion, leading to the formation of structural defects such as buckling, folding, curling and kinking [43]. A tensile strain of ~20% is theoretically predicted for CNTs [44], which has been experimentally observed up to 15% and 12% for SWCNTs [45] and MWCNTs [37], respectively. Axial compression followed by buckling is also common in CNTs showing large elastic strains [43]. In bending, CNTs are reported to be fully reversible up to large angles, i.e. 110°, and show the remarkable flexibility of the hexagonal network of carbon bonds in graphene tubes avoiding bond breakage up to very high strain values, i.e. 16% [46-48]. Furthermore, strains up to 7.6% have been theoretically calculated under torsion [49]. Radial compression is also reported to transform CNTs from circular to elliptical/polygonal cross-sections [43] and produce fully reversible strain up to ~40% [50]. Finally, peanut-like shapes of SWCNTs and radially corrugated cross-sections of MWCNTs are observed under hydrostatic compression [43]. Superplasticity has also been observed stretching an individual SWCNT up to 280% at high temperature of 2000°C due to the formation and motion of kinks [45]. This data indicates the presence of structural flexibility in CNTs, which may have an effect on the properties of CNT-glass/glass-ceramic matrix composites.

d. Electrical conductivity

The room temperature electrical conductivity of metallic SWCNTs was found to be 10^5-10^6S/m but only 10S/m was noted for semiconducting SWCNTs [51]. The bundles of SWCNTs show a range of electrical conductivity values: 1x10^4S/m to 3x10^6S/m [52-54] , which approaches the in-plane conductivity of graphite: 2.5x10^6S/m [55].

The electrical conductivities of individual MWCNTs have been found in the range of 20 and 2x10^7S/m [7]. The helicity of the outermost tubes [56], ballistic effects [57], and the presence of defects [58] significantly affect the measured electrical conductivity of CNTs. Moreover, CNTs can transport currents up to 10^9A/cm^2, which is higher than obtained in conventional metallic wires: 10^4-10^5A/cm^2 [59-60].

e. Thermal conductivity

High thermal conductivity values have been theoretically predicted for individual SWCNTs, i.e. 6600W/m.K [61-63], although, yet to be proved experimentally. Bulk specimens of disordered and aligned SWCNTs have, however, demonstrated considerably lower values, i.e. ≤36W/m.K [61] and ~200W/m.K [64-65], respectively. Individual MWCNTs have experimentally shown high thermal conductivity values, i.e. ~3000W/m.K [66], which are reported to be greater than that of diamond and the basal plane of bulk graphite, i.e. 2000W/m.K [20], but their bulk forms also show values ranging from 25W/m.K [67] to 200W/m.K [68]. A report on randomly-oriented MWCNTs, consolidated by SPS, demonstrated a very low value of only 4.2W/m.K [69]. The bundles, ropes, nests and mats of CNTs similarly show considerably lower values, sometimes as low as 0.7W/m.K [61]. This sharp decrease in thermal conductivity of bulk CNT specimens can be associated with the interfacial resistance.

2.1.4 Applications

The notable physical and mechanical properties of CNTs suggest numerous scientific and engineering applications such as supercapacitors, transparent electrodes for organic light emitting diodes, lithium ion batteries, nanowires, field-effect transistors, molecular switches, sensors and filters. The conductivity, robustness, high surface area, accessible network formation, and facile functionalisation of CNTs are promising features for use as electrochemical electrodes and catalyst supports. Catalytically active sites can be used in fuel cells, immobilization of biomacromolecules and for organic reaction catalysis. In addition, CNTs can be used in the fields of catalysis and biomedical applications [70].

For mechanical and structural applications, which are of relevance in the context of the present work, individual CNTs can be used as nanoscale reinforcing elements in composites to achieve improved properties. Moreover, CNT-arrays can be shaped into bundles, ropes and strands, or two-ply yarns, which can be assembled into sheets for subsequent use as reinforcement [70].

2.2 Composites containing carbon nanotubes

Ideal CNTs possess extraordinary physical and mechanical properties in combination with unique geometrical features, i.e. high aspect ratio and diameter in the nanoscale. Such outstanding characteristics along with the low density make CNTs an attractive reinforcement for advanced composites. This new class of materials, i.e. CNT-reinforced composites, aims at exploiting the high strength of CNTs in the absence of macroscopic defects, due to their small size leading to high quality structural materials, although atomic scale defects exist [71], such as pentagon-heptagon defects in otherwise perfect hexagonal carbon network.

CNTs have been used extensively as reinforcing agents in metals [72], polymers [8], and glasses/ceramics [73], in order to exploit their remarkable features and to overcome the intrinsic limitations of these materials. For example, CNTs are usually introduced in polymeric and metallic matrices to increase strength and stiffness along with other functional properties. Glasses/ceramics incorporated with CNTs, can exhibit reduced brittleness to become structurally more reliable materials [73]. In addition, CNTs can offer improvements in thermal and electrical properties of inorganic matrices.

2.3 Glasses and glass-ceramics

Glasses and glass-ceramics are sub-classes of ceramics. The term “ceramics” captures a wide array of inorganic and non-metallic materials ranging from traditional monolithic ceramics, i.e. bricks, tiles and pottery, to high performance ceramics, i.e. oxides, nitrides, borides and carbides of silicon, boron, aluminium, titanium and zirconium [74]. Ceramics can have crystalline and/or amorphous structure with either ionic or covalent bonding. Glasses are amorphous, whereas ceramics other than glasses are crystalline. The crystalline ceramics have long range order of atomic arrangement in three dimensions while glasses lack such a regular atomic pattern, but their structure contains random clusters of short-range ordered atoms.

“Glass” is a term used for ceramic materials, which are cooled rapidly from their melts into solids without crystallisation. In precise words, glasses includes all materials, which are structurally similar to a liquid but which have a viscosity so great at normal ambient temperatures that they can be considered as solids [75]. Figure 2.1 displays a typical plot showing the variation of specific volume with temperature for glasses and crystalline ceramics. Crystalline ceramics show a sudden drop in volume at the melting point (T_m) on cooling while glasses show a gradual change in the slope of the curve at the glass transition temperature (T_g). Below T_g, glasses behave like a rigid solid material and show resistance to a shear force by obeying Hooke's law [76]. Silica (SiO_2) is a good example that exists in both crystalline, i.e. quartz, tridymite and cristobalite, and amorphous state, i.e. fused silica. On slow cooling, it crystallises into a number of polymorphs with a fully ordered lattice (Figure 2.2(a)) while the rapid cooling results into short-range ordered network in a glassy matrix (Figure 2.2(b)) [76].

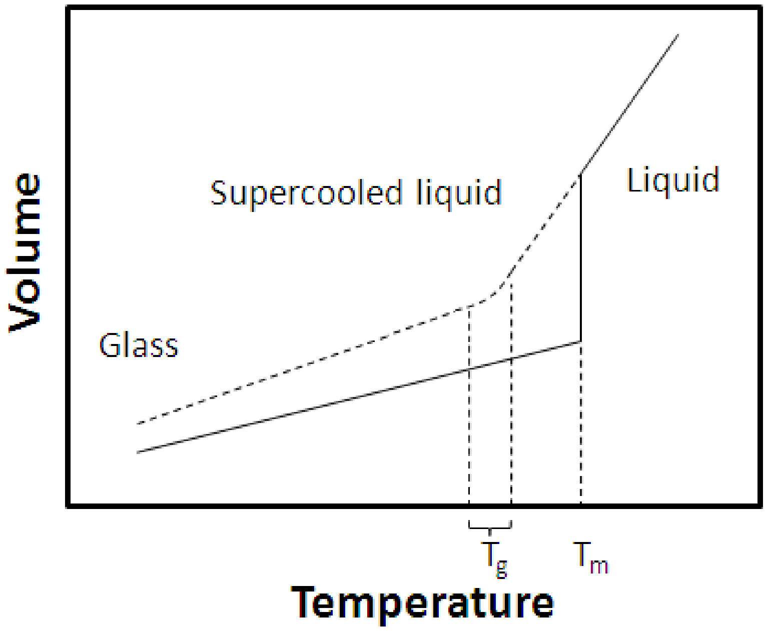

Figure 2.1: Variation of specific volume with temperature showing the relationship between liquid, crystalline and glassy states [76].

The main inorganic materials possessing the capability of forming glasses are the oxides of silicon, boron, germanium, phosphorous and arsenic, called glass formers. However, the glassy state is not limited to oxides, as several sulphur and selenium compounds, metallic alloys and organic liquids also transform into glassy states at low temperatures [75]. Glasses can be classified by many ways; for example, depending upon their chemical compositions, structures, properties, manufacturing techniques and applications. However, the most widely used classification is based on composition, which relates to the type of the principal glass former. Metallic constituents, called glass modifiers, are usually added to change the bonding relationships and structural groupings in order to modify the physical, mechanical and chemical characteristics of the parent glasses. A two dimensional crystal structure of soda-silica glass is presented in Figure 2.3 showing the presence of sodium atoms within the structure of silicon and oxygen atoms, as already shown in Figure 2.2(b) [76].

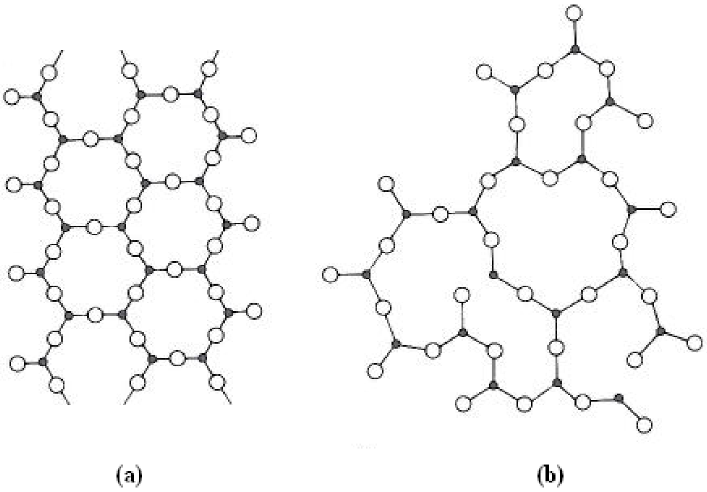

Figure 2.2: Two dimensional structure of (a) crystalline and (b) amorphous silica. Open circles are oxygen atoms and black dots are silicon atoms [76].

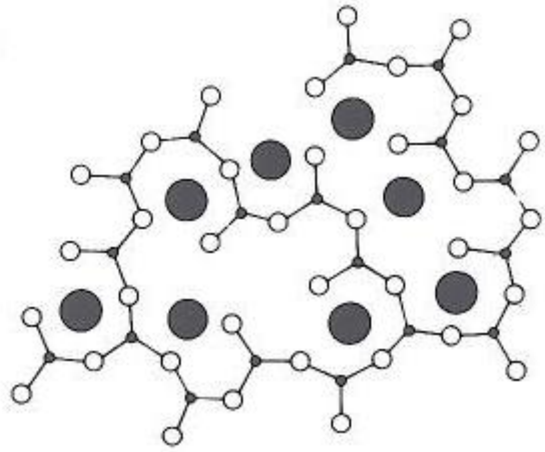

Figure 2.3: Two dimensional structure of soda-silica glass. Open circles are oxygen atoms, black dots are silicon atoms and large black dots are sodium atoms [76].

Oxides of silicon (silica) form an important class of glasses with various compositions and properties. The building block of all these glasses is always a tetrahedron of four oxygen atoms with a silicon atom at the centre (Figure 2.4). The composition of a single tetrahedron is SiO_4. However, due to the sharing of each oxygen atom by two tetrahedra, the bulk composition becomes SiO_2 [77]. The important groups of silica-based glasses are borosilicate, aluminosilicate, soda-lime-silicate, lead-silicate, high silica and fused silica (Table 2.1). Being inexpensive, soda-lime-silicates are commonly used for applications in daily life, while other types are special purpose glasses, i.e. aluminosilicates have better chemical durability, strength and resistance to devitrification, borosilicates are corrosion and thermal shock resistant, lead-silicates have high refractive index, high silica (>96% SiO_2) is chemically resistant, and fused silica (>99% SiO_2) is used for high temperature applications.

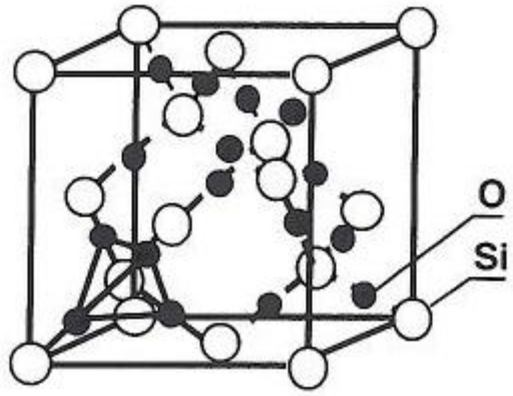

Figure 2.4: Crystal structure of cubic silica with SiO_4 tetrahedral [77].

Raw materials required for making glass are weighed to the required composition, mixed and melted, followed by the desired shaping process. Other methods such as sol-gel techniques, colloidal processing, microwave sintering and self-propagating high temperature synthesis are also used for making glasses.

Generation of ceramic crystals in a glassy matrix by heat treatment develops a different class of ceramic, called glass-ceramics [74]. Nucleating agents, such as TiO_2, ZrO_2, P_2O_5, may be added in the glass composition to encourage crystallisation, which converts a glass into a glass-ceramic, containing closely interlocked ceramic crystals in the glassy phase [76].

Alternatively, glass-ceramics can be produced by powder processing route and sintered for densification, followed by a heat-treatment process to nucleate and grow crystals. The content of the ceramic crystals varies from 50vol% to 98vol% [76] and their grain size is around 1μm [74]. Many parameters including (a) the difference between elastic modulus and thermal expansion coefficients of the two phases, (b) the interface in-between and (c) the size and amount of crystalline phase, define the properties of glass-ceramics [76].

Table 2.1: Compositions of different silica-based glasses [77]

Glasses	**Composition wt%**							
	SiO_2	**Na_2O**	**K_2O**	**CaO**	**PbO**	**B_2O_3**	**Al_2O_3**	**MgO**
Soda-lime-silicate	70-75	12-18	0-1	5-14	-	-	0.5-2.5	0-4
Lead-silicate	53-68	5-10	1-10	0-6	15-40	-	0-2	-
Borosilicate	73-82	3-10	0.5-1	0-1	1-10	5-20	2-3	-
Aluminosilicate	57	1	-	5.5	-	4	20.5	12
High silica	96	-	-	-	-	3	-	-
Fused silica	99.9	<0.001	<0.001	<0.001	-	-	0.005	-

2.4 Glass/glass-ceramic matrix composites

As opposed to metallic and polymeric materials, ceramics including glasses and glass-ceramics are generally characterised by higher hardness, stiffness, compressive strength, high temperature stability, chemical inertness, wear resistance and low density, but they suffer from their inherent brittleness. The problem is specifically severe for glasses [78], which have an amorphous matrix with limited ability to hinder to crack propagation and possess low fracture toughness, i.e. <1MPam$^{1/2}$. This brittle behaviour of glasses and ceramics is the main driving force for incorporation of reinforcements, such as fibres and particulates, in order to manufacture composites of toughness higher than that of the matrix materials, along with additional benefits of increased fracture strength, thermal shock resistance and wear/friction properties. Other objectives of producing composites are to attain enhanced characteristics such as electrical and thermal conductivity. However, the need of high temperatures for processing has hindered extensive development of these composites. Another problem is a large difference in thermal expansion coefficients between the matrix and reinforcement that leads to thermal stresses on cooling from the processing temperatures and results in matrix-cracking.

The improvement in fracture strength and toughness of composites containing discontinuous reinforcements, i.e. short fibres, whiskers or particles, is limited compared to monolithic matrices (Figure 2.5). In contrast, continuous reinforcements such as long unidirectional fibres are more efficient for significant improvements in these properties and possess significant load carrying ability even after the failure. However, they are more expensive and more difficult to incorporate in glass/ceramic matrices.

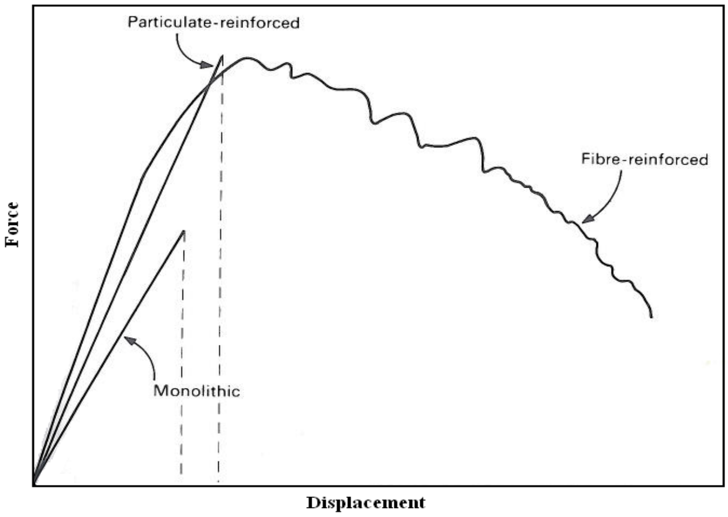

Figure 2.5: Typical force-displacement curve for a monolithic glass/ceramic, particle reinforced and fibre reinforced glass/ceramic matrix composite [76].

The incorporation of reinforcements in glass/ceramic matrices introduces various energy dissipating phenomena, depending upon their nature. Commonly observed toughening mechanisms include debonding, crack-deflection, fibre-bridging and fibre-pullout. Fibre/matrix debonding creates new surfaces and releases any stored strain energy associated with the interface. Moreover, it encourages the process of interfacial frictional sliding of fibres, which can absorb significant amount of energy depending upon the interfacial roughness, contact pressure and sliding resistance [79]. The frictional sliding typically operates during the fibre-pullout and fibre-bridging mechanisms after fibre/matrix debonding. A relatively weak interface promotes frictional sliding of fibres, while a strong fibre/matrix bonding results in the fibre fracture during the crack propagation. In case of weak interface, fibre fracture is also observed but only when fibres possess a length greater than a critical value, called the critical length, which depends upon the fracture strength and diameter of fibres and the interfacial shear strength [76]. The deflection of an advancing crack from its principal direction due to the presence of reinforcement also increases the fracture energy. This process reduces the stress at the crack tip, which is related to the interface strength and the emergence of microcracks in response to the stress field around the crack tip along with the presence of residual stresses [80].

The versatility of glasses in processing, properties and compositions, makes them an attractive choice for matrix materials in composites for a variety of applications in aerospace, automotive, electronic, biomedical and other specialised fields [81]. Silica-based glasses can be produced with a broad range of chemistries to control the fibre/matrix chemical interactions. This chemical composition flexibility also enables the development of glasses with a wide range of thermal expansion coefficients (TECs) in order to match the TEC of the reinforcement. In addition, by controlling the viscosity of glasses, high composite densities can be achieved by promoting viscous flow during sintering. Finally, the low elastic modulus of most glasses means that high modulus fibres can provide a true reinforcement, unlike in crystalline ceramic matrix composites, where the ratio of fibre/matrix moduli is close to one [74]. However, the main drawback of glasses is the low temperature capability compared to crystalline ceramics, which limits their applications to modest temperatures.

Carbon, silicon carbide, alumina, boron and metallic reinforcements have been used in glasses and glass-ceramics in a variety of shapes, including continuous and chopped fibres, particles, platelets and whiskers [81]. Continuous carbon fibres were the first to be considered to reinforce silica glass [82], producing excellent toughness, crack growth resistance and non-catastrophic failure. Borosilicate glasses and lithium aluminosilicate glass-ceramic matrices have also been reinforced with continuous [83] and discontinuous [84] carbon fibres for improved composite toughness, which was attributed to low fibre/matrix interface strength promoting crack deflection. The combination of carbon fibres with a glass matrix offers other benefits, since carbon fibres impart lubricity to the composite surface while the glass matrix provides high hardness, wear resistance and dimensional stability.

A wealth of literature on silicon carbide (SiC) fibre reinforced glass/glass-ceramic composites is available, showing improved fracture strength and toughness together with the potential for high temperature oxidation resistance. Monofilaments and large diameter SiC fibres have been used as reinforcements in different glass matrices [85-87]. Moreover, SiC yarns have been used to develop high strength composites [87-88]; the highest strength was achieved by using a glass-ceramic matrix, i.e. lithium-aluminosilicate [89].

Glass and glass-ceramic matrix composites containing nano-reinforcements such as CNTs are discussed in the next section.

2.5 Glass/glass-ceramic matrix composites containing carbon nanotubes

Since the emergence of CNTs in 1991 [2], the motivation to exploit their remarkable properties triggered the interest to fabricate CNT-based nanocomposites. Especially, the last decade has witnessed a tremendous use of CNTs, both SWCNTs and MWCNTs, in both the aligned [90] and random orientation [91], as reinforcements in polymers, metals/alloys, and glasses/ceramics, in order to overcome the intrinsic limitations of these matrices and to develop new materials for futuristic demands. Furthermore, the enormous interfacial area generated due to the incorporation of nano-fillers in composites may give rise to new kinds of composites, possessing improved properties.

The utilisation of CNTs in glasses/ceramics was, however, aimed at the desire to transform inherently brittle glasses and ceramics into structurally reliable materials. As a result, a range of inorganic matrices, both polycrystalline and amorphous, have been studied in combination with CNTs, including oxides (Al_2O_3 [92], TiO_2 [93], ZrO_2 [94], MgO [95], MnO_2 [96], $MgAl_2O_4$ [97], Co/Mo-$MgAl_2O_4$ [98], $BaTiO_3$ [99]), nitrides (Si_3N_4 [100], Si-C-N [101], TiN [102], Fe_2N [102]), carbides (SiC [103], WC [104]) and glasses/glass-ceramics such as silica [91], borosilicate [105-106], mullite [107], barium-aluminosilicate [108], alumina-borosilicate [109] and vanadium-doped silicate [110]. Of these, CNT-glass/glass-ceramic matrix composites represent an emerging family of composites that potentially exploits the small size of high strength fillers in complete and partially crystallised matrices.

The manufacturing processes used for the CNT-glass/glass-ceramic matrix composites and their advantages and limitation are discussed below, together with the comprehensive mechanical and functional characterisation of these composites, available in literature, and the potentially beneficial properties of these composites for technological applications, yet to be investigated.

2.5.1 Manufacture

The manufacturing of CNT-glass/glass-ceramic composites comprises two stages: (a) preparation of composite mixtures using a suitable CNT dispersion process and (b) their densification by an appropriate sintering technique, as discussed below.

a. Composite powder preparation

The techniques used to prepare composite mixtures of CNTs and glass/glass-ceramic matrices include conventional powder mixing [111], sol-gel processing [106] and colloidal mixing [91]. Conventional powder mixing process usually yields a poor dispersion of CNTs due to the lack of driving force to distribute them. As a result, CNT-agglomerates are readily formed in the sintered composites due to the high aspect ratio, high surface area and poor interaction of CNTs with the matrix material. On the other hand, sol-gel [109] and colloidal mixing [91] techniques have successfully produced homogeneous dispersions of CNTs up to 10wt% and 15wt%, respectively, due to the means of modifying the wettability/adhesion between CNTs and the matrix material. *In-situ* synthesis of CNTs in matrix material is another convenient technique, which has been predominantly utilised for CNT-CMC mixtures [112] but never applied to obtain CNT-GMC mixtures.

i. Conventional powder mixing

One of the earliest techniques used to prepare composite mixtures was conventional powder mixing. In this process, as-synthesised CNTs are mixed with glass/glass-ceramic powders and a composite slurry or suspension is prepared, which is ultrasonicated and/or ball-milled to disperse CNTs. The composite slurry/suspension is then dried, ground and sieved before the final compaction and sintering to obtain composite bodies. Composite powders containing both glasses [105,111,113] and glass-ceramics [107-108,110] have been prepared by this technique. Crystalline ceramics including alumina [114] and silicon nitride [115] have also been prepared with this technique to prepare composites in combination with CNTs.

In the first investigation on powder mixing process, CNTs ranging from 3.75wt% to 22.5wt% were incorporated in silica (SiO_2) glass powder [113] to prepare CNT-SiO_2 glass composites. However, the CNTs could not be well dispersed in the composite, even at low loadings (3.75wt%). Another study on borosilicate (BS) glass powder found similarly unsatisfactory CNT dispersion results [105].

Attempts to produce CNT-glass-ceramic composite powders also remained unsuccessful; the examples include, 1wt% CNTs in vanadium-doped silicate [110], 3.75wt% CNTs in mullite [107] and 11.25wt% CNTs in barium aluminosilicate [108].

The lack of dispersion is not surprising in these systems, given that the matrix particles are typically large compared to the desired CNT-CNT separation, and the fact that the CNTs tend to be forced into mutual contact around the perimeter of the matrix particles. There is no effective mechanism, during consolidation, to disagglomerate these CNTs, or distribute them within the original matrix particles. On the other hand, if an electrically conducting network is required, at low loadings, this type of longer length scale structuring can be beneficial.

ii. Sol-gel techniques

Sol-gel processing has shown potential to provide good dispersion of CNTs in glass/glass-ceramic matrix composites [109]. In this process, CNTs are mixed in a (usually aqueous) solution (sol) of molecular precursor of the destined matrix, which is subsequently gelled (gel) and dried to obtain a composite body that is either used as the final composite after heat-treatment [116] or crushed, ground, sieved and then sintered to obtain composite bodies of the desired shape [106]. Although, earlier studies showed a degree of CNT-agglomeration [117-118], later investigations demonstrated a better dispersion of CNTs after their functionalisation, up to 3wt% [106] and then 10wt% loadings [109]. However, higher loadings of CNTs (15wt%) still produce agglomerates due to improper dispersion of CNTs [109]. Different types of CNTs such as SWCNTs [116,119-121], DWCNTs [122] and MWCNTs [106,109] have been incorporated in glass/glass-ceramic matrices by sol-gel processing including silica [123], borosilicate [106], and alumina borosilicate [120].

In one of the earliest studies on sol-gel processing [123], tetraethoxysilane (TEOS) was used as the precursor in acidified water destined to produce a silica glass matrix. CNTs were mixed with the solution and after condensation, the mixture produced a composite body containing MWCNTs, which was milled to powder and densified by pressureless sintering [124] and laser treatment [125]. In the earlier attempts, CNTs without functionalisation were incorporated in the precursor of the desired matrix [126]; however, later investigations focused on using appropriate surfactants or coupling agents for improved CNT dispersion in composites [119,127-133].

Transparent silica GMCs were also prepared by reinforcing SWCNTs [129] and MWCNTs [134] by sol-gel processing. CNT-SiO_2 glass composites for nonlinear optical properties [134-135], microwave attenuation [136] and electromagnetic interference shielding effectiveness [137] are other examples of sol-gel processing. In addition to bulk composites, thin glass composite films of CNT-SiO_2 were also produced by this technique and deposited by spin-coating [138] and dip-coating techniques [116,128,139]. Finally, mesoporous CNT-SiO_2 glass composites were also produced by this technique to develop novel biomaterials [140].

iii. Colloidal mixing

Colloidal mixing processing is an emerging technique to homogeneously disperse CNTs in glass/glass-ceramic matrices [91]. In this process, the surface chemistry of CNT and the glass/glass-ceramic powder suspensions is adjusted to encourage the coating of glass particles on CNTs or vice versa, depending upon their size. The manipulation of the surface chemistry of the two composite constituents results in the development of opposite surface charges on them; as a result, similarly charged particles repel each other but attract oppositely charged particles during the mixing of the two suspensions, a process called heterocoagulation. Organic surfactants and dispersants are used to develop positive or negative surface charges on CNTs and matrix powders, which are usually removed during sintering [73]. Alternatively, a calcination step, at temperatures less than 400°C, can be introduced before sintering to eliminate the surfactants/dispersants, which could provide undesirable effect via residual impurities in the composites. In addition to glasses/glass-ceramics, colloidal processing has also been used for CNT-crystalline CMCs including alumina [141], titania [142], and silicon nitride [143], as matrices.

The earliest works on colloidal mixing techniques find their roots in sol-gel processes, where surface charges were developed on CNTs by using surfactants, and functionalised CNTs were then mixed with the precursor of the desired matrix. In one of these studies, CNTs were dispersed in an aqueous solution of cetyltrimethyl ammonium bromide (CTAB), which served as the cationic surfactant before mixing it with the alcoholic TEOS solution to form the silica glass matrix [118]. CNT-SiO_2 glass composite powders displayed better CNT dispersion quality than obtained by direct mechanical mixing processes. In another study, CNTs were dispersed in silica glass using different surfactants to prepare composite films [138].

In the second stage of the development of colloidal processing, surfactant assisted CNT dispersions were mixed with commercially available colloidal glass particle suspensions to prepare CNT-glass composite powders. For example, CNTs were mixed with colloidal silica to obtain composite powders [144-146] leading to a better dispersion quality.

More recently, colloidal mixing processes have been developed, which provide high quality CNT dispersions in glass matrices [91,147]. Aqueous CNT dispersions are obtained by treating CNTs with a mixture of sulphuric and nitric acids [148], which not only purify them from catalyst particles and amorphous carbon produced during their synthesis but also shorten their lengths and decorate them with acidic surface functionalities, i.e. carboxylic and other oxygen-containing groups. As a result, CNTs were electrostatically stabilised in aqueous suspensions and developed a negative surface charge. The development of negative surface charge on CNTs requires positive surface charge on glass particles to encourage heterocoagulation, which is produced using cationic surfactants. Finally, the composite powder suspension, obtained by colloidal mixing of the two suspensions, is dried, ground and sieved to obtain composite powders for subsequent sintering into solid compacts. In the earliest of these studies, 1wt% CNTs were dispersed in silica glass [147] but high CNT contents were loaded successfully, i.e. 15wt% (19vol%) in subsequent investigations and densified by SPS [91].

iv. *In-situ* CNT synthesis in matrix

In-situ synthesis involves the direct growth of CNTs on matrix powders by CVD processes. The matrix particles clearly have to be stable at the synthesis conditions (elevated temperatures in hydrocarbon atmospheres) and to be compatible with the CNT catalyst system used. To date, several crystalline ceramic matrices have been directly grafted with CNTs including Al_2O_3 [112], SiC [149], TiN [150], Fe_2N [102] and $BaTiO_3$ [151], but glass/glass-ceramic matrix composite powders have not yet been prepared by this method. Possible problems associated with this technique include the retention of metal catalyst and amorphous carbon produced during the CNT growth, non-uniform dispersion of CNTs, little opportunity of manipulating interface and the poor density of composites after consolidation. On the other hand, the technique can be used to develop composites with highly ordered array of aligned CNTs in the matrix, as observed in MWCNT-Al_2O_3 composites [152].

b. Composite densification techniques

Two specific densification techniques, namely spark plasma sintering (SPS) [91] and uniaxial [111] / isostatic [100] hot-press sintering (HPS), are often used to consolidate CNT-glass/glass-ceramic composites, although high temperature extrusion [153], laser-treatment [125] and high pressure techniques [121] have also been reported. Surprisingly, however, little attention has been paid to the consolidation of CNT-glass/glass-ceramic composites using pressureless sintering (PLS), except for a few deliberate attempts to densify CNT-glass composites [105,147] but without good result. In contrast, CNT-ceramic matrix composites have been sintered using PLS including CNT-Al_2O_3 composites [154-157].

In SPS, composite powders are internally heated by passing pulsed DC current through a graphite die, while in HPS and PLS, composite powders are consolidated by an external heat source [158]. Rapid heating in SPS causes lower sintering temperatures and shorter durations compared to HPS and PLS. 100% relative densities have sometimes been achieved by HPS [108] and SPS [144]. However, alignment of CNTs has been observed in densified composites, sintered by SPS and HPS [159], as these techniques involve uniaxial pressure. In contrast, hot-isostatic pressing (HIP) and PLS can provide randomly oriented CNTs in the final composites, provided composite powders are pre-compacted in PLS by isostatic pressing. Moreover, interest in conventional PLS can be driven by its cost-effectiveness and its adaptability to parts with different shapes and dimensions. In short, SPS is a time efficient and effective route to good densities, but PLS is cheaper and more flexible in terms of composite size and shape, but at the cost of a comparatively lower density.

Good composite density is not only related to the densification technique employed but it is also associated with the uniformity of CNT dispersion in the matrix. A suitable composite mixing process to homogeneously disperse CNTs in a well packed particulate matrix along with the densification through PLS can provide a suitable combination to manufacture CNT-glass/glass-ceramic matrix composites. Initial attempts to use conventional PLS did not show good densification results; for example, 10wt% CNT-borosilicate glass composites showed relative densities of only 51% [105]. However, a change in the composite powder processing technique from direct powder mixing to colloidal mixing provided good composite density, i.e. 95% with 1wt% CNTs [147].

Degradation of CNTs is often reported during the sintering of composites involving high temperatures [95,97,105,153,160]. Vacuum or protective atmospheres of nitrogen or argon are, therefore, used during sintering to avoid the oxidation of CNTs.

2.5.2 Characterisation

a. Microstructure

The microstructural characterisation of CNT-glass/glass-ceramic composites is usually performed by x-ray diffraction, scanning and transmission electron microscopy, as given below.

i. X-ray diffraction

The amorphous structure of glass matrices after sintering or their extent of devitrification is determined by XRD [91,105,111,113,117,119,122,131,147]. In glass-ceramic matrices, XRD identifies the presence of crystallites in the glassy phase [107,109-110,120]. Cristobalite usually forms in silica and borosilicate glass matrices when SPS [122,144], HPS [105,113] or PLS [147] are used. However, careful control of sintering conditions can avoid crystallisation that can considerably affect the composite microstructure and properties, confounding attempts to understand the underlying science [91,113]. Cristobalite can also be suppressed by the addition of Al_2O_3 but it causes the crystallisation of mullite and transforms an amorphous glass into a glass-ceramic matrix, as observed in CNT-alumina borosilicate composites [109,120].

XRD is also used to detect the retention of CNTs in composites after sintering involving high temperatures, i.e. up to 1200°C, as in CNT-SiO_2 glass composites [91]. A characteristic (002) XRD peak of as-synthesised CNTs confirms the presence of CNTs in composites.

It can be argued that a large interfacial surface area in composites should accelerate matrix crystallisation through heteronucleation, but studies on CNT-SiO_2 glass composites have instead identified a suppression of matrix devitrification, possibly due to the dissolution of carbon [91].

ii. Scanning electron microscopy

The dispersion quality of CNTs and their presence in composites after sintering is observed by SEM. Micrographs of composites prepared by mechanical mixing generally show agglomerates associated with inhomogeneous CNT dispersion [105]. However, images of the composites produced by sol-gel and especially colloidal mixing technique show well-dispersed CNTs in matrices [91,106,109].

SEM also characterises as-synthesised CNTs, CNT-suspensions, and CNT-composite green bodies. The location of CNTs in glass-ceramic matrix composites is also evidenced by SEM, as CNTs generally occupy one of the four locations in crystalline matrices, i.e. (a) within grains, (b) along grain boundaries, (c) bridging the grains and (d) within intergranular pores. Conversely, in composites containing amorphous matrices, CNTs are only expected to disperse in a continuous bulk matrix without any effect of grains or grain boundaries. The toughening mechanisms in CNT-composites including the debonding, crack-deflection, bridging and pullout are also revealed by SEM.

Finally, the densification quality of composites including the presence of porosity is witnessed by SEM. The grain size variation due to the presence of CNTs and the formation of cracks after thermal treatments are other microstructural features, observed by SEM.

iii. Transmission electron microscopy

The information on the actual state of embedded CNTs in composites is produced by TEM, i.e. their dispersion and orientation, as well as the degree of crystallinity after processing, and the state of the fibre/matrix interface. Moreover, TEM reveals the structural characteristics of CNTs before and after their incorporation in matrices including any damage because of the chemical functionalisation. Due to their flexible nature, images of bent CNTs are common in composites with glass [106,118,133-135] and glass-ceramic [90,108-109] matrices. Localised curvatures in the CNT walls are also observed, which may be due to structural defects produced during synthesis [128] or due to the effect of pressure applied during sintering to densify composites. In addition, folds and kinks have been noted in the walls of CNTs [90] and curled and imperfect CNT layered structures are other commonly observed features [135].

Another aspect of considerable importance is the interface, as the interfacial characteristics can significantly affect the composite properties. High resolution TEM (HRTEM) is used to reveal the type of contact between the CNTs and the matrices. Mechanical bonding is reported to form predominantly in CNT-glass/glass-ceramic matrix composites without the existence of an intermediate phase [90,106,108-109,118]. However, chemical bonding at the CNT/matrix interface due to carbothermal reduction has also been reported [124].

b. Physical properties

i. Density

The densities of CNT-glass/glass-ceramic matrix composites directly affect their properties. Indeed, the achievement of near complete densification is a prerequisite for enhanced mechanical properties. SPS and HPS have provided dense CNT-glass/glass-ceramic composites [108-109,159] and in some cases, 100% densification of composites has been reported [144].

In contrast, conventional PLS is showing a gradual improvement in densification results; for example, 51% relative density in 10wt% CNT-borosilicate glass composites, followed by a satisfactory rise of 90% in 1wt% CNT-CaO-ZrO_2-SiO_2 and CNT-CaO-ZrO_2-SiO_2-V_2O_5 composites and more recently 95% densification has been achieved in 1wt% CNT-SiO_2 glass composites [147]. More attention is needed to revive the use of PLS for the densification of CNT-glass/glass-ceramic matrix composites. Figure 2.6 summarises published densification results for a variety of CNT-glass/glass-ceramic matrix composites produced by HPS, SPS and PLS.

c. Mechanical properties

Four mechanical properties of CNT-glass/glass-ceramic matrix composites have been investigated in most of the studies, namely hardness, elastic modulus, fracture strength and fracture toughness. The incorporation of CNTs in composites has led to different effects on these properties, as explained below.

i. Hardness

Hardness of CNT-glass/glass-ceramic matrix composites has been investigated several times but the actual effect of CNTs on hardness is still unclear. In the absence of a hardness value of individual CNTs, their effect on the hardness of composites is difficult to predict. As a result, three different trends of hardness have been revealed in literature, i.e. (a) an increase in hardness, which has been associated with dense matrices and good interfacial bonding, although no evidence of a strong chemical interface between CNTs and the matrix is usually shown, except the existence of a simple mechanical bonding; (b) a continuous decrease in hardness, which has been associated with inhomogeneous dispersion of CNTs and poor density of sintered composites; and (c) an initial increase followed by a decrease in hardness, which has been explained by a combination of (a) & (b), i.e. good interfacial bonding and/or uniform dispersion at low CNT loadings and inhomogeneous distribution of CNTs at higher contents, leading to the formation of CNT-agglomerates and hence poor composite densities.

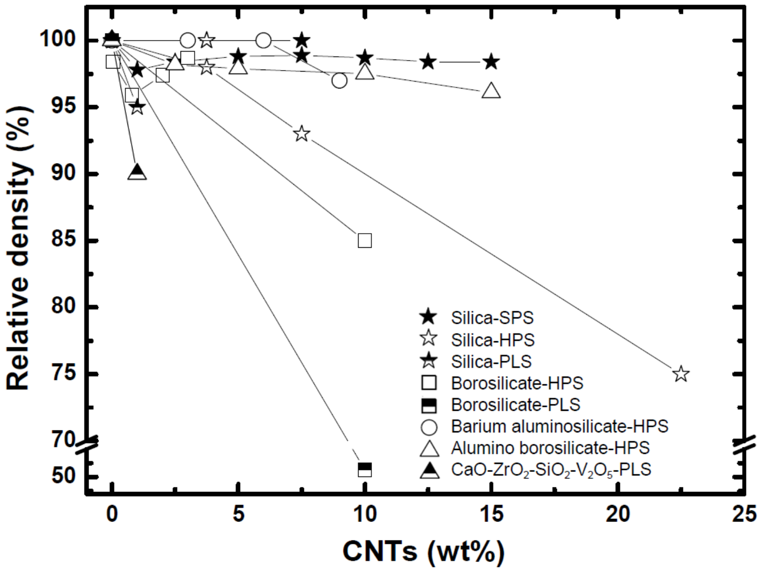

Figure 2.6: Percentage relative densities of glass and glass-ceramic matrix composites containing carbon nanotubes (published data) [91,105-106,108-110,113,118,144,147].

An early investigation on 4wt% CNT-SiO$_2$ glass composites showed a 28% increase in hardness in comparison to that of unreinforced silica glass [116]. Surprisingly, another study on the similar CNT-SiO$_2$ glass composites showed 44% improvement in hardness of composites by adding only 0.075wt% CNTs [121]. Borosilicate GMCs containing 10wt% CNTs demonstrated 22% decrease in hardness that was attributed to inhomogeneous dispersion of CNTs, as a direct mixing technique was used to prepare composite powder [111]. In contrast, a study on borosilicate

GMCs, prepared by a sol-gel technique, demonstrated an increase in hardness of 13% by adding 2wt% CNTs but further CNT addition (3wt%) was reported to produce agglomerates and a decreased hardness to a value 7% less than that of pure borosilicate glass [106].

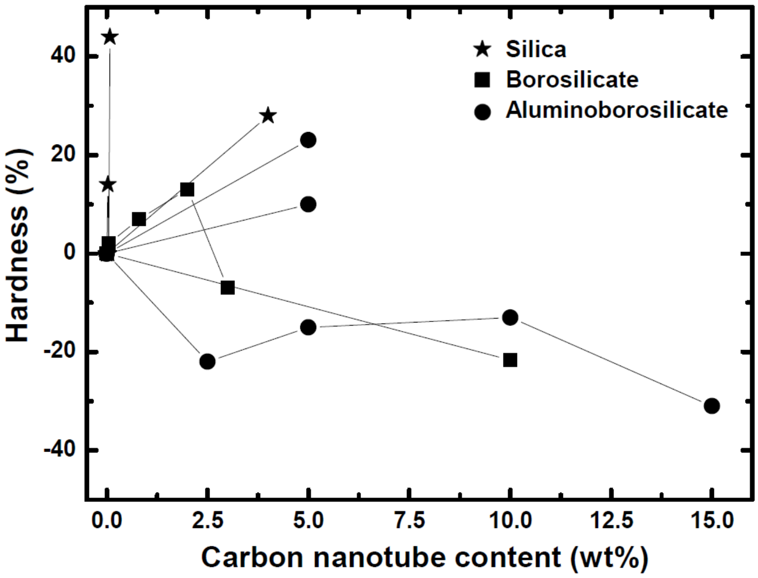

Figure 2.7: Percentage variation of the hardness of glass and glass-ceramic matrix composites containing carbon nanotubes (published data) [106,109,111,120-121,138,161].

CNT-composites containing glass-ceramic matrices have also shown a mixed trend in hardness. In a study on 5wt% CNT-alumina borosilicate composites, an increase in hardness of 10% and 23% was observed on adding MWCNTs and SWCNTs, respectively [120]. However, another study of the same authors showed a 31% decrease in hardness of 15wt% CNT-alumina borosilicate composites [109]. Figure 2.7 shows the published hardness data of CNT-glass/glass-ceramic matrix composites, obtained by Vickers macro/microhardness and Berkovich nanohardness techniques. None of the CNT-glass/glass-ceramic matrix composites showed a continuous increase in hardness to high CNT loadings, although improvements up to 5wt% are reported in several systems. Sharp increases at low CNT contents are most likely to be related to changes in matrix morphology.

ii. Elastic modulus

Like hardness, published data for elastic modulus of CNT-glass/glass-ceramic matrix composites shows different trends, as a direct result of different composite microstructures and the quality of CNTs used. Since the focus of CNT-glass/glass-ceramic composites is usually toughness, therefore, relatively less data is available (Figure 2.8), which is generated by disparate techniques depending on available sample size, i.e. three or four point bending tests, instrumented indentation and ultrasonic techniques. Some of the reports show increased composite stiffness; for example, a 38% enhancement in silica glass composites at 7.5wt% CNTs, which may be due to the matrix crystallisation [138,144].

Improvements in stiffness of CNT-borosilicate GMCs at low CNT loadings (2wt%) have been noted in the absence of crystallisation effects; however, at higher CNT loadings (3wt%), agglomeration and other consolidation issues lead to a net reduction in performance [106]. In other cases, monotonic reductions in stiffness have been attributed to inhomogeneous dispersion of CNTs, their degradation during processing and insufficient densification of composites, in both glass [106,111] and glass-ceramic matrix composites [109].

iii. Fracture strength

Significant increases in the fracture strength of CNT-glass/glass-ceramic matrix composites have been observed at low to moderate CNT loadings, i.e. <10wt%, using three and four point flexural and compression strength tests (Figure 2.9). However, further increases in CNT contents usually lead to composites with reduced mechanical strength [113] [106,111], although the optimum loading varies with the study and processing. Microstructure and degree of agglomeration is again key, as illustrated by the extra enhancement obtained from 65% to 88% in 3.75wt% CNT-SiO_2 composites [113] on introducing a better surfactant system [118].

iv. Fracture toughness

Fracture toughness is the property that has received most attention, since brittleness is the key limitation of many glass/glass-ceramic systems. The interest was, however, propelled by an early investigation on CNT-Al_2O_3 composites, which showed a three times improvement in fracture toughness compared to monolithic alumina [114]. Although, this substantial increase was seen in a crystalline ceramic, the studies on glass matrices also explored the possibility of the introduction of toughening mechanisms through the incorporation of CNTs. However, such a level of improvement in toughness was never observed in later studies in any of the amorphous or crystalline ceramic matrix composites containing CNTs [73].

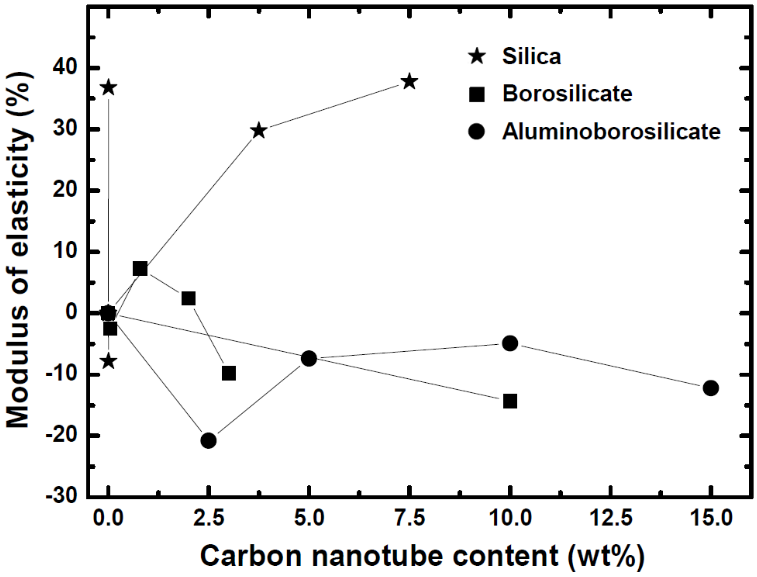

Figure 2.8: Percentage variation in modulus of elasticity of glass and glass-ceramic matrix composites containing carbon nanotubes (published data) [106,109,111,138,144].

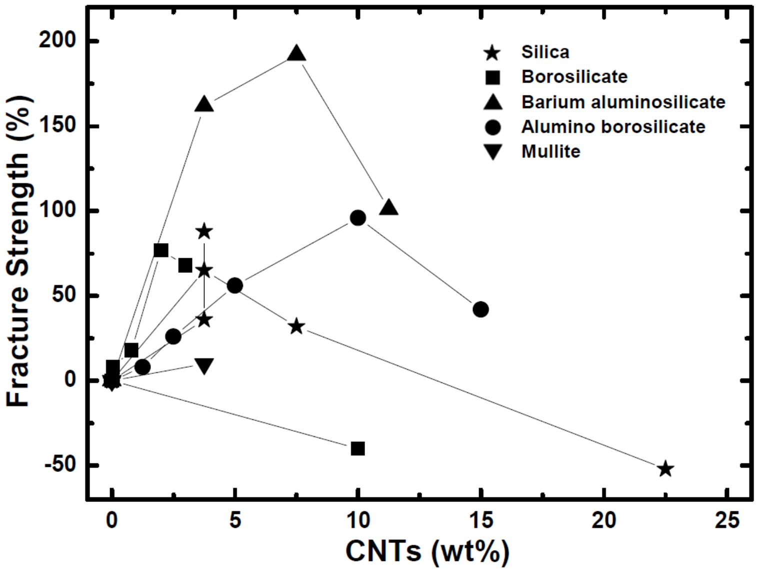

Figure 2.9: Percentage variation in fracture strength of glass and glass-ceramic matrix composites containing carbon nanotubes (published data) [106-109,111,113,118,131].

Due to the small available sample volumes, a large number of studies on CNT-glass/glass-ceramic matrix composites have employed Vickers indentation fracture (VIF) toughness techniques to assess fracture toughness. VIF is a simple technique which enabled the comparison between toughness values of the composites and those of unreinforced glass/glass-ceramic matrices based on the length of cracks emanating from the indentation corners. However, there has been some discussion about the validity of such measurements, particularly in poorly consolidated materials [162]. Single edge V-notch (SEVNB) and chevron V-notch (CVNB) techniques are the better guide for absolute fracture toughness values. Nevertheless, comparative studies have shown that both approaches can offer similar trends, though VIF tends to overestimate CVNB values, for well-processed systems [91].

An increase in fracture toughness has been observed in all composites so far developed (Figure 2.10), although in some cases, a drop again occurs at high CNT loadings due to inhomogeneous CNT dispersion. However, the extent of improvement in fracture toughness, although significant, is limited and the maximum increase of ~150% has been observed [118,144]. This level of improvement in fracture toughness is, in itself, not expected to deliver structurally-reliable composite materials and conventional fibre reinforced composites usually exhibit higher fracture toughness. Nevertheless, the improvements observed using CNTs may provide useful benefits along with the other properties.

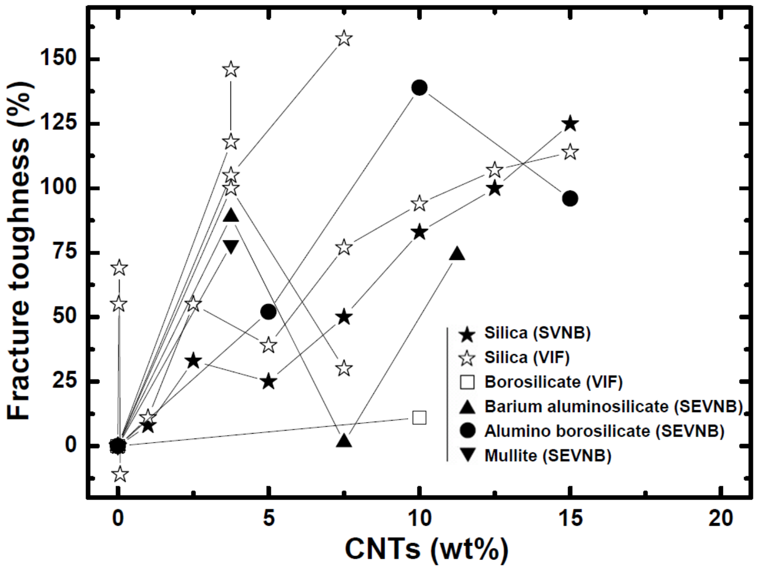

Figure 2.10: Percentage variation in fracture toughness of glass and glass-ceramic matrix composites containing carbon nanotubes (published data) [91,107-109,111,113,118,121,131,137,139,144].

Improvements in toughness of composites are usually attributed to conventional fibre mechanisms, such as debonding, crack deflection, fibre-bridging and fibre-pullout, as these characteristic features are often observed by fractography. However, scaling considerations [91] highlight the lower absolute performance expected for nanofibres compared to microfibres, if only these conventional mechanisms operate. It may, therefore, be useful to consider the possibility of enabling fundamentally new toughening mechanisms such as shear banding of hollow nanostructures.

d. Functional properties

The incorporation of CNTs in glass/glass-ceramic matrices also influences their functional properties including both electrical and thermal conductivities. For completeness, a brief account of these properties is given below.

i. Electrical conductivity

The incorporation of CNTs in glass/glass-ceramic matrices tremendously increases the electrical conductivity of insulating glasses and glass-ceramics (Figure 2.11). At very low CNT contents, electrical conductivity is not increased significantly [126] but the formation of a conducting percolating network of CNTs rapidly increases electrical conductivity by several orders of magnitude. Most of the systems in Figure 2.11 have a percolation threshold between 1wt% and 3wt% CNTs [106,137,159,163]. These values are consistent with the excluded volume theory for high aspect ratio particles, i.e. CNTs of typical aspect ratio of 100-1000.

Low percolating thresholds represent agglomeration of CNTs [122] or their structuring around large micron-size grains in glass-ceramic matrices, while a value >1.0wt% shows a homogeneous dispersion of CNTs with individual CNTs well-separated from others [164]. Higher aspect ratio CNTs give lower percolation threshold and higher absolute conductivity of the composite system due to fewer junctions but are susceptible to alignment effects, i.e. anisotropy in electrical conductivity [90]. This effect was specifically observed in CMCs after extrusion, i.e.

CNT-Fe/Co/$MgAl_2O_4$ composites, where an improvement of a factor of ~30 was seen along the extruded direction due to the alignment of CNTs [153].

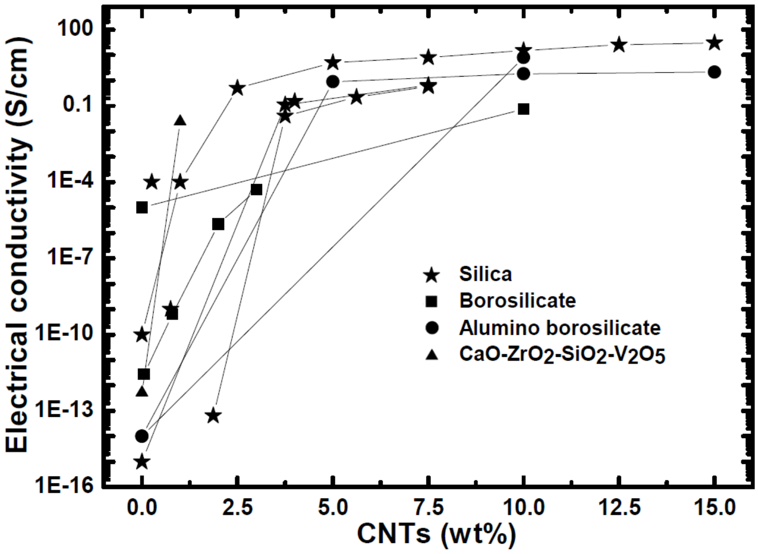

Figure 2.11: Increase in electrical conductivity of glass and glass-ceramic matrix composites containing carbon nanotubes (published data) [90,106,110-111,122,145,163].

ii. Thermal conductivity

Since CNTs exhibit high individual thermal conductivities, i.e. 3000W/m.K, which is greater than graphite (2000W/m.K) and diamond (900W/m.K) [165], it was hoped that composites of extremely high thermal conductivity might be produced. However, the extent of increment (Figure 2.12) is typically rather low (<100%), due to the high interfacial density associated with nanoscale particles. Similar levels of enhancement have been observed at elevated temperatures, i.e. 650°C [117].

The characteristic percolation behaviour observed for electrical conductivity is not mirrored in the thermal response. The fundamental reason is that there are far fewer orders of magnitude of variation between the thermal conductivities of CNTs and glass/glass-ceramic matrices than in the electrical case. Only modest improvements in thermal conductivity are possible on incorporating discontinuous CNTs in glass/glass-ceramic matrices. Many reasons may limit the enhancement, including the presence of structural defects in CNTs, non-uniform dispersion of CNTs producing agglomerates, insufficient densification of composites leading to porosity, preferential alignment of CNTs producing anisotropic composite properties, and the presence of new phases at the CNT/glass interfaces; however, even apparently good quality composites disappoint. Simple rule of mixtures expectations have never been met, even when the random CNT orientation is taken into account, due to the strong influence of interfaces [159].

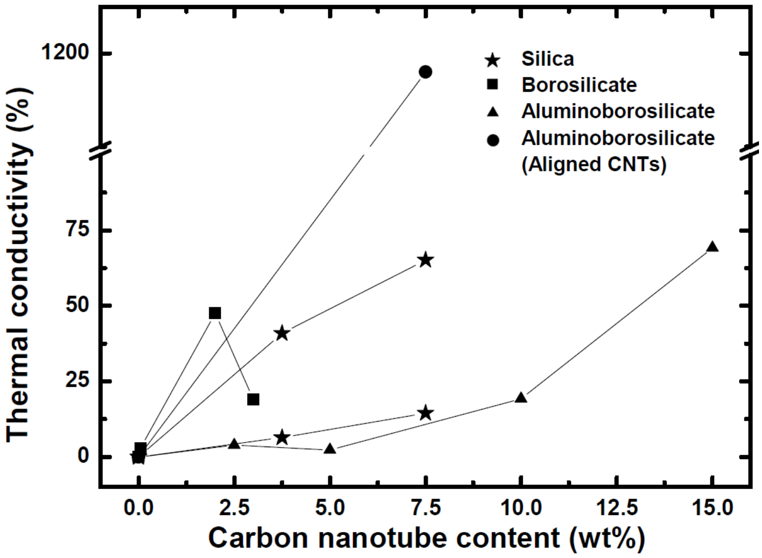

Figure 2.12: Percentage increase in thermal conductivity of glass and glass-ceramic matrix composites containing carbon nanotubes (published data) [90,106,117,146,163].

e. Technological properties

A variety of technological properties of CNT-glass/glass-ceramic composites are particularly relevant to potential industrial applications, such as thermal shock, cycling and ageing behaviour, and wear and friction resistance. No data on these properties is available; however, related reports on CNT-ceramic matrix composites and carbon fibre-glass/glass-ceramic matrix composites highlight the importance of these technological characteristics, as discussed below.

i. Thermal shock resistance

Some of the glasses are sensitive to sudden temperature variations because of their inherent brittleness, high thermal expansion coefficient and elastic modulus, and low tensile strength and thermal conductivity [166]. The internal stresses produced due to the thermal gradients usually result in the catastrophic failure of materials; local strain exceeds the failure strain [165]. One approach to improving their thermomechanical properties has been the manufacture of composites by using suitable reinforcing materials. As a result, a range of GMCs containing different glass matrices, such as borosilicate and silica, and reinforcement types, including SiC, ZrO_2, Al_2TiO_5, NiCrAlY, carbon, oxycarbides, have been developed showing an improvement in thermomechanical properties [82,167-171]. In particular, carbon fibre-reinforced silica glass can avoid cracking on quenching from 1200°C to room temperature [82]. As CNTs possess high strength and thermal conductivity, their incorporation in glasses is also expected to produce thermally conductive composites with enhanced resistance to thermal shock.

For fibre-reinforced GMCs, the thermal shock resistance is experimentally found by subjecting a specimen to a sudden change (i.e. quenching) in temperature from an initial (T_i) to final (T_f) value and observing the damage results, i.e. presence of cracks [167]. T_f is generally kept constant, i.e. room temperature, while T_i is increased until the critical temperature (T_c) is achieved, at which specimen damages. The difference between the two temperatures ($\Delta T = T_c - T_f$) is the safe range wherein a specimen remains unaffected by thermal shock. The damage induced to specimens after thermal shock is determined quantitatively by different mechanical tests, such as flexural or diametral compression tests, to evaluate the decrease in fracture strength or qualitatively by observing the presence of cracks using microscopic or non-destructive techniques, such as forced resonance [167,169]. An alternative technique, the indentation quench test can also be used to determine the critical quenching temperature [171]. In this case, the extension in the length of cracks around the Vickers indentation is measured after quenching at different temperatures.

The resistance to thermal shock is characterised [168] by a parameter (R), which corresponds to the safe temperature range (ΔT) in dense glasses wherein cracks can be avoided, as discussed above and is related to the fracture strength (σ), Poisson's ratio (ν), thermal expansion coefficient (α) and modulus of elasticity (E) of a composite [172], as given below; a high value of R shows better thermal shock resistance.

$$R = \frac{\sigma(1-\nu)}{\alpha E}$$ **Equation 2.1**

Moreover, other factors including the fracture toughness, thermal conductivity, specific heat capacity, geometry and surface roughness of the specimen, and the dispersion quality of the reinforcing phase affect the thermal shock resistance of composites. The presence of microcracks and isolated porosity may provide a means to accommodating some thermal strain and thereby cause reduction of thermal stress under thermal shock loading [168].

ii. Thermal cycling resistance

Sometimes, the thermal shock treatment is repeated for a number of cycles at a particular temperature, at which the composite is intended to be used in the real application. The purpose is to determine the extent of the damage inflicted to the specimen after multiple thermal cycles [167,169]. It has been observed that the thermal shock induced damage increases with repeated cycles, which include the oxidation of reinforcing phases, matrix microcracks, increased matrix crystallisation, matrix softening due to viscous flow above the glass transition temperature, porosity/cavity formation, and interfacial separation/cracking between the reinforcing phase and the matrix. These microstructural changes lead to a decrease in the fracture strength, elastic modulus and a simultaneous increase in the internal friction [167,169].

iii. Thermal ageing behaviour

Thermal ageing of fibre-reinforced GMCs is another significant area of research and has been extensively investigated in carbon fibre-reinforced glass/glass-ceramic matrix composites [169-170,173-174] in order to find the maximum working temperature at which these composites could be used for long periods of time without the substantial deterioration in their microstructure and properties.

In relation to CNTs, the thermal ageing of carbon fibre-reinforced GMCs deserves a special mention here. In an inert atmosphere or vacuum, carbon fibres not only survive but also retain their mechanical properties at temperatures >2000°C; however, they start burning away in oxidising atmosphere at temperatures >400°C [175]. At higher temperatures, particularly

~700°C, carbon fibres completely oxidise leaving behind a porous glass matrix with the considerable decrease in mechanical properties [174]. The oxidation of carbon fibres is, therefore, the main disadvantage to limit the use of carbon fibre-reinforced glass/ceramic matrix composites for high temperature applications in oxidising atmospheres.

The oxidation of fibres also accelerates with the presence of matrix microcracks [176], which are generated after cooling from the sintering temperature due to the difference in the coefficients of thermal expansion between the two phases, and serve as short-circuit diffusion paths for oxygen to access carbon fibres. However, at a temperature above the glass-transition of the glass matrix, the microcracks heal by the viscous flow and the rate of fibre oxidation reduces, as observed in borosilicate glass matrices [176]. It shows that the composition of glasses also affects the carbon fibre oxidation; glasses containing boric trioxide (B_2O_3) tend to be less porous and protect carbon fibres by forming a thin layer around fibres due to their increased viscosity in the temperature range of 600-1100°C, thus reducing the available surface area of fibres exposed to oxidation [177]. In contrast, more viscous silica-based glasses offer a temperature advantage over B_2O_3 containing glasses but do not perform well at lower temperature ranges.

Coatings on carbon fibres also reduce their oxidation but the coating quality determines the fibre protection level; CVD-coated SiC was observed to increase the oxidation rate while dip-coated SiC reduced it [177]. The increase in the oxidation rate was associated with cracking and debonding of the CVD-coating during fabrication, which provided diffusion paths between the coating and the carbon fibres. Both silicon carbide and silicon nitride are the leading candidate materials for the protection of carbon fibres against oxidation [177]. Other protective CVD-grown coatings, including pyrolytic carbon and titanium nitride have also been developed on carbon fibres [178], in particular, titanium carbide using a molten salt method [179].

The above literature survey shows that the thermal shock, cycling and ageing behaviour of different types of fibre-reinforced GMCs have been comprehensively studied; however, no related reports on CNT-glass/glass-ceramic matrix composites are available except a single letter on CNT-ceramic matrix composites, i.e. CNT/Si_3N_4 composite system [180], which only discusses the thermal shock resistance using an indentation-quench method. In this letter, an increase in thermal shock resistance was observed with the addition of 1wt% CNTs in composites, which decreased to a temperature lower than that of the pure Si_3N_4 after increasing the amount of CNTs to 3wt%. A decrease in the strength of the composites and thermal shock resistance was attributed to the agglomeration of CNTs.

iv. Friction and wear resistance

Graphite is known as a solid lubricant [181]. Its outstanding lubricating properties are due to the layered graphitic structure, i.e. graphene sheets containing weak van der Waals bonding, which permits an easy shear and thus provides a low friction [182].

Wear and friction behaviour of carbon fibre GMCs has been extensively studied, with varying types of carbon fibres, glass matrices, testing parameters, and counter sliding bodies, i.e. cast iron, steel, aluminium alloys, alumina and silicon carbide [183-189]. The addition of high modulus fibres has been shown to lead to a lower wear rate and friction coefficient due to their higher graphiticity [183]. However, a parallel opinion relates the wear rate to matrix property only and excludes the role of the graphitic quality of carbon fibres [187]. The impregnation quality of carbon fibres is also reported to improve the wear resistance [186].

Generally, discontinuous carbon fibre GMCs show a higher wear rate and friction coefficient than continuous fibre systems [184]. The orientation of fibres with respect to the sliding direction, i.e. parallel, antiparallel or normal, is another factor; lowest wear rate is claimed in parallel [183] and antiparallel directions [184] against a smooth counter surface, while the normal direction is favoured while abrading against a rough surface, i.e. SiC paper [185].

Two wear types are commonly observed, depending upon the sliding velocity, i.e. mild and severe; mild wear is characterised by a minimal surface pitting of the composites and less plastic deformation of metallic counter bodies, which results in a low wear rate and friction coefficient and vice versa [188]. In hybrid composites, the presence of hard reinforcing phases with carbon fibres, such as SiC particles, reduces the wear rate but causes severe damage to the counter body [186]. The wear mechanisms include the fibre fracture, glass particle detachment and abrasion [190] . The temperature rises as a result of the sliding contact between the counter bodies but stabilises after a given time [190]. However, further increases in the sliding velocity increase the temperature linearly [188]. Wear tests performed at the higher temperatures, i.e. 400°C, have also shown an increased friction coefficient [189]. Due to the intense grinding, the fragmentation of the matrix and fibres lead to the formation of a third body, which forms a bed of glass powder, the compaction of which causes velocity accommodation. Wear rate decreases when the adhesion quality of this third body improves with the counter bodies [187]. A layer of graphite is reported to form on the counterbody, which provides adequate lubrication during the experiment, leading to a decreased friction coefficient and wear rate [188,190]. The transfer of glass particles on the counter body is also observed.

After an insight into the wear and friction characteristics of carbon fibre-reinforced GMCs, it can be expected that the incorporation of CNTs in glasses/glass-ceramics will contribute to enhanced wear and friction properties of the composites. Although, no such published data on CNT-GMCs is available, related studies on CNT-CMCs, both as coatings [191-193] and as bulk composites, including alumina [194-198], silicon nitride [199-200] and carbon-carbon [201] as matrices, indicate better wear and friction properties compared to the CNT-free matrices. The friction coefficient of CNT-ceramic matrix composites always decreases with an increase in CNTs. However, a strong dependence of the friction coefficient on the applied load has been observed; a higher load provides a high friction coefficient [192,194]. Generally, an increase in wear resistance has been shown with increasing amounts of CNTs in composites [192-193,197,199]; however, a few of the studies show a decrease in wear rate at low CNT contents (<5wt%), which reverses (increases) with increasing CNT content (>10wt%) [194,198,200]. The wear volume, however, always increases with the applied load and the test duration [192].

Wear and friction experiments on CNT-ceramic matrix composites are performed by different methods; commonly available techniques are pin-on-disc and ball-on-disc tests [194,196-199]. These micrometer scale wear/friction tests use a ball or a pin of a hard material, which slides under pressure against the surface of the composite specimen. A variety of materials ranging from hardened steels [191,195] to ceramics (Si_3N_4 [194], ZrO_2 [193] and WC [192]) are used with varying applied loads and sliding speeds, depending on the type of composites to be tested. The techniques using diamond indenter have also been used at the nanometer length scale [193,195].

The main wear mechanism in CNT-ceramic matrix composites is abrasion [194]. Wear debris is produced during the test, which consists of pulled-out ceramic particles, deformed CNTs and fine crushed particles generated due to the fragmentation of large particles during surface abrasion. The restriction of crack propagation by the bridging of CNTs has also been observed, which indicates the role of enhanced fracture toughness in restraining the cracks and hence reduce wear. The two competing phenomena of graphitisation and amorphisation of CNTs have also been discussed in literature, attributed to densification and deformation of CNTs under sliding loads, respectively [192-193]. However, amorphisation is more likely to be present due to the severe damage of CNTs. The deformed CNTs are anticipated to exist at the sliding surface as a CNT-derived graphitic film, which develops during the sliding of counter bodies [196,202]. The resulting friction behaviour is related to the development of a graphitic film over the contact area, which is expected to permit easy shear and assist in achieving a lubricating effect [196,202]. However, some undamaged CNTs have also been noticed within the cavities on the wear scar [194,199].

2.6 Summary

A comprehensive analysis of the published data of CNTs and glasses/glass-ceramics reveals their remarkable properties, which make them attractive to be used as reinforcement and matrix, respectively, in order to produce a novel class of nanocomposites, i.e. CNT-glass/glass-ceramic matrix composites. However, processing issues related to the retention and dispersion of CNTs and composite densification are still hindering their further development. As a result, the few available studies provide insufficient information about the actual potential of these composites, especially, given the tendency for matrix microstructural changes.

Uniform CNT dispersion and good composite densification are the key requirements and are mutually dependent; an inhomogeneous dispersion of CNTs without full densification is as deleterious to the properties of composites as a complete consolidation with poorly dispersed CNTs. A combination of the optimum outcome of these two processes can only provide high-quality composites for reliable property characterisation. Moreover, the associated microstructural changes in the matrix materials, i.e. degree of crystallinity, crystallite size and the location of CNTs, within or along the grain boundaries, make it difficult to interpret the true role of the incorporated CNTs. Due to the relatively low CNT loadings in composites, their influence on the matrix microstructure often dominates over their intrinsic and specific effects on the composite properties. Moreover, the high surface area, network forming ability and the distribution of CNTs along matrix particles can strongly influence the processing particularly the viscous flow densification of glass matrices.

Improvements in fracture toughness, fracture strength, and electrical and thermal conductivity are promising but the extent of their increase in relation to the intrinsic effect of CNTs in an amorphous and brittle matrix must be determined after obtaining high quality CNT dispersion and the good composite densification. In particular, quantification of the potential toughening effects due to the CNT-derived mechanisms, including crack deflection, pullout, bridging and debonding is required, in order to understand the significance of their relative contribution to toughening. Surprisingly, it is not yet clear whether the incorporation of CNTs in hard and brittle matrices increases the stiffness and hardness of composites or otherwise. The effect of the hollow core of CNTs and their flexible nature are other issues, which require to be related to the mechanical properties of the composites. No reports describing the wear and friction behaviour, and thermal resistance, i.e. thermal shock and ageing, are available highlighting these aspects of CNT reinforced GMCs.

The SEM/TEM composite microstructures rarely show the CNT dispersion at a large specimen area, which indicates a good CNT dispersion limited only to local areas. Similarly, the existence of a good quality bonding between CNTs and the inorganic matrices, is generally reported without relating the type of bonding to the properties of the composites. Interfaces form a large surface area in CNT composites and play a dominant role in defining their properties. Finally, the scaling effect of CNTs, i.e. diameter, length and aspect ratio on the composite mechanical and functional properties, requires exploration in inorganic matrix composites.

In light of the above, a comprehensive study on the manufacturing and characterisation of CNT reinforced inorganic matrix composites is required, which could address the manufacturing issues and explore the true effect of the incorporation of CNTs without the influence of indirect effects. In relation to these secondary effects of CNTs, the amorphous glass matrices are particularly interesting, since they can avoid matrix microstructural changes. In addition, good quality CNTs are required to be used as the reinforcement, if the intention is to manufacture good quality composites for subsequent comprehensive characterisation. Only the development of such composites can provide the clear understanding of the effects of CNTs on a wide range of mechanical, functional, and technological properties in inorganic matrices, as planned in this thesis.

3. Aims and objectives

The aims and objectives of the present study are highlighted along with the strategy to achieve them. In the end, a schematic diagram is shown, relating the tasks with the manufacturing and characterisation techniques.

In the light of the comprehensive literature review in Chapter 2 and the summary outlined at the end, the following aims were defined at the beginning of this research work:

1. To develop a composite system based on good quality CNTs and a brittle and amorphous matrix to serve as a model system for inorganic matrix composites.

2. To comprehensively characterise the model composite system, in order to understand the intrinsic role of the incorporation of CNTs without the indirect effects on matrix.

3. To apply the developed CNT reinforced model composite system to at least one commercially-available glass to ensure the reliability and reproducibility of the manufacturing technology to other inorganic matrix composites.

In order to achieve the aforementioned aims, the following objectives were defined:

1. Use of good quality CNTs with different sizes, preferably synthesised by the same technique to avoid any variation in their quality. Moreover, perform microstructural, thermal and dimensional characterisation of CNTs before incorporating them in composites.

2. Selection of a suitable inorganic material to act as a brittle and amorphous matrix in composites.

3. Application of the most appropriate CNT dispersion technique and optimisation of its parameters in order to achieve a high quality dispersion of CNTs up to high loadings, i.e. 10wt%, without the formation of agglomerates.

4. Use of a suitable sintering process and optimisation of its parameters in order to consolidate the composite mixtures into dense material without CNT degradation or matrix crystallisation.

5. Investigation of the true effect of incorporating CNTs on the mechanical properties of composites, such as hardness, stiffness, fracture toughness and strength, while considering the hollow core and flexible structure of CNTs.

6. Assessment of the extent of improvement in electrical and thermal conductivity in composites, as they relate to the size and geometric characteristic of the CNTs used.

7. Investigation of the effect of CNTs as a potential lubricating agent on the wear and friction resistance of composites.

8. Characterisation of the effect of CNTs on the thermal shock resistance of composites after single and repeated quenching cycles.

9. Determination of the thermal stability of the composites at different temperatures and durations and detailed investigation of the oxidation of MWCNTs and of the degradation of matrix.

10. Study of the effect of different sizes (diameter, length, aspect ratio) of CNTs on the properties of composites by developing composites with a range of CNT dimensions.

To develop a model composite system, as described above, MWCNTs of four different types were synthesised by CVD and a commercially available amorphous silica powder was chosen as the matrix material. Borosilicate glass was chosen in combination with MWCNTs to manufacture another composite system as an example of the successful implementation of the developed composite fabrication technology. The technique of heterocoagulation upon colloidal mixing was chosen to homogeneously disperse MWCNTs in glass matrices. MWCNT suspensions were prepared by the conventional acid-treatment process. PLS was chosen to densify the composite powder by considering its cost effectiveness, simple processing and adaptability to different sizes and shapes.

The sintered composites were comprehensively characterised in terms of microstructure and properties. Archimedes method was used to determine composite densities while Vickers and Berkovich indentation, and diametral compression tests were chosen to measure the hardness, elastic modulus, fracture strength, and fracture toughness of composites. Impedance spectroscopy was selected to measure electrical conductivity while laser flash method and differential scanning calorimetry (DSC) were selected to measure thermal conductivity of composites. A reciprocating rig was chosen to perform wear and friction tests while the water quench method was used to perform thermal shock and cycling tests. A muffle furnace was used for heating the specimens at high temperatures for thermal ageing experiments. Raman spectroscopy (RS) was used to indicate the crystallinity of MWCNTs at each stage of the composite manufacturing while XRD was used to confirm the amorphous state of the glass matrix. Finally, SEM and TEM were utilised in order to investigate the microstructure of the composites. All these characterisation techniques are comprehensively described in Chapter 4 and the synthesis of MWCNTs and manufacturing of composites along with the results and discussion are presented in Chapters 5-7.

To guide the readers, Figure 3.1 schematically displays the tasks and the chosen manufacturing and characterisation approaches.

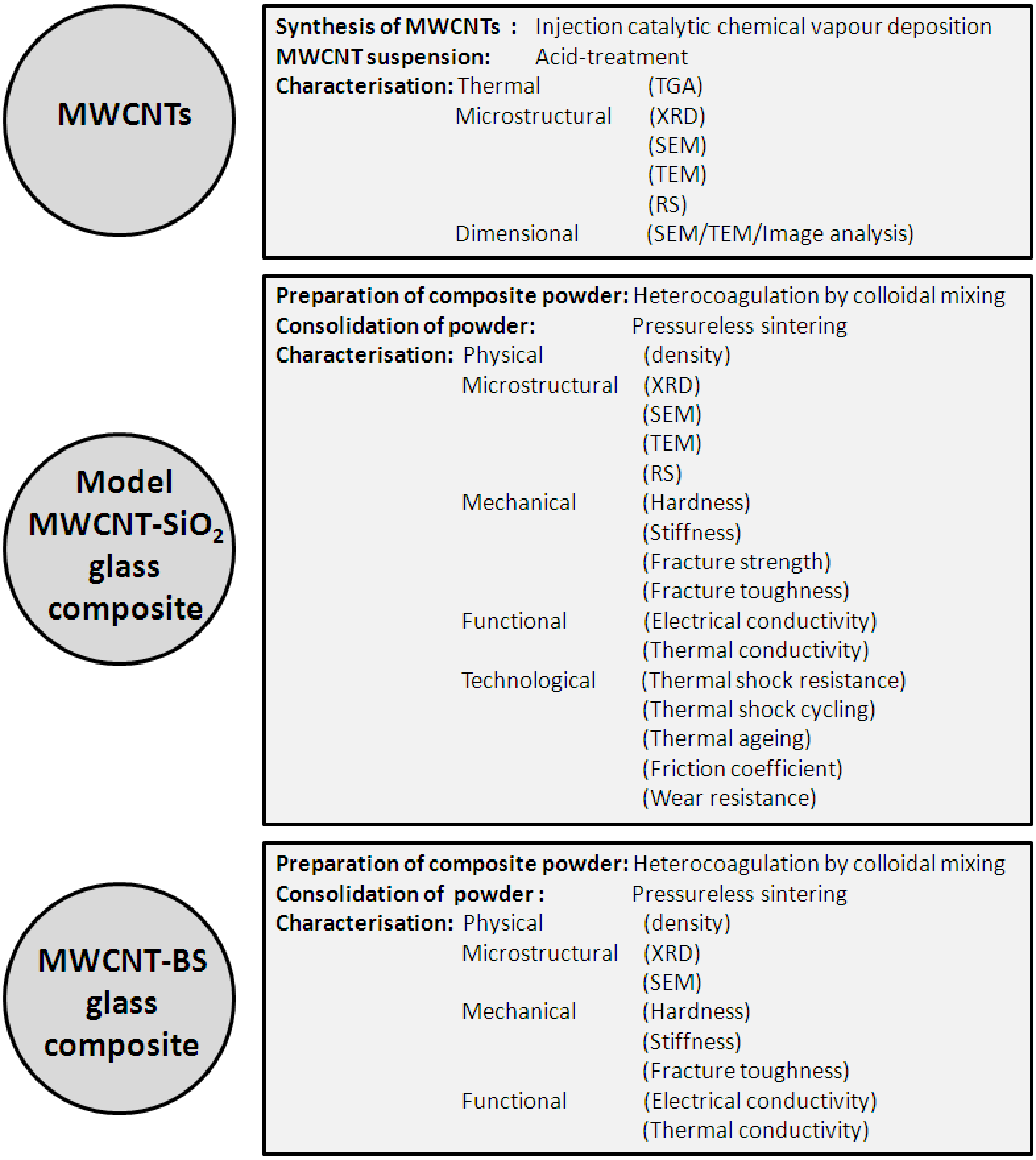

Synthesis of MWCNTs : Injection catalytic chemical vapour deposition
MWCNT suspension: Acid-treatment
Characterisation: Thermal (TGA)
Microstructural (XRD)
(SEM)
(TEM)
(RS)
Dimensional (SEM/TEM/Image analysis)

Preparation of composite powder: Heterocoagulation by colloidal mixing
Consolidation of powder: Pressureless sintering
Characterisation: Physical (density)
Microstructural (XRD)
(SEM)
(TEM)
(RS)
Mechanical (Hardness)
(Stiffness)
(Fracture strength)
(Fracture toughness)
Functional (Electrical conductivity)
(Thermal conductivity)
Technological (Thermal shock resistance)
(Thermal shock cycling)
(Thermal ageing)
(Friction coefficient)
(Wear resistance)

Preparation of composite powder: Heterocoagulation by colloidal mixing
Consolidation of powder : Pressureless sintering
Characterisation: Physical (density)
Microstructural (XRD)
(SEM)
Mechanical (Hardness)
(Stiffness)
(Fracture toughness)
Functional (Electrical conductivity)
(Thermal conductivity)

Figure 3.1: Schematic diagram showing the main tasks and the chosen manufacturing and characterisation approaches.

4. Characterisation techniques

The physical, microstructural, thermal, mechanical, functional and technological characterisation techniques used throughout the present investigation are summarised in this chapter along with their parameters employed.

4.1 Physical characterisation

4.1.1 Density

The density of specimens was measured using the Archimedes principle:

$$\rho = (\frac{M_d}{M_w - M_s})\rho_s \qquad \textbf{Equation 4.1}$$

where ρ and ρ_s are the densities of specimen and water, respectively, and M_d, M_w and M_s correspond to dry mass, water-saturated mass, and water-submerged mass of the specimen. The mass of the dry specimen was first measured after drying the specimen in an oven at 120°C. The specimens were then immersed in water and allowed to saturate. Water penetrated into open pores accessible from the surface. A vacuum pump was employed to force out any air bubbles present in the pores. Now the mass of the specimen was measured in water submerged and saturated condition. Finally, the mass of the water-saturated specimen was measured after taking it out of the water and carefully removing the water from the specimen surface; the only water left in the specimen was in open pores. The obtained density was divided by the theoretical density to find the relative density, as a percentage of the theoretical density. The theoretical density was calculated using the rule of mixtures. At least five measurements were taken for each glass and composite system and the average density values along with the standard deviations are presented.

4.2 Microstructural characterisation

4.2.1 X-ray diffraction

XRD was performed to characterise as-synthesised MWCNTs, as-received glass powders and densified glass and composite specimens in both the green and sintered states. A PANalytical XPert Pro Multi Purpose X-Ray Diffraction System (XPert Pro MPD) was employed in θ-θ reflection mode, using Cu K_α radiation with a nickel filter, electronically controlled divergence slits and a beam width of 10mm. A 2θ range from 15° to 70° was selected with a step size of 0.0334° and scan time of one second per step. The sintered specimens were polished with a diamond suspension of 1μm particle size while the glass and composite powders were pressed in a small die to prepare flat surface discs.

4.2.2 Raman spectroscopy

RS was used to examine the degree of crystallinity of MWCNTs in both the as-synthesised and acid-treated states, and also after reinforcing glass matrices in green and sintered states. A Raman spectrophotometer (LabRAM Infinity, HORIBA Jobin Yvon Ltd) was used with a 633nm He-Ne laser. A total of five scans were acquired with an acquisition time of 40sec per scan.

The graphitic (G) and disorder (D) peaks were measured at 1580cm^{-1} and 1350cm^{-1}, respectively, and the degree of crystallinity of MWCNTs was qualitatively determined by comparing the intensities of D and G peaks; a low I_D/I_G ratio indicates high crystallinity [203]. The G peak is inherent in graphite lattices and corresponds to in-plane stretching modes, while the D peak appears due to the presence of defects in graphitic structure, such as individual graphene layer edges, stacking disorder between layers and atomic defects within layers [204]. In single graphite crystals and highly ordered pyrolitic graphite, the D peak is absent, while it is observed in other forms of graphite, including commercial graphite and CNTs [205-206].

4.2.3 Scanning electron microscopy

SEM was performed on as-synthesised and acid-treated MWCNTs, as-received glass powders, and fractured surfaces of green and sintered specimens. Field Emission Gun Scanning Electron Microscope (FEM-SEM) Leo Gemini, Carl Zeiss was used in secondary electron imaging (SEI) mode at 5kV. As-synthesised aligned MWCNTs were attached to aluminium stubs with carbon tape, while diluted suspensions of acid-treated MWCNTs and glass powders were dried on stainless steel substrates attached to aluminium stubs. The glass and composite specimens were sputter-coated with chromium (K550 Emitech, UK) for 1min at 75mA to avoid electron charging, while MWCNTs were imaged without coating. Microstructural features of the specimens, including the MWCNT dispersion, residual porosity and toughening mechanisms, such as pullout, crack deflection and crack bridging, were also observed by SEM.

The dimensions of as-synthesised and acid-treated MWCNTs, and MWCNT pullout lengths from the fractured specimen surfaces were measured using the SEM images in combination with image analysis software (Image J, NIST, US), where the scale bar on images was used as reference length. At least 500 measurements were taken to acquire the average values, which were shown with standard deviations.

SEM was fitted with an energy dispersive X-ray spectrometer (EDS) (Oxford Instruments INCA, UK), which was used for the qualitative elemental analysis of the worn specimen surfaces, after wear tests, with and without the presence of graphitic films at 20kV operating voltage.

4.2.4 Transmission electron microscopy

TEM was performed on as-synthesised and acid-treated MWCNTs and composites using the transmission electron microscopes (JEM 2000FX and 2010, JEOL Ltd., Tokyo, Japan). Microstructures were examined in the microscopes, operated at a voltage of 200kV, using the bright-field (BF) imaging and selected area electron diffraction (SAED) modes. Holey carbon films (Agar, UK) were used as the supporting grids to image MWCNTs, while thin sections of specimens were prepared by using a dual focused ion beam (FIB) equipment (FEI Helios 600

Nanolab). A selected area of the composite was milled using gallium ions [207]. A beam current of 21nA was used for initial rough cuts, followed by 9nA, 6.5nA and 93pA for finer cuts, at an acceleration voltage of 30kV. Final clean milling and polishing were performed using a beam current of 47pA and 28pA at an acceleration voltage of 5kV and 2kV, respectively.

The inner and outer diameters of MWCNTs were also measured using the TEM images; scale bar was used as a reference length. At least 100 measurements were taken to acquire the average values, which are presented with standard deviations.

4.3 Thermal characterisation

4.3.1 Thermogravimetric analysis

TGA was used to determine the MWCNT oxidation stability (related to their graphitic quality) and their concentration in suspensions and composites. Approximately 1.0mg and 2.0mg of as-synthesised MWCNTs and composite powders, respectively, and a volume of ~60µl of MWCNT suspensions was heated at 10°C/min in air in a TGA setup (Perkin Elmer Pyris 1). A maximum temperature of 800°C was chosen for as-synthesised MWCNTs and acid-treated MWCNTs in suspensions, while 900°C was selected for silica glass composite powders. MWCNT suspensions were sonicated before acquiring the representative sample for TGA. At least three measurements were performed to determine the concentration of MWCNTs in suspensions and composites.

4.4 Mechanical characterisation

4.4.1 Hardness

The Vickers micro-indentation technique was employed to measure the hardness of specimens. A microhardness tester (Zwick/Roell Indentec ZHV) equipped with Vickers pyramid diamond indenter was used to produce indentations at room temperature at a load of 500g (4.9N) for 10sec. At least, 10 indents were taken for each specimen. The diagonal lengths of the indentations were measured using an optical microscope attached to the microhardness tester; the optical micrographs were also recorded. The diagonal lengths were further verified by acquiring the SEM images of the indents and measuring the lengths using scale bar as a reference length. The specimen surfaces were polished with a diamond suspension of 1μm particle size before hardness testing. The measured diagonal lengths (d) along with the applied load (F) were used in the following expression [208] to calculate the Vickers hardness values (H_v):

$$\boldsymbol{H_v = \frac{2\,sin\left(\frac{136^{\,o}}{2}\right)F}{d^{\,2}}} \qquad \textbf{Equation 4.2}$$

In addition, the Berkovich nano-indentation technique was utilised to determine the hardness of specimens. A nano-indentation instrument (Nanotest, Micro Materials Ltd. UK) equipped with a diamond Berkovich indenter was operated at a load of 500mN at room temperature. At least, 30 indentations were performed on each specimen. The average hardness values obtained from the two techniques are presented along with the standard deviations.

In the nano-indentation technique, an indenter is pushed into the specimen surface to produce a small indent (micrometer size), which cannot be accurately measured by an optical microscope. Therefore, the projected area of the indent is indirectly determined from the depth of penetration (indenter displacement) and geometry of the indenter tip. An established method of Oliver and Pharr [209-210] is usually followed to extract the hardness from the load-displacement data (Figure 4.1) of a complete cycle of loading and unloading in a nano-indentation test, which provides the contact area of indentation. Hardness is then obtained using the maximum load (P_{max}) and the contact area (A_c) in the following equation:

$$\boldsymbol{H = \frac{P_{max}}{A_c}} \qquad \textbf{Equation 4.3}$$

The errors in the nano-indentation measurements can come from the specimens as well as the indenter. Therefore, smooth specimen surfaces were obtained after polishing the specimens with a diamond suspension of 1μm particle size before hardness testing. The area calibration was carried out to include the effect of the diamond indenter tip bluntness.

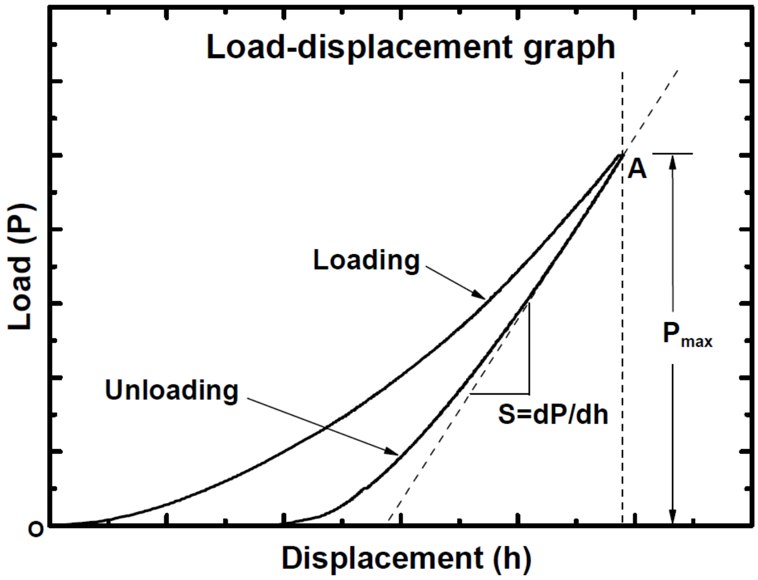

Figure 4.1: Typical load-displacement data obtained from an instrumented Berkovich nano-indentation, showing the loading and unloading curves, and important parameters.

4.4.2 Elastic modulus

Elastic moduli of the specimens were determined simultaneously with the hardness measurements in the nano-indentation tests (Section 4.4.1). The slope (S) of the unloading curve in the load-displacement diagram (Figure 4.1) and the contact area (A_c) provide the reduced modulus (E_r), which combines the elastic displacements in both the indenter and the specimen:

$$E_r = \frac{S}{2}\sqrt{\frac{\pi}{A_c}}$$ **Equation 4.4**

The elastic modulus of the specimen is then derived by eliminating the contribution from indenter, using the following expression, where E and ν are the elastic modulus and Poisson's ratio of the specimen, while E_i and ν_i corresponds to the values of the indenter, respectively. If E_i, ν_i, and ν are known, E can be calculated.

$$\frac{1}{E_r} = \frac{(1-\nu^2)}{E} + \frac{(1-\nu_i^2)}{E_i}$$ **Equation 4.5**

At least, 30 indentations were performed on each specimen to acquire the data for elastic modulus and average values along with the standard deviations are presented.

4.4.3 Indentation fracture toughness

Indentation fracture toughness is based on measuring the length of radial cracks emanating from the corners of the indentations. Vickers indentation method was used to produce at least 10 indents on each specimen at a load of 2kg (19.6N) for 10sec. The specimen surfaces were polished with a diamond suspension of 1μm particle size before producing indents. The diagonal lengths of the indents and the resultant crack lengths were measured by optical microscope attached to the microhardness tester (Zwick/Roell Indentec ZHV); the optical micrographs were also recorded. To further verify the length of the cracks and the size of the indents, SEM images of the indents were acquired and the measurements were taken. The expression derived by Anstis et al. [211] was used to calculate the indentation fracture toughness (K_{IC}), as frequently used for CNT-glass/ceramic matrix composites [73]:

$$K_{IC} = 0.016 \left(\frac{E}{H}\right)^{1/2} \left(\frac{P}{C^{3/2}}\right) \qquad \textbf{Equation 4.6}$$

where E, H, P and C represent the elastic modulus, Vickers hardness, indenter load and average radial crack length, respectively. The average indentation fracture toughness values are presented along with the standard deviations.

4.4.4 Diametral compression strength

Thermally-shocked composite specimens (diameter 6mm, thickness 1mm) were tested under diametral compression (Brazilian test) in a mechanical testing machine (Zwick/Roell Z010, Germany) at a crosshead speed of 0.1mm/min. At least five specimens were tested for each condition and average values are presented along with the standard deviations. The expression used to measure the diametral compression strength (σ) is given below [212]:

$$\sigma = \frac{2P}{\pi D t} \qquad \textbf{Equation 4.7}$$

where P, D and t are the applied load, diameter and thickness of the specimen, respectively. The diametral compression test is an easy way to indirectly measure the tensile strength of materials, such as coal, concrete, rocks, glasses, ceramics, polymers and composites [212]. The diametral compression test is based on the fact that compressive stresses are developed along the loaded diameter, when a circular disc is compressed diametrally, while tensile stresses develop perpendicular to it. These perpendicular tensile stresses at the centre of the disc initiate a crack, which causes the disc to fracture along the diametral plane of the applied compressive load. A schematic diagram of the diametral compression test is given in Figure 4.2 showing the direction of tensile stress produced in the specimen due to the applied compressive stress. For the present experiments, specimens of diameter 5.5mm and thickness 1.5mm were used [212].

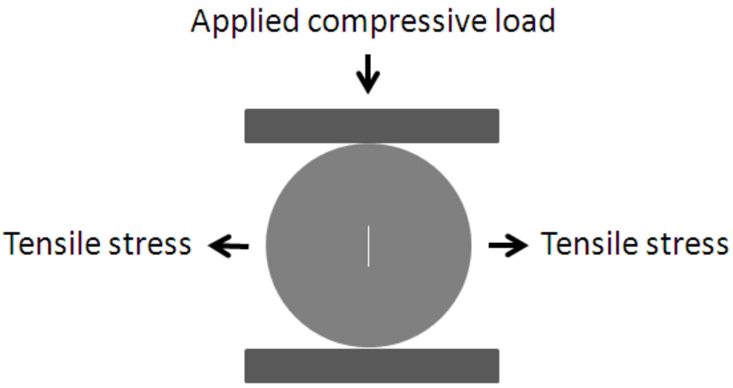

Figure 4.2: Schematic diagram of the diametral compression (Brazilian) test.

4.5 Functional characterisation

4.5.1 Electrical conductivity

Electrical conductivity of the specimens was measured by impedance spectroscopy. The specimens were gripped in the parallel platinum electrodes. The opposite surfaces of the disc-shaped specimens were coated with the conducting silver paint in order to establish a good contact with the electrodes. The platinum electrodes were connected to a potentiostat/galvanostat (Type SI 1287, Solatron) and to a frequency response analyzer (Type 1255, Solatron). The frequency was changed from 1MHz to 1Hz while the AC voltage was kept at 1000mV. At least five measurements were performed for each specimen and the average electrical conductivity values are shown along with the standard deviation. The impedance (Z) of the specimen is a complex number, which can be represented as the following expression [213]:

$$Z(\omega) = Z_{real} + jZ_{img}$$ **Equation 4.8**

where Z_{real} and Z_{img} are the real and imaginary parts of the impedance, respectively.

$$Z_{real} = |Z| \cos \phi$$ **Equation 4.9**

$$Z_{img} = |Z| \sin \phi$$ **Equation 4.10**

Electrical conductivity was determined by normalising the real impedance against the change in frequency.

$$\sigma_c = \frac{A}{Z_{real}\, d}$$ **Equation 4.11**

where A and d represent the area and thickness of the specimens, respectively.

4.5.2 Thermal conductivity

Thermal conductivity (K_c) of the specimens was calculated by measuring the thermal diffusivity (α), specific heat capacity (C_p) and density (ρ) of the specimens, and using these values in the following expression:

$$K_c = \alpha\, C_P\, \rho$$ **Equation 4.12**

Specific heat capacities were determined by the differential scanning calorimetry (DSC) while thermal diffusivities were measured using the laser flash method (LFA 447, Nanoflash) at room temperature. This technique involves increasing the temperature on one side of the specimen by heating with a laser flash and measuring the temperature rise of the other side as a function of time by an infrared detector. The analysis of the temperature-time data is performed by a well-known half-time method:

$$\alpha = 0.1388 \frac{l^2}{t_{50}}$$ **Equation 4.13**

where l is the thickness of the specimen and t_{50} corresponds to the 50% increase in temperature of the rear of the specimen. At least 10 measurements were performed for each specimen and the average thermal conductivity values are presented along with the standard deviations.

The colloidal graphite coating was used on the two flat surfaces of the disc-shaped specimens before thermal diffusivity measurements. The front surface coating prevents the laser transpassing and the rear surface coating prevents the infrared detector to be affected before the heat pulse travels to the rear surface, which can be a source of error providing increased thermal diffusivity values.

4.6 Technological characterisation

4.6.1 Thermal shock

Thermal shock resistance tests were performed by the conventional water quench method [214]. The specimens (diameter 6mm, thickness 1mm) were heated in a muffle furnace (P330 Nabertherm, Germany) in air at the temperatures of 500°C, 1000°C and 1200°C followed by quenching into an unstirred water bath maintained at room temperature, i.e. 20°C. This simple process was performed manually with tongs but the reproducibility was ensured with regards to the time span for transferring the specimens from the furnace into the water bath in ~3sec. Five samples were heated every time to a predetermined temperature at a heating rate of 10°C/min in the furnace and held for 10min followed by dropping into the water bath. The specimens were kept in water bath for 5min and later inspected visually and by SEM for the appearance of any macroscopic damage such as surface cracking, change of dimensions, colour or shape, or any other surface defects. Diametral compression tests were also performed to observe any change in the fracture strength of the specimens, as discussed in Section 4.4.4.

4.6.2 Thermal cycling

In thermal cycling resistance tests, the specimens (diameter 6mm, thickness 1mm) were heated up to 1000°C at a heating rate of 10°C/min in the furnace (P330 Nabertherm, Germany), held for 10min and dropped into water bath and kept there for 5min. The process was repeated for 10 and 20 times on the same specimens; before performing the next thermal cycle, they were dried in an oven at 150°C for 1h to remove the moisture from their surface due to dropping them into water. At least, five specimens were thermally cycled for each test conditions. After thermally shocking the specimens for defined number of cycles, they were inspected visually and by SEM to observe any damage. Diametral compression tests were also performed to observe any change in the fracture strength of the specimens, as discussed in Section 4.4.4.

4.6.3 Thermal ageing

Thermal aging tests involved the exposure of the specimens (diameter 6mm, thickness 1mm) in a muffle furnace (P330 Nabertherm, Germany) at moderate to elevated temperatures, i.e. 500^{o}C to 1200^{o}C, in air for the durations of 6h to 96h after heating at 10^{o}C/min, which was followed by furnace cooling to room temperature. The specimens were later carefully inspected visually and by SEM for any damage, such as cracking, crystallisation, dimensions or colour change, and the oxidation of MWCNTs. The depth of MWCNT oxidation (decarburisation) in composite specimens was measured using the SEM images of the cross-sectional fractured specimen surfaces. At least 100 measurements were taken before presenting the average decarburised depth, along with the standard deviation, in the X-Y plane of the specimens and normal to it (Figure 6.49).

4.6.4 Wear and friction

Wear and friction tests were performed by ball-on-disc and pin-on-disc techniques on a high frequency reciprocating rig (PCS instruments, UK), wherein hardened steel pin or ball of the hardness 750HV were slid against the polished (1μm) specimen surfaces (discs) in a reciprocating motion at room temperature. Two sets of parameters were chosen, i.e. (i) CPM10V steel pin of diameter 36mm for a sliding distance of 72m with a load of 0.15GPa for 60min and (ii) CPM10V steel ball of diameter 6mm for a sliding distance of 36m with a load of 0.50GPa for 30min. The reciprocating frequency and stroke length in each case was 10Hz and 1mm, respectively, and the sliding speed was set at 20mm/s. At least two specimens were tested under the two sets of parameters.

The glass and composite specimen surfaces were polished with a diamond suspension of 1µm particle size to avoid the experimental error coming from specimen surfaces of different roughness.

The frictional force was recorded by a load cell attached to the rig to find the friction coefficient (µ), which is the ratio of the frictional force (F_f) to the normal applied force (F_n) between the sliding bodies, i.e. ball/pin and the composite specimen:

$$\mu = \frac{F_f}{F_n}$$ **Equation 4.14**

The volume loss (wear volume) of the specimens was calculated using an optical profiler (Veeco, Wyko NT9100). Optical profilers are used to measure height variations such as surface roughness using wavelength of light. Optical profiling uses wave properties of light to compare the optical path difference between a test surface and a reference surface. Wear rate (W) was calculated by inserting the wear volume (V), sliding distance (L) and the applied force (F_n) in the following expression:

$$W = \frac{V}{LF_n}$$ **Equation 4.15**

The wear scars produced on the specimens and the deformed steel pin/ball surfaces were observed in SEM together with the wear debris and the graphitic layer produced due to the smearing of MWCNTs.

5. MWCNTs: synthesis and suspension

This chapter describes the synthesis of MWCNTs by injection catalytic chemical vapour deposition and the preparation of their stable suspensions by acid-treatment. Microstructural characterisation of as-synthesised and acid-treated MWCNTs is established using X-ray diffraction, Raman spectroscopy, scanning and transmission electron microscopy. Dimensional measurements are performed by image analysis. Finally, thermal stability is assessed by thermogravimetric analysis.

5.1 Synthesis of MWCNTs

5.1.1 Injection catalytic chemical vapour deposition

MWCNTs were grown by injection catalytic chemical vapour deposition (ICCVD), in which a solution of ferrocene (F) in toluene (T) was injected into a horizontal quartz tube inserted in a tubular furnace. Ferrocene provided an iron catalyst to nucleate MWCNTs while toluene acted as a carbon feedstock for their growth. A motorised injection machine was used to feed the solution of 3wt%F/T into the tube at a rate of 5ml/h through a nozzle system surrounded by an electric heater operated at 200°C. The injected solution evaporated and was carried by the flowing argon at a rate of 2l/min into the quartz tube maintained at 760°C. Aligned arrays of MWCNTs grew on the inner wall of the quartz tube (60mm diameter). The synthesis process was continued for 2h followed by cooling the furnace to room temperature under continuous argon flow to avoid the oxidation of MWCNTs, which were later removed from the tube using a rubber blade and weighed. 2.2±0.1g of MWCNTs were produced in a single run, which is consistent with previous results [159]. A schematic diagram of the process is shown in Figure 5.1, which is similar to one reported earlier [215].

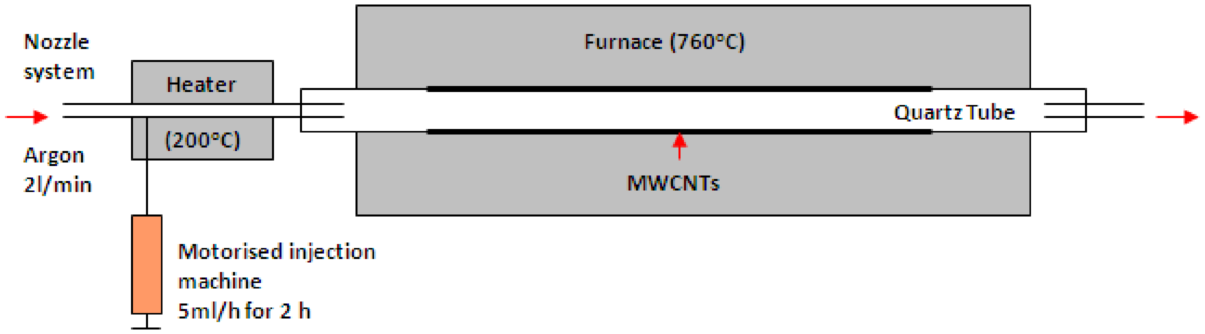

Figure 5.1: Schematic diagram of the synthesis of MWCNTs by injection catalytic chemical vapour deposition (ICCVD).

5.1.2 Microstructural characterisation

As-synthesised MWCNTs were microstructurally characterised by SEM, TEM, XRD and RS. Figure 5.2(a) shows an SEM image of as-synthesised aligned MWCNTs. The high density of nucleation sites provided by ferrocene forced the aligned growth of overcrowded MWCNTs perpendicular to the substrate. The morphology of MWCNTs at their tip, centre and base is shown in Figure 5.2(b-d). A base growth mechanism was observed, wherein the catalyst remains attached to the substrate, as supported by the presence of metallic particles at the roots of MWCNTs (Figure 5.3). EDS and XRD analysis has previously shown the presence of α-iron and iron-carbide using ferrocene as catalyst [215-216]. BF-TEM images of as-synthesised MWCNTs (Figure 5.4) further support the base growth mechanism; straight growth of nanotubes at their roots and closed ends at their tips are evident.

The effect of processing parameters, i.e. furnace temperature, gas flow rate, ferrocene concentration, injection rate and duration, on the diameter, length, alignment and yield of MWCNTs have been previously investigated [159,203,215]. The temperature range of 590°C to 940°C provides aligned MWCNTs while their diameter increases with temperature within this range. At 760°C, the maximum yield of MWCNTs is produced. Raising the ferrocene concentration from

1.5wt% to 9wt% increases the diameter of MWCNTs but reduces their length, while an increase in the injection rate of F/T solution from 1ml/h to 15ml/h increases both the length and diameter. The mass of iron catalyst, however, increases with both the ferrocene concentration in toluene and injection rate of the solution. Varying the carrier gas flow rate had no effect on the MWCNT dimensions [215].

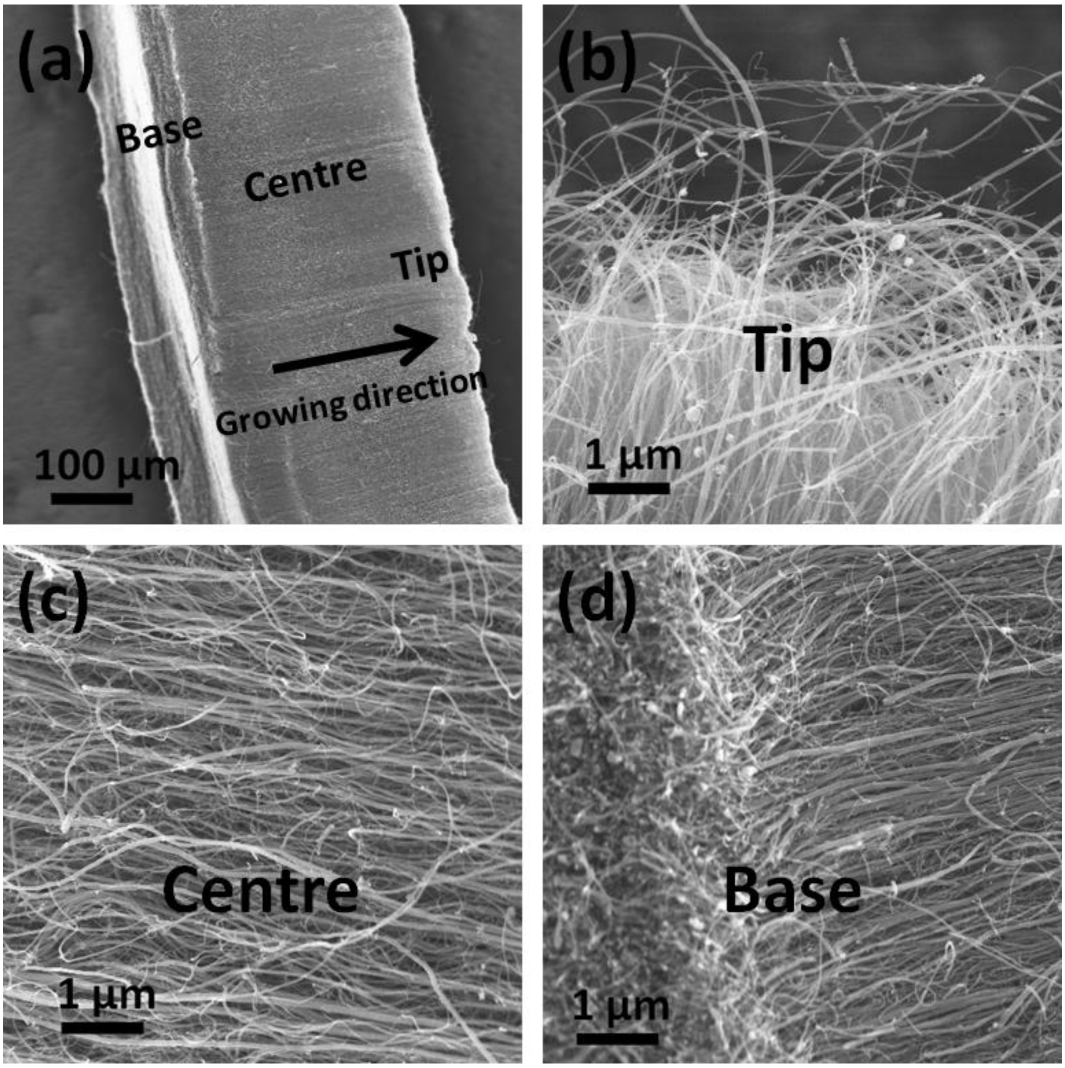

Figure 5.2: SEI-SEM images of (a) aligned MWCNTs synthesised by 3wt% ferrocene in toluene showing morphology of the (b) tip, (c) centre and (d) base of the MWCNTs.

Raman spectroscopy was performed to determine the quality of as-synthesised MWCNTs (Figure 5.5). Typical D and G peaks were observed showing the (I_D/I_G) intensity ratio of 0.40±0.03, as calculated from five spectra of independent MWCNT regimes, which indicates the good crystallinity of MWCNTs; the values matches with published data [203,215].

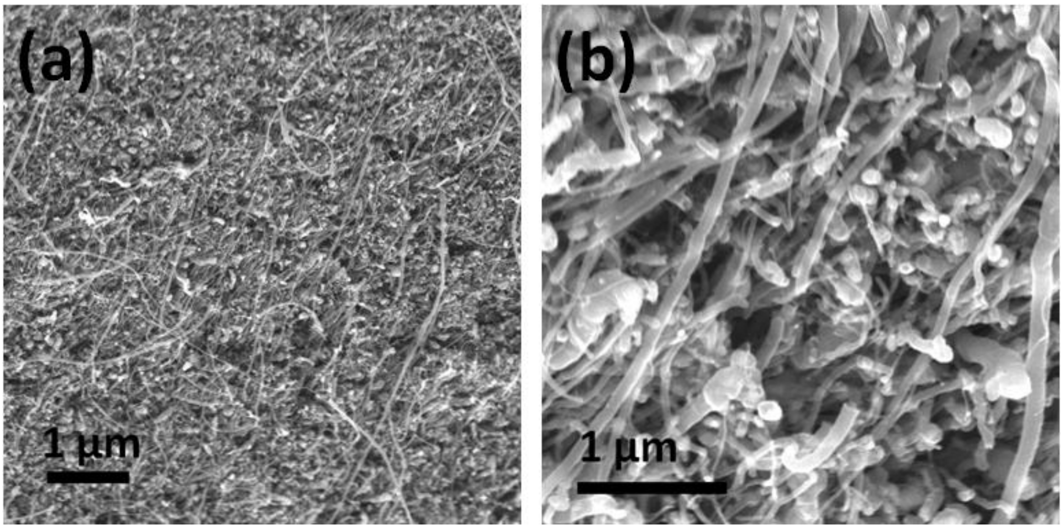

Figure 5.3: (a-b) SEI-SEM images of the roots of MWCNTs showing the presence of catalyst particles, which indicate the base growth mechanism of MWCNTs.

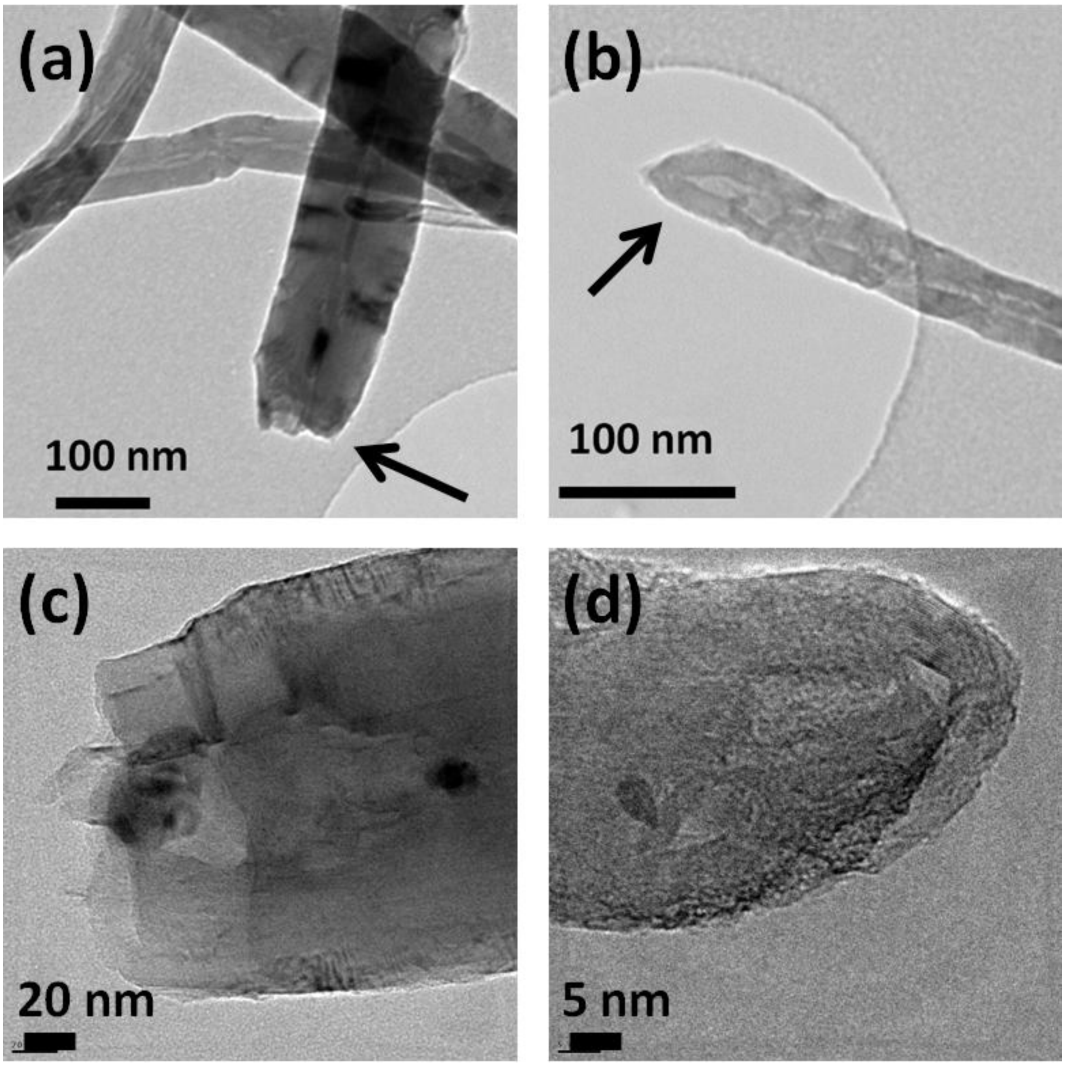

Figure 5.4: BF-TEM images showing (a,c) base and (b,d) tip of as-synthesised MWCNTs.

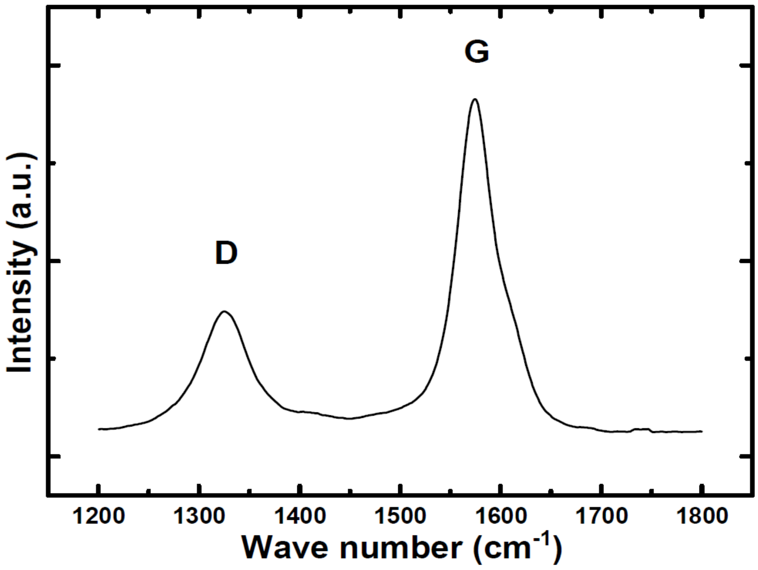

Figure 5.5: Raman spectrum of as-synthesised MWCNTs, showing D and G peaks.

XRD of as-synthesised MWCNTs (Figure 5.6) shows a sharp graphitic peak (002) at 2θ=26.30. Small peaks corresponding to the (100), (110) and (004) planes of MWCNTs were also identified at 2θ=42.60, 44.80 and 54.20, respectively, as also observed elsewhere [117].

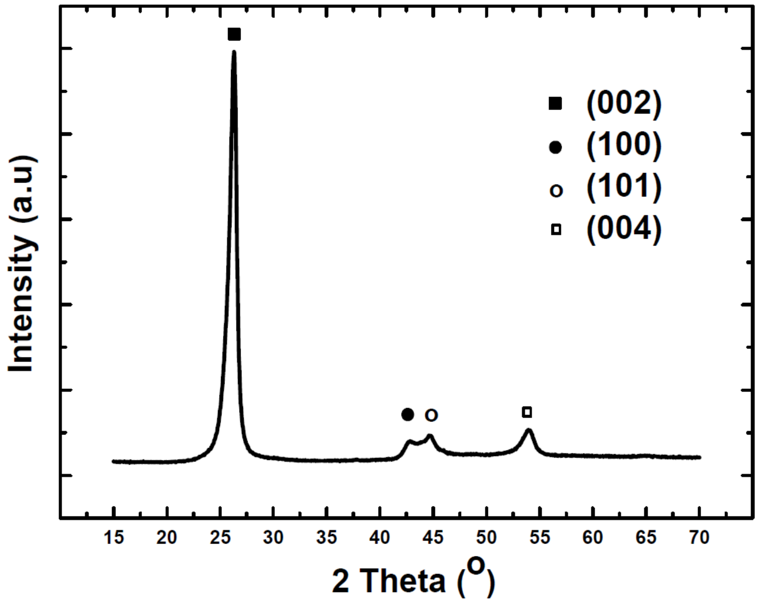

Figure 5.6: XRD of as-synthesised MWCNTs, showing sharp graphitic peak of (002) plane.

5.1.3 Dimensional measurement

The dimensions of MWCNTs were measured using their SEM images taking the scale bar as a reference length. The average diameters of the tip and base of MWCNTs along with the standard deviation were found to be 45±27nm and 70±32nm, respectively. The average values of diameter and length of MWCNTs, along with the standard deviation, were measured to be 58±32nm and 382±14μm, respectively with an aspect ratio >6000. The distributions of tip, base and average diameter, and length are given in Figure 5.7.

The increase in the base diameter of MWCNTs is associated with the catalyst particle size. During the growth of MWCNTs, their diameter gradually increased due to the continuous supply of ferrocene, which steadily increased the size of catalytic iron particles at the roots of MWCNTs. It can be argued that reducing the supply of catalyst after the initial nucleation may provide constant diameter MWCNTs but a previous study shows that the growth of MWCNTs stops if the ferrocene supply is terminated, possibly due to the loss of iron [215]. An uninterrupted supply of ferrocene only provides a continuous growth of MWCNTs but it increases the catalyst particle size leading to an increase in MWCNT diameter. Another associated drawback is the encapsulated metallic catalyst, which lifts upwards into the core of MWCNTs during their growth causing the loss of catalyst at the base of MWCNTs and making them impure (Figure 5.8).

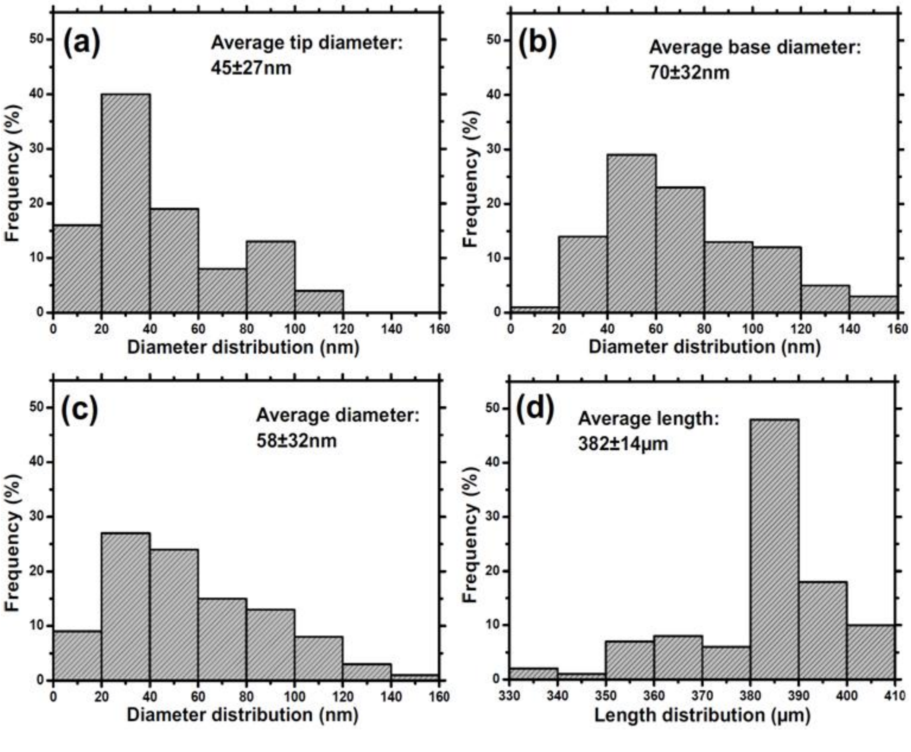

Figure 5.7: (a-d) Length and diameter distributions of as-synthesised MWCNTs.

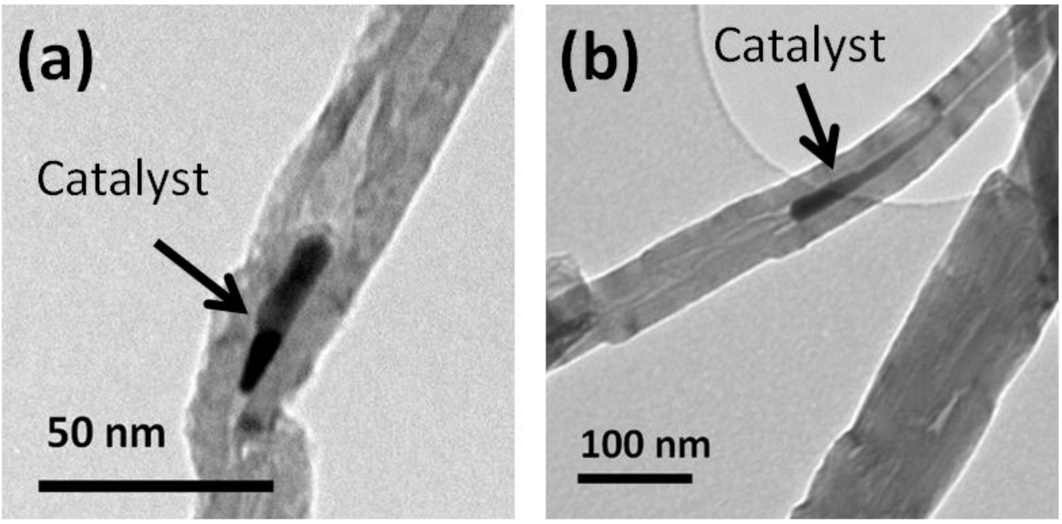

Figure 5.8: (a-b) BF-TEM images of as-synthesised MWCNTs showing the presence of encapsulated catalyst in their core.

5.1.4 Thermal stability

TGA was performed to observe the thermal stability of as-synthesised MWCNTs (Figure 5.9); the oxidation of MWCNTs showed a smooth combustion curve with a sharp combustion peak at ~650°C. The oxidation temperature of MWCNTs matches with the CVD-grown MWCNTs [159]. A 2.63wt% residue relates to the metallic mass used to catalyse the growth of MWCNTs.

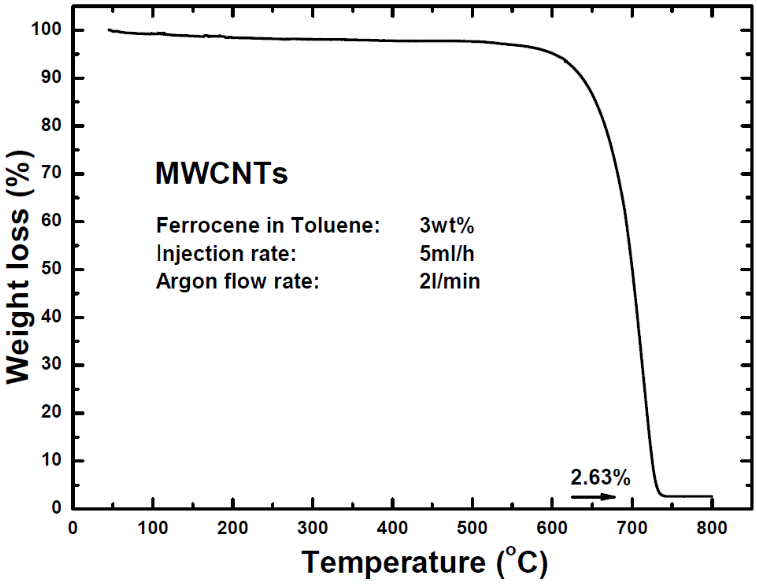

Figure 5.9: TGA of as-synthesised MWCNTs showing the combustion curve.

Generally, CNTs grown by high temperature synthesis processes are reported to be more resistant to oxidation (695°C) than other forms of carbon, i.e. graphite (645°C), diamond (630°C), soot (585°C), and C_{60} (420°C) [217]. However, the presence of defects in CNTs lowers their combustion temperature [159]. As CVD-grown CNTs inherently possess structural defects (Section 5.1.5), they have low decomposition temperatures. Annealing of CVD-grown CNTs at 2200°C is reported to increase their combustion temperature by reducing the number of structural defects [218]. The reaction of gases with carbon materials is slowest within the basal plane but highest at defects including vacancies, steps, and the termination of the basal planes [217]. The seamless graphene tubes in CNTs are considered to be more oxidation resistant, as their outermost layers are only accessible to oxygen. Also, the conformational strain, which makes C_{60} more susceptible to oxidation due to curvature, is lower in CNTs providing them more thermal stability. Oxygen initially reacts at the ends of CNTs; the curvatures along the length of CNTs are the other likely sites of oxidation [219]. CNTs, however, show no thermal transformation in argon [217] up to 1000°C. The diameter of CNTs also influences their oxidative stability; smaller diameter CNTs have higher reactivity due to their higher degree of curvature [218].

5.1.5 Structural features and defects

In addition to the aforementioned features of as-synthesised MWCNTs, other significant structural features observed under SEM (Figure 5.10) were the presence of amorphous carbon, MWCNT fracture and the lack of their straightness, which can be associated with their high aspect ratio and their flexible nature. A large variation in the MWCNT diameter was also witnessed, as quantified in a previous section (Section 5.1.3).

In the TEM, it is possible to observe the structural defects such as local/sharp bends in MWCNTs and the local disruption/disorder in the continuity of the rolled graphene layers (Figure 5.11). Other structural defects including kinking, buckling, twisting and the collapse of MWCNTs resulting in the closure of the inner cavity were also observed (Figure 5.12).

Published data verify the presence of such structural features and defects in CNTs [43]. Single and multiple kinks have been observed, while fully reversible bending up to large angles (>110°) has also been noted. This is due to the remarkable flexibility of the hexagonal network, which resists bond breaking to high strains [46]; size and reversible buckling mechanisms are the key.

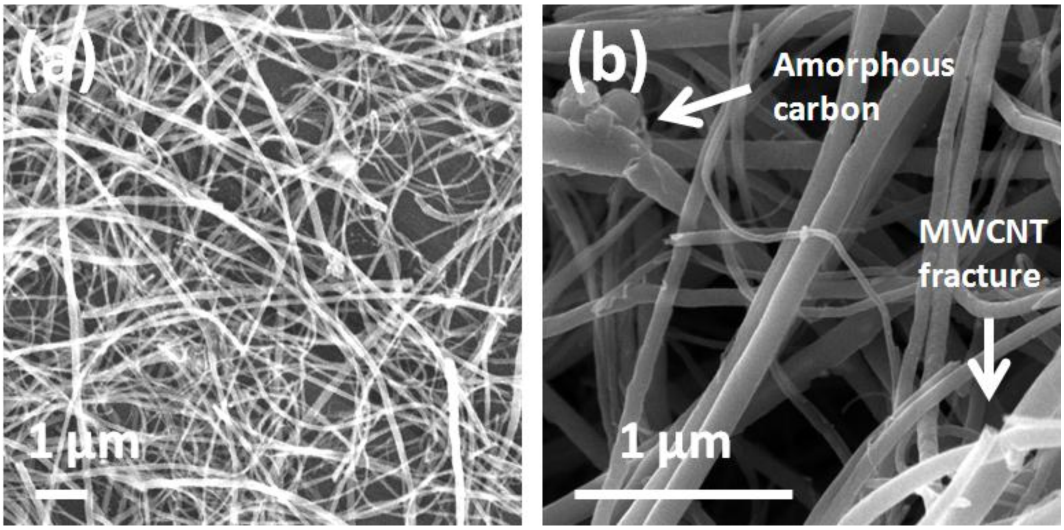

Figure 5.10: (a-b) SEI-SEM images of as-synthesised MWCNTs dispersed in distilled water. The diameter variation, fracture and waviness in MWCNTs are evident along with the presence of amorphous carbon.

5.2 MWCNT suspensions

5.2.1 Acid-treatment

As-synthesised CNTs are hydrophobic, relatively entangled and contain amorphous carbon and catalytic particles. A purification process is required to improve their surface chemistry for better dispersability, and removing unwanted by-products. In addition, incorporating these high aspect ratio (>6000) MWCNTs in glass matrices is difficult and full densification has not previously been achieved in either aligned [90] or randomly-oriented [105] embodiments. To overcome such problems, it is a standard practice to treat CNTs with a mixture of acids [148,220-221]. Acid-treatment removes the impurities from CNTs by preferential consumption [222] and attaches functional groups, such as carboxyl, hydroxyl and carbonyl [223] to the CNT surfaces to obtain stable dispersion in aqueous and organic polar solvents by electrostatic stabilisation. Additional effects of acid-treatment are the length and diameter reduction of MWCNTs by etching [224-227].

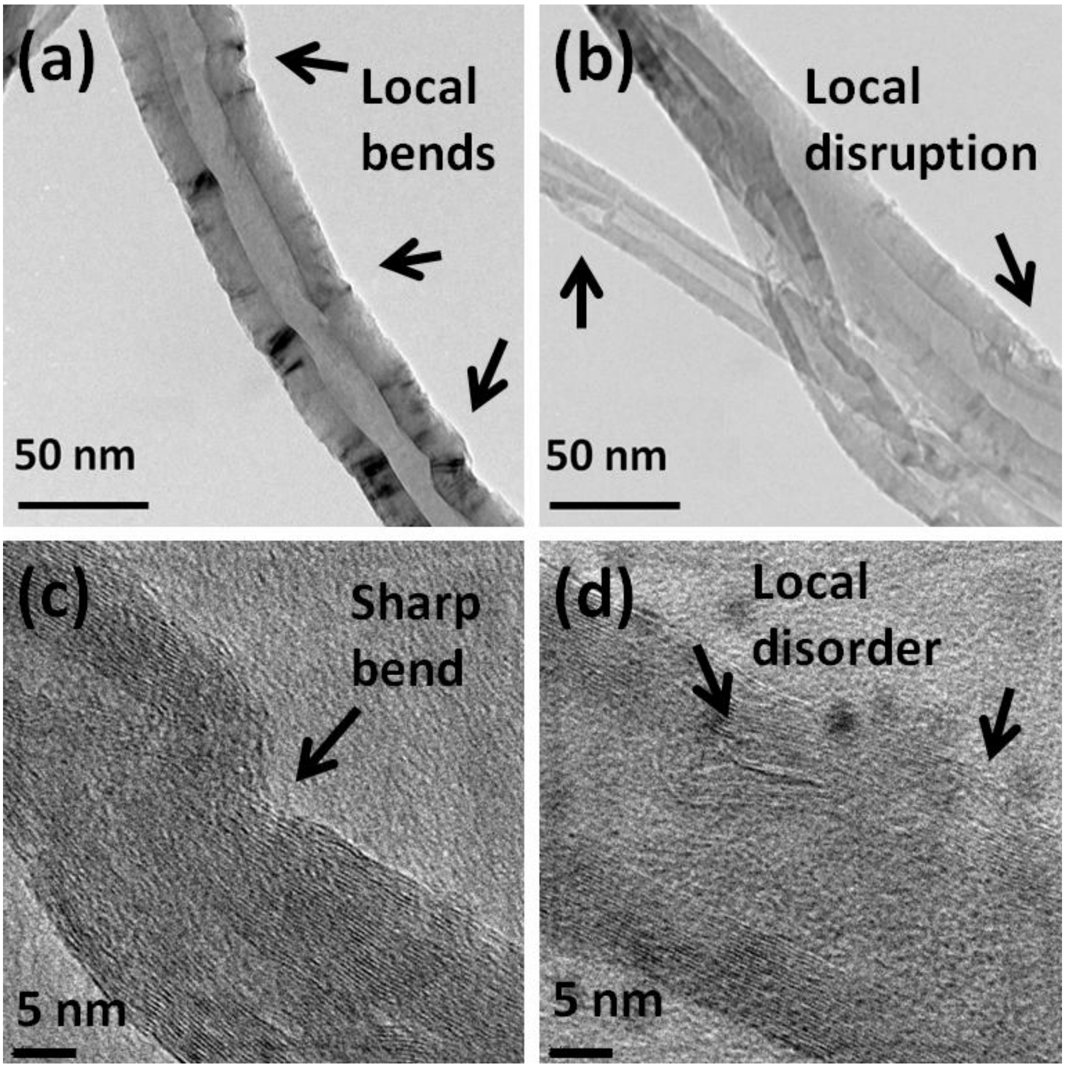

Figure 5.11: BF-TEM images of as-synthesised MWCNTs, showing (a,c) local/sharp bends and (b,d) local disruption/disorder in rolled graphene layers.

In each run, 1g of MWCNTs was acid refluxed in 40ml of 3:1 volume ratio of concentrated sulphuric and nitric acid (95-98% and 70% respectively, Sigma Aldrich Ltd.) at 120°C for 30min. The oxidised MWCNTs were washed with distilled water on a 0.2μm polytetrafluoroethylene membrane, until the filtrate showed pH ≥5.5-6.0. MWCNT suspension was sonicated and centrifuged at 3000rpm for 15min to remove any remaining aggregates and the concentration of MWCNT suspension in distilled water was adjusted to ~0.5mg/ml. A ~50% yield was obtained after treating MWCNTs with 40ml of acid mixture, which is close to those previously reported [159]. A systematic decrease in yield with increasing volume of acid is known [159].

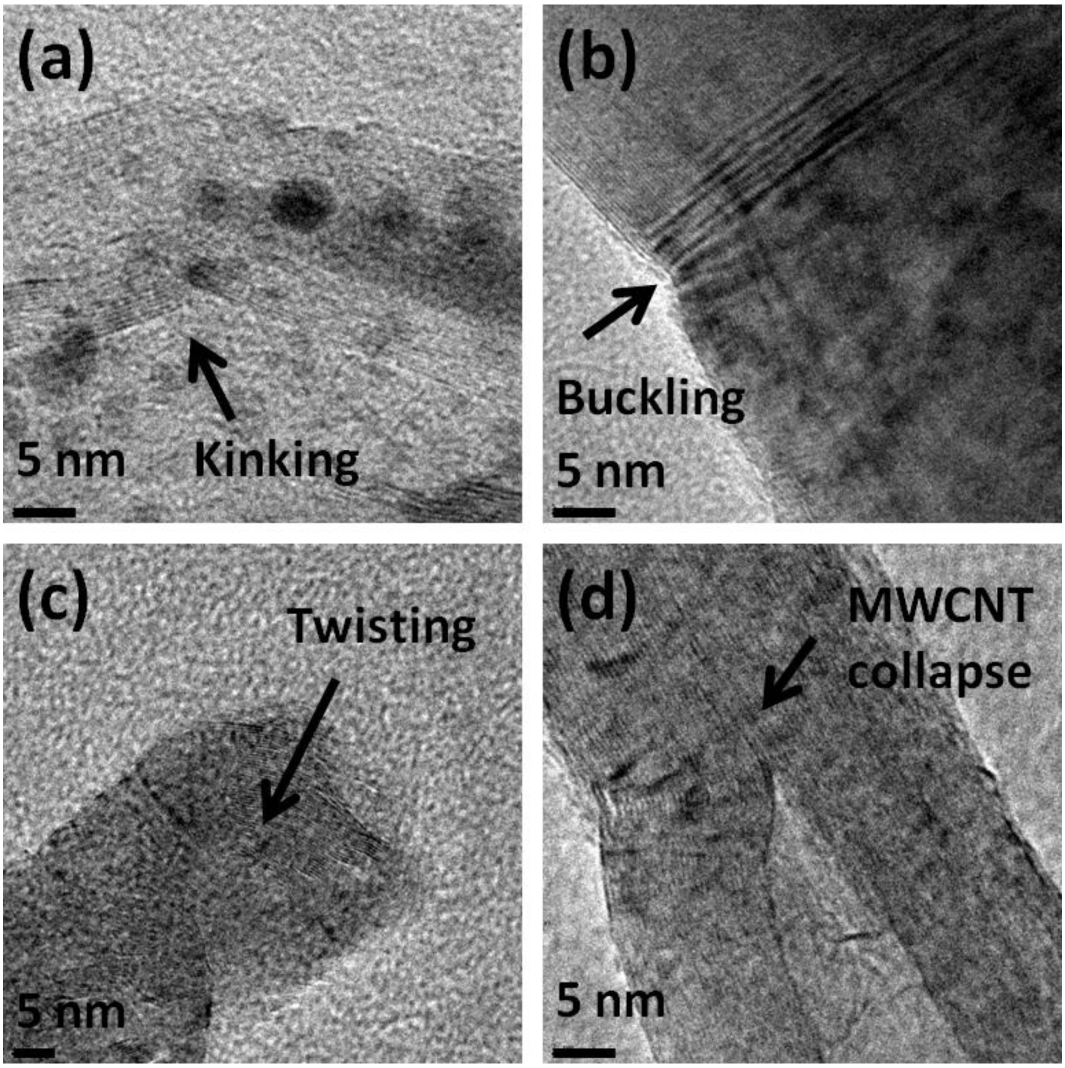

Figure 5.12: HRTEM images of as-synthesised MWCNTs, showing (a) kinking (b) buckling (c) twisting and (d) collapse, resulting in the closure of the inner cavity.

To explore the effect of different diameters and aspect ratios of MWCNTs on the properties of GMCs (Sections 6.2.3 and 6.2.4), aqueous suspensions of three other types of MWCNTs, synthesised by using 1.5wt%, 6.0wt% and 9.0wt% F/T were also prepared. The growth and acid-treatment parameters of these MWCNTs were similar to those synthesised by using 3.0wt% F/T. Moreover, the same ICCVD setup was used for the synthesis of the four types of MWCNTs.

5.2.2 Microstructural characterisation

Acid-treatment produced stable aqueous suspensions of MWCNTs and reduced their levels of entanglement by cutting them in shorter lengths (Figure 5.13(c-d)) compared to as-synthesised entangled MWCNTs, which produced large agglomerates when simply suspended in water without acid-treatment (Figure 5.13(a-b)).

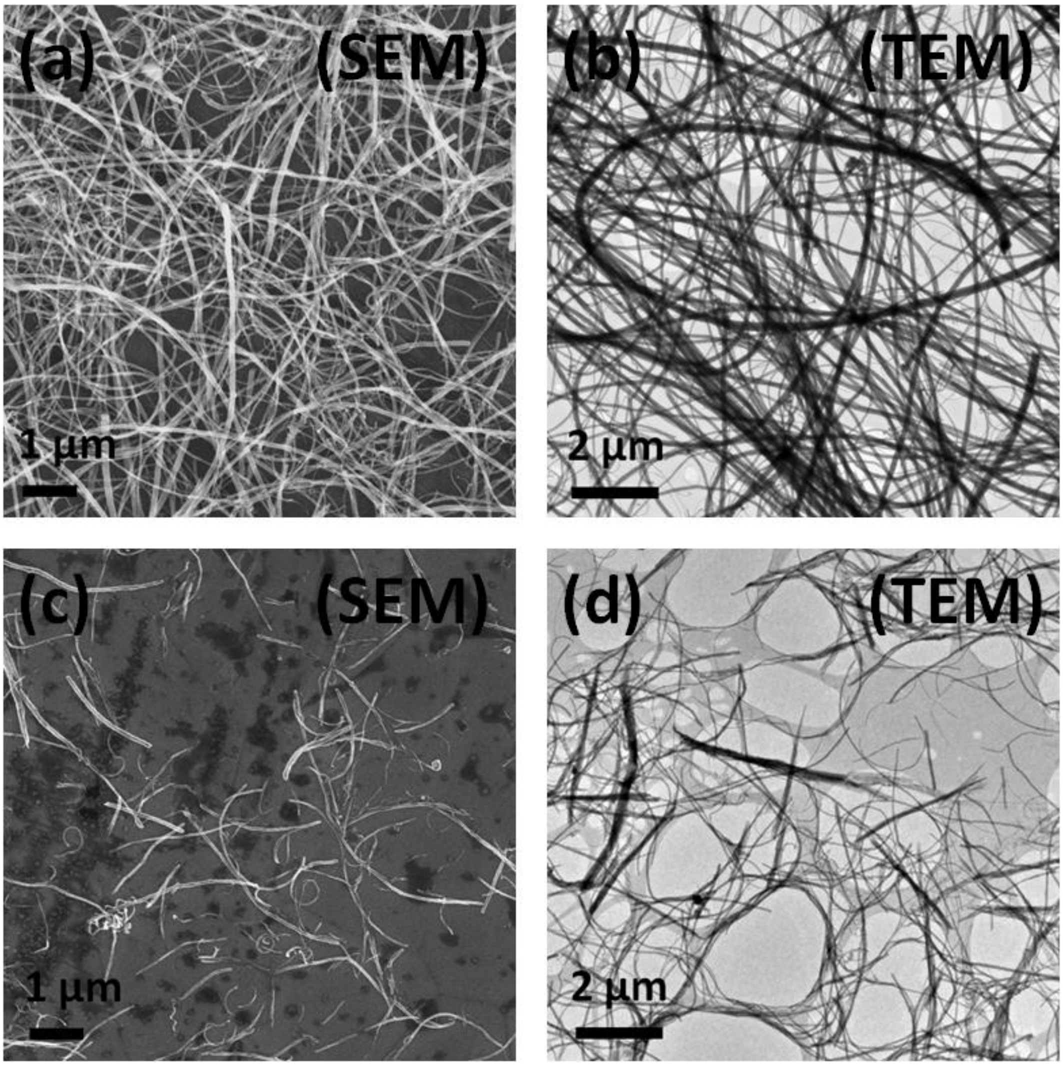

Figure 5.13: SEI-SEM and BF-TEM images of MWCNTs (a-b) before and (c-d) after acid-treatment. The shorter and less entangled MWCNTs are evident after acid-treatment.

HRTEM images confirmed the chemical attack on the MWCNTs resulting in their cutting and thinning (Figure 5.14). The cutting action progresses from the surface into the core of MWCNTs by their etching and is likely to follow the shape of twin-cones joined at their apexes, finally separating a single MWCNT into two conical-end fragments.

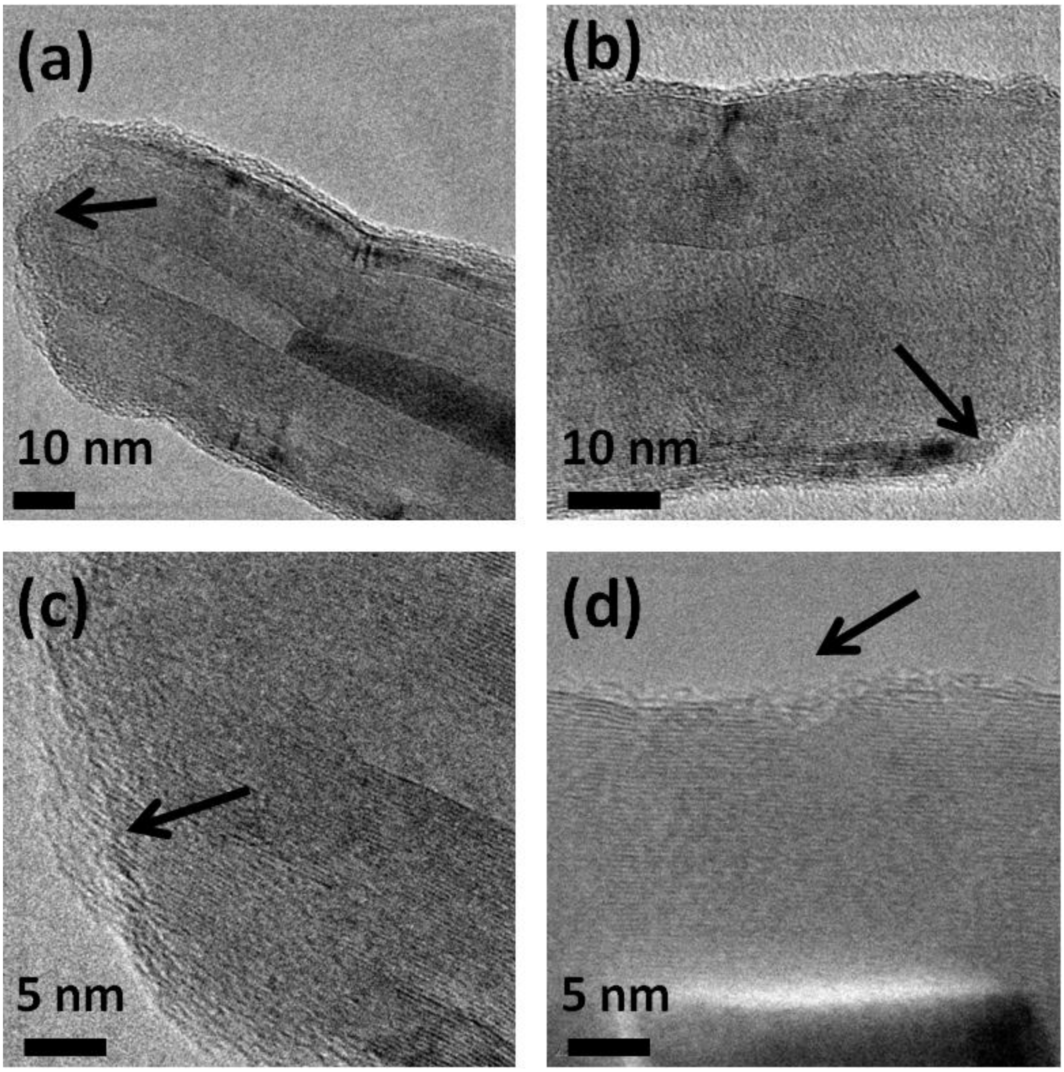

Figure 5.14: HRTEM images of the MWCNTs after acid-treatment showing (a, c) cutting and (b, d) thinning action.

As described in Section 4.2.2, Raman spectra indicate the extent of crystallisation of the oxidised CNTs (Figure 5.15). An increase in the intensity of D peaks shows a significant rise in the disorder of acid-treated MWCNTs due to the introduction of graphite sheet terminals (Figure 5.14). I_D/I_G ratios in the range of 0.8-0.9 were found for the four types of acid-treated MWCNTs compared to 0.40 for as-synthesised MWCNTs (Figure 5.5). The similar extent of damage in each case is not surprising given the similar nature of the materials and oxidation protocol, particularly the same ratio of acid mixture to the quantity of CNTs used; the similarity is helpful for further comparisons of composite performance.

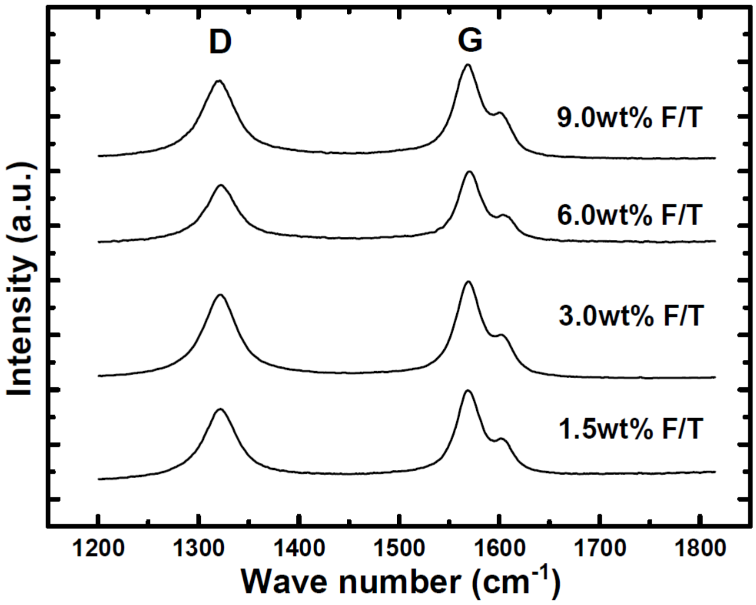

Figure 5.15: Raman spectra of four types of acid-treated MWCNTs, synthesised by different concentrations of ferrocene (F) in toluene (T).

5.2.4 Dimensional measurement

A systematic decrease in length and aspect ratio, and an increase in diameter was observed after acid-treatment in the four types of MWCNTs. (Table 5.1); MWCNT dimensions were measured using their SEM images where the scale bar was used as a reference length. The average values are shown along with the standard deviation.

Table 5.1: Dimensions of four types of MWCNTs after acid-treatment.

Ferrocene concentration in toluene (wt%)	Length (μm)	Diameter (nm)	Aspect ratio
1.5	2.42±1.45	37±14	65±46
3.0	2.22±1.13	44±19	50±33
6.0	2.07±1.09	51±24	40±28
9.0	1.78±0.79	57±27	31±20

As mentioned earlier, an increase of ferrocene in toluene decreases the length but increases the diameter of as-synthesised MWCNTs. After acid-treatment, the four types of

MWCNTs synthesised by different F/T concentrations maintained their relative geometries i.e. decreased length and increased diameter. The acid effect was more pronounced on length compared to diameter. For example, length of 3wt%F/T MWCNTs reduced from 382±14μm to only 2.22±1.13μm while diameter decreased from 58±32nm to 44±19nm. The significant reduction in length had a direct effect on the aspect ratio, which reduced from >6000 to ~50. Similar effects on the dimensions of CNTs were observed previously [159]. The length and diameter distributions of the four types of MWCNTs after acid-treatment are given in Figure 5.16 and Figure 5.17. The length distribution in MWCNTs reduced with an increase in the quantity of ferrocene in toluene. However, the majority of the MWCNTs in the four types had lengths ranging from 1-2μm. An opposite effect was seen for the diameter distribution, where MWCNT diameter distribution increased with increasing concentration of ferrocene in toluene.

5.2.4 Thermal stability

TGA data (Figure 5.18) of the acid-treated MWCNTs shows a decrease in their thermal stability due to the structural disorder and the presence of carbonaceous fragments on their surface. As-synthesised MWCNTs showed a single and sharp combustion peak around 650^{o}C (Figure 5.9) while thermal degradation of acid-treated MWCNTs showed a multi-stage process, as also observed elsewhere [223]. The first stage corresponds to the evaporation of adsorbed water from the hydrophilic surfaces up to 200^{o}C. The second stage, between 200^{o}C to 500^{o}C is attributed to the removal of oxygen containing groups, especially hydroxyls, carbonyls, and carboxylics; these groups are covalently bound to the outer surfaces of CNTs and called oxidation debris. In the third stage, disordered carbon starts decomposing at ≥500^{o}C and finally the oxidation of MWCNTs began and continued up to complete combustion at around 700^{o}C [223,228]. TGA data supports the presence of the oxidation debris and surface defects. In addition, the onset of the final combustion moved to lower temperature compared to as-synthesised MWCNTs (Figure 5.9). The effect was more intense in MWCNTs of smaller diameter produced by using 1.5wt%F/T. Carbon fibres have also been treated with acids and the presence of polyaromatic fragments on their surfaces was witnessed [229].

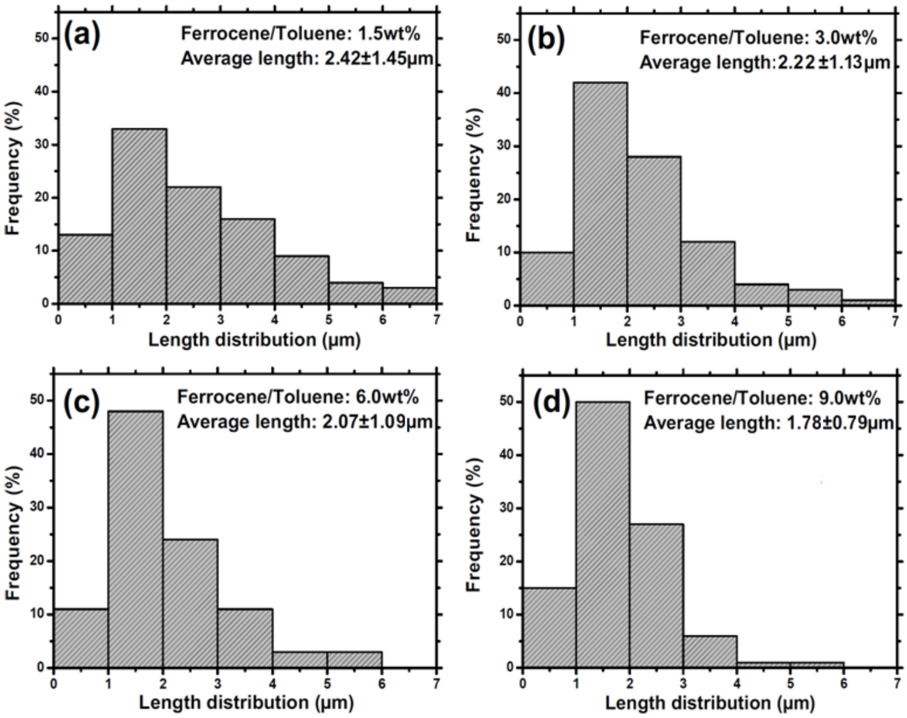

Figure 5.16: Length distributions of MWCNTs produced by (a) 1.5wt% (b) 3.0wt% (c) 6.0wt% and (d) 9.0wt% ferrocene in toluene.

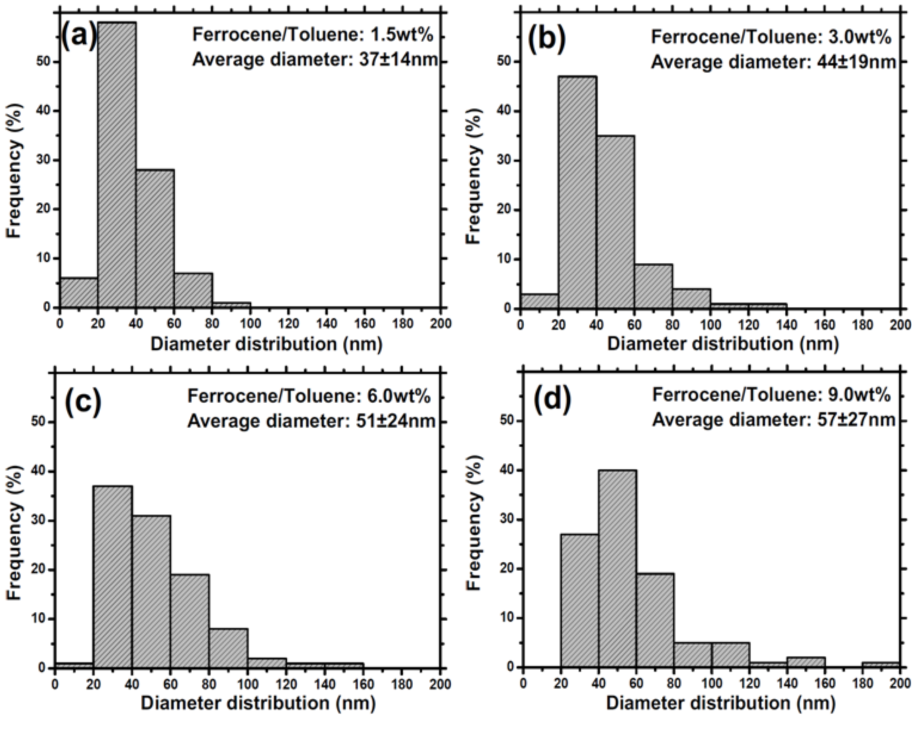

Figure 5.17: Diameter distributions of MWCNTs produced by (a) 1.5wt% (b) 3.0wt% (c) 6.0wt% and (d) 9.0wt% ferrocene in toluene.

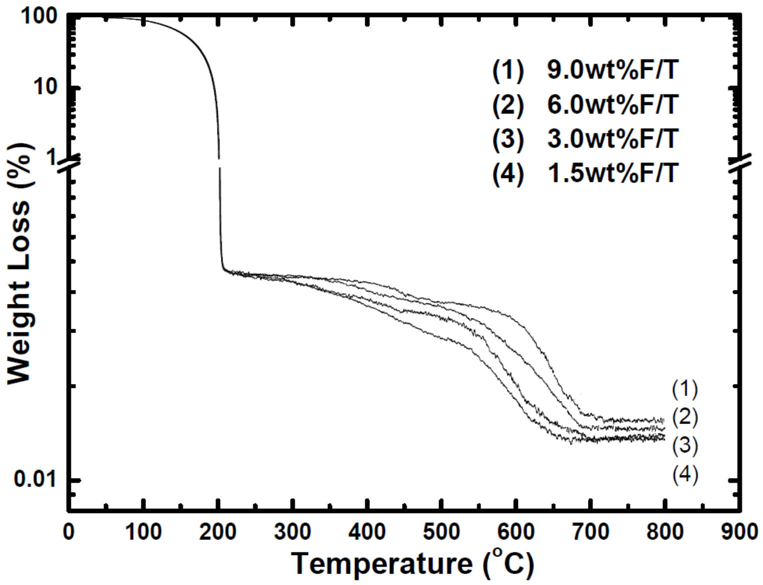

Figure 5.18: TGA data showing the decomposition curves of acid-treated MWCNTs, synthesised by using different ferrocene (F) concentrations in toluene (T).

5.3 Summary

MWCNTs were synthesised by ICCVD to provide materials to be used for reinforcing GMCs (Sections 6.1 and 7.1). A gradual thickening of the MWCNTs occurred during the growth due to the growing size of the catalyst particles. The closed tips of the MWCNTs and the presence of catalyst particles at their roots confirmed the base growth mechanism. A high level of crystallinity was obtained compared to commercial CVD-grown CNTs; however, structural defects were still observed.

Acid-treatment was confirmed to increase the dispersion quality of as-synthesised entangled MWCNTs by significantly shortening their lengths and attaching functional group to their surfaces. Impurities, including catalyst particles and amorphous carbon, were also removed. However, the surface quality of MWCNTs was impaired due to the introduction of oxidation debris, which lowered the thermal stability of MWCNTs. Nevertheless, the acid-treatment provided dispersed, shortened and purified MWCNTs for subsequent composite manufacture. Acid-treatment also supplied a range of MWCNT dimensions, suitable for the investigation of their size effects in GMCs (Sections 6.2.3 and 6.2.4).

6. MWCNT-silica glass composites

Manufacture and characterisation of silica glass matrix composites containing 2.5-10wt% (3.3-13.2vol%) MWCNTs are described. Manufacturing includes the heterocoagulation of the suspensions of MWCNTs and silica glass nanoparticles by colloidal mixing in order to prepare composite powders, which were subsequently densified by pressureless sintering. Characterisation comprises the physical, microstructural, mechanical, functional and technological property evaluation by measuring density, hardness, elastic modulus, fracture toughness, thermal and electrical conductivity, thermal shock, cycling and ageing behaviour, wear and friction resistance, X-ray diffraction, Raman spectroscopy, scanning and transmission electron microscopy.

6.1 Manufacture

6.1.1 Materials

Four types of MWCNTs, synthesised by using 1.5wt%, 3.0wt%, 6.0wt% and 9.0wt% ferrocene (F) in toluene (T) in a ICCVD setup (Figure 5.1), were used as nano-reinforcements to manufacture four sets of composites containing 2.5wt% to 10wt% MWCNTs. Commercially-available fumed silica (SiO_2) glass powder (Aerosil RA200HS, Evonik, Germany) served as a matrix precursor. This glass powder is typically used to reduce the moisture pick-up and improves the flowability of toners. It was chosen for the present investigation due to its ready availability, reproducible chemical composition and average particle size in nano-meter range, i.e. ~20nm, in order to assist heterocoagulation with MWCNTs, as discussed in the next section.

6.1.2 Composite powder preparation

The process of heterocoagulation of MWCNTs and silica glass powder by colloidal mixing of their suspensions was chosen to prepare composite powders. The preparation of stable aqueous suspensions of MWCNTs by acid-treatment was described in Section 5.2, while silica glass suspension was obtained by dispersing nanoparticles (5mg/ml) in ethanol (99.7-100%, VWR) due to their hydrophobic nature, as a result of surface coating with hexamethyldisilazane and aminosilane in their as-received state. Silica/ethanol suspension was stabilised by sonicating with an ultrasonic probe (Branson 25, UK) at 30W for 30min after adding 3.65mM of aqueous hydrochloric acid (HCl) solution (38%, Sigma Aldrich).

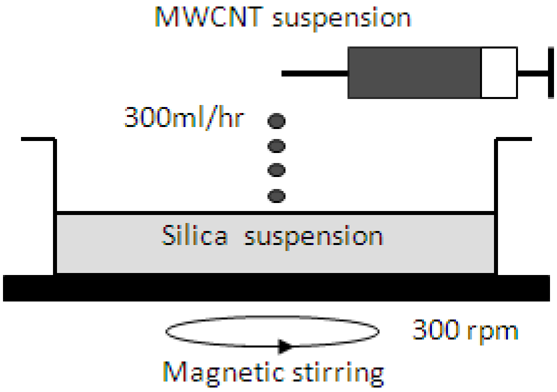

Figure 6.1: Colloidal mixing of acid-treated MWCNT and silica nanoparticle suspensions.

To prepare MWCNT-SiO_2 glass composite powders, aqueous MWCNT suspensions were added at a rate of 300ml/h using a peristaltic pump to the silica glass suspension stirred at 300rpm (Figure 6.1); however, before combining the two suspensions, equal amounts of distilled water and ethanol were added to silica glass and MWCNT suspensions, respectively. The mixing of two suspensions promoted electrostatic attraction between reinforcing MWCNTs and glass matrix nanoparticles. In the selected pH range of 4.0-5.0, silica nanoparticles were positively charged and acid-treated MWCNTs negatively charged [91], as determined by the zeta-potential measurements (see below). Thus silica nanoparticles were deposited on the MWCNT surfaces by heterocoagulation, as shown schematically in Figure 6.2(a) and observed by SEM (Figure 6.2(b)). Silica nanoparticles shielded the attractive interactions between MWCNTs and isolated them from each other, which improved the dispersion quality by avoiding agglomerates. MWCNT-SiO_2 glass composite suspensions were dried in an oven at 120^{o}C to obtain powders, which were ground in a mortar with a pestle, sieved under 300 mesh size, and calcined at 400^{o}C for 3h to remove any undesirable organic residues. Four sets of MWCNT-SiO_2 glass composite powders were obtained, each having different types of MWCNTs with loading range from 2.5wt% to 10wt%.

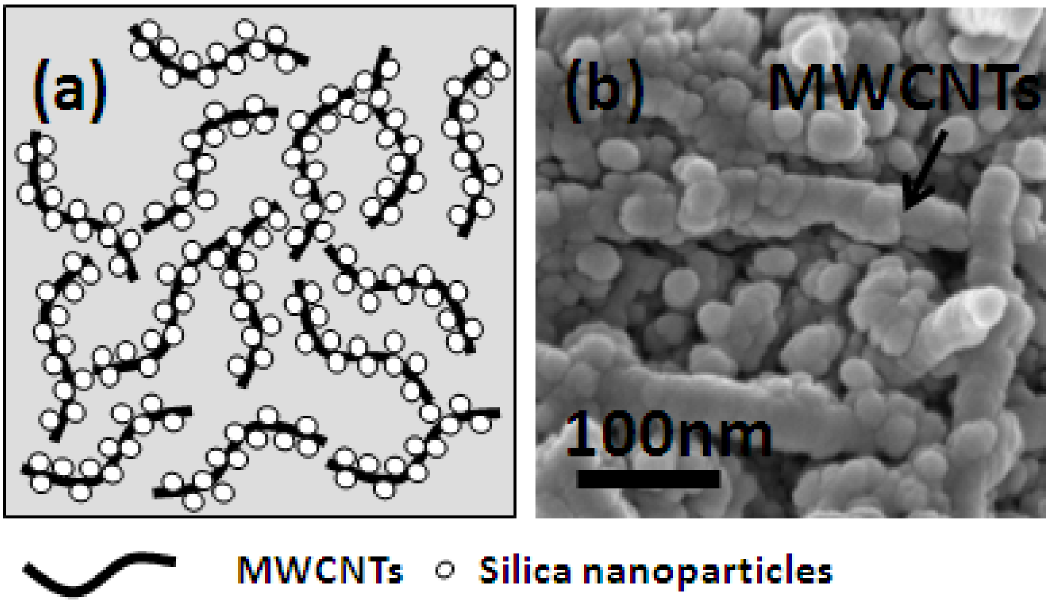

Figure 6.2: (a) Schematic diagram and (b) SEI-SEM image showing heterocoagulation of the oppositely charged acid-treated MWCNTs and silica glass nanoparticles.

To obtain pure silica glass reference specimens, silica nanoparticle suspension was dried without mixing MWCNTs but following a similar regime of grinding, sieving and calcination as applied to the composite powders. To ensure effective heterocoagulation of silica glass nanoparticles and MWCNTs, their surface properties were identified by zeta (ζ) potential measurements. Surface charges and the degree of repulsion between similar particles in a suspension can be determined by measuring their ζ-potential. In cases of high ζ-potential, either positive or negative, repulsion forces exceed attraction forces and an electrostatically stabilised suspension of particles is achieved; flocculation of particles occurs in systems with low absolute ζ-potential magnitudes. Figure 6.3 thus confirms the strategy of achieving uniform suspensions of MWCNTs and silica glass nanoparticles depending upon their ζ-potential. MWCNTs showed negative surface charge due to the presence of oxygen-containing functional groups, as described in Section 5.2.1 and high ζ-potential magnitude of 40-50mV providing stable suspensions of MWCNTs in the pH range of 4.0-5.5.

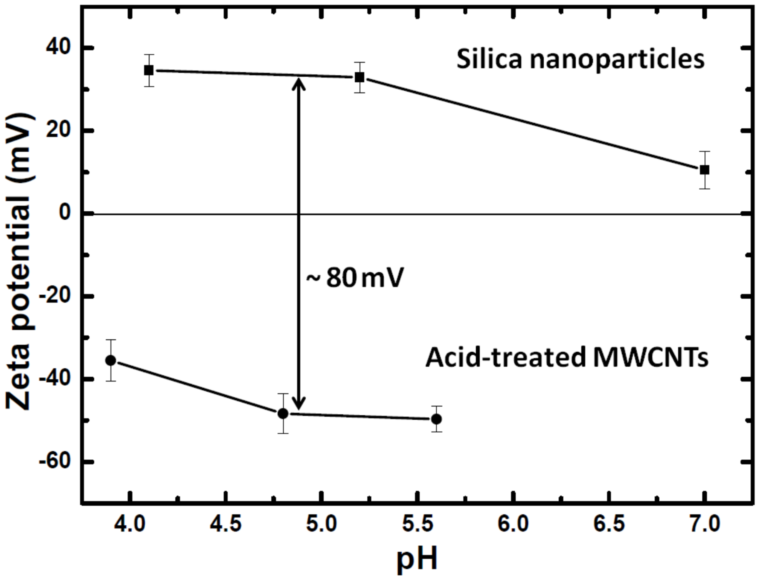

Figure 6.3: Zeta potential measurements of acid-treated MWCNT and silica glass nanoparticle suspensions at different pH values.

As silica glass nanoparticles were treated with hexamethyldisilazane and aminosilane in their as-received state [159], they were hydrophobic and showed positive surface charge after dispersing in ethanol. However, a low ζ-potential value, i.e. ~10mV was found at a pH of 7.0 (Figure 6.3), which was insufficient to obtain a stable suspension. As a result, sedimentation of silica glass nanoparticles occurred (Figure 6.4(a)) and their aggregates are shown in Figure 6.4(c). However, decreasing the pH of the suspension in a range of 4.0-5.0 significantly increased the ζ-potential to around 35mV, which resulted in a stable suspension of silica glass nanoparticles over a long period of time, i.e. several months, without sedimentation (Figure 6.4(b)) or aggregation of nanoparticles (Figure 6.4(d)). A pH range of 4.0-5.0 was, therefore, selected for heterocoagulation, as it provided a high potential difference (~80mV) for strong electrostatic attraction between the oppositely-charged MWCNTs and silica glass nanoparticles to prepare composite powders with well-dispersed MWCNTs.

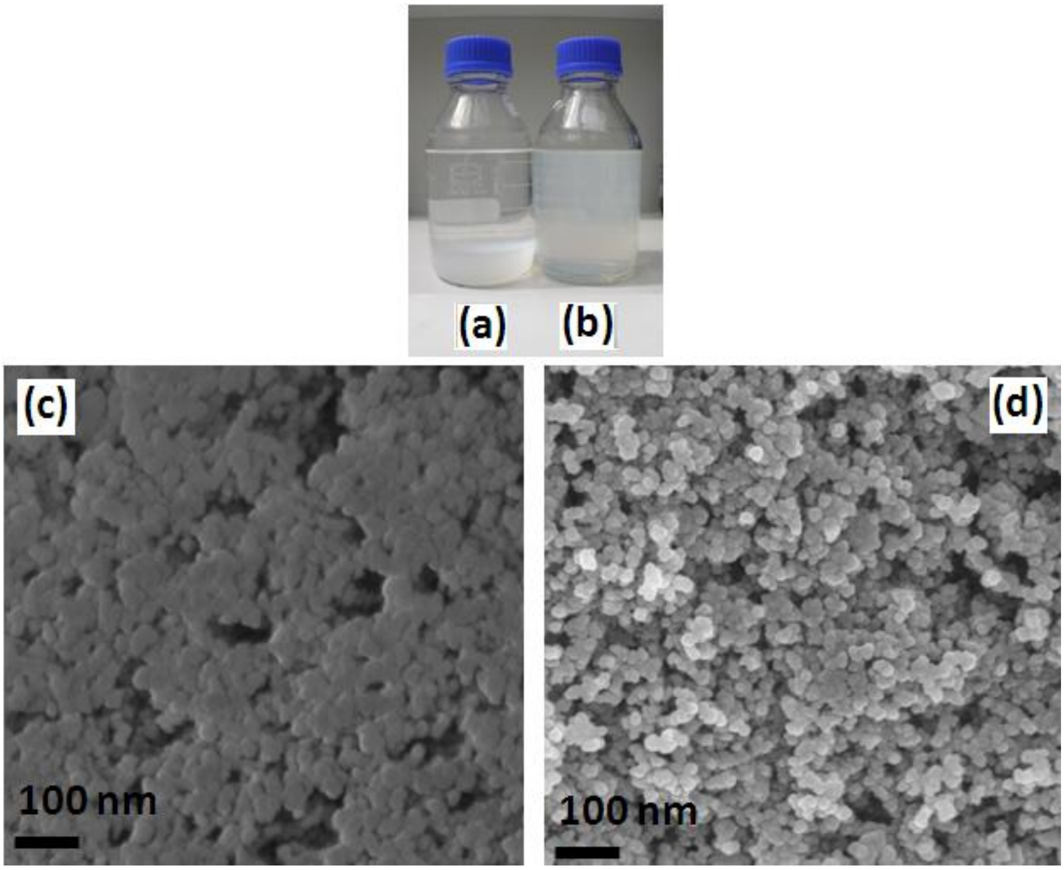

Figure 6.4: Photographs showing (a) sedimentation and (b) stable suspension of silica glass nanoparticles at pH 7 and pH 4-5, as verified by SEI-SEM images in (c) and (d), respectively; powders were dried on aluminium stubs for SEM.

6.1.3 Composite powder compaction

PLS was employed for the consolidation of silica glass and MWCNT-SiO_2 glass composite powders. Green bodies were first prepared by uniaxial pressing of powders in a steel die at a pressure of 120MPa, while further compaction was performed by cold isostatic pressing (CIP) at 400MPa. The compacted green discs of diameter ~10mm and thickness ~2.0mm were sintered at ambient pressure in a tube furnace under an inert atmosphere of argon to avoid the oxidation of MWCNTs. Sintering temperatures from 1050°C to 1400°C were chosen with a holding time of 3h; the heating rate was 10°C/min and specimens were furnace cooled after sintering. The temperature/time profile was selected bearing in mind the available sintering parameters of silica glass [230] and silica GMCs [91,147]. Four sets of MWCNT-SiO_2 glass composites with 2.5wt% to 10wt% MWCNTs were sintered, each having a different type of MWCNTs, synthesised by using

1.5wt%, 3.0wt%, 6.0wt% and 9.0wt% F/T as the ICCVD precursor. The composite powders containing 2.5wt% MWCNTs (3.0wt%F/T) were used as a test system to optimise sintering conditions. A temperature of 1150°C was chosen for the sintering of silica glass specimens while a higher temperature (1200°C) was adopted for the sintering of 2.5wt% to 10wt% MWCNT-SiO_2 glass composites. The reasons to select these temperatures are discussed in the next section.

6.2 Characterisation

6.2.1 Physical characterisation

a. Density

The sintered silica and 2.5wt% MWCNT-SiO_2 glass composite specimens were ground and polished using diamond suspension of 1μm particle size in order to measure their densities by the Archimedes method. The average density values from five separate measurements were calculated along with the standard deviation. The densities are shown as relative densities (actual/theoretical) after calculating the theoretical densities by taking a typical value of 2.2g/cm^3 for silica glass and 1.65g/cm^3 for MWCNTs [91]. Silica glass sintered for 3h at 1050°C and 1100°C showed relative densities of <60% and <70%, respectively (Figure 6.5). However, fully dense glass specimens were obtained at 1150°C. Further increases in temperature, up to 1400°C, showed similar densities but encouraged devitrification (Figure 6.8(a)).

The composite specimens also showed low densities at temperatures of 1050°C and 1100°C, i.e. <55% and <65%, respectively (Figure 6.5). An increase in temperature to 1150°C showed a significant improvement by raising the density to ~95% but it was still less than desired. A further rise in temperature to 1200°C provided a density of >99% and so was selected as the optimised temperature. Similar to silica glass specimens, further increases in composite sintering temperature, up to 1400°C, simply initiated devitrification (Figure 6.8(b)). The densities of the composites achieved in the present investigation are higher than obtained in a previous study [147] with only 1wt% CNTs in a glass matrix, i.e. ~95%.

The silica glass showed comparatively higher densities than composites at sintering temperatures from 1050°C to 1150°C. Moreover, silica glass was completely densified at a lower temperature of 1150°C than composite specimens, i.e. 1200°C. The requirement of a higher temperature for composites may be attributed to an increase in their viscosity due to the presence of MWCNTs. If considered as inclusions, MWCNTs make the composite system more viscous and impede viscous flow densification of the silica glass matrix [231].

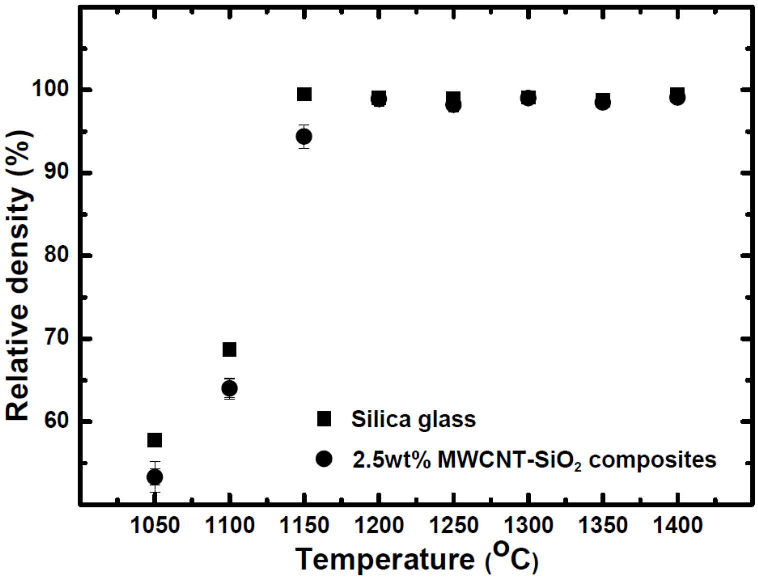

Figure 6.5: Relative densities (actual/theoretical) of sintered silica glass and 2.5wt% MWCNT-SiO_2 glass composites after 3h at different temperatures.

The sintering temperature of MWCNT-SiO_2 glass composites containing higher loadings of MWCNTs, i.e. 5.0wt% to 10wt% were also optimised at 1200°C. Figure 6.6 shows the green and sintered densities of silica glass and 2.5wt% to 10wt% MWCNT-SiO_2 glass composites. A systematic decrease in relative densities after sintering at the optimised sintering conditions was observed, with pure silica glass showing the highest value and 10wt% MWCNT-SiO_2 glass composite the lowest. The gradual decrease in sintered densities with increasing content of MWCNTs is consistent with the observation of the requirement of an increased sintering temperature of silica glass in the presence of MWCNTs, if it is considered that MWCNTs hinder the viscous flow densification. Therefore, at constant sintering temperature of 1200°C for composites, an increase in MWCNT content decreases their relative densities.

It can be argued that an increase in the sintering temperature for composites with high MWCNT loadings, i.e. 5.0wt% to 10wt% could provide densities comparable to that of 2.5wt% MWCNT-SiO_2 glass composites but XRD results showed a significant increase in the crystallisation of silica glass matrix at temperatures above 1200°C (Figure 6.8). Hence, the sintering temperature for composites with MWCNT loadings from 2.5wt% to 10wt% was maintained at 1200°C. Nevertheless, the present densification results obtained by PLS are better than many published results of CNT-glass/ceramic matrix composites obtained by SPS [92,94,114,232-233] and HPS [95,97-100,108-109,113,118,197,234].

It is surprising to note that the reverse trend (increase) in the green densities of the composites was observed on adding more MWCNTs (Figure 6.6). This weak effect may be due to the compressed state of flexible MWCNTs during uniaxial and isostatic pressing in green state, which is likely to be partially recovered during PLS.

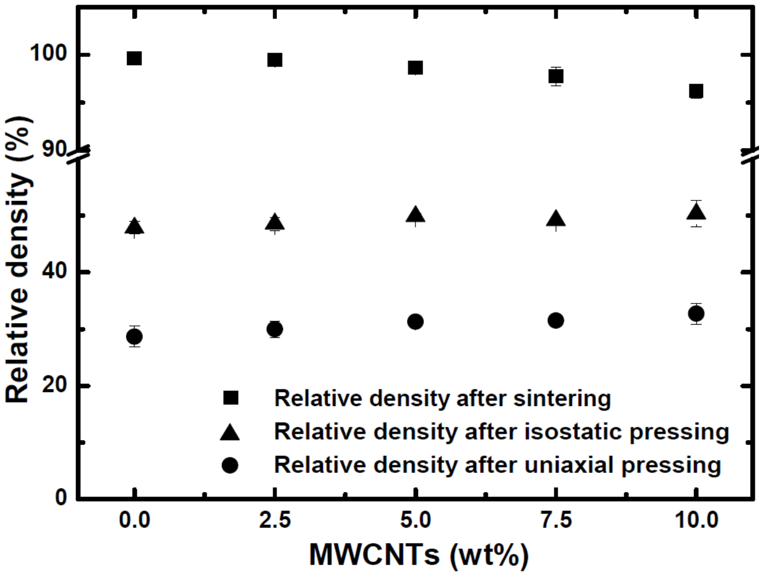

Figure 6.6: Relative densities (actual/theoretical) of silica glass and 2.5wt% to 10wt% MWCNT-SiO_2 glass composites in green and sintered states.

After optimising sintering conditions with 3wt%F/T MWCNT-SiO_2 glass composites, the other three sets of composites were similarly sintered. At 2.5wt% MWCNT content, the densities of the four sets of composites (Figure 6.7) are similar, however, at higher MWCNT loadings, the densities diverged, although the effect was small. It can be argued that 10wt% MWCNT-SiO_2

glass composites clearly demonstrated the effect of MWCNT length to limit densification. This effect is consistent with the known difficulties of packing high aspect ratio particles at higher volume fractions. Nevertheless, the achieved densities of all the composites with different types of MWCNTs at 10wt% loading are >95%.

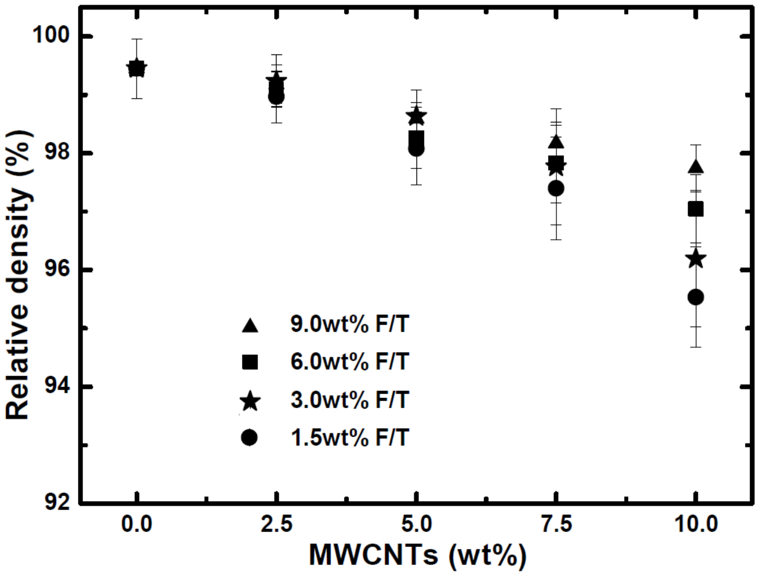

Figure 6.7: Relative densities (actual/theoretical) of silica glass and 2.5wt% to 10wt% MWCNT-SiO$_2$ glass composites containing four types of MWCNTs produced by different ferrocene content in toluene (F/T).

6.2.2 Microstructural characterisation

a. X-ray diffraction

XRD data of silica glass and 2.5wt% MWCNT-SiO$_2$ glass composites obtained during the optimisation of their sintering temperatures is shown in Figure 6.8. An amorphous matrix, manifest by the broad hump at 20-25^o 2θ, is evident in both the silica glass and composite specimens at their optimised temperatures, i.e. 1150^{o}C and 1200^{o}C, respectively, with low degree of crystallisation, due to cristobalite formation (2θ=21.80), which is not expected to affect their properties significantly. The degree of crystallisation increased with temperature, and crystallisation peaks became visible in silica glass and composite specimens at higher temperatures, i.e. >1200^{o}C.

In addition to XRD peaks related to glass crystallisation, small graphitic peaks (002) corresponding to MWCNTs ($2\theta=26.20$) are also visible in the XRD of composites confirming the retention of MWCNTs after sintering.

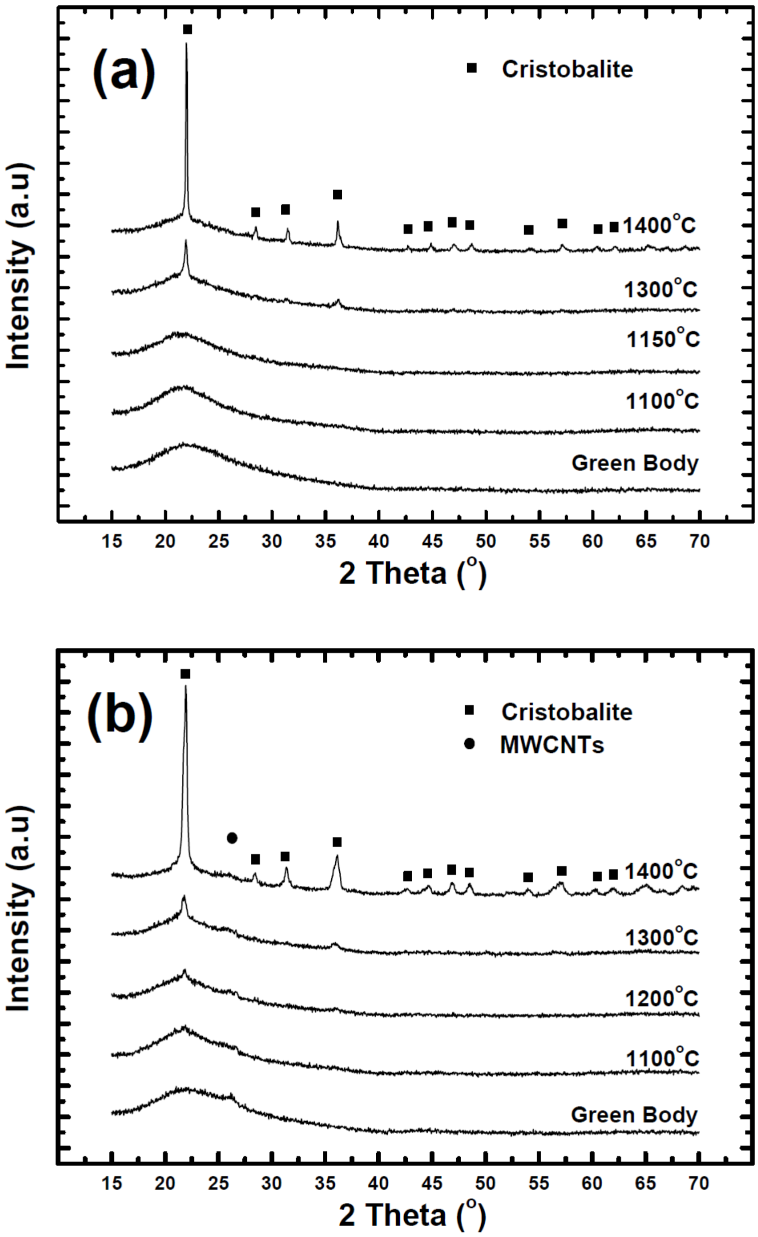

Figure 6.8: XRD of (a) silica glass and (b) 2.5wt% MWCNT-SiO_2 glass composites during the optimisation of their sintering temperatures.

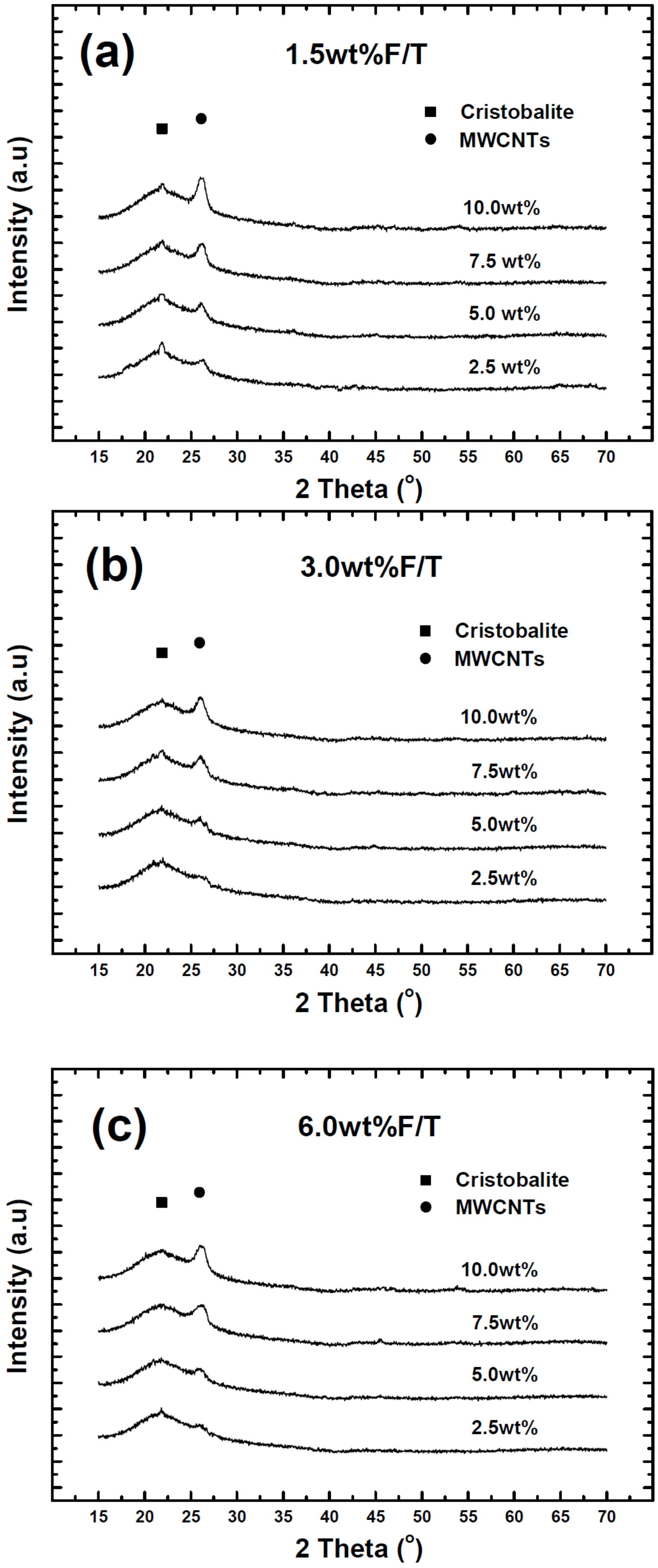

(Continued to next page)

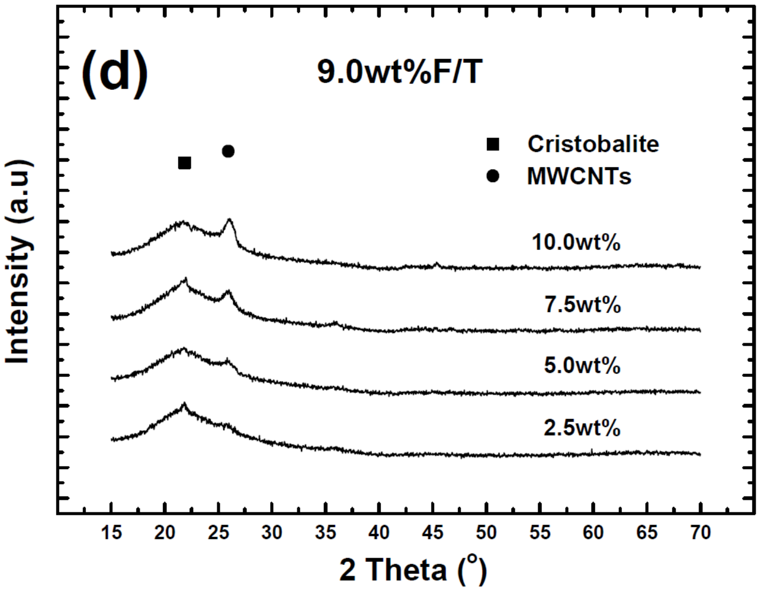

Figure 6.9: (a-d) XRD of four sets of composites with different types of MWCNTs produced by 1.5wt%, 3.0wt%, 6.0wt% and 9.0wt% ferrocene in toluene (F/T); each set of composites comprises four different MWCNT loadings, i.e. 2.5wt% to 10wt%. An amorphous matrix with low degree of crystallisation was observed. A graphitic peak corresponding to MWCNTs is also visible, the intensity of which increases with their content in composites.

XRD from the four sets of composites containing 2.5wt% to 10wt% MWCNTs (Figure 6.9) similarly confirmed the existence of an amorphous glass matrix at the optimised sintering temperatures with limited crystallisation. Small peaks corresponding to cristobalite were observed above a characteristic amorphous silica background. However, the crystallisation peaks are weak and show a low level of crystallinity, which was estimated to be less than 3% by normalising the area under the peaks to the area of background amorphous signal obtained in the XRD spectrum. No new crystalline phases emerged as a result of any potential reaction between the MWCNTs and the silica glass. The total degree of crystallinity was similarly low as found in a previous study on the same type of composites but sintered by SPS [91].

If MWCNTs in composites are considered to act as heterogeneous nucleation sites, the degree of crystallisation should increase with their content due to increased interfacial surface area or particle number density. However, the degree of crystallinity remains approximately constant with different MWCNT loadings (Figure 6.9).

A similar effect of the retardation of crystallisation has been previously observed in GMCs containing 1wt% to 15wt% MWCNTs [91]. However, the true effect of MWCNT content on the extent of crystallisation remains to be investigated, as it was beyond the scope of the present work. In the XRD of composites, peaks related to MWCNTs are also visible and their intensity increases in proportion to their content in composites.

b. Raman spectroscopy

Severe sintering conditions are reported both to damage [105] and graphitise CNTs [235]. To observe the effect of harsh sintering conditions on MWCNTs, Raman spectroscopy was performed on one set of composites containing 3wt%F/T MWCNTs, which allowed a comparison of MWCNT crystallinity at each stage of the composite processing (Figure 6.10).

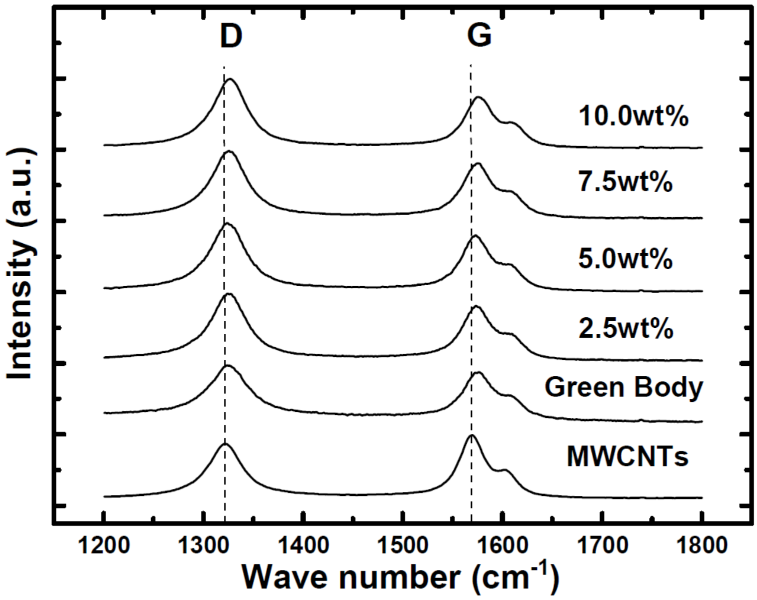

Figure 6.10: Raman spectra of acid-treated (3wt%F/T) MWCNTs and 2.5wt% to 10wt% MWCNT-SiO$_2$ glass composites in green and sintered states. The ratios of D and G peaks qualitatively show the crystallinity of MWCNTs.

The ratios of the intensities of D and G peaks (I_D/I_G) are 0.9±0.04, 1.0±0.03 and 1.1±0.04 for the acid-treated MWCNTs before and after inclusion in the silica glass matrix in both the green and sintered states, respectively; the results confirm that the MWCNTs were neither severely degraded nor graphitised.

A slight shift to higher Raman wave number in composite specimens was also observed, which may be attributed to the residual stresses that developed due to the application of load during green-body consolidation or due to cooling from sintering temperature; the tendency is stronger in composites containing higher contents of MWCNTs. Similar Raman results have been reported in CNT-glass composites densified by SPS [159], although sintering conditions in both techniques were different. The Raman data contradicts the general perception that only SPS or HPS can provide CNT-glass/ceramic matrix composites without severely degrading CNTs.

c. Scanning electron microscopy

The fractured surfaces of the silica glass specimens sintered at 1150°C and 1400°C for 3h (Figure 6.11) show fully densified amorphous matrix and typical cristobalite spheres [159], respectively. XRD in Figure 6.8 has already indicated the presence of amorphous matrix and the cristobalite crystals in silica glass specimens sintered at 1150°V and 1400°C, respectively. A TEM image showing the cristobalite crystals is displayed further below (Figure 6.16(c)) and discussed in Section 6.2.2(d).

The quality of MWCNT dispersion and the porosity level in silica glass and composite specimens, both in green and sintered states, were observed by SEM. The homogeneity of MWCNT distribution was found to be retained in the green state after compaction of the composite powders (Figure 6.12(a)). MWCNT agglomerates were not observed; instead, individual MWCNTs were identified by pullout from the fractured surfaces (Figure 6.12(b)).

Porosity level in green state was high due to the low relative density, i.e. ~50%. However, it decreased to ~35% after sintering at 1100°C (Figure 6.13(a-b)). The consolidation at 1200°C showed a fully dense matrix in the 2.5wt% MWCNT-SiO_2 glass composite (Figure 6.13(c-d)). Uniform dispersion of MWCNTs was retained even after the matrix crystallisation at higher temperatures, i.e. 1300°C (Figure 6.13(e-f)).

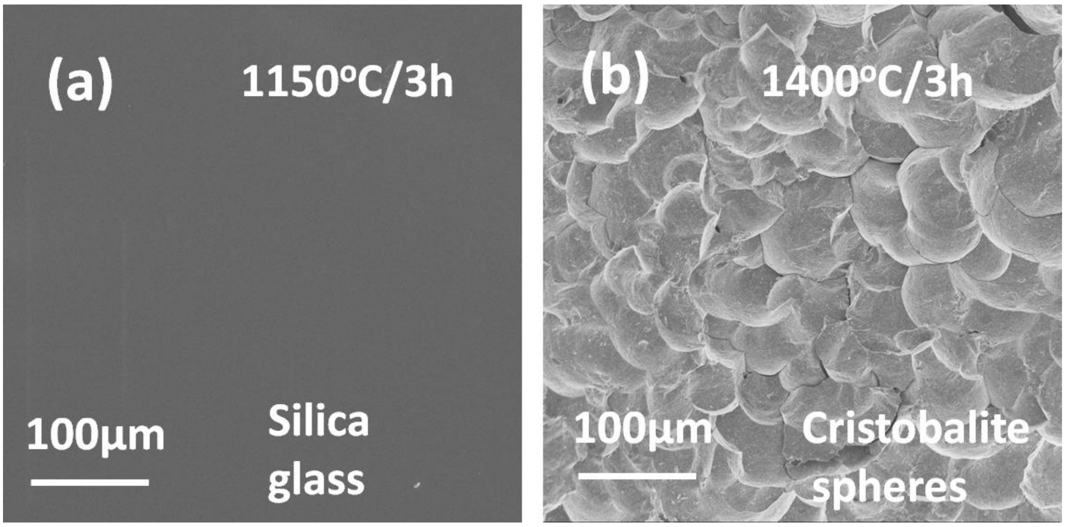

Figure 6.11: SEI-SEM images of the fractured surfaces of silica glass specimens sintered at 1150°C and 1400°C for 3h showing (a) amorphous matrix and (b) cristobalite spheres, respectively.

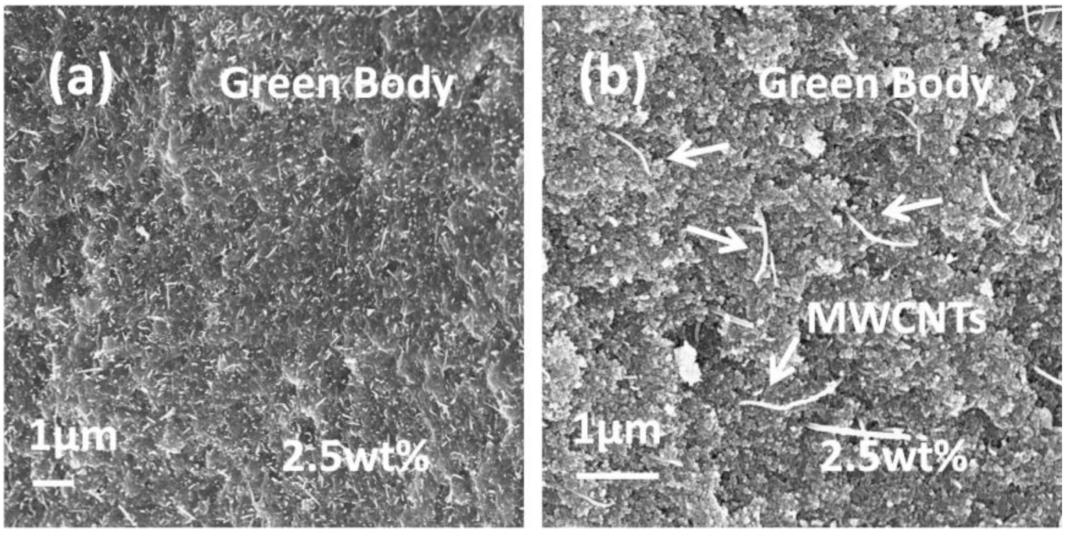

Figure 6.12: SEI-SEM images of the fractured surfaces of MWCNT-SiO$_2$ glass composites in green state showing (a) homogeneous dispersion and (b) pull-out of MWCNTs.

It is difficult to establish the dispersion quality of CNTs in glass/ceramic matrices. All the available published images show homogeneity at a local level making it hard to judge the dispersion quality over a large volume. Moreover, CNT-agglomerates and CNT-depleted regions are also observed [105]. By comparing from different magnifications (Figure 6.14), it is possible to confirm the homogeneity of MWCNT distribution over large regions and also to demonstrate their random orientation and the quality of local dispersion in the dense glass matrix.

Microstructural images showing such a good quality of CNTs distribution are rarely found in literature.

Uniform dispersion is also evident in the four sets of composites prepared by incorporating four different types of MWCNTs ranging from 2.5wt% to 10wt% loading (Figure 6.15). An interesting feature is the pullout lengths of MWCNTs, which are up to ~1μm in all images. However, the number of MWCNT pulled-out at longer lengths is greater in 1.5wt%F/T MWCNT composites than in others. One of the causes may be the longer lengths and higher aspect ratios of 1.5wt%F/T MWCNTs and another may be the comparatively lower densities of these composites.

d. Transmission electron microscopy

TEM can reveal features of MWCNTs embedded in the glass matrix, such as their retention after sintering or any damage produced during the processing. Moreover, the structural deformation in MWCNTs can be highlighted along with the identification of the crystallisation in the glass matrix and the presence of porosity. TEM evidence of the extent of CNT dispersion and their orientation in amorphous has not been published. A cross sectional TEM image can reveal the dispersion quality of CNTs in a matrix along with their orientation. TEM can also be used to qualitatively analyse the structural flexibility of CNTs after reinforcing brittle matrices to observe if CNTs retain their stiff character after the application of load during the consolidation of composites or deform by producing disorder in their structure due to their flexible character.

Figure 6.16(a) shows a representative BF-TEM image of 10wt% MWCNT-SiO_2 glass composite sintered at 1200^{o}C for 3h, revealing retention of the MWCNTs in the dense silica glass matrix. Longitudinal and transverse cross sections of MWCNTs are evident, while arrows specifically indicate transverse cross-sections. SAED pattern verifies the amorphous nature of the matrix (Figure 6.16(b)). No apparent porosity or the crystallisation was observed in the glass matrix.

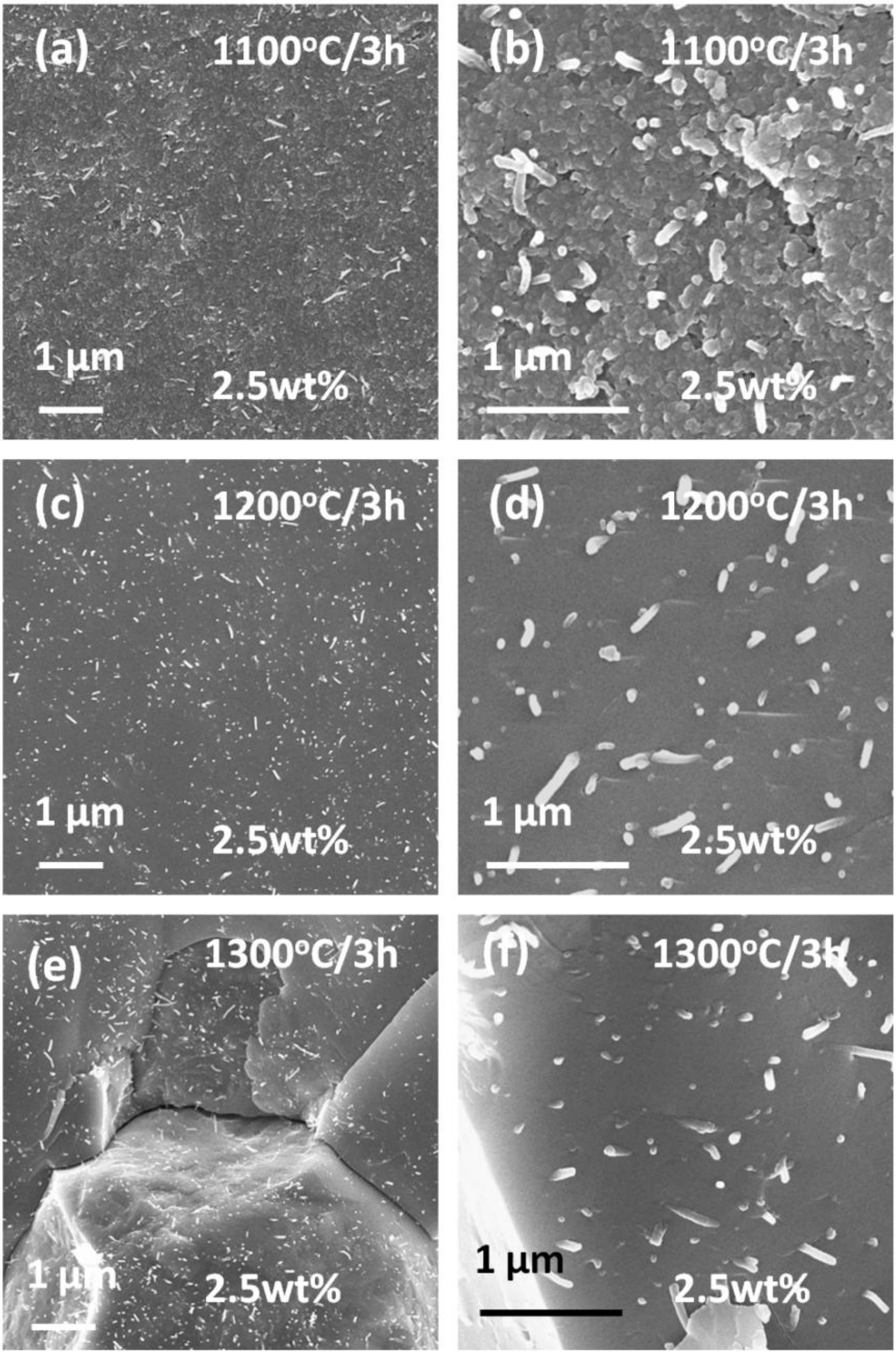

Figure 6.13: SEI-SEM images of 2.5wt% MWCNT-SiO_2 glass composites sintered at three temperatures showing (a-b) incomplete and (c-d) complete densification, and (e-f) crystallisation. MWCNT dispersion quality is maintained at all sintering temperatures.

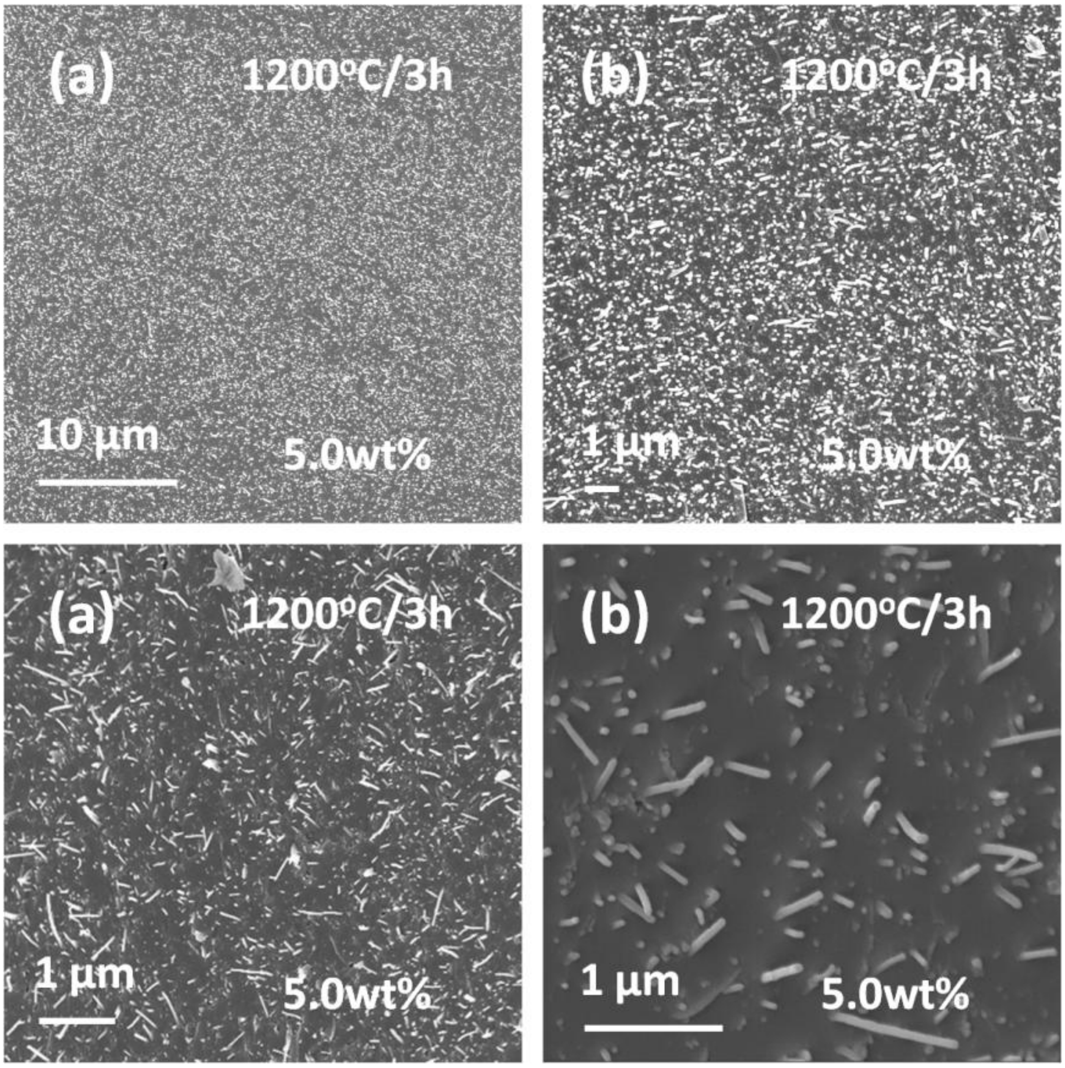

Figure 6.14: (a-d) SEI-SEM images of 5.0wt% MWCNT-SiO_2 glass composites showing uniform distribution of MWCNTs at low to high magnifications.

Another interesting feature in Figure 6.16(a) is the presence of bent/curved MWCNTs, which indicate their flexible nature. Although the flexibility of CNTs is well-known [46-47], the effects on the properties of CNT-brittle matrix composites are not often discussed. The literature is replete with reports on the deformation of high aspect ratio CNTs under axial, bending, torsional and radially compressed states, showing strains up to 15% [37], 16% [46-48], 7.6% [49] and 40% [50], respectively. In contrast, glasses and ceramics do not show much deformation at room temperatures. Hence, CNTs are likely to be strained/deformed in brittle matrices, especially, under pressure during the consolidation of composites.

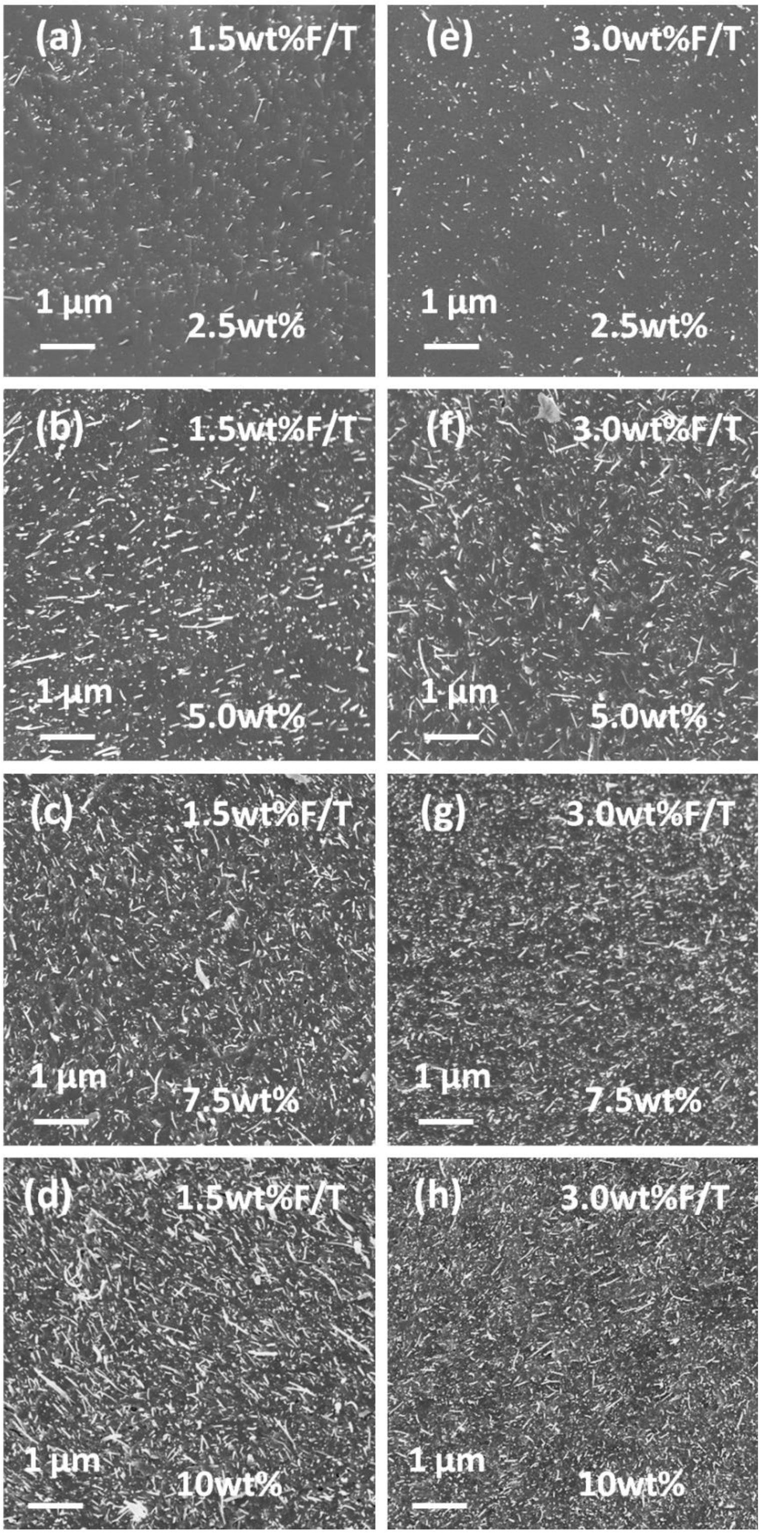

(Continued to next page)

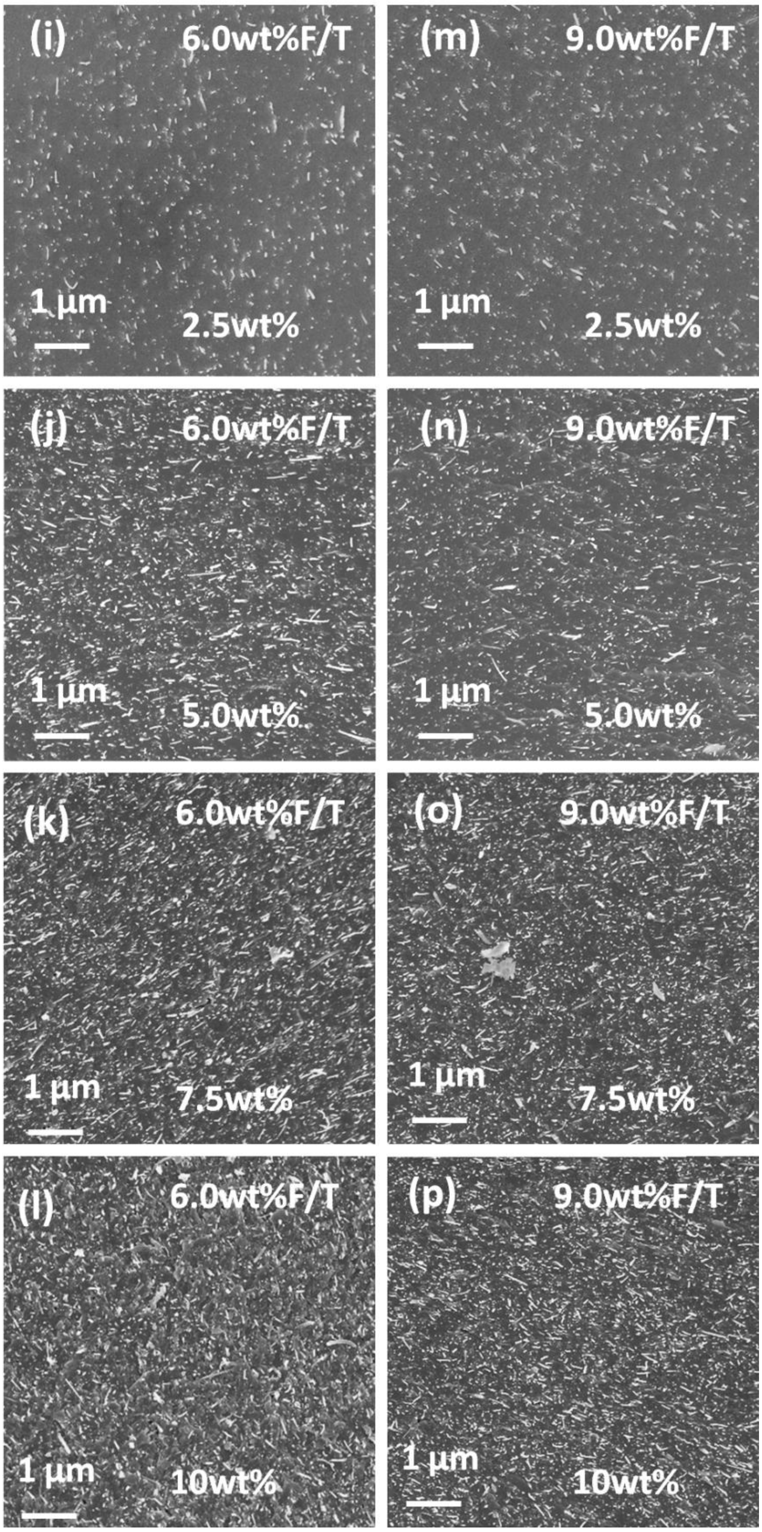

Figure 6.15: SEI-SEM images of four sets of MWCNT-SiO_2 glass composites containing four types of MWCNTs synthesised by using 1.5wt% (a-d), 3.0wt% (e-h), 6.0wt% (i-l) and 9.0wt% (m-p) ferrocene in toluene (F/T). Each set of composites was developed with a range of MWCNTs from 2.5wt% to 10wt%.

Figure 6.16(c) shows the presence of cristobalite crystals in 2.5wt% MWCNT-SiO_2 glass composite specimens sintered at 1300°C for 3h. Such a morphology of the cristobalite crystals has been observed previously [236] and related to the tridymite-like stacking faults [237].

HRTEM can reveal a number of structural and interfacial features of MWCNTs embedded in a matrix. The structural flexibility and mechanical instability of the outer layers of MWCNTs was observed leading to the deformation that produced elliptical and radially corrugated cross-sections (Figure 6.17(a,c)); compression of the inner layers of MWCNTs led to the squeezing and elliptical deformation (Figure 6.17(b,d)). The longitudinal cross-section of embedded MWCNTs revealed the non-uniform central cavity (Figure 6.17(e)) and deformed graphene layers (Figure 6.17(f)). Such images of deformed MWCNTs indicate the structural flexibility of MWCNTs and suggest that the MWCNTs embedded in the glass matrix may be present in a stressed state, as also observed by the Raman peak shifts (Figure 6.10) indicating strain in MWCNTs. The deformation of layers was also observed in the images of as-synthesised and acid-treated MWCNTs (Figure 5.11, Figure 5.12 and Figure 5.14).

Another area of considerable importance is the interface in CNT-glass/ceramic matrix composites, as it can significantly affect the composite properties. Figure 6.18 shows HRTEM images of the MWCNT/SiO_2 interface in the present composites, indicating the existence of mechanical bond without any new phase formed due to chemical reaction between MWCNTs and silica glass. A good quality mechanical bond is shown and the physical attachment of MWCNTs with the surrounding glass matrix can be clearly seen. The absence of an intermediate phase has also been reported in composites containing glass and glass-ceramic matrices, such as silica [118], borosilicate [106], barium-aluminosilicate [108] and alumina-borosilicate [90,109].

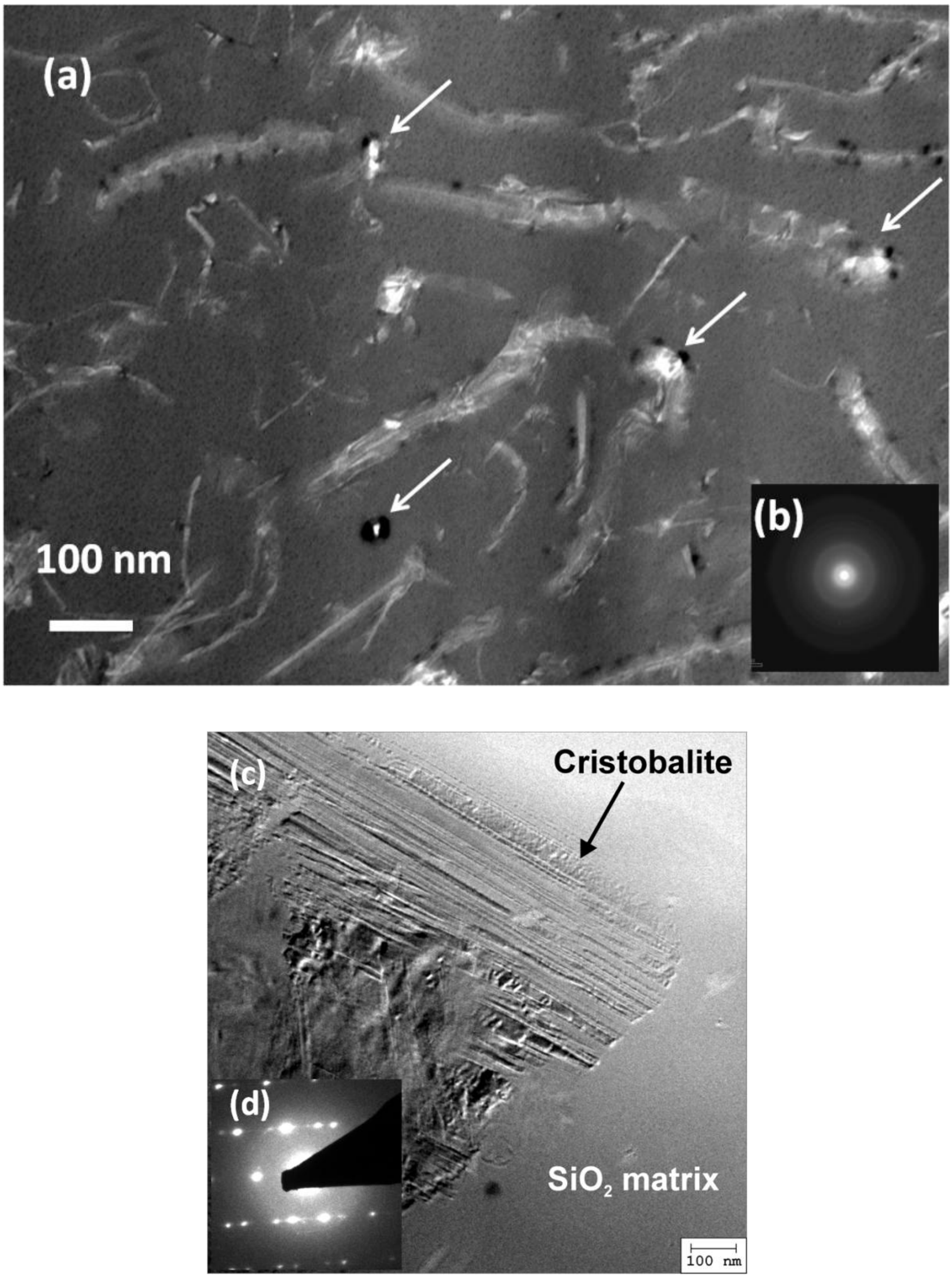

Figure 6.16: (a) BF-TEM image of 10wt% MWCNT-SiO_2 glass composite sintered at 1200°C for 3h showing uniform dispersion, random orientation and longitudinal and transverse (arrows) cross-sections of MWCNTs in dense silica glass matrix; (b) SAED shows the amorphous composite matrix. (c) BF-TEM image of 2.5wt% MWCNT-SiO_2 glass composite sintered at 1300°C for 3h along with (d) diffraction pattern shows the presence of cristobalite crystals in silica glass matrix.

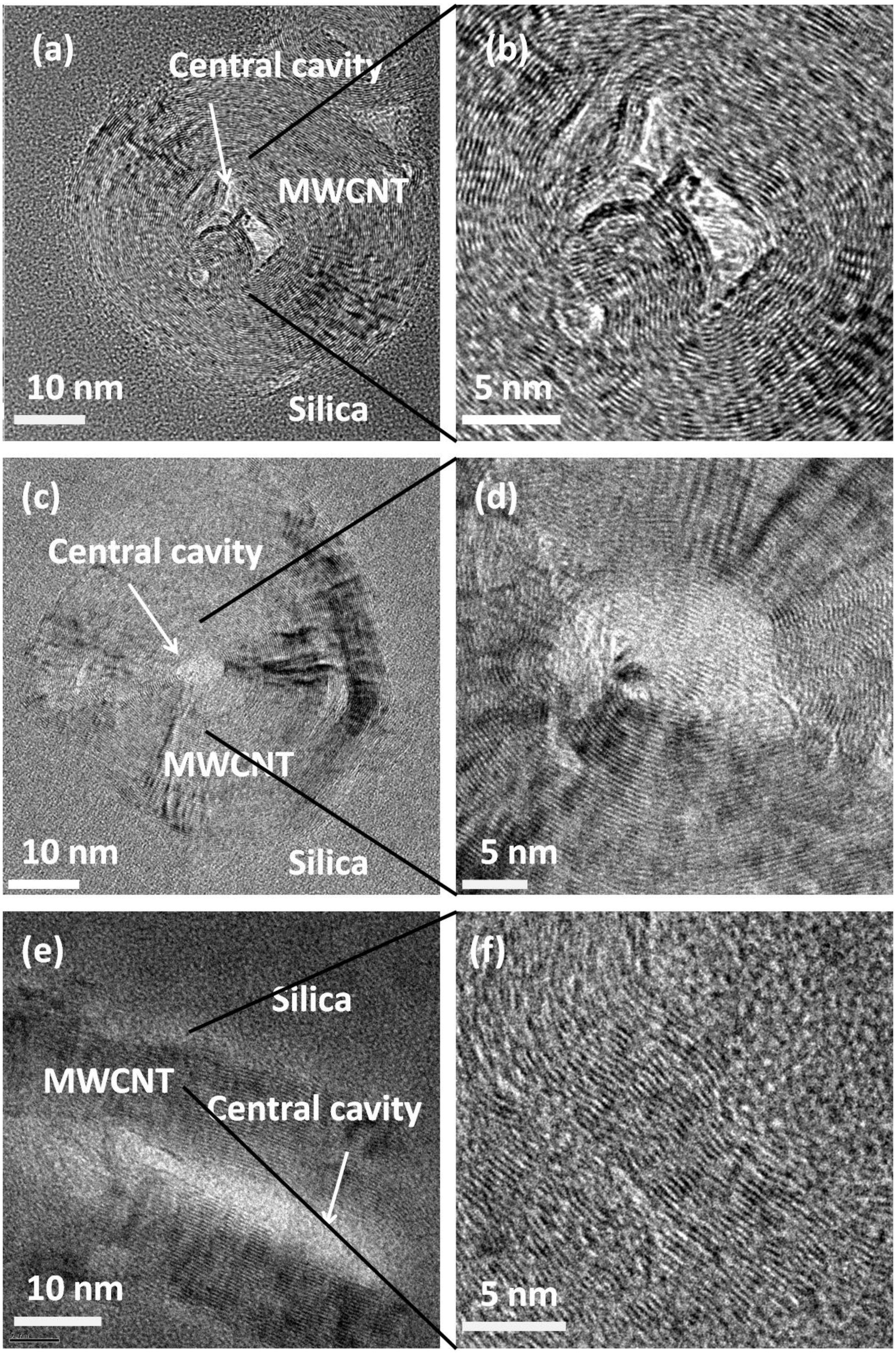

Figure 6.17: HRTEM images of MWCNTs embedded in silica glass matrix showing (a-d) transverse and (e-f) longitudinal cross-sectional views. MWCNTs are radially compressed showing deformed graphene layers. Squeezing of the central cavity to (b) irregular and (d) elliptical shapes is also evident.

In the present study, the acid-treatment performed on MWCNTs corroded the outer layers (Figure 5.14) and during viscous flow sintering, the soft silica glass flowed into surface defects providing an anchoring effect, similar to that observed in MWCNT-Al_2O_3 composites, where grains grew into defects of MWCNTs during sintering [238]. Therefore, mechanical interlocking due to rough MWCNT surfaces may be considered to be the likely cause of bonding between CNTs and silica glass matrix. When using pristine CNTs to reinforce glasses/ceramics without functionalisation, structural defects produced during the synthesis of CNTs, can serve to develop a keying effect providing a mechanical bond. However, poor distribution of as-synthesised CNTs in ceramics without their surface functionalisation produces agglomerates and reverses the beneficial effect of the mechanical bonding with the matrix by providing large flaws [111]. Another reason for good bonding between MWCNTs and the silica glass matrix is the compressed state of MWCNTs in the sintered composite. Such a stressed condition of MWCNTs is likely to be partially retained in the sintered composites. The resultant interfacial stress should increase fibre/matrix interaction leading to intimate contact. In short, mechanical interlocking and residual stress may be the possible causes of good bonding between CNTs and the silica glass matrix.

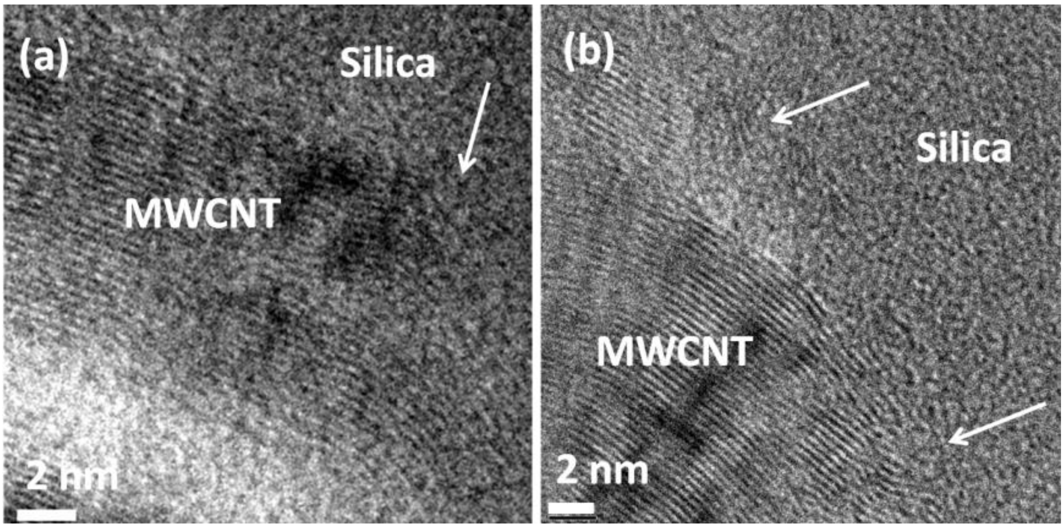

Figure 6.18: HRTEM images of MWCNT-SiO_2 glass composites showing a mechanical interface. Corroded MWCNT outer layers (arrowed) on (a) longitudinal and (b) transverse cross-sections are embedded in glass matrix providing mechanical interlocking.

6.2.3 Mechanical characterisation

a. Hardness

The hardness of silica glass and MWCNT-SiO_2 glass composites was measured by manual Vickers micro-indentation and instrumented Berkovich nano-indentation techniques. Both Vickers (Figure 6.19) and Berkovich (Figure 6.20) data indicate the highest hardness of silica glass specimens, while the composites demonstrate a continuous decrease in hardness with MWCNT addition. Although, the hardness trends in the two techniques are similar, the absolute values differ, which is due to the different applied loads, i.e. 4.9N and 0.5N, in Vickers and Berkovich indentations, respectively. A higher load produces more cracks underneath the indents and causes the reduction in hardness values. Such a trend of lower hardness at higher indentation loads, or vice versa, has been reported previously [239].

The hardness data also show a systematic difference between composites containing different size MWCNTs; at higher MWCNT loadings, i.e. ≥5.0wt%, the hardness values diverge. The set of composites containing the lowest aspect ratio and the shortest length MWCNTs (9.0wt%F/T) demonstrates the highest hardness. The same set of composites has shown (Figure 6.7) higher sintered densities than others. Therefore, the size of MWCNTs might have an influence on the hardness by providing different composite densities. Vickers and Berkovich hardness values have also been plotted against the relative densities of the composites. It is clear that composites with low densities demonstrated lower hardness values.

The instrumented Berkovich nano-indentation technique was employed to avoid the manual analysis of the Vickers micro-hardness data, i.e. measuring the diagonal lengths of an indent; instead, the indent area was calculated indirectly by relying on the depth of indenter penetration. The two different hardness measuring approaches were utilised in order to find the real trend of hardness in MWCNT-SiO_2 glass composites, which is unclear in CNT-glass/ceramic matrix composites. It might be argued that the Berkovich nano-indenter is small enough to be influenced by the intrinsic heterogeneities of the nanocomposites, i.e. silica glass and MWCNTs, rather than testing the representative MWCNT-SiO$_2$ glass composite hardness. To avoid this potential difficulty, a relatively high load of 0.5N was applied in order to create a sufficiently large indentation (Figure 6.21(a)) to average out the filler-matrix effects. The TEM cross-section of a Berkovich indentation (Figure 6.21) confirms the size of the indent in μm, which is much larger than the average diameter of individual MWCNTs in nm (Table 5.1).

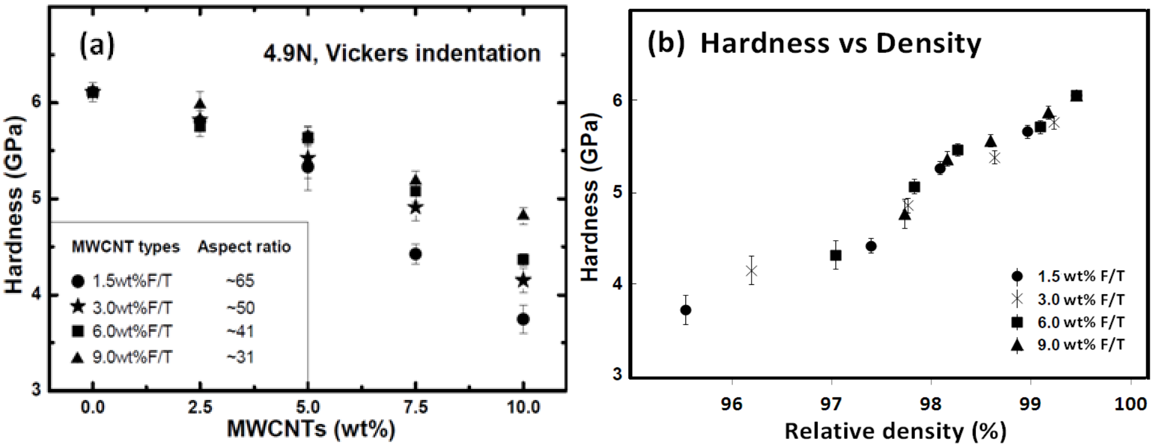

Figure 6.19: (a) Vickers hardness values of silica glass and four sets of 2.5wt% to 10wt% MWCNT-SiO$_2$ glass composites (b) Vickers hardness against relative density.

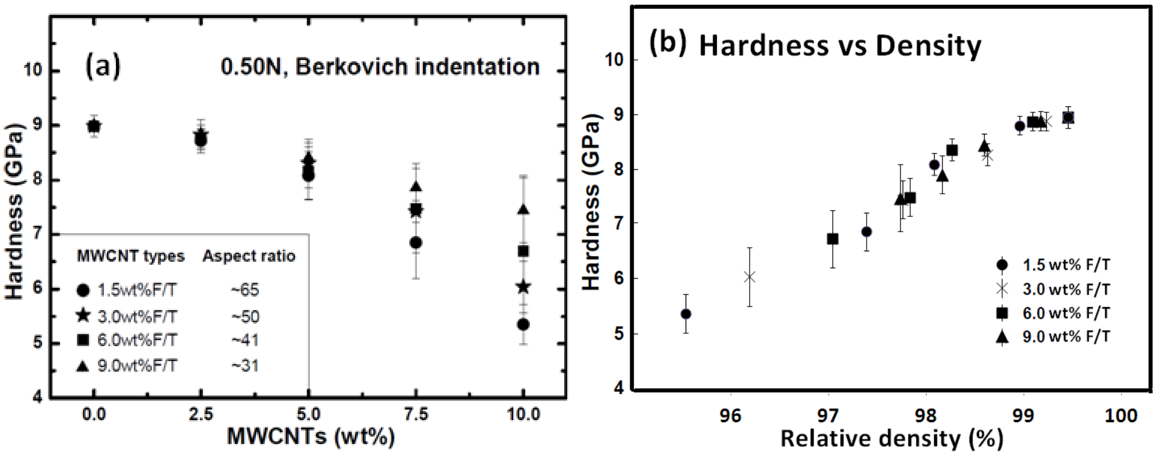

Figure 6.20: Berkovich hardness values of silica glass and four sets of 2.5wt% to 10wt% MWCNT-SiO$_2$ glass composites (b) Vickers hardness against relative density.

An enlarged view of a section of the same indent (Figure 6.21(b)) reveals the dimensions of MWCNTs compared to the indent size. Such an indent size is expected to show the representative hardness value of the composites. The TEM images in Figure 6.21 are quite unusual. These first images through the CNT-glass/ceramic composites under an indent indicate the preferential alignment of MWCNTs along the indenting surface, although the effect is weak due to the random orientation and the flexible structure of MWCNTs. The cracks at the indentation edge are also shown, which were effectively deflected by the MWCNTs (Figure 6.28(b)). Cracks beneath the indentation were also successfully arrested by MWCNTs (Figure 6.27).

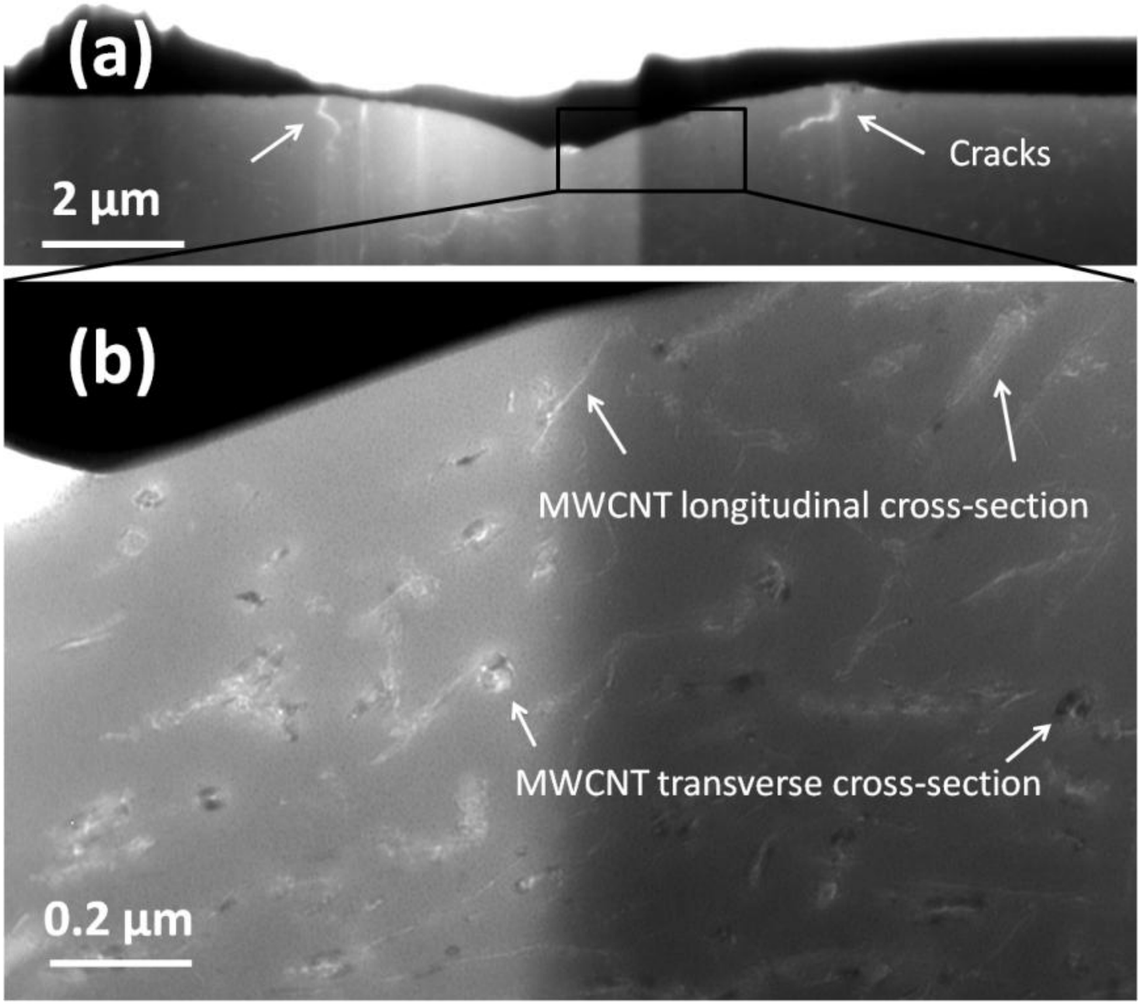

Figure 6.21: (a) BF-TEM image of the cross-section of a Berkovich indentation on 5.0wt% MWCNT-SiO$_2$ glass composite. (b) HRTEM image of a section of the same indent relates the size of MWCNTs with Berkovich indent.

b. Elastic modulus

The elastic moduli of silica glass and MWCNT-SiO$_2$ glass composites were measured by the instrumented Berkovich nano-indentation technique (Figure 6.22). Again, the silica glass shows the highest elastic modulus (70.9GPa), which is comparable to the typical silica glass value [210] of 72.0GPa. The incorporation of MWCNTs produced a continuous decrease in the elastic moduli of the composites. Considering the theoretical CNT stiffness value, i.e. 1000GPa, an increase in the elastic moduli of the composites was expected; however, the experimental data shows an opposite (decreasing) trend. To relate the experimental results and to find the effective stiffness of MWCNTs incorporated in the composites, the theoretical elastic moduli of the composites were obtained from the rule of mixtures.

For a three-dimensional randomly-oriented short fibre composite system, which could represent the present composites, a modified rule of mixtures (Krenchel's rule [240]) incorporating the orientation efficiency factor (η_o) and length efficiency parameter (η_L) was used:

$$E_c = \eta_o \, \eta_L \, E_f \, V_f \; + E_m\left(1 - V_f\right) \qquad \textbf{Equation 6.1}$$

where, E$_c$, E$_f$, and E$_m$ are the elastic moduli of composite, fibres and matrix, respectively, while V$_f$ is the fibre volume fraction. The value [76] of η_o for three-dimensional random orientation of fibres is 0.2, while the value of η_L depends upon the fibre length (L), diameter (D), inter-fibre spacing (2R) and shear modulus of the matrix (G$_m$), as given below:

$$\eta_L = 1 - \left[\frac{\tanh(\left(\frac{1}{2}\right)\beta L)}{\left(\frac{1}{2}\right)\beta L}\right] \qquad \textbf{Equation 6.2}$$

$$\beta = \left[\frac{8\, G_\mathrm{m}}{E_\mathrm{f}\, D^2 \, log_e \, \left(\frac{2R}{D}\right)}\right]^{1/2} \qquad \textbf{Equation 6.3}$$

The modified rule of mixtures was applied to one set of MWCNT-SiO$_2$ glass composites containing 2.5wt% to 10wt% (3.0wt%F/T) MWCNTs. The MWCNT length and diameter are given in Table 5.1, inter-MWCNT spacing was determined by SEM image analysis and a literature value of shear modulus of silica glass [159], i.e. 31GPa, was used for calculations. The parameter that remains to be investigated is the elastic modulus of MWCNTs; different stiffness values of MWCNTs were used, ranging from 1000GPa to 100GPa, while the experimental stiffness value of silica glass, i.e. 70.9GPa, was taken. The largely different stiffness values of MWCNTs were chosen in order to fit the model to the experimental data; the other reason was a huge variation in the stiffness values of CNTs (Table 9.1) synthesised by different techniques [24,34], as discussed in Section 2.1.3(a). Also, the hollow core is excluded when the elastic modulus of CNTs is reported but its effect should be considered in the context of composite reinforcement. Finally, this simple analysis also assumes the negligible transverse properties of MWCNTs, which may be reasonable given the relatively weak interfacial bonding and the hollow/collapsible nature of the MWCNT structure. The higher composite values should be obtained if MWCNTs possess the theoretically estimated elastic modulus (1000GPa), but even for the maximum loading (10wt%) of idealised MWCNTs, the predicted increase in stiffness is small, i.e. 86GPa. The modest increase is due to both a high elastic modulus of silica glass, i.e. 70.9GPa, and the random-orientation of MWCNTs, which provide a reduced value of the effective MWCNT stiffness. A stiffness value of 350GPa for MWCNTs almost retains the elastic modulus of the composites by providing similar value as that of silica glass. Therefore, the model suggests an increase in the elastic modulus in three-dimensional randomly-oriented MWCNT-SiO_2 glass composites, if the stiffness is >350GPa for the chosen MWCNT size (3wt%F/T). Indeed, further decrease in the MWCNT stiffness (100GPa) lowers the elastic modulus of composites (~64GPa) below the silica glass matrix (70.9GPa). However, this value (~64GPa) is still higher than the experimental values for 10wt% MWCNT-SiO_2 glass composites. Even zero MWCNT stiffness value in the above equation provides a higher elastic modulus of composites than found experimentally. This indicates the presence of porosity in composites, which must have reduced the elastic modulus further [165]. Porosity in MWCNT-SiO_2 glass composites can come from the insufficient densification of the matrix and may also be due to the hollow cores of the MWCNTs. The effect of porosity on elastic modulus of the composites will be discussed further below (Section 6.2.3(d).

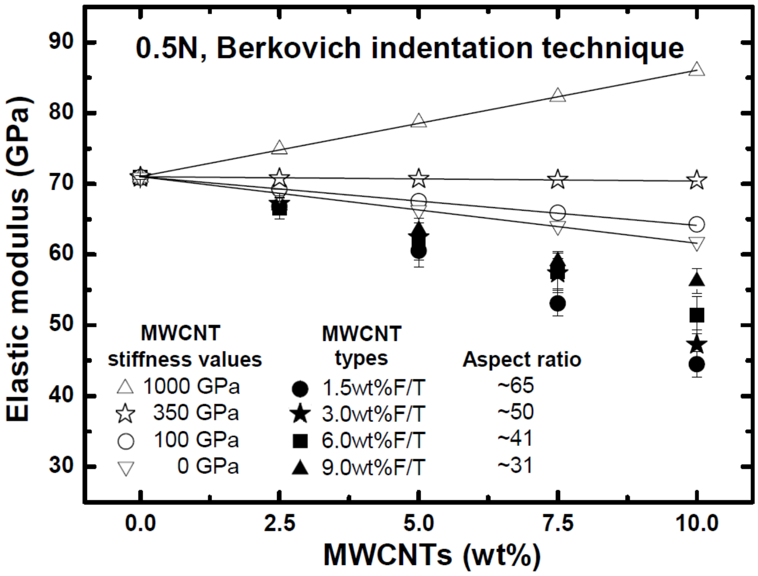

Figure 6.22: Elastic moduli of silica glass and four sets of 2.5wt% to 10wt% MWCNT-SiO$_2$ glass composites; the composite elastic moduli were predicted by applying the modified rule of mixtures with different stiffness values of MWCNTs.

Another interesting feature in Figure 6.22 is the difference in elastic moduli of the four sets of composites containing different size MWCNTs. Although the elastic moduli values fall close to their error range, composites containing the lowest aspect ratio and the shortest length MWCNTs (9.0wt%F/T) showed systematically higher values than others; a possible reason again is the higher sintered densities of these composites. The lowest stiffness, with higher aspect ratio MWCNTs, indicates that composites do not follow the length efficiency parameter, as given in Equation 6.1.

c. Indentation fracture toughness

The fracture toughness of silica glass and MWCNT-SiO$_2$ glass composites was evaluated by the Vickers indentation technique in combination with the Anstis et al's. expression [211], as discussed in Section 4.4.3, which proved useful for determining the relative toughening effect of MWCNTs in silica GMCs (Figure 6.23). The indentation fracture toughness of silica glass was found to be in the range 0.75-0.85MPa.m$^{1/2}$, which increased roughly linearly with the addition of MWCNTs and reached a value of 1.40-1.70 MPa.m$^{1/2}$ in composites with 10wt% MWCNTs in the four sets of composites. A similar increasing trend in toughness was found in a previous study on CNT-glass composites consolidated by SPS [91]. Although the validity of the indentation fracture toughness technique has been questioned and the use of conventional techniques has been suggested for absolute fracture toughness values [162], the indentation techniques can indicate the relative change in the fracture toughness of materials. The current results obtained by indentation technique (Figure 6.23) clearly show an improvement in the fracture toughness of the monolithic glass matrix by adding MWCNTs. Previous work [91] on CNT-glass composites, using indentation and chevron techniques, showed similar trends, although the two techniques provided different absolute values.

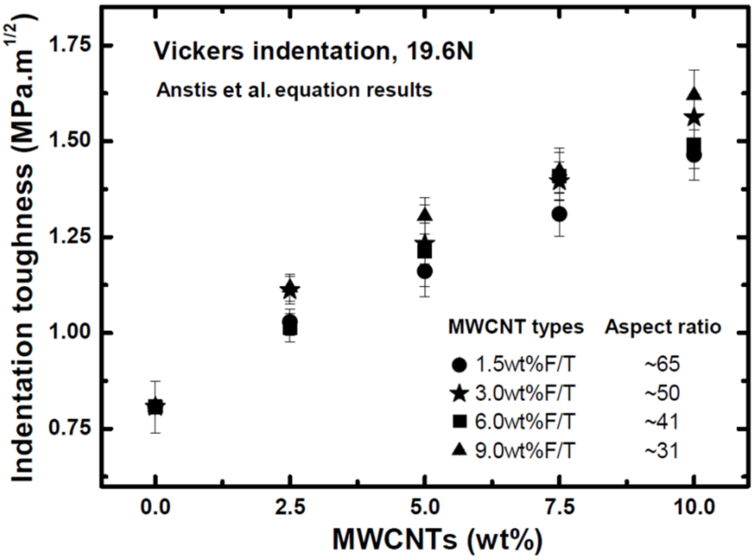

Figure 6.23: Indentation fracture toughness of silica glass and four sets of 2.5wt% to 10wt% MWCNT-SiO_2 glass composites.

One of the aims of the present work was to study the effect of different MWCNT dimensions on the fracture toughness of the composites compared to its effect on the glass matrix. The present toughness data indicate that the incorporation of different length/aspect ratio MWCNTs did not lead to a significant difference in fracture toughness and the results were within their error range. Nevertheless, composites containing 1.5wt%F/T MWCNTs showed values in the lower range and those containing 9.0wt%F/T MWCNTs displayed upper range values; the lower densities of 1.5wt%F/T MWCNTs composites may be a reason for the decreased values. In short, the selected range of MWCNT dimensions, i.e. diameter: 37nm to

57nm, length: 1.78μm to 2.42μm, and aspect ratio: 31 to 65, is not likely to have a significant effect on fracture toughness, especially, in the presence of its effect on composite densification. The toughening mechanisms appeared in the present composites are discussed in Section 6.2.3(e).

d. Effect of porosity on mechanical properties

It is well known that the mechanical properties of glasses and ceramics decrease with porosity [208]. As observed earlier (Section 6.2.1(a)), the high aspect ratio of MWCNTs contributes indirectly to the development of porosity due to the incomplete composite densification. Moreover, the hollow core of MWCNTs may also contribute to porosity in composites. A ratio of ~10:3 was measured for outer and inner diameter of 100 independent 3.0wt%F/T MWCNTs from the TEM images. These values imply that ~10% of the total MWCNT volume comprises the hollow core, which further suggests that the porosity volume coming from the hollow core of MWCNTs in 10vol% MWCNT-SiO_2 glass composites is ~1.0%. Considering this argument, it can be inferred that the composites actually contain porosity of similar shape to that of the embedded MWCNTs but smaller in diameter, comparable to their hollow core (Figure 6.24(a)). Although, the porosity volume due to hollow MWCNT structure is small, the uniform distribution of this kind of porosity in composites may have pronounced effects. A counter argument could suggest that the porosity due to the hollow core is shielded due to its presence inside the MWCNTs. However, it can still affect the mechanical properties, especially under indenter loading during hardness testing, where MWCNTs might compress or collapse radially.

To explore the porosity effect on the elastic modulus and hardness of composites and to observe any contribution of MWCNTs to the composite mechanical properties, a set of composites containing 2.5wt% to 10wt% (9.0wt%F/T) MWCNTs was oxidised at 750°C for 48h to completely oxidise MWCNTs and to produce a porous silica matrix (Section 6.2.5(c)). The oxidised composites were then mechanically characterised for elastic modulus and hardness measurements by the same technique as used for sintered composites, i.e. Berkovich indentation technique. Figure 6.24 shows schematically the porosity volume of the composite specimens with the presence of MWCNTs and after their oxidation.

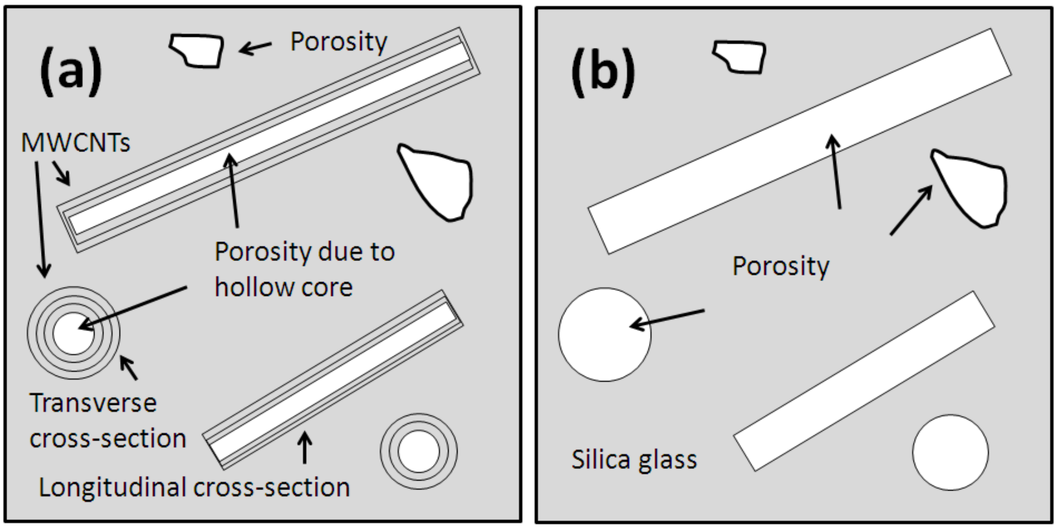

Figure 6.24: Schematic diagrams showing porosity in MWCNT-SiO_2 glass composites due to (a) the hollow core of MWCNTs and (b) after the oxidation of MWCNTs.

The elastic moduli of oxidised composites containing 2.5wt% to 10wt% MWCNTs (Figure 6.25(a)) displayed lower stiffness values after MWCNT oxidation, as expected. Also, a continuous decrease was noticed in composites containing increasing MWCNT content, which corresponds to increased porosity after MWCNT oxidation. Similarly, the hardness of the oxidised composites showed a declining trend (Figure 6.25(b)) and the hardness values of the composites were greater before their oxidation. It can be inferred that the presence of MWCNTs in composites provides increased values of the stiffness and hardness compared to when they were completely oxidised leaving behind an increased level of porosity. However, MWCNTs also act as a source of porosity and, therefore, could not increase the stiffness and hardness of GMCs.

e. Toughening mechanisms in composites

In fibre composite systems, energy-absorbing mechanisms emerge during crack growth, such as crack deflection, fibre/matrix debonding, fibre bridging and pullout, which are absent during the failure of monolithic materials. Features corresponding to these mechanisms were observed in the MWCNT-SiO_2 glass composites; MWCNT pullout was observed on the fractured composite surfaces (Figure 6.14 and Figure 6.15), while MWCNT fracture and bridging were seen (Figure 6.26) along the crack, including at angles other than perpendicular to the crack plane (Figure 6.28(a)). Images of the crack tip (Figure 6.27) suggest that MWCNTs may provide traction against the crack opening and hence impede crack propagation. During MWCNT pullout, the slots produced due to partial MWCNT pullout are shown (Figure 6.28(a)). Finally, multiple deflections of the cracks clearly occur due to MWCNTs (Figure 6.28(b)). The cracks shown in these TEM images were observed around the indents produced during nanoindentations.

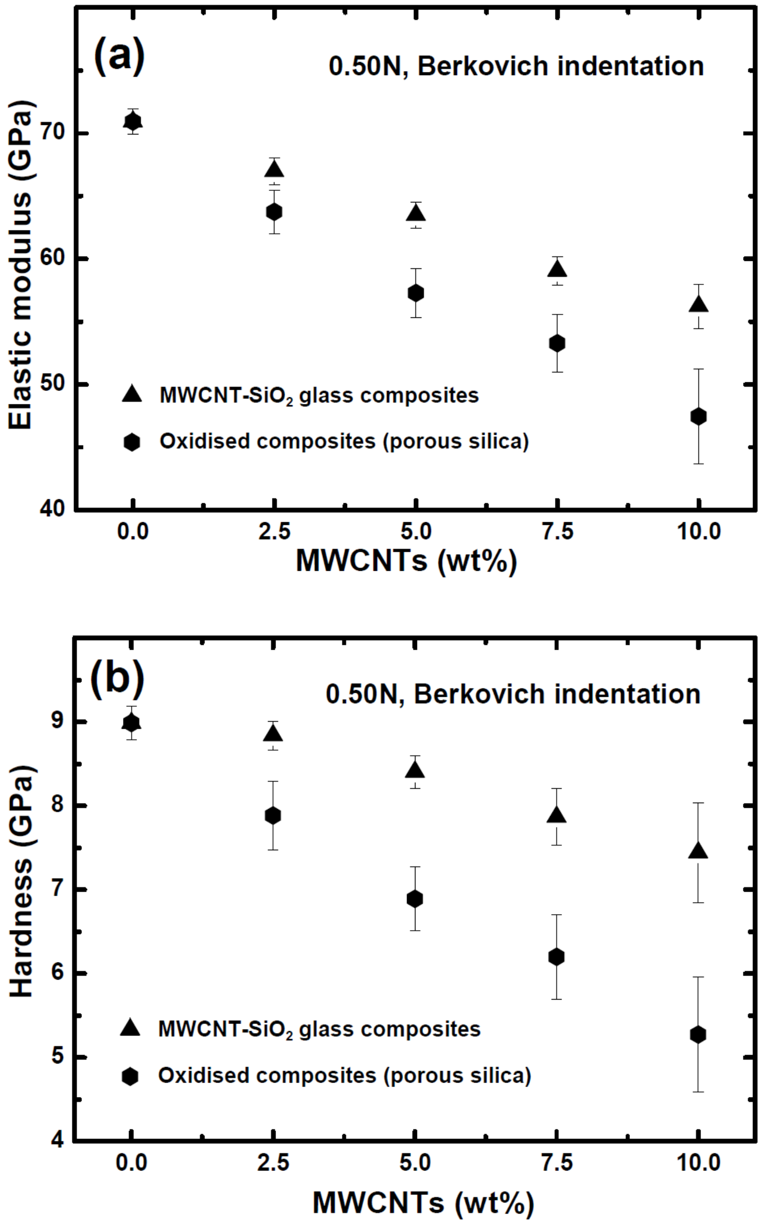

Figure 6.25: (a) Elastic moduli and (b) hardness of silica glass and 2.5wt% to 10wt% (9.0wt%F/T) MWCNT-SiO_2 glass composites before and after the oxidation of MWCNTs.

The aforementioned energy absorbing mechanisms, as also previously observed [159], qualitatively indicate a significant improvement in the fracture toughness of CNT-glass/ceramic composites but still not enough to transform the brittle matrices into structurally reliable materials. Moreover, it is unclear which modes contribute to significant toughening. A qualitative analysis of these toughening mechanisms is provided in the following paragraphs to indicate their contributions.

In standard fibre composite theory, toughness maximises when the fibre length approaches a critical value known as the critical fibre length (L_c), which is the maximum length at which shear failure at the fibre/matrix interface occurs without fracturing the fibre. L_c is related to the fracture strength (σ_f) and radius (R_f) of the fibres, and the interfacial shear strength (τ_i):

$$\frac{L_c}{\mathrm{R}_f} = \frac{\sigma_f}{2\tau_i}$$ **Equation 6.4**

In short fibre composites [76,241], the pullout length varies between zero to $L_c/2$. Therefore, varying MWCNT pullout lengths were observed on the composite fractured surfaces (Figure 6.14 and Figure 6.15), which were measured by SEM images. At least, 500 MWCNTs were measured independently to acquire the pullout length data for the four types of 10wt% MWCNT-SiO_2 glass composites containing different size MWCNTs.

The maximum (L_{mp}) and average (L_{ap}) MWCNT pullout lengths for the four composites are given in (Table 6.1); based on L_{mp} and L_{ap}, the values of maximum (L_{mc}) and average (L_{ac}) critical MWCNT lengths were estimated, given in the same table. As the reinforcing MWCNTs showed a large variation in their lengths, L_{mc} may overestimate, while L_{ac} may underestimate the real L_c. Therefore, it was considered appropriate to take both the values to act as L_c and estimate separately the toughening contribution of each of them; subsequent comparison with the practically achieved toughness values will reveal their appropriateness.

Based on the measured L_c (L_{mc} & L_{ac}) and R_f values (Table 5.1) of the four sets of 10wt% MWCNT-SiO_2 glass composites, the fracture strength values of MWCNTs were calculated using

Equation 6.4 and are given in Table 6.2. Since the value of τ_i for CNT-glass/ceramic composites is not available, a value based on carbon fibre-reinforced GMCs [242-243] was used, i.e. 10MPa, although values as high as 35MPa have been reported [244].

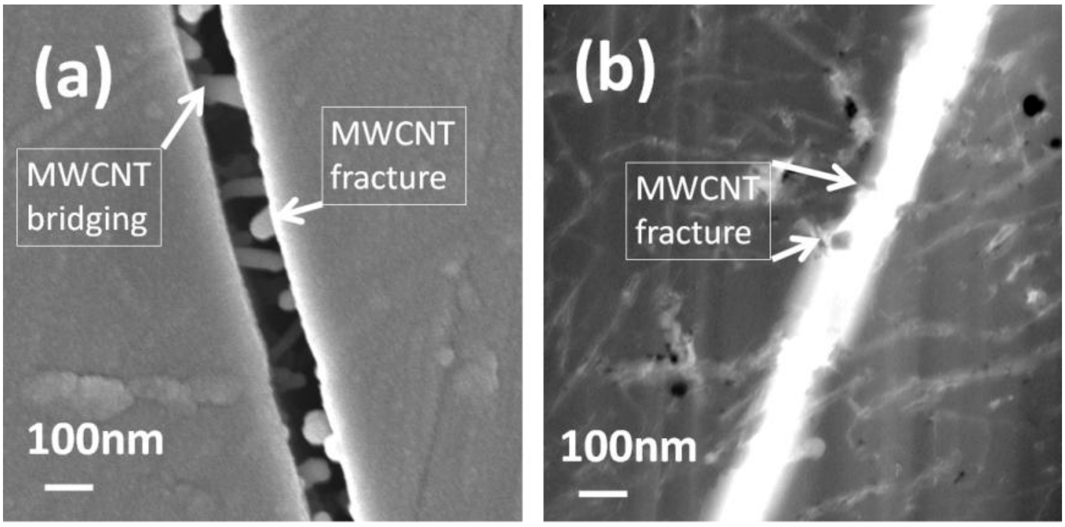

Figure 6.26: (a) SEI-SEM and (b) BF-TEM images showing the MWCNT fracture and bridging in (3.0wt%F/T) MWCNT-SiO_2 glass composites.

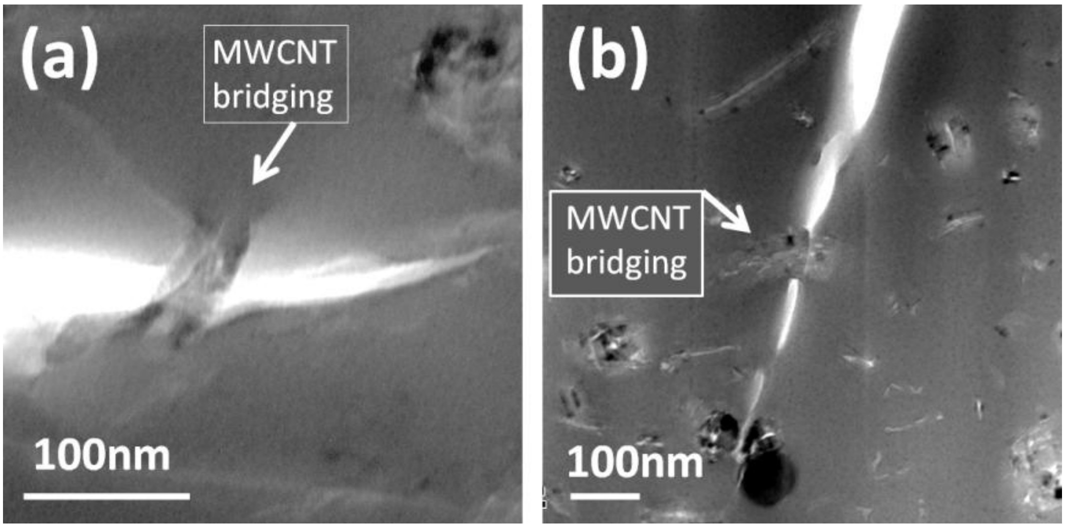

Figure 6.27: BF-TEM images showing the bridging of cracks due to MWCNTs in MWCNT-SiO_2 glass composites. Cracks were produced under the indentation during hardness testing.

To estimate the MWCNT contribution to toughening silica glass, uniaxial short fibre composite theory was applied to 10wt% MWCNT-SiO_2 glass composites using the following expressions for the three energy absorbing mechanisms, i.e. debonding, crack bridging and pullout [245]; the debonding and bridging provide similar results:

$$G_{debond} = \frac{V_f R_f {\sigma_f}^3}{6E_f \tau_i} \qquad \textbf{Equation 6.5}$$

$$G_{bridging} = \frac{V_f R_f {\sigma_f}^3}{6E_f \tau_i} \qquad \textbf{Equation 6.6}$$

$$G_{pullout} = \frac{V_f R_f {\sigma_f}^2}{12\tau_i} \qquad \textbf{Equation 6.7}$$

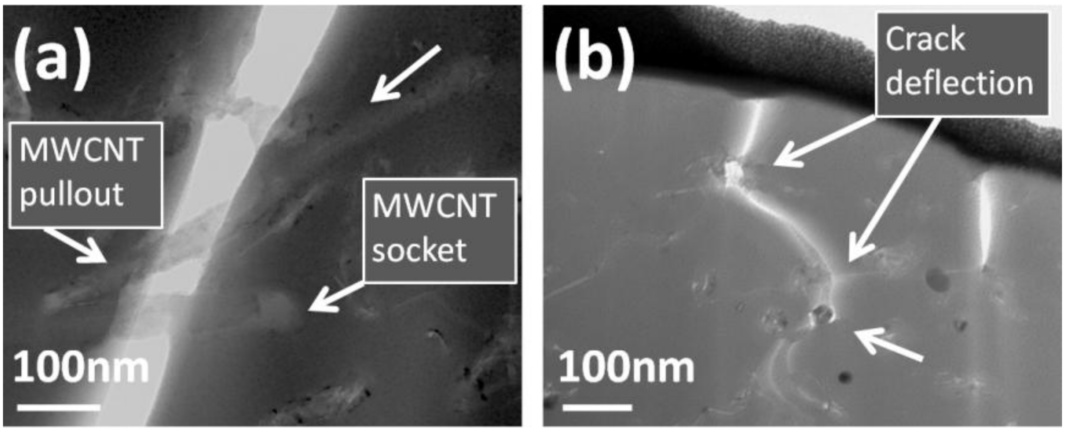

Figure 6.28: (a) BF-TEM image showing MWCNT pullout along the crack plane; corresponding slots due to partial pullout are also evident along with (b) the multiple deflections of surface cracks due to MWCNTs.

Table 6.1: Measured maximum (L_{mp}) and average (L_{ap}) pullout lengths of MWCNTs in four types of 10wt% MWCNT-SiO_2 glass composites. Maximum (L_{mc}) and average (L_{ac}) critical lengths were estimated from L_{mp} and L_{ap}, respectively.

MWCNT types	1.5wt% F/T	3.0wt% F/T	6.0wt% F/T	9.0wt% F/T
L_{mp} (μm)	1.01	0.95	0.93	0.90
L_{ap} (μm)	0.37±0.25	0.29±0.22	0.28±0.21	0.22±0.19
L_{mc} (μm)	2.02	1.90	1.86	1.80
L_{ac} (μm)	0.74±0.50	0.58±0.44	0.56±0.42	0.44±0.38

All the parameters required in the above expressions are available, i.e. V_f, R_f, σ_f and τ_i are 0.133 (10wt%), 18.5-28.5nm, 1.26-2.18GPa and 10MPa, respectively; the only parameter still unknown is the stiffness (E_f) of MWCNTs, which was estimated to be an order of magnitude higher than their strength. This ratio was further verified by taking upper values of experimental elastic modulus (1000GPa) and tensile strength (100GPa) of CNTs (Table 9.1 and Table 9.2), as also observed in the published data [34].

The contribution of the three toughening mechanisms, i.e. debonding, bridging and pullout is given in Table 6.2 for both the L_{mc} & L_{ac}. It is to be noted that a fraction of (L_c/L) was estimated to pullout in composites and the debonding length (L_d) was taken to be the same as the critical length for stress transfer at the end of MWCNTs, i.e. L_d=L_c. Hence, the total work of the fracture of composites is obtained by combining the above three equations:

$$G_{total} = \frac{V_f R_f {\sigma_f}^3}{6E_f \tau_i} + \frac{V_f R_f {\sigma_f}^3}{6E_f \tau_i} + \frac{V_f R_f {\sigma_f}^2}{12\tau_i} \qquad \textbf{Equation 6.8}$$

The total energy consumed (G_{total}) by adding the three energies ($G_{pullout}$+G_{debond}+$G_{bridging}$) is provided in Table 6.2 for both the L_{mc} & L_{ac}, which can be compared with the observed toughening contribution of MWCNTs calculated by using Equation 6.9 after putting the experimental values of K_{IC} and E of 10wt% MWCNT-SiO_2 glass composites and subtracting the intrinsic toughness of glass, i.e. 0.8MPam$^{1/2}$ (8.7J/m^2).

$$G = \frac{(1 - \nu^2)\, {K_{IC}}^2}{E} \qquad \textbf{Equation 6.9}$$

where, ν, K_{IC} and E represent Poisson's ratio, fracture toughness and elastic modulus of the composites, respectively. The resulting MWCNT contribution is 32.6-41.4J/m^2, which falls within the upper and lower bound estimation obtained by using L_{mc} & L_{ac} as L_c (Table 6.1). Although, the contribution of MWCNTs to toughening the brittle glass matrix is twofold, the absolute magnitude of the effect is small when compared with carbon fibres; a toughening contribution of 350J/m^2 was observed in randomly oriented 20vol% carbon fibre-reinforced borosilicate GMCs [84]. The scaling argument can explain this discrepancy by relating the toughening mechanisms with the fibre diameter. The expressions above show that pullout energy increases with fibre radius and fracture strength but decreases with interfacial shear strength. The diameter of CNTs (1-100nm) is 2-4 orders of magnitude smaller than carbon fibres (~10μm), showing a significant decrease in the pullout toughening as diameter reduces from micrometer (carbon fibres) to nanometer (CNTs) scale.

Table 6.2: Pullout ($G_{pullout}$), debonding (G_{debond}) and bridging ($G_{bridging}$) energies for both maximum (L_{mc}) and average (L_{ac}) pullout lengths along with total energies (G_{total}) for the four types of 10wt% MWCNT-SiO_2 glass composites containing different size MWCNTs. Experimentally obtained energies ($G_{total\text{-}exp}$) based on K_{IC} and E, and toughening energies ($G_{toughening\text{-}exp}$) due to MWCNT contribution are also displayed.

Composite types	**1.5wt%F/T**	**3.0wt%F/T**	**6.0wt%F/T**	**9.0wt%F/T**
L_f (μm)	2.42±1.45	2.22±1.13	2.07±1.09	1.78±0.79
R_f (nm)	18.5±7.0	22.0±9.5	25.5±12.0	28.5±13.5
L_{mc} (μm)	**2.02**	**1.90**	**1.86**	**1.77**
σ_f (GPa)	2.18±0.82	1.73±0.74	1.46±0.68	1.26±0.59
E_f (GPa)	21.8±8.2	17.3±7.4	14.6±6.8	12.6±5.9
G_{debond} (J/m^2)	16.3±16.8	12.4±13.5	10.8±12.6	9.6±11.1
$G_{bridging}$ (J/m^2)	16.3±16.8	12.4±13.5	10.8±12.6	9.6±11.1
$G_{pullout}$ (J/m^2)	81.6±72.2	62.2±56.1	54.0±52.2	50.9±45.2
G_{total} (J/m^2)	114.2±76.1	87.1±59.2	75.6±55.1	67.8±47.9
L_{ac} (μm)	**0.74±0.50**	**0.58±0.44**	**0.56±0.42**	**0.44±0.38**
σ_f (GPa)	0.80±0.61	0.52±0.46	0.43±0.38	0.30±0.30
E_f (GPa)	8.0±6.1	5.2±4.6	4.3±3.8	3.0±3.0
G_{debond} (J/m^2)	0.80±1.45	0.35±0.71	0.29±0.59	0.14±0.33
$G_{bridging}$ (J/m^2)	0.80±1.45	0.35±0.71	0.29±0.59	0.14±0.33
$G_{pullout}$ (J/m^2)	4.01±5.17	1.77±2.48	1.47±2.08	0.74±1.13
G_{total} (J/m^2)	5.61±5.57	2.47±2.68	2.06±2.24	1.04±1.22
$G_{total\text{-}exp}$ (J/m^2)	45.9±2.1	50.2±2.0	41.4±1.8	44.9±1.8
$G_{toughening\text{-}exp}$ (J/m^2)	37.1±2.2	41.4±2.1	32.6±1.9	36.1±2.0

The greater CNT strength can significantly increase the toughening effect by an increased pullout length [246]; also, it is squared/cubed in the above expressions. However, published data (Table 9.2) shows that the fracture strength of CNTs ranges between 1GPa and 100GPa; the lower-end values are comparable to carbon fibres but only the upper-end values of CNTs provide a 10 times increase in strength over carbon fibres. Moreover, CNTs grown by CVD processes are generally used for composite manufacturing, which possess lower strength values due to the presence of structural defects. Hence, the net improvement in the fracture toughness due to the expected increased strength of CNTs is insignificant. Finally, a decrease in interfacial shear strength can lead to increased fracture toughness but increased CNT critical length would be required to exploit it (Equation 6.4). Generally, the aspect ratio of pullout lengths of MWCNTs in composites remains relatively similar to that of conventional fibre composites, i.e. 10-100, which suggests that the fracture strength to interfacial strength ratio (σ_f/τ_i) is constant. It is still unclear which mechanisms contribute most to increased toughening in CNT-glass/ceramic composites. It has been suggested that CNT bridging across the crack provides the dominant contribution [109]. However, based on the current observations and estimations, the increase in fracture toughness in MWCNT-SiO_2 glass composites is due to the combined contribution of the three mechanisms, i.e. debonding, bridging and pullout, although pullout provides the major contribution. The rearrangement of Equation 6.8 [245] into Equation 6.10 confirms the fibre pullout mechanism to be the most important energy absorbing mechanism during composite fracture.

$$G_{total} = \frac{V_f R_f {\sigma_f}^2}{12\tau_f}\left(\frac{4\sigma_f}{E_f}+1\right) = G_{pullout}\left(\frac{4\sigma_f}{E_f}+1\right) \qquad \textbf{Equation 6.10}$$

In short, high CNT volume fraction (V_f), fracture strength (σ_f) and radius (R_f), and low interfacial shear stress (τ_i) increase the fracture energy. Other energy absorbing mechanisms remain to be analysed quantitatively, such as crack deflection (Figure 6.28(b)) and pullout of CNTs not oriented at 90^o to the crack plane (Figure 6.28(a)), which increases friction. Finally, new mechanisms, potentially operative at the nanoscale, such as the collapse of hollow CNTs, springiness of coiled CNTs and telescopic failure of CNTs may also emerge in future [91].

6.2.4 Functional characterisation

a. Electrical conductivity

The addition of CNTs significantly increased the electrical conductivity of insulating silica glass, which has, otherwise, low electrical conductivity, i.e. 10^{-10}S/cm (Figure 6.29). The electrical conductivity of the four sets of MWCNT-SiO_2 glass composites containing 2.5wt% to 10wt% MWCNTs ranges between 1S/cm and 100S/cm, which is 10-12 orders of magnitude higher than that of silica glass. The relative difference between the conductivities of the composites containing different MWCNT sizes is also evident; clearly, the composites containing longer (high aspect ratio) MWCNTs (1.5wt%F/T) demonstrated higher electrical conductivities compared to others. These composites are also expected to have lower percolation threshold than those containing shorter (low aspect ratio) MWCNTs (9.0wt%F/T) [164].

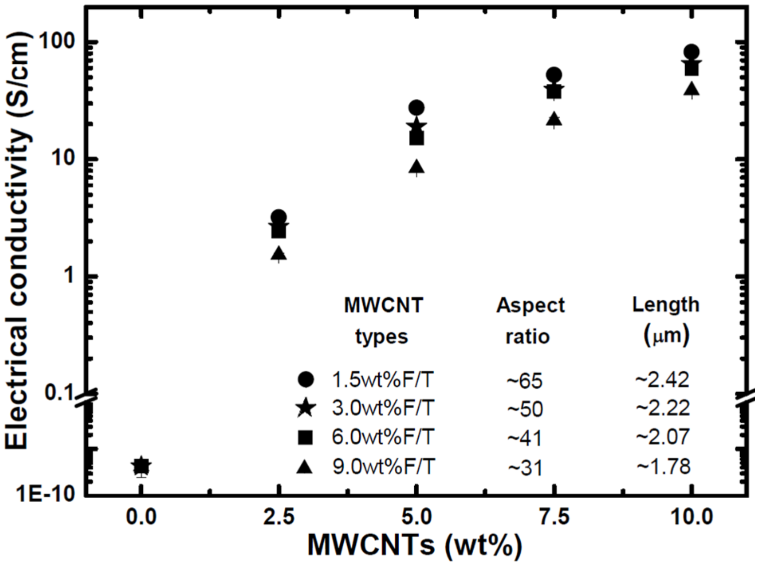

Figure 6.29: Electrical conductivities of silica glass and the four sets of 2.5wt% to 10wt% MWCNT-SiO_2 glass composites. MWCNTs were synthesised by different ferrocene concentrations in toluene (F/T).

A sudden change in the conductivity of 2.5wt% MWCNT-SiO_2 glass composites suggests that the percolation threshold lies between zero to 2.5wt% MWCNTs. According to percolation theory [247], an increase in the electrical conductivity (σ) should follow the scaling law:

$$\sigma \propto (p - p_c)^t \qquad \textbf{Equation 6.11}$$

where p is the volume fraction of MWCNTs, p_c is the percolation threshold of MWCNTs and the exponent t reflects the dimensionality of the system.

Figure 6.30 shows the conductivity values versus the MWCNT volume fractions for the four sets of composites containing different sized MWCNTs; the inserted plots in log-log scale display the electrical conductivity (σ) values as a function of p-p_c showing well fitted data obeying the scaling law of the percolation theory. Percolation threshold (p_c) steadily increased, i.e. 1.80vol%, 2.04vol%, 2.16vol% and 2.70vol% (1.37wt%, 1.54wt%, 1.64wt% and 2.04wt%), in the four types of composites containing different sized MWCNTs (Table 5.1); the values of exponent (t) were 1.6, 1.5, 1.4 and 1.1, respectively. As expected, the composites containing longer (higher aspect ratio) MWCNTs demonstrated a comparatively lower percolation threshold than the others. The percolation threshold of CNTs, close to 1wt%, is generally observed in composites [94,97,159]; however, values as low as 0.05wt% [248] and as high as 5.0wt% [163] have also been reported in CNT-glass/ceramic matrix composites. A high percolation value indicates either a low aspect ratio of CNTs or their good dispersion in the composites, while a low value suggests the presence of high aspect ratio and/or entangled CNTs producing agglomerates. The high percolation threshold values of composites obtained in the present study, i.e. 1.37-2.04wt% indicate uniformly dispersed and well-separated MWCNTs, as already witnessed in SEM/TEM images (Figure 6.14, Figure 6.15 and Figure 6.16(a)).

b. Thermal conductivity

The room temperature thermal conductivities of silica glass and the four sets of MWCNT-SiO_2 glass composites containing 2.5wt% to 10wt% MWCNTs were obtained from their thermal diffusivities, specific heat capacities and sintered densities using Equation 4.12. A linear increase in thermal conductivity was observed in the silica glass matrix after reinforcing with MWCNTs (Figure 6.31). However, the improvement was relatively modest because no percolation effect is expected in thermal conductivity as observed in electrical conductivity of the composites. Also a difference of only three orders of magnitude exists between the thermal conductivity of MWCNTs [66], i.e. 3000W/m.K, and the silica glass matrix, i.e. 1.38W/m.K.

On the basis of Maxwell-Garnett effective medium approach, the thermal conductivity of a fibre composite (K_c) can be calculated by the following equation [249]:

$$K_c = K_m + K_f \, cos^2\theta \, V_f \qquad \textbf{Equation 6.12}$$

where, K_m and K_f are the thermal conductivities of the matrix and the fibres, respectively; V_f is the fibre volume and θ is the angle between fibre axis and the given direction. For aligned and randomly orientated fibres, $cos^2\theta$ is taken as 1 and 1/3, respectively [249]. Using the measured thermal conductivity (K_m) of silica glass (1.38W/m.K), a published value for thermal conductivity (K_f) of MWCNTs (3000W/m.K) [66], the volume fraction of MWCNTs (V_f) in 10wt% MWCNT-SiO_2 glass composites (0.132), and assuming random orientation ($cos^2\theta$ = 1/3) of MWCNTs, the thermal conductivity of composites (K_c) was calculated to be 133W/m.K. This value is two orders of magnitude higher than the experimental value of only ~2.0W/m.K for 10wt% MWCNT-SiO_2 glass composites and indicates the involvement of other factors leading to the modest increment of thermal conductivity. The thermal resistance due to large interfacial surface area between MWCNTs and glass matrix could be the possible reason, as the applied model (Equation 6.12) assumes a perfect contact between MWCNTs and glass matrix and ignores any interfacial resistance. An expression to calculate the thermal conductivity of composites incorporating interfacial thermal resistance is given below [250]:

$$K_C = K_m + \frac{K_f \, L}{2R_i K_f + L} cos^2\theta \, V_f \qquad \textbf{Equation 6.13}$$

where L is the length of fibres and R_i is the interfacial thermal resistance, also known as Kapitza resistance; other parameters are the same as used in Equation 6.12. Using the average (1.5wt%F/T) MWCNT length of 2.42μm (Table 5.1) and R_i values, which is reported to be $8x10^{-8}m^2K/W$ in CNT matrix composites; this value is of the same order of magnitude in other composite materials and polycrystals [250], the value of K_c for 10wt% MWCNT-SiO_2 glass composites was found to be 2.04W/m.K, which is close to the measured value of 2.03W/m.K.

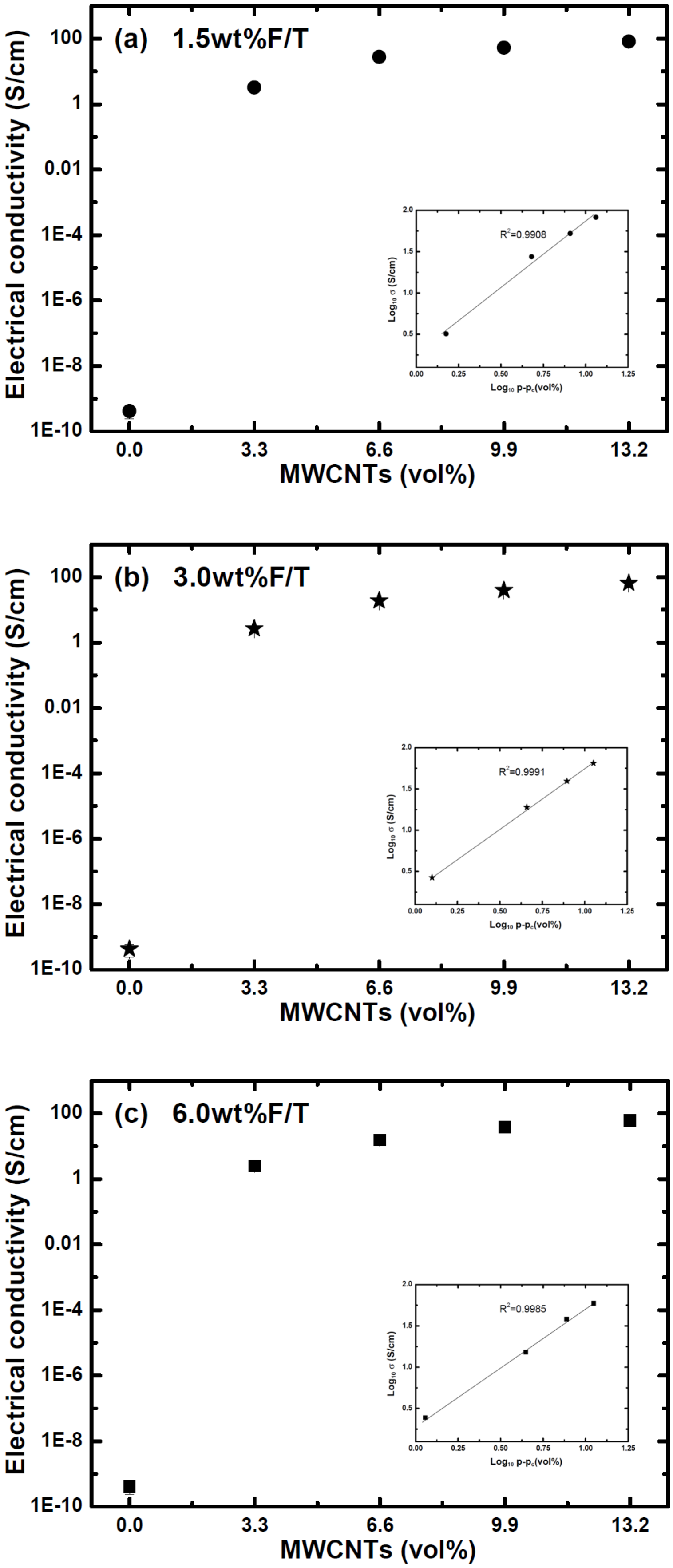

(Continued to next page)

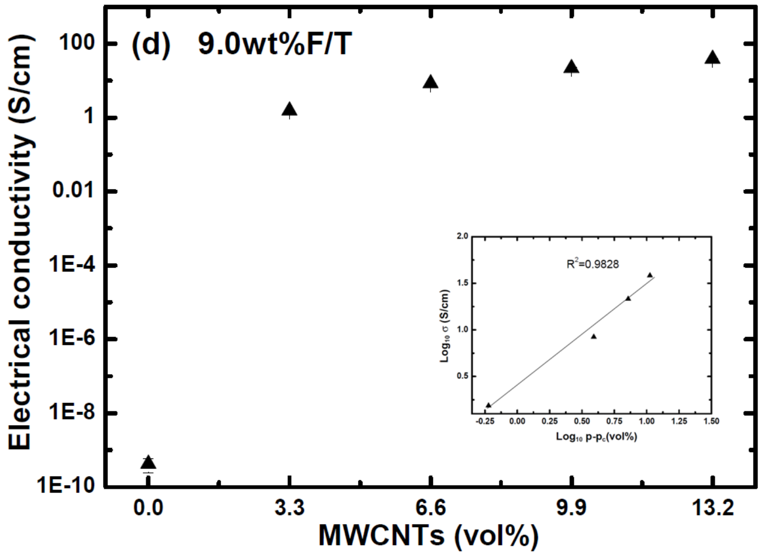

Figure 6.30: (a-d) Experimental electrical conductivity data as a function of MWCNT content for the four sets of composites containing MWCNTs synthesised by using different ferrocene concentrations in toluene (F/T); inserted plots in log-log scale show well fitted electrical conductivity values by the scaling law of the percolation theory.

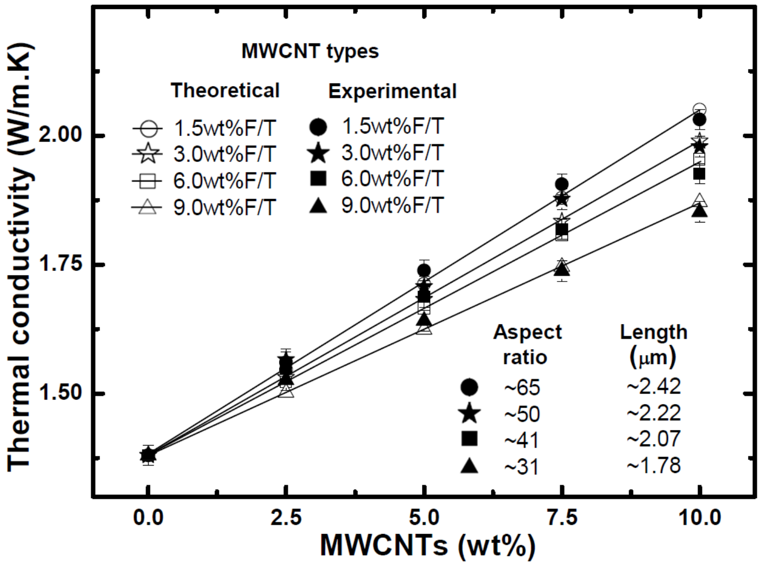

Figure 6.31: Room temperature thermal conductivity of silica glass and of the four sets of 2.5wt% to 10wt% MWCNT-SiO$_2$ glass composites. The theoretically predicted values (using Equation 6.13) are shown along with the experimental thermal conductivities.

The thermal conductivity values for the four sets of composites containing 2.5wt% to 10wt% were calculated using the above expression and compared with experimental results

(Figure 6.31). A relatively good match was observed between the calculated and the experimental values of the composites containing MWCNTs of different lengths ranging from 1.78µm to 2.42µm. It was also revealed that 10wt% MWCNT-SiO_2 glass composites containing longer MWCNTs (1.5wt%F/T) showed an increment of 47% compared to silica glass, which is greater than that in composites containing shorter MWCNTs (9.0wt%F/T), i.e. 34%.

6.2.5 Technological characterisation

Silica glass and a set of MWCNT-SiO_2 glass composites containing 2.5wt% to 10wt% MWCNTs synthesised by 3.0wt% ferrocene/toluene were characterised for the following technological properties.

a. Thermal shock resistance

Silica glass and 2.5wt% MWCNT-SiO_2 glass composites were tested for thermal shock resistance by the water quench method from 500°C, 1000°C and 1200°C to a room temperature of 20°C, which was followed by diametral compression testing for strength evaluation. A typical diametral compression failure mode [251] was observed (Figure 6.32).

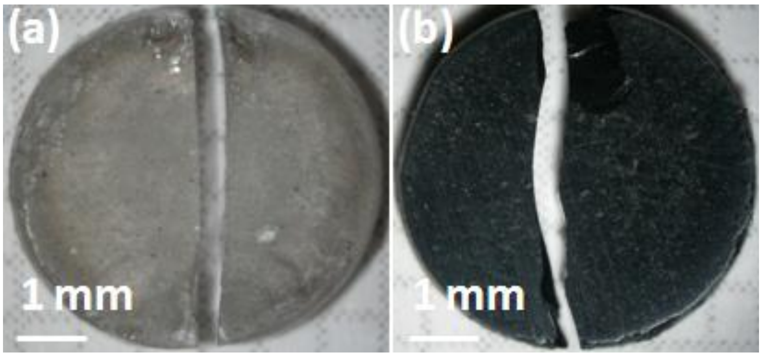

Figure 6.32: Photographs of diametrally compressed (a) silica glass and (b) 2.5wt% MWCNT-SiO_2 glass composite specimens after thermal shock from 500°C to 20°C.

Silica glass and composite specimens showed comparable diametral compression strength values within the error range. The specimens, without performing thermal shock tests, also showed similar results. However, a slight decrease in the composite values was observed at 1200°C (Figure 6.33). The decrease in the strength of composites matches with the trend of their other mechanical properties, i.e. elastic modulus and hardness, as discussed earlier (Section 6.2.3(a-b)). Nevertheless, no considerable decrease in the strength was observed until 1200°C. Similar results, showing the retention of strength up to 1200°C, have been reported while investigating carbon fibre reinforced silica GMCs [82]. XRD (Figure 6.34) shows the presence of cristobalite at 1200°C, while no indication of crystallisation was seen in specimens thermally shocked from 500°C and 1000°C. The presence of cristobalite in silica glass after heating in air above 1000°C has also been observed by others [252]. The composite specimens (Figure 6.35(a-f)) did not experience any structural change or the appearance of cracks due to thermal shock from 500°C and 1000°C. However, surface cracking was observed in specimens thermally shocked from 1200°C (Figure 6.35(g-i)). It is likely that these microcracks are due to the surface crystallisation (cristobalite formation) in the specimens. This crystallisation phenomenon causes cracking, when β-cristobalite converts into α-cristobalite on cooling below 272°C, as a result of the different thermal expansion coefficients of the two polymorphs of cristobalite [253].

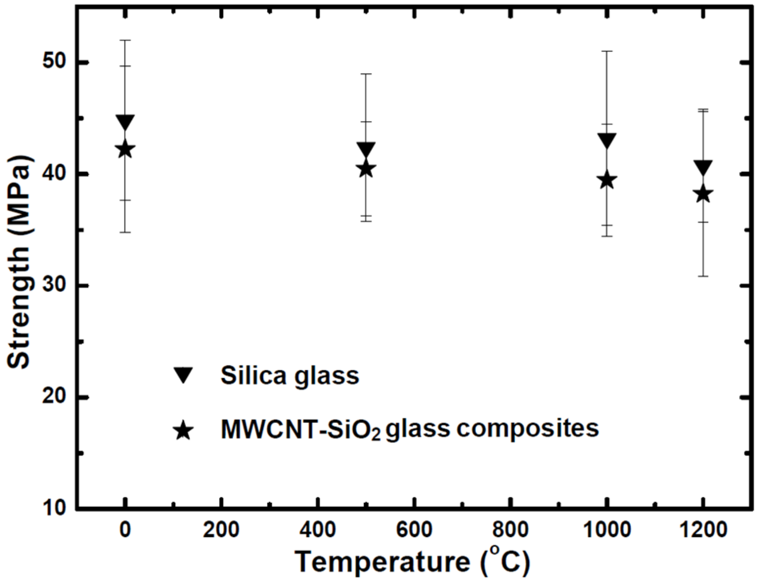

Figure 6.33: Diametral compression strength of silica glass and 2.5wt% MWCNT-SiO$_2$ glass composites after thermal shock tests from 500°C, 1000°C and 1200°C to 20°C. The composite strength values without thermal shock are given for comparison.

In short, the addition of 2.5wt% MWCNTs to the silica glass matrix did not lead to obvious cracks due to the thermal shock in water from 500°C, 750°C, 1000°C and 1200°C to a room temperature of 20°C; however, cristobalite formed at 1200°C and caused cracking on cooling due to the α-β cristobalite transformation.

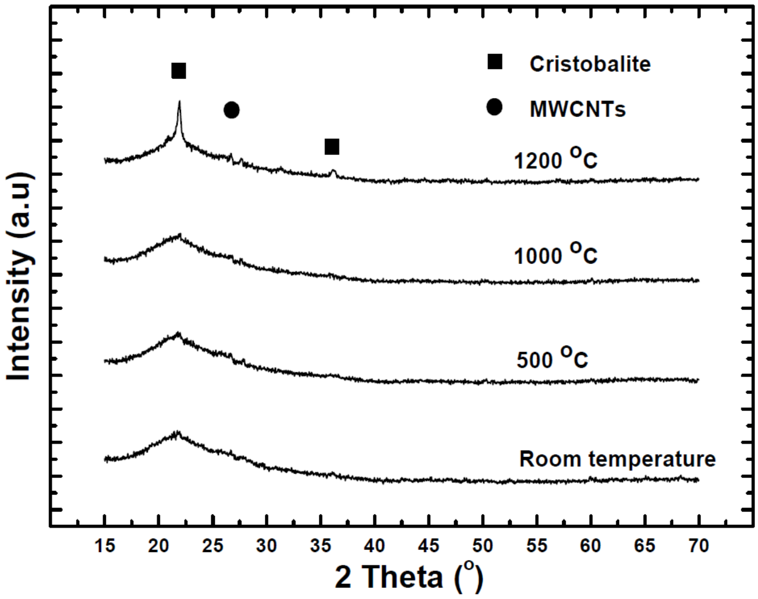

Figure 6.34: XRD of 2.5wt% MWCNT-SiO$_2$ glass composites thermally shocked from 500°C, 1000°C and 1200°C to 20°C; cristobalite was formed at 1200°C. The room temperature XRD of composites without performing thermal shock test is shown for comparison.

b. Thermal cycling resistance

As no indication of crystallisation was observed after thermal shock from 500°C, 750°C and 1000°C, 2.5wt% MWCNT-SiO$_2$ glass composites were tested for repeated thermal shock cycles, i.e. quenching from 1000°C in water at 20°C for 10 and 20 times. Thermally cycled specimens were later subjected to diametral compression tests to measure any change in their strength and observed in SEM for the presence of any thermal cracks. A gradual decrease in the strength of specimens after 10 and 20 thermal shock cycles was observed (Figure 6.36), which may be due to the crystallisation effect. Nevertheless, a clear reduction in strength due to the formation of quench cracks was absent. XRD primarily showed an amorphous matrix with few cristobalite peaks emerging from the amorphous bump, revealing the start of devitrification, on increasing the number of thermal cycles (Figure 6.37).

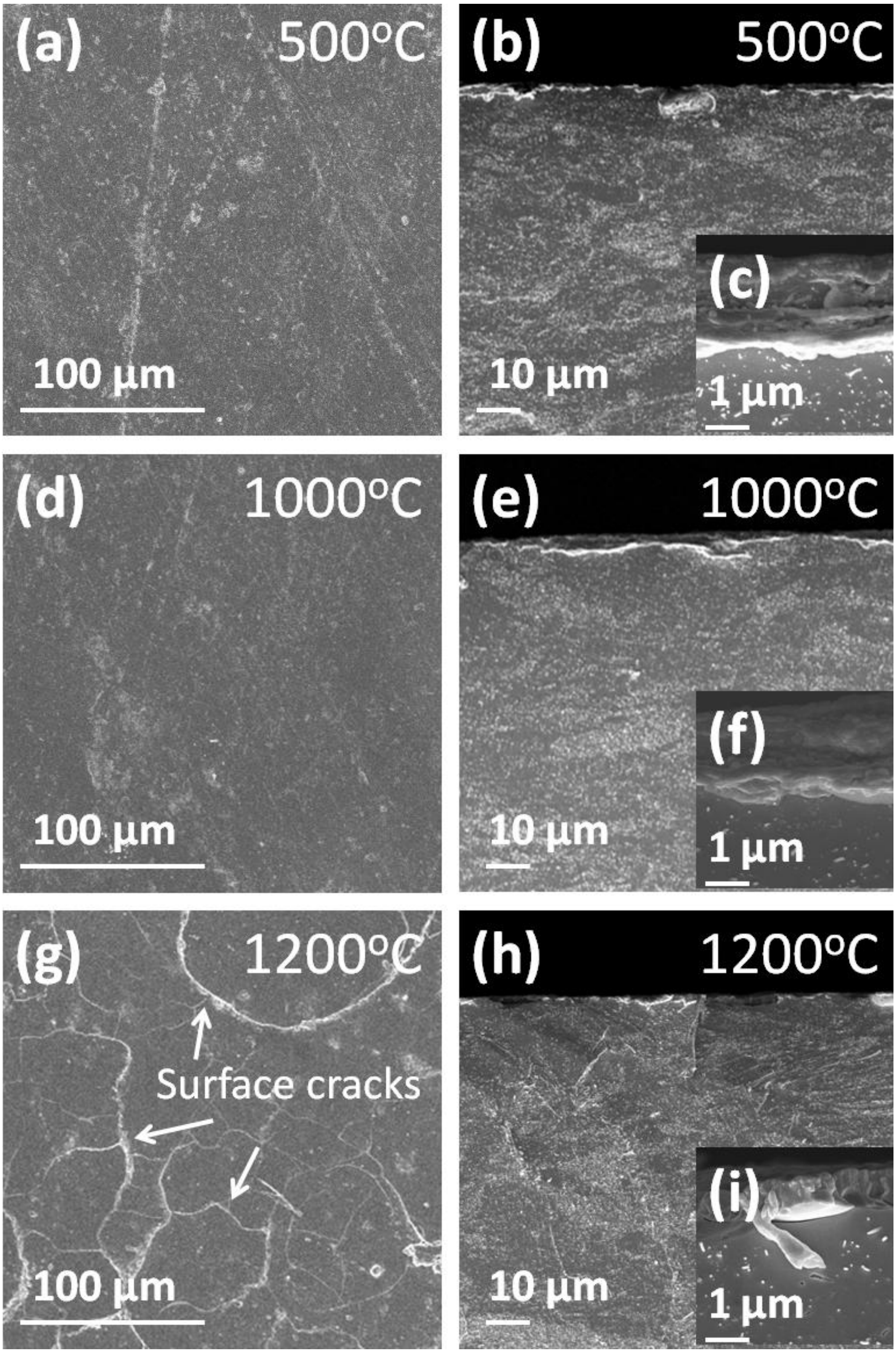

Figure 6.35: SEI-SEM images of 2.5wt% MWCNT-SiO$_2$ glass composites thermally shocked from 500°C, 1000°C and 1200°C to 20°C; cristobalite was formed at 1200°C. (a,d&g) show top surfaces while (b,e&h) show cross sectional images of the specimens; Inset (c,f&i) show the magnified images of the specimen edges.

SEM images (Figure 6.38(a)) show surface cracking in composite specimens thermally shocked for 10 times, which is due to the crystallisation, as indicated in XRD (Figure 6.37) and the resultant α-β cristobalite transformation on cooling, as discussed in Section 6.2.5(a). The surface cracks comparatively grew to a higher extent after 20 thermal cycles (Figure 6.38(c)). The cross-sectional images of the specimens (Figure 6.38(b,d)) also verified the presence of surface cracks. In comparison, no cracks were observed in specimens thermally shocked for a single time (Figure 6.35(d-f)).

Another feature is the appearance of oxidation of MWCNTs (Figure 6.38(b,d)). These cross-sectional images of the specimens show a partial decarburised (MWCNT oxidised) surface regions where the concentration of MWCNTs decreased after their oxidation, as shown in the marked areas. This effect may be the possible reason of the slight decrease in the strength of composites, as the oxidation of MWCNTs produces empty slots, which act as porosity.

In short, 10 and 20 thermal shock cycles from 1000°C to 20°C showed no evidence of thermal cracking in 2.5wt% MWCNT-SiO_2 glass composites; however, cristobalite started forming after repeated heating at 1000°C (thermal cycles) and caused cracking on cooling.

c. Thermal ageing behaviour

The thermal stability of 2.5wt% to 10wt% MWCNT-SiO_2 glass composites was evaluated by heating them at higher temperatures, i.e. 500-1200°C, for longer holding times, i.e. 6-96h. The performance of the composites was observed at these severe conditions along with the oxidation behaviour of embedded MWCNTs.

i. Effect of ageing temperature

To explore the effect of ageing temperature on the behaviour of composites, 2.5wt% MWCNT-SiO_2 glass composites were exposed at medium to high temperature range of 500°C to 1200°C for a fixed duration of 6h. At 500°C, MWCNTs did not completely oxidise (Figure 6.40 (a)), as is also evident from the TGA performed on these MWCNTs in the as-synthesised (Figure 5.9) and acid-treated (Figure 5.18) conditions.

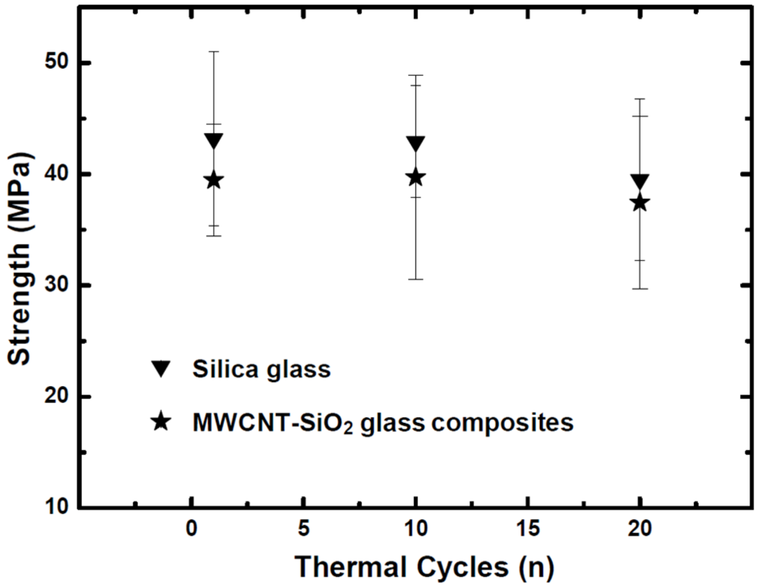

Figure 6.36: Diametral compression strength of silica glass and 2.5wt% MWCNT-SiO$_2$ glass composites after thermal shock cycling for 1, 10 and 20 times. A thermal cycle comprised heating at 1000°C and quenching at 20°C.

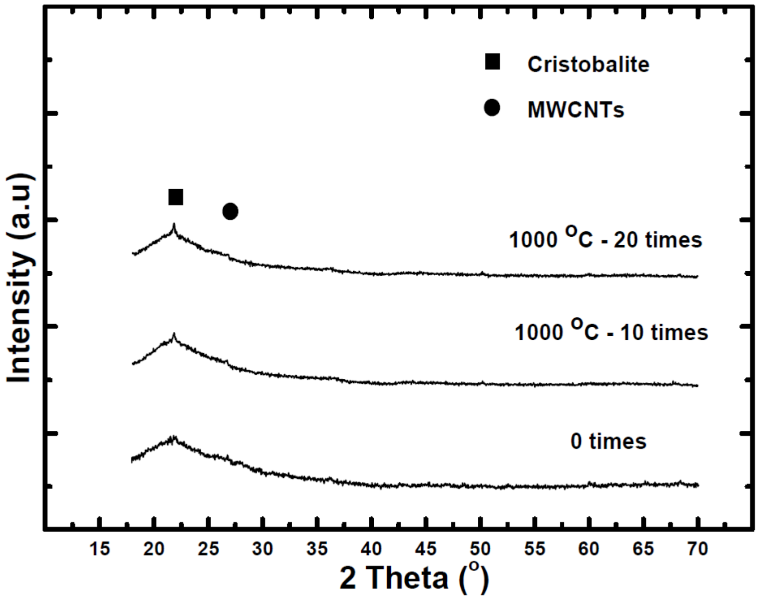

Figure 6.37: XRD of 2.5wt% MWCNT-SiO$_2$ glass composites thermally shocked at 1000°C for 10 and 20 times, showing the start of cristobalite formation.

TGA shows that as-synthesised MWCNTs oxidise in the temperature range of 600-750°C, while debris generated on acid-treated MWCNTs oxidises at lower temperatures, i.e. ≥400°C. When nanoparticles were coated on the surface of MWCNTs after the colloidal mixing process to produce MWCNT-SiO$_2$ glass composite powders (Figure 6.2), the oxidation temperature of

MWCNTs increased to 650-800^{o}C (Figure 6.39) due to the limited access of oxygen to the MWCNTs. However, a continuous removal of the MWCNT surface functional groups and the silica particle surfactant, and the oxidation of the MWCNT surface debris and/or defective MWCNTs was observed to 650^{o}C.

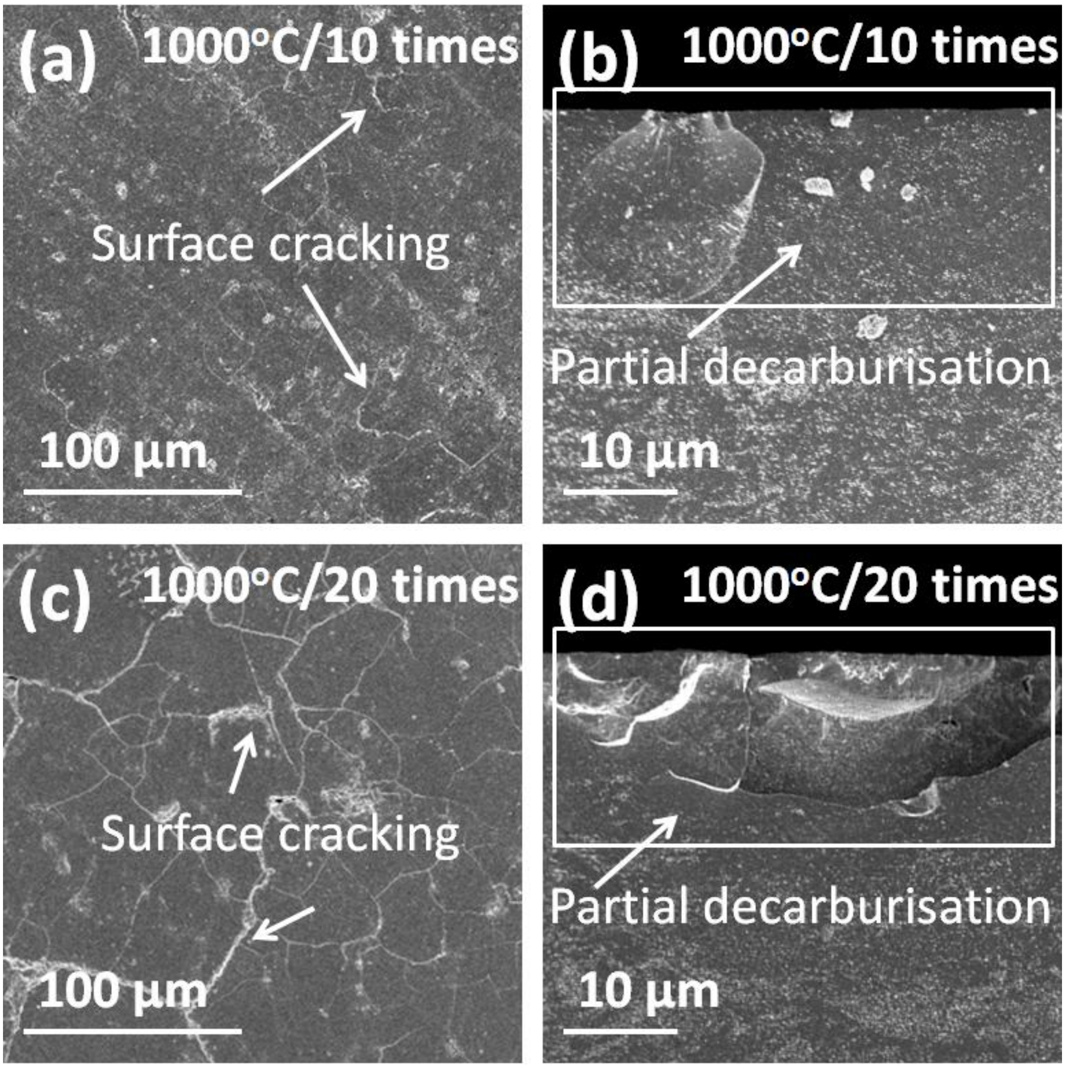

Figure 6.38: SEI-SEM images of 2.5wt% MWCNT-SiO$_2$ glass composites thermally shocked at 1000^{o}C for (a-b) 10 and (c-d) 20 times, showing cracks on the surface (a,c) and cross-section (b,d) of specimens possibly due to the formation of cristobalite in silica glass matrix. Partial oxidation of MWCNTs is also evident along the surface of the specimens; (b,d) with in marked areas.

Similarly, no significant change in the microstructure of composite specimens was observed at 750^{o}C after 6h of ageing (Figure 6.40(b)). However, when composites were aged at

1000°C for 6h, a partial decarburisation near the surface was observed due to the oxidation of MWCNTs (Figure 6.40(c)) in a similar way to the specimens thermally shocked for 10 and 20 times at 1000°C (Figure 6.38). Further increase in temperature, to 1200°C, devitrified the amorphous silica glass producing cristobalite, which resulted in the extensive surface cracking on cooling (Figure 6.40(d)). XRD verified the presence of cristobalite in composites thermally aged at 1200°C, while cristobalite formation was not indicated in composites treated at 500°C, 750°C and 1000°C (Figure 6.41).

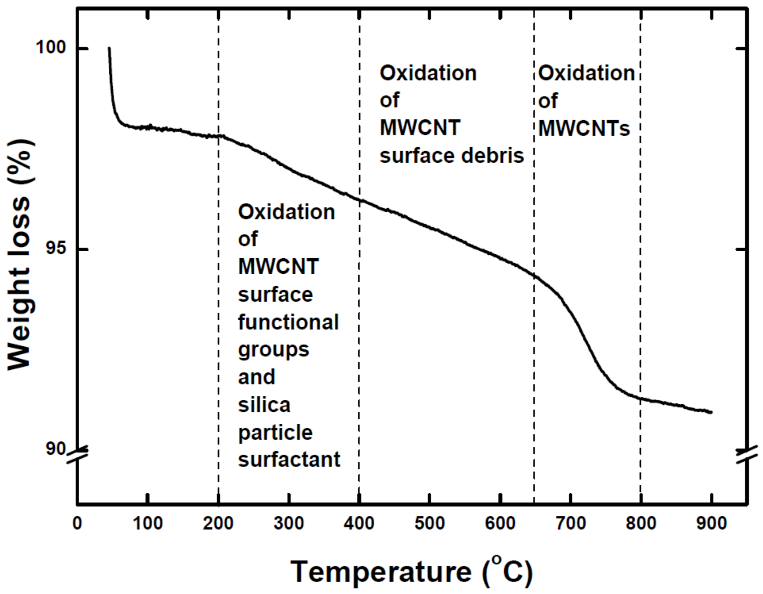

Figure 6.39: TGA of MWCNT-SiO_2 glass composite powder before sintering, indicating the removal of MWCNT surface functional groups and the silica particle surfactant, oxidation of MWCNT debris up to 650°C and the oxidation of MWCNTs.

Another argument may be the presence of surface cracking, which should accelerate the decomposition of MWCNTs by providing exposed surfaces, as observed in carbon fibre reinforced GMCs [176]. However, these cracks were not present at high temperature but formed during the cooling at a temperature lower than the oxidation temperature of MWCNTs, as explained in Section 6.2.5(a). The complete oxidation of MWCNTs in sintered composite specimens was not observed even after thermal ageing at 750°C and 1000°C for 6h, although MWCNTs oxidised in MWCNT-SiO_2 glass composite powder between 650°C and 800°C in TGA (Figure 6.39). The reason may be the presence of densified silica glass matrix encapsulating

MWCNTs. The oxidation of MWCNTs could start from the surface progressing inwards but all MWCNTs in 2.5wt% MWCNT-SiO_2 glass composites were probably not the part of a percolating network and isolated MWCNTs surrounded by densified glass were also present that survived.

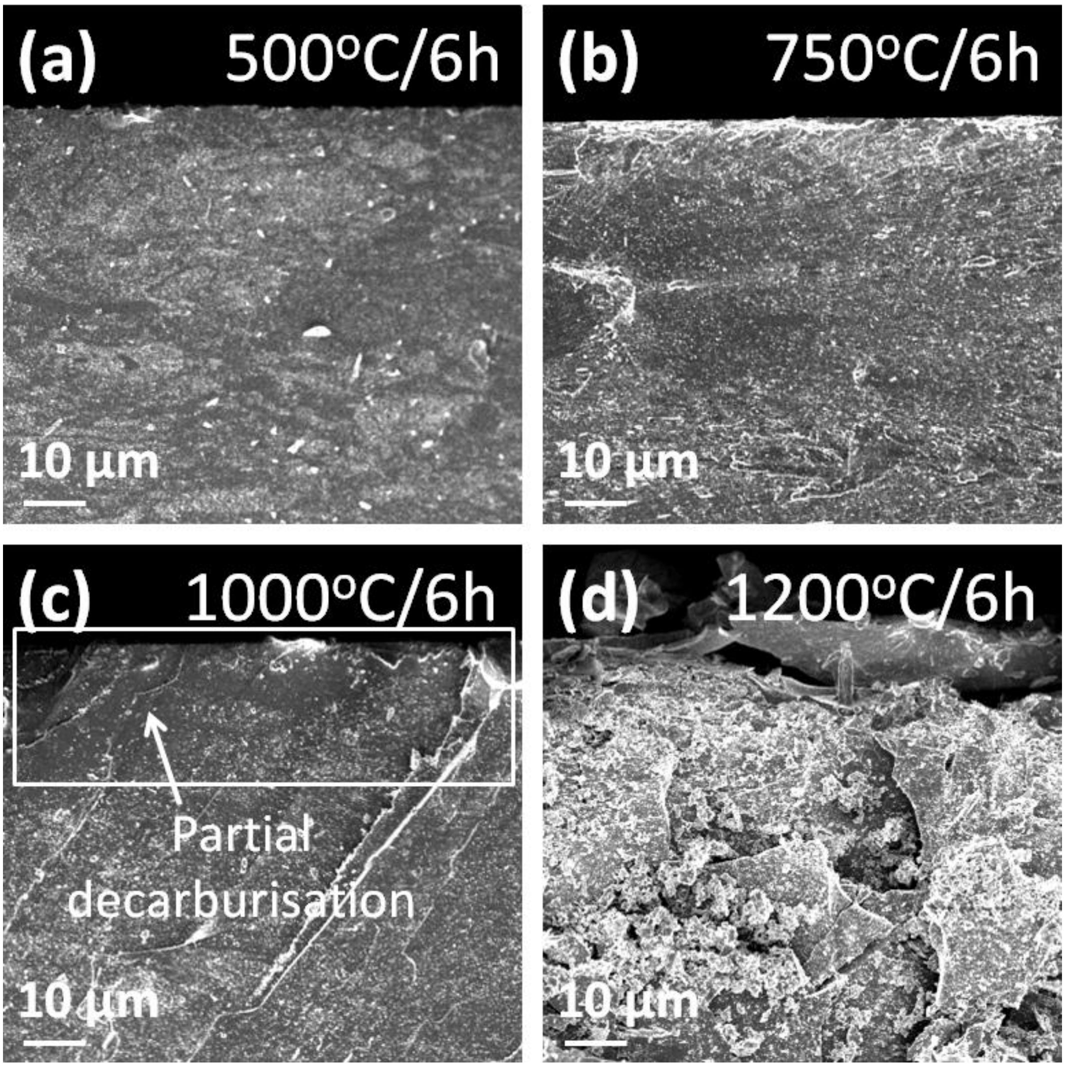

Figure 6.40: SEI-SEM images of 2.5wt% MWCNT-SiO_2 glass composites thermally aged at (a) 500°C (b) 750°C (c) 1000°C and (d) 1200°C for 6h. Partial surface decarburisation at 1000°C and cracking at 1200°C are evident.

ii. Effect of ageing time

To observe the effect of ageing time on the behaviour of composites, 2.5wt% MWCNT-SiO_2 glass composites were exposed at three different temperatures, i.e. 500°C, 750°C and 1000°C for the times of 6h, 12h, 24h, 48h and 96h. At the ageing temperature of 500°C, a partial decarburised surface was observed due to MWCNT oxidation that grew deeper into the specimen with ageing time (Figure 6.42). After 12h, partially decarburised surface was seen due to the oxidation of interconnected MWCNTs but the depth of partial decarburisation was limited to few µm (Figure 6.42(c)). The longer ageing time (96h) increased the partial decarburisation depth but still a surface completely devoid of MWCNTs could not be observed (Figure 6.42(d)). Also, no indication of a large degree of crystallisation was observed at 500°C even after 96h of exposure (Figure 6.43(a)).

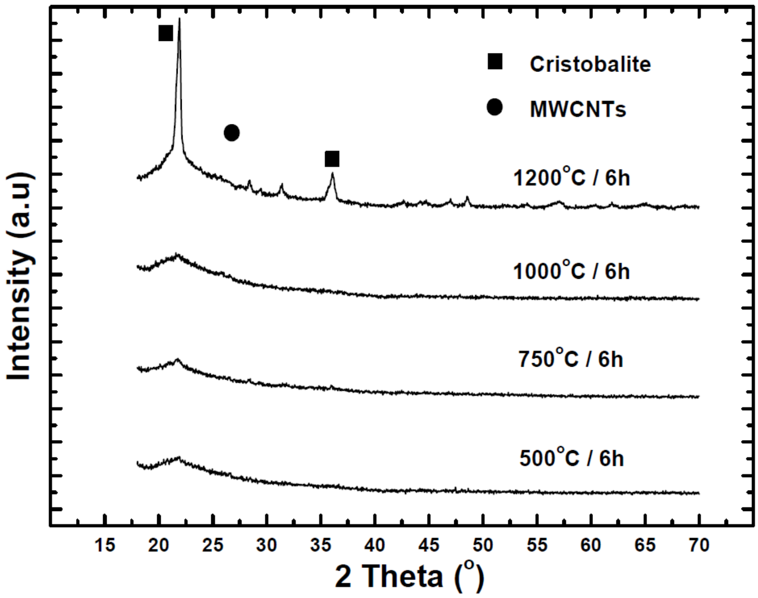

Figure 6.41: XRD of 2.5wt% MWCNT-SiO$_2$ glass composites thermally aged at (a) 500°C (b) 750°C (c) 1000°C and (d) 1200°C for 6h.

When composites were thermally aged at 750°C for times from 6h to 96h, the oxidation of MWCNTs started from the outer surface of the specimens and progressed inwards with time (Figure 6.44(a-b)). A partially decarburised surface region is visible in specimens aged for 12h (Figure 6.44(c)) due to partial MWCNT oxidation starting from the surface of specimens but an increase in ageing time (96h) showed a completely decarburised surface layer (Figure 6.44(d)) due to the complete MWCNT oxidation starting from the surface of specimens. Figure 6.45 displays magnified images of Figure 6.44(b) for the specimens aged at 750°C for 96h. It is possible to identify three distinct regions, i.e. the region “X” with completely oxidised MWCNTs (Figure 6.45(b)), region “Y” with partially oxidised MWCNTs (Figure 6.45(c)) and region “Z” without the oxidation of MWCNTs (Figure 6.45(d)). The completely decarburised region follows a partially decarburised region during the oxidation of MWCNTs. Only those MWCNTs, which were part of the percolation network, were first oxidised, while the individual MWCNTs isolated from the percolation network remained undamaged. The interconnected sockets, developed due to the oxidation of percolating MWCNTs, served as the channels for the penetration of oxygen from the specimen surfaces to develop a partially decarburised region. However, at longer durations (96h), oxygen is likely to successfully penetrate through the silica glass to reach and oxidise isolated MWCNTs to form a completely decarburised region. No indication of crystallisation was observed in specimens aged at 750°C after 96h of exposure (Figure 6.43(b)).

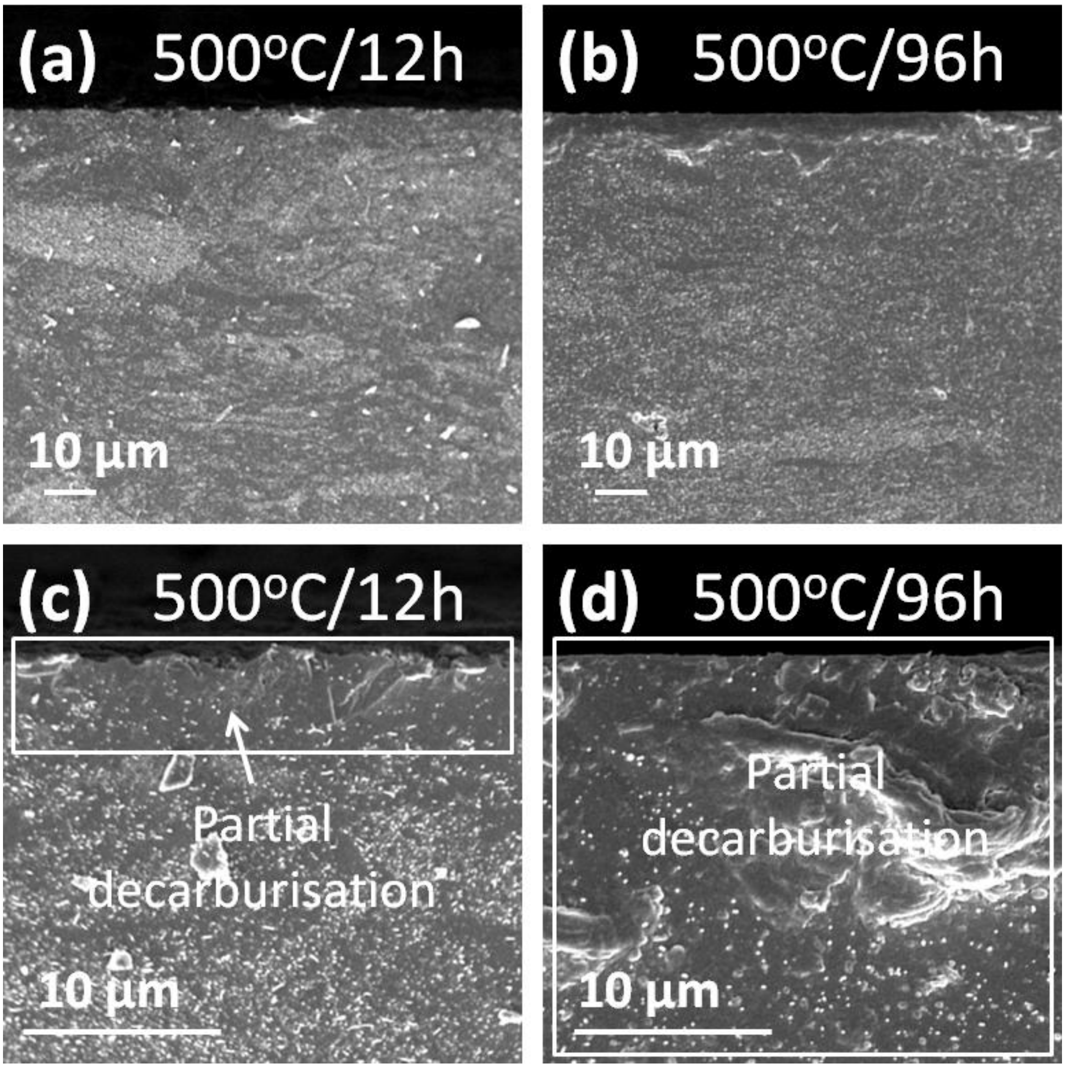

Figure 6.42: SEI-SEM images of 2.5wt% MWCNT-SiO_2 glass composites thermally aged at 500°C for (a,c) 12h and (b,d) 96h. Partial surface decarburisation due to MWCNT oxidation is evident, which increased with time.

A similar trend of the oxidation of MWCNTs was witnessed when 2.5wt% MWCNT-SiO_2 glass composites were thermally aged at 1000°C for the times from 6h to 96h (Figure 6.46); however, the depth of decarburisation increased compared to that in specimens aged at 750°C. It was also observed that the decarburisation depth along the XY-plane (Figure 6.49) was comparatively higher than normal to it (Figure 6.47); XY-plane is perpendicular to the applied load in uniaxial pressing during green body preparation. A possible reason could be the preferred orientation of MWCNTs perpendicular to the applied load causing their more connecting links along the XY-plane, although no such evidence could be obtained from SEM and TEM images in Sections 6.2.2(c-d).

It is interesting to mention here that no indication of crystallisation was observed at 1000°C until 6h of exposure but for longer ageing times up to 96h, amorphous silica started devitrifying and the degree of crystallisation increased with ageing time (Figure 6.43(c)). An increase in the devitrification of silica glass in air has been reported at 1000°C for longer firing times [254].

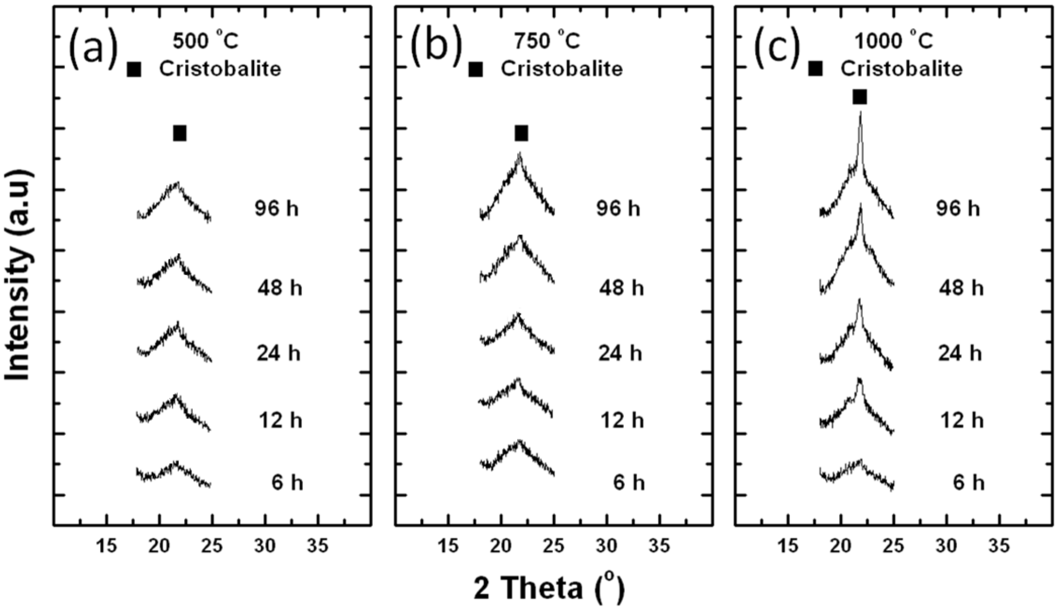

Figure 6.43: XRD of 2.5wt% MWCNT-SiO_2 glass composites thermally aged at (a) 500°C, (b) 750°C and (c) 1000°C from 6h to 96h. An increase in ageing time at 1000°C encouraged crystallisation in specimens, while no significant increases in the degree of crystallisation were observed in composites aged at 500°C and 750°C.

Figure 6.48(a) shows a schematic diagram of the cross-section of a composite specimen exhibiting the decarburised surface layer due to the oxidation of MWCNTs and the core of the specimen confirming their retention, while Figure 6.48(b-c) display the cross-sections of fractured 2.5wt% MWCNT-SiO_2 glass composites actually showing the outer specimen region without MWCNTs and the core containing MWCNTs.

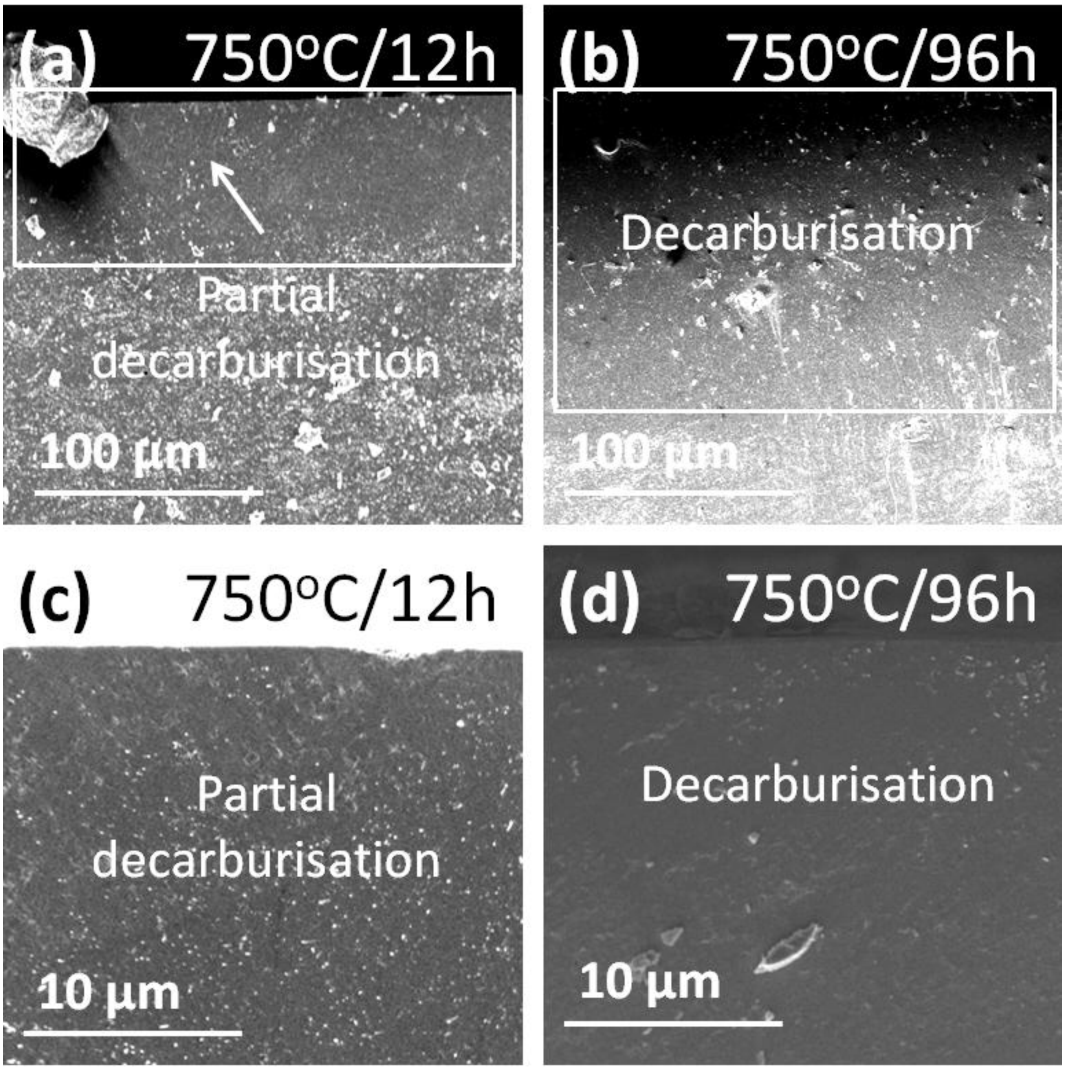

Figure 6.44: SEI-SEM images of 2.5wt% MWCNT-SiO_2 glass composites thermally aged at 750°C for (a,c) 12h and (b,d) 96h. Partial and complete surface decarburisations were observed after 12h and 96h of ageing, respectively.

The depth of complete decarburisation was calculated for the specimens aged at 500°C, 750°C and 1000°C for the times from 6h to 96h (Figure 6.49). A low oxidation rate of MWCNTs was observed at 500°C, which significantly increased at higher temperatures. A parabolic increase in the oxidation was observed at the three selected temperatures. In a study on carbon fibre GMCs [177], a parabolic increase in the oxidation of carbon fibres was also observed. The depth of decarburised surface layer along the XY-plane was found to be greater than normal to it, which may be related to the preferred alignment of MWCNTs along the XY-plane. In another investigation on carbon fibre reinforced GMCs, the oxidation rate was similarly found to be higher in the direction of aligned fibres [175].

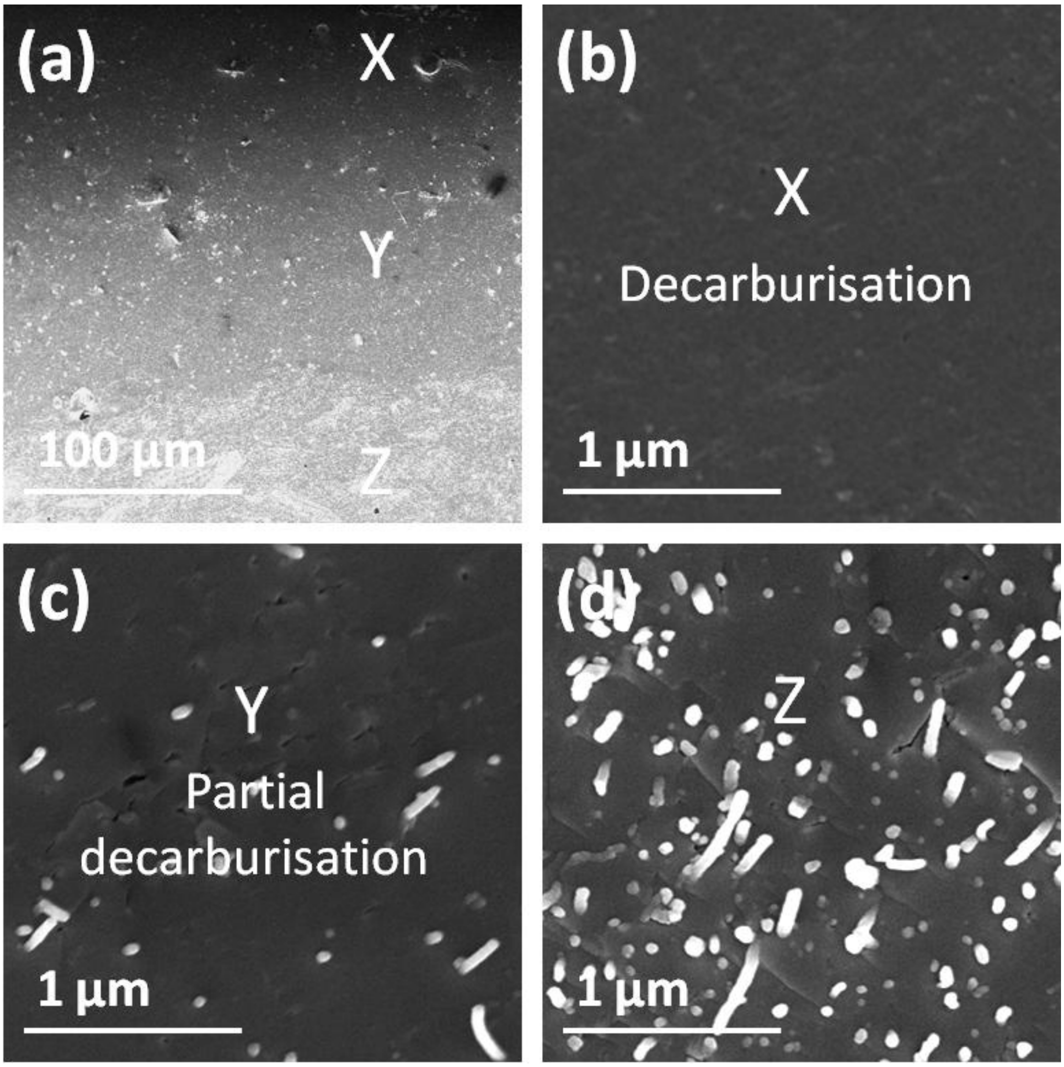

Figure 6.45: (a) SEI-SEM image of 2.5wt% MWCNT-SiO_2 glass composites thermally aged at 750°C for 96h. Three regions are identified, showing (b) complete (c) partial and (d) no decarburisation.

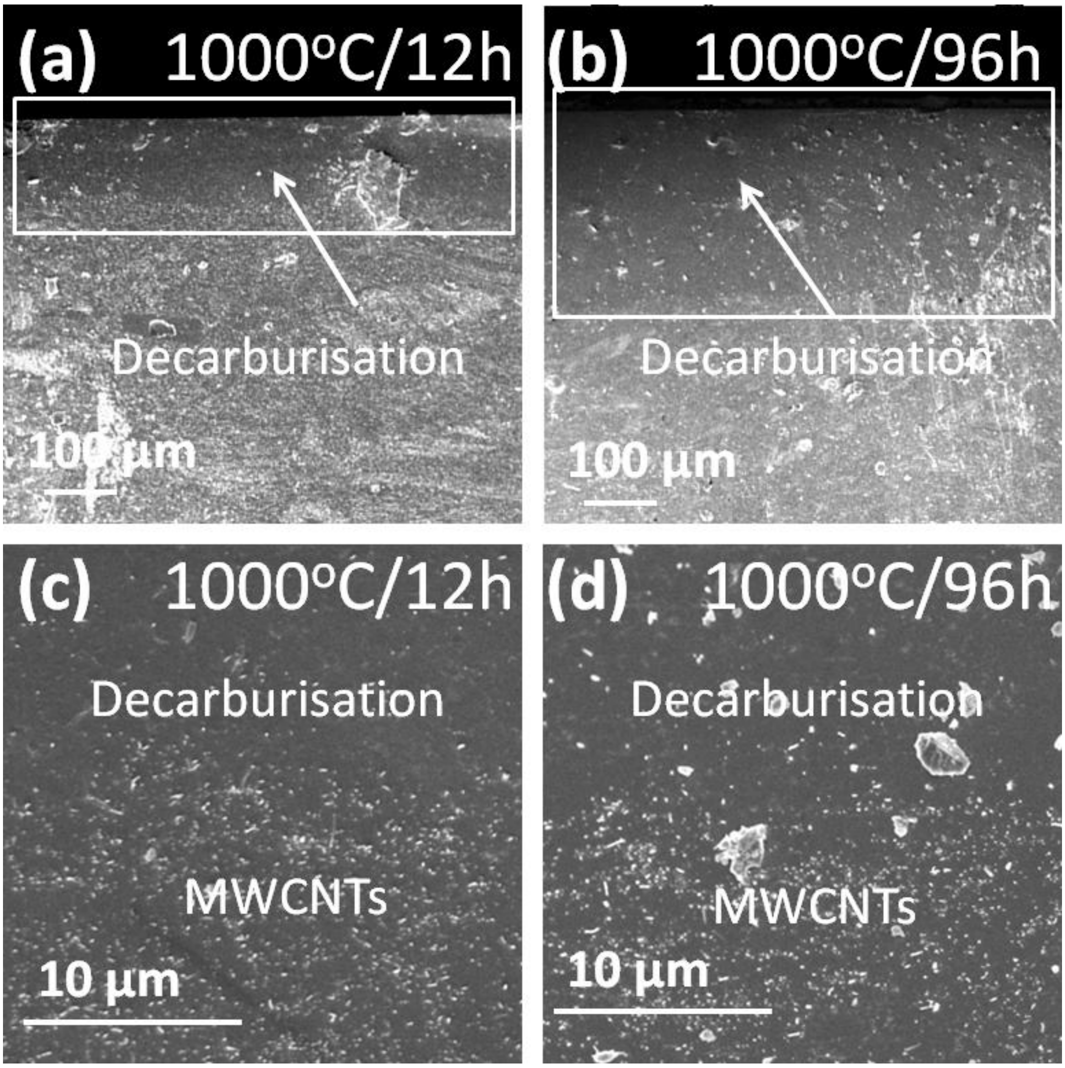

Figure 6.46: SEI-SEM images of 2.5wt% MWCNT-SiO_2 glass composites thermally aged at 1000°C for (a,c) 12h and (b,d) 96h. The completely decarburised surface layer can be seen in (a) and (b), while the boundary between the oxidised and survived MWCNTs is shown in (c) and (d).

iii. Effect of MWCNT content

To investigate the effect of MWCNT loading fractions upon the ageing behaviour of composites, 5.0wt% to 10wt% MWCNT-SiO_2 glass composites were thermally aged at three different temperatures, i.e. 500°C, 750°C and 1000°C for a fixed duration of 48h. 2.5wt% MWCNT-SiO_2 glass composites were already investigated and discussed in the previous section for the selected temperature/time profile.

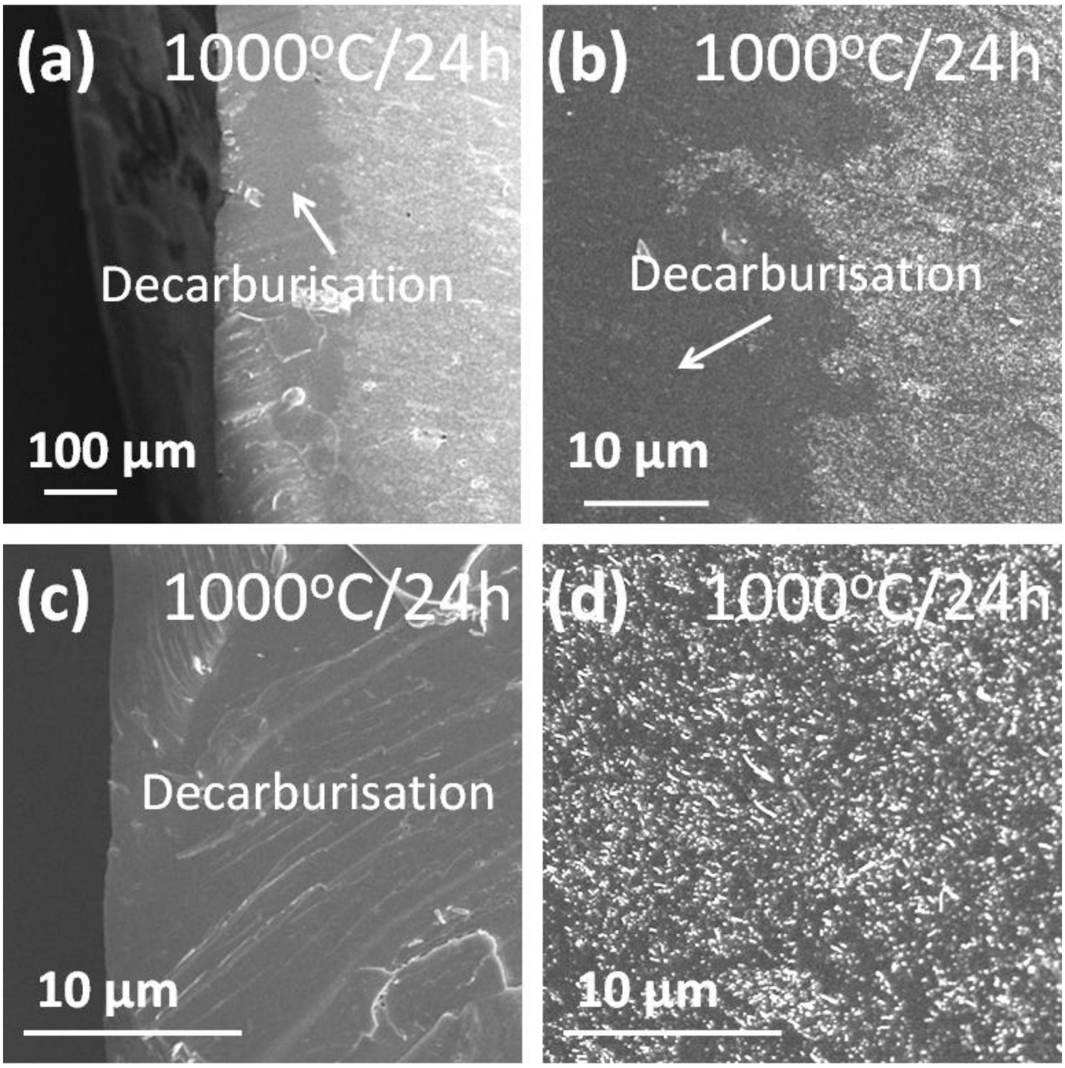

Figure 6.47: SEI-SEM images of (a-b) 2.5wt% MWCNT-SiO_2 glass composites thermally aged at 1000°C for 24h; the magnified images of the regions with (c) oxidised and (d) survived MWCNTs are also shown.

In 5.0wt% to 10wt% MWCNT-SiO_2 glass composites, the MWCNTs started oxidising from the specimen surface at 500°C after 48h of exposure and a decarburised depth of few µm was noted (Figure 6.50(a-c)). However, at 750°C, MWCNTs were completely oxidised in 5.0wt% MWCNT-SiO_2 glass composites (Figure 6.50(d)) leaving behind the silica glass matrix containing slots (porosity) where MWCNTs were present before oxidation (See Figure 6.53 for slots after MWCNT oxidation). Similarly, composites containing 7.5wt% and 10wt% MWCNTs provided porous structures without MWCNTs after thermal ageing (Figure 6.50(e-f)); the only difference with increased MWCNT content is the increased volume of nanoporosity in the specimens. It can be inferred from these results that at 5.0wt% loading, almost all the MWCNTs were part of a percolation network without any isolated MWCNTs.

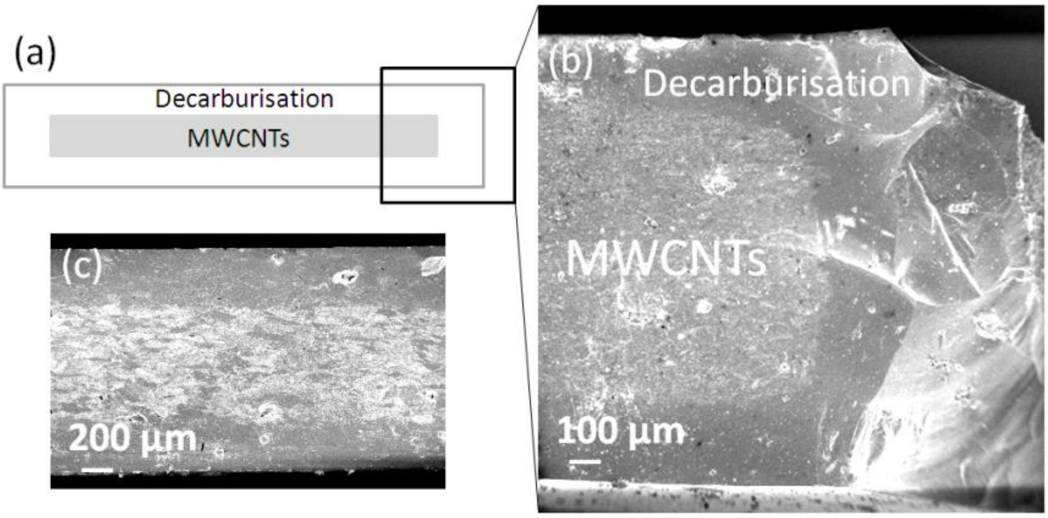

Figure 6.48: (a) Schematic diagram and (b-c) SEI-SEM images of 2.5wt% MWCNT-SiO$_2$ glass composites showing the decarburised surface layer without MWCNTs and the core of the specimen showing the presence of MWCNTs.

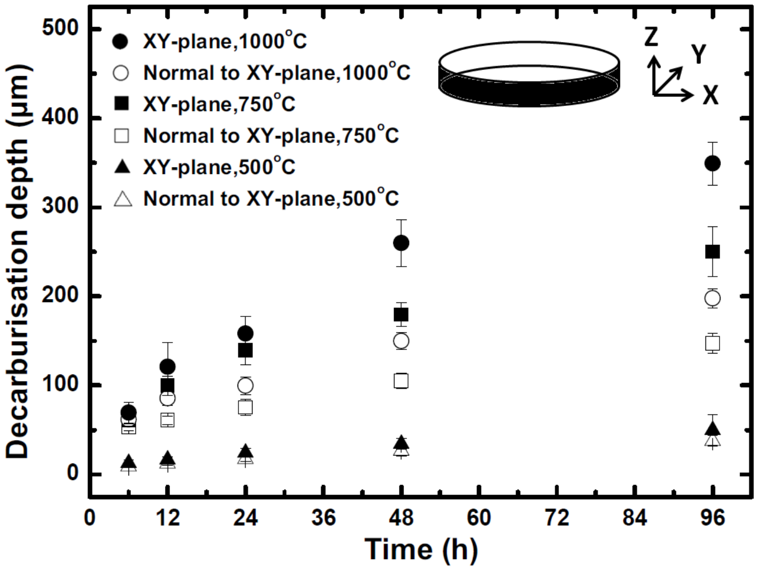

Figure 6.49: Decarburisation depth of 2.5wt% MWCNT-SiO$_2$ glass composites thermally aged at 500°C, 750°C and 1000°C from 6h to 96h. The decarburised depth was more along the XY-direction than normal to it.

Similarly, the thermal ageing of composites containing 5wt% to 10wt% MWCNTs at 1000°C for 48h provided a porous glass without MWCNTs but surface cracking was observed

(Figure 6.50(g-i)) likely due to the formation of cristobalite (Figure 6.51). In comparison, no indication of significant crystallisation of the glass matrix was noted in specimens aged at 500°C and 750°C (Figure 6.51).

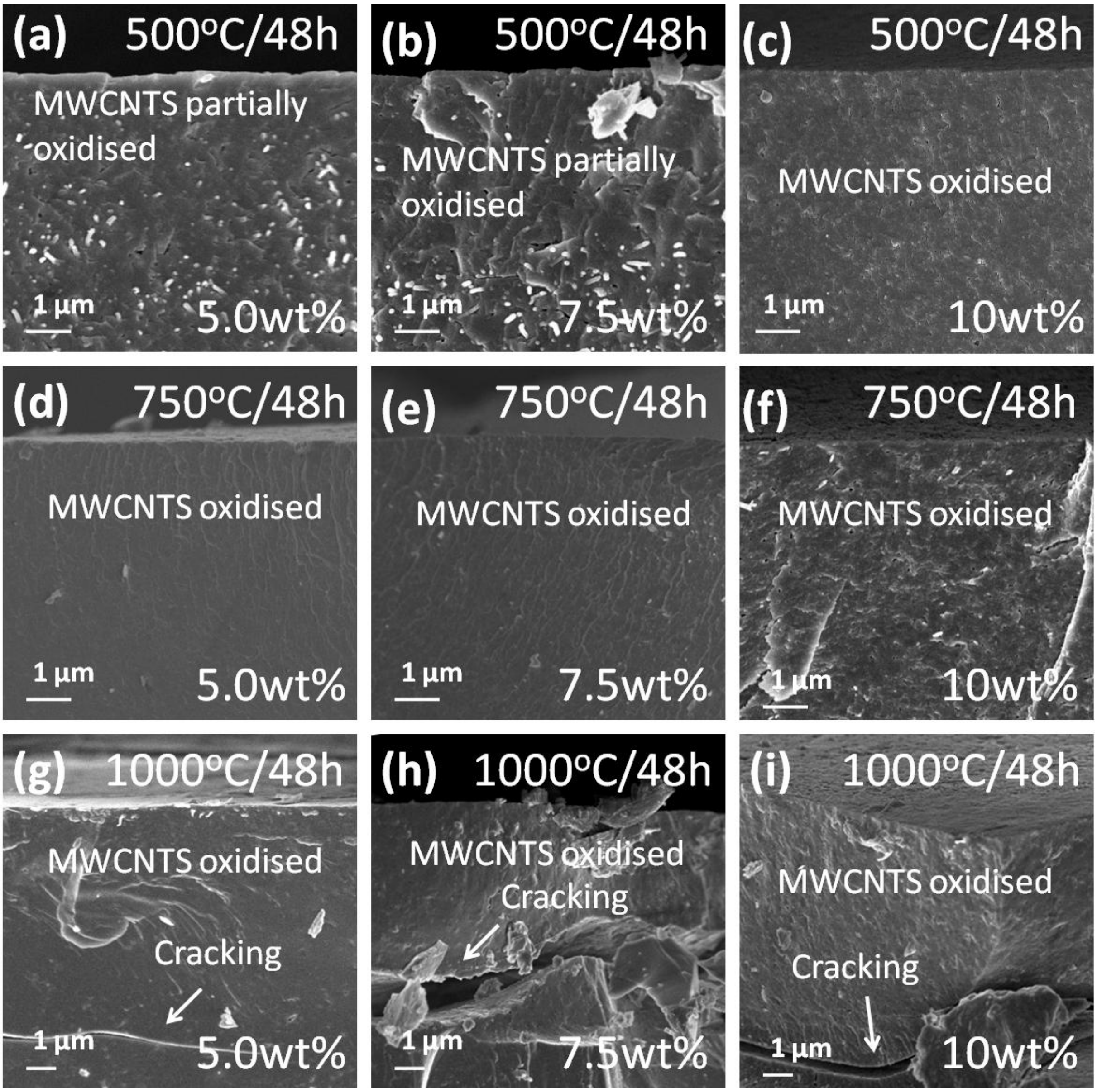

Figure 6.50: SEI-SEM images of 5.0wt% to 10wt% MWCNT-SiO_2 glass composites thermally aged at 500°C, 750°C and 1000°C for 48h.

Figure 6.52 shows 2.5wt% and 10wt% MWCNT-SiO_2 glass composites after thermal ageing at 750°C for 48h. MWCNTs survived in 2.5wt% MWCNT composites and only partial surface decarburisation was observed while MWCNTs were completely oxidised in 10wt% MWCNT composites. Figure 6.53 shows the slots (voids) after the oxidation of MWCNTs in

10wt% MWCNT composites. These slots not only indicate the random orientation of MWCNTs but also the curviness of their structure due to their flexible nature. The use of MWCNTs with different sizes and varying concentrations can provide porous silica glass of tailorable volume and shape of porosity after suitable heat-treatment of composites. The mechanical properties of the porous composites have been discussed in Section 6.2.3(d).

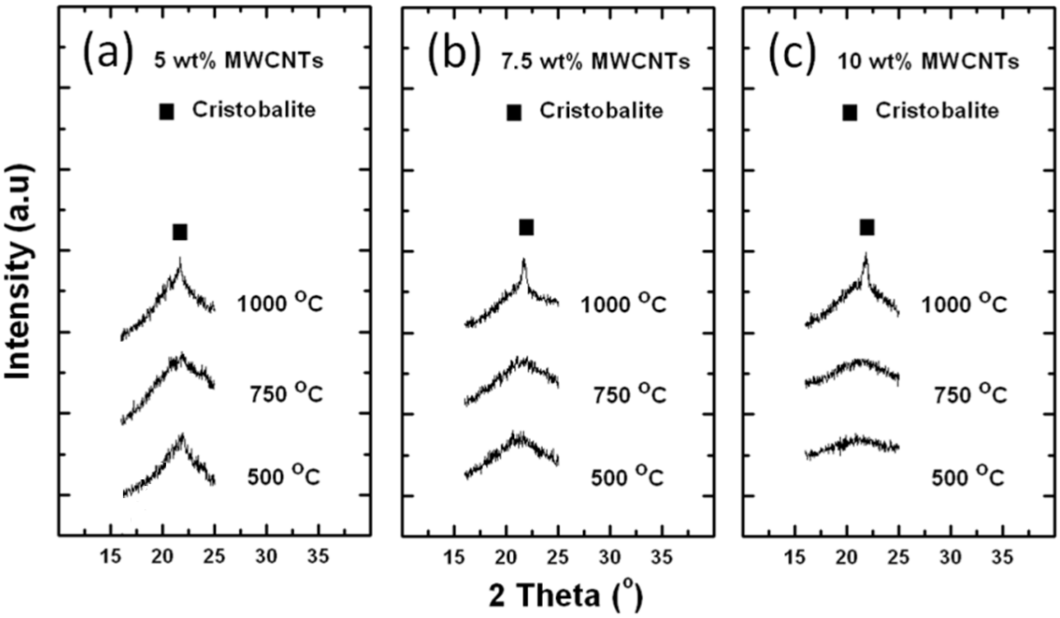

Figure 6.51: XRD of 5.0wt% to 10wt% MWCNT-SiO$_2$ glass composites thermally aged at 500°C, 750°C and 1000°C for 48h. The crystallisation peaks can be seen at 1000°C, emerging from the amorphous background, indicating the presence of cristobalite.

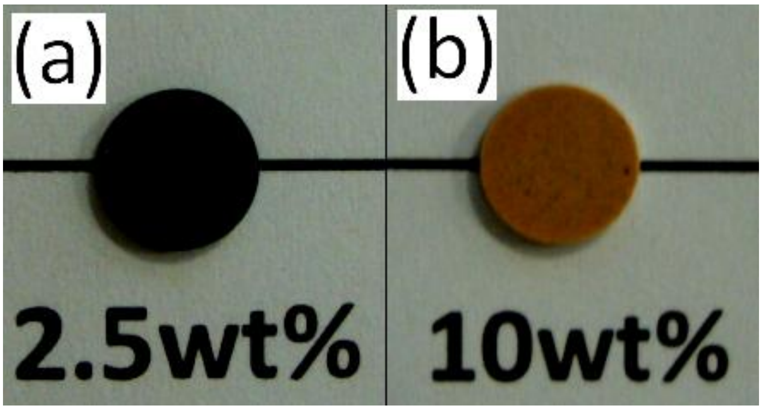

Figure 6.52: Photographs of 2.5wt% and 10wt% MWCNT-SiO$_2$ glass composites after thermal ageing at 750°C for 48h; (a) MWCNTs are present in 2.5wt% MWCNT composites while (b) a complete decarburisation is evident in 10wt% MWCNT composites.

In short, the thermal ageing of 2.5wt% MWNT-SiO_2 glass composites at 500°C, 750°C and 1000°C for 6h showed no signs of devitrification; however, partial decarburisation was observed at 1000°C; at 1200°C, devitrification was observed after the same ageing time (6h). An increase in the ageing time from 6h to 96h at 500°C increased the depth of partial surface decarburisation of 2.5wt% MWNT-SiO_2 glass composites, while both partial and complete surface decarburisation was observed at 750°C, the depth of which increased at 1000°C. The amorphous glass composite matrix did not devitrify at 500°C and 750°C; however, cristobalite formed at 1000°C.

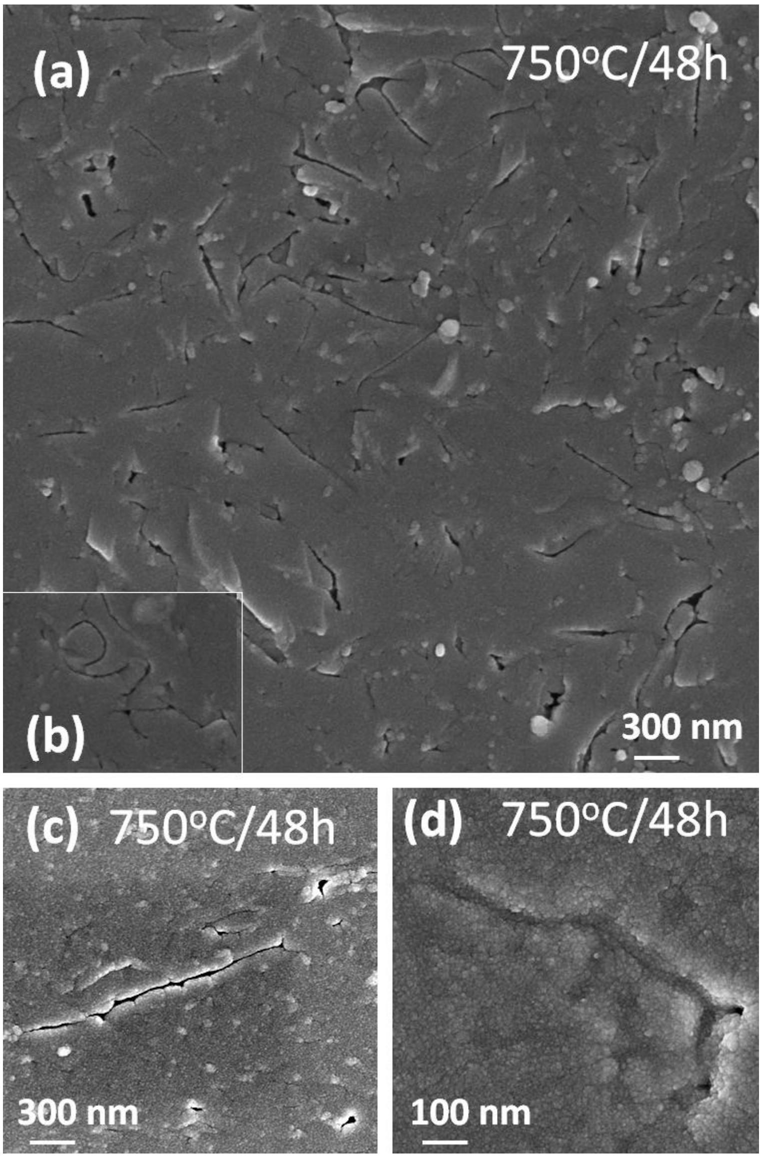

Figure 6.53: SEI-SEM images of (a-d) 10wt% MWCNT-SiO_2 glass composites showing the slots after MWCNT oxidation at 750°C for 48h.

5.0wt% to 10wt% MWCNT-SiO_2 glass composites showed partial surface decarburisation after thermal ageing at 500°C for 48h. However, the composites showed complete MWCNT oxidation at 750°C after 48h, leaving behind porous silica glass matrix. Further increase in temperature up to 1000°C produced surface cracking due to cristobalite formation. However, no such indication of devitrification and cracking was observed at 500°C and 750°C. Different MWCNT contents in composites, i.e. 5.0wt% and 10wt%, produced porous composites but the porosity content increases with increase in MWCNT content.

d. Friction and wear resistance

The wear resistance and friction coefficient of silica glass and 2.5wt% to 10wt% MWCNT-SiO_2 glass composites were evaluated as a function of the MWCNT content and the applied load. The wear and friction tests were performed by pin-on-disc and ball-on-disc methods. Figure 6.54 shows the specimens fixed in specimen holders and the steel pin and ball used.

In wear tests, an increased wear rate is observed at a higher load [194]. In the present study, wear volumes were determined at two different sliding loads, i.e. 0.15GPa and 0.50GPa (Figure 6.55). At a higher load (0.50GPa), lower wear volumes were observed (Figure 6.55(a)), which is due to the shorter test duration (30min), as compared to the tests at longer duration (60min) but at a lower load (0.15GPa). However, Figure 6.55(b) displays the volume loss as wear rate, which shows the increased wear rate when applying a higher load.

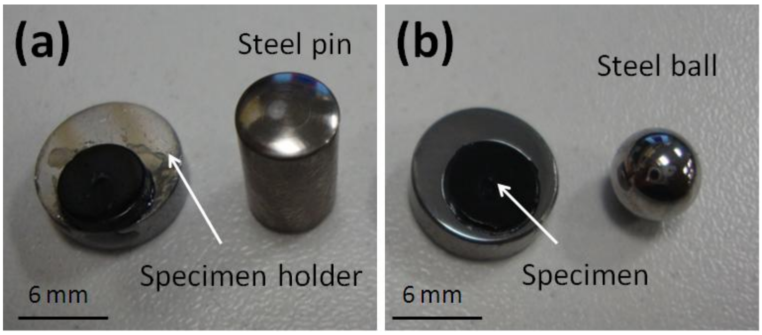

Figure 6.54: (a-b) Photographs of 2.5wt% MWCNT-SiO_2 glass composite specimens fixed in specimen holders and steel pin/ball used in wear and friction tests.

Nevertheless, the main feature of Figure 6.55(b) is an increase in the wear rate on adding up to 7.5wt% MWCNTs in silica GMCs, as compared to pure silica glass. A further increase in MWCNT content, i.e. 10wt%, however, resulted in a sudden drop in wear rate, which may be related to the establishment of the graphitic layer, as discussed further below. A similar sudden drop in the friction coefficients of 10wt% MWCNT-SiO_2 glass composites was noticed at the two different loads (Figure 6.56). However, unlike wear rate, the friction coefficients of the composites never increased compared to silica glass but continuously decreased on adding up to 7.5wt% MWCNTs, after which a sudden fall was observed.

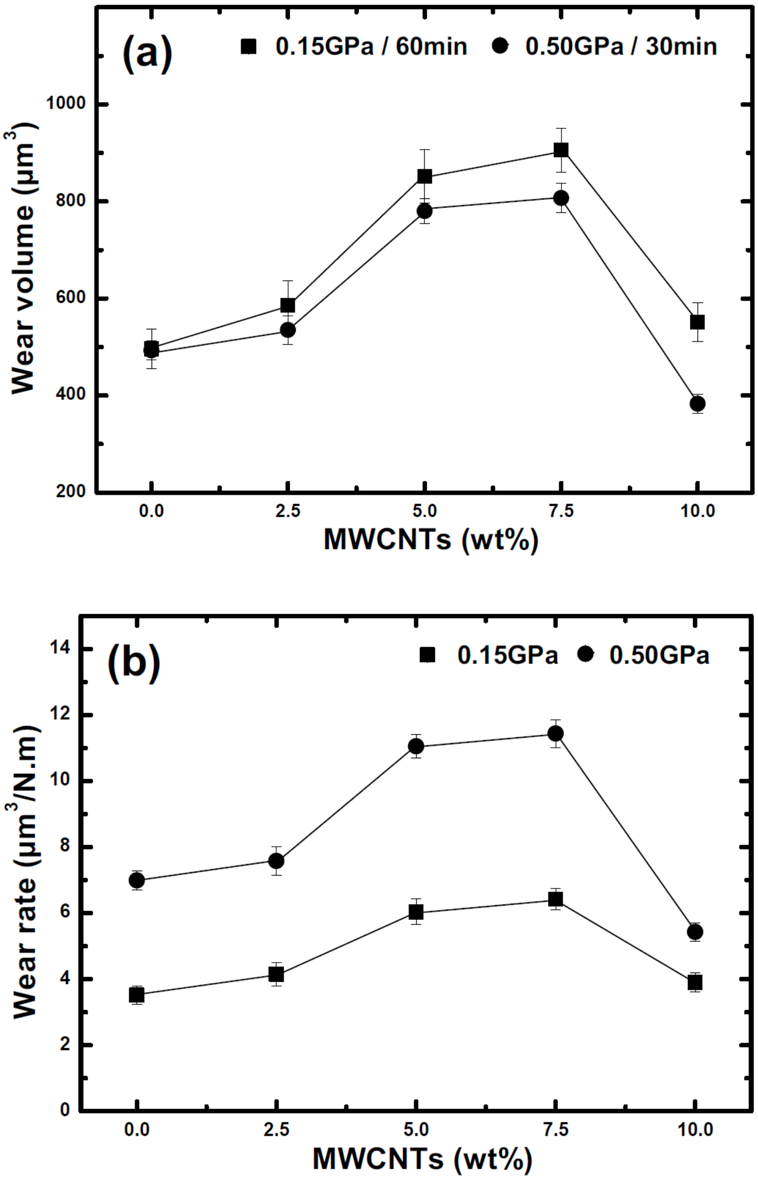

Figure 6.55: (a) Wear volumes and (b) wear rates of silica glass and 2.5wt% to 10.0wt% MWCNT-SiO_2 glass composites at two different loads of 0.15GPa and 0.50GPa.

A decrease in the friction coefficient has always been observed in related published data on the friction behaviour of CNT-reinforced CMCs [194,199]. As CNTs are expected to provide a lubricating effect similar to graphite, their presence at the sliding surfaces causes an easy shear and hence decreases the friction coefficient [191]. Published friction coefficients of bulk graphite and solid SWCNTs, densified by SPS, are 0.20 and 0.22-0.24, respectively [202]. In the present study, 10wt% MWCNTs has significantly reduced the friction coefficient of the silica glass matrix (0.29-0.39), which was otherwise 0.81-0.91.

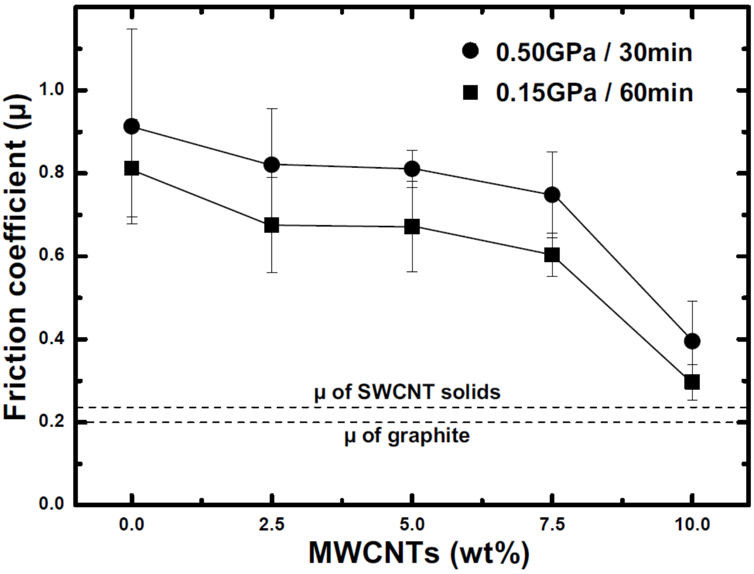

Figure 6.56: Friction coefficients of silica glass and 2.5wt% to 10.0wt% MWCNT-SiO$_2$ glass composites at two different loads of 0.15GPa and 0.50GPa.

The evaluation of the friction coefficient (Figure 6.57) against the sliding time reveals comparatively high friction coefficients and large scatter in data for the higher load (0.50GPa). Indeed, the higher load causes more abrasion of the specimen and develops increased friction. The presence of spikes in some of the friction coefficient/time graphs may be related to the displacement of wear debris from the sliding surfaces resulting in the exposure of the nascent surfaces. Nevertheless, no change in the friction coefficient values was observed after the dislocation of wear debris, as fresh debris were formed upon further sliding.

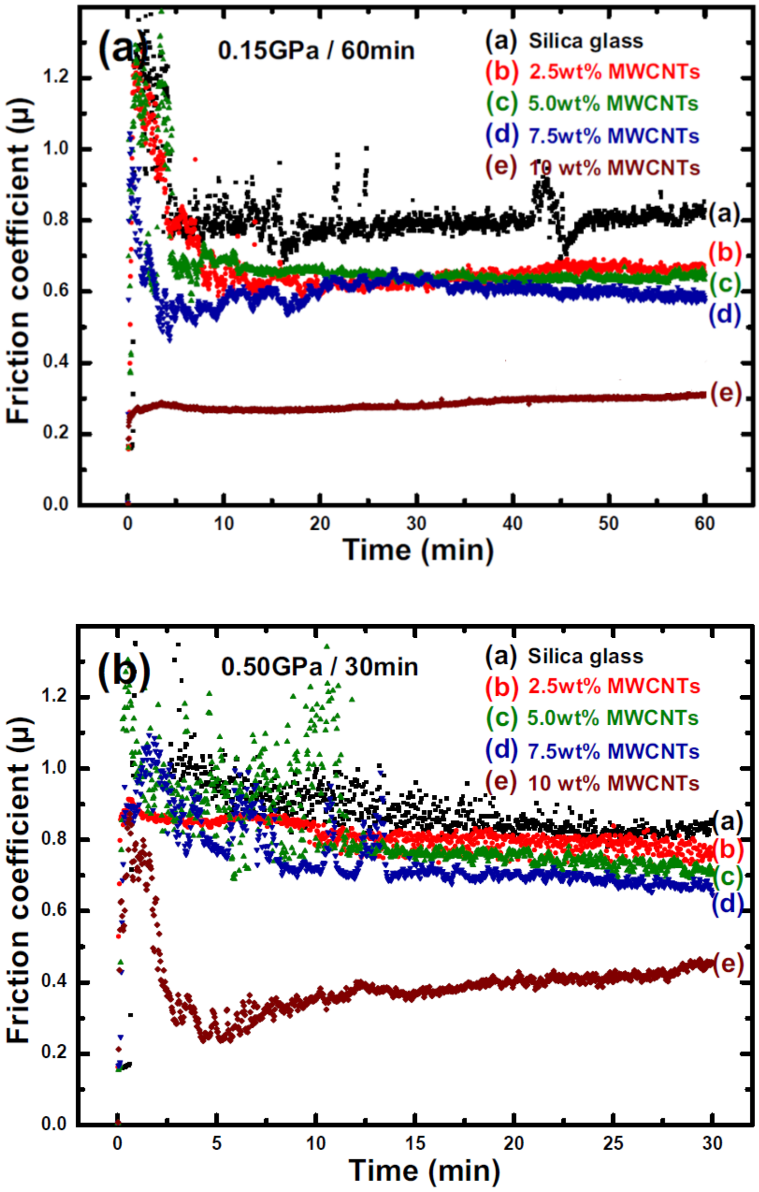

Figure 6.57: Friction coefficients of silica glass and 2.5wt% to 10wt% MWCNT-SiO_2 glass composites against the sliding time at two different loads of (a) 0.15GPa and (b) 0.50GPa.

The wear results obtained in the present investigation on CNT-amorphous GMCs are largely different from those obtained on CNT-crystalline CMCs, wherein either a continuous decrease in wear rate is observed [193,199] or an initial decrease in wear rate at low CNT contents (<5wt%) is followed by a sharp rise at higher CNT contents [194,198]. An increase in hardness due to grain refinement of the ceramic matrix may be the likely reason for a decrease in wear rate at low CNT content. However, the effect reverses in composites containing higher CNT contents likely due to the presence of CNT-agglomerates leading to poor density and hence low hardness and high wear rate.

In the present investigation, the hardness of composites reduces with the addition of MWCNTs in the amorphous glass matrix. Neither an indirect effect of CNTs on grain size refinement is expected nor are CNT-agglomerates present. Therefore, in the absence of these two effects of CNTs, which are otherwise observed in CMCs, the real wear and friction effects of CNTs in brittle matrices emerged.

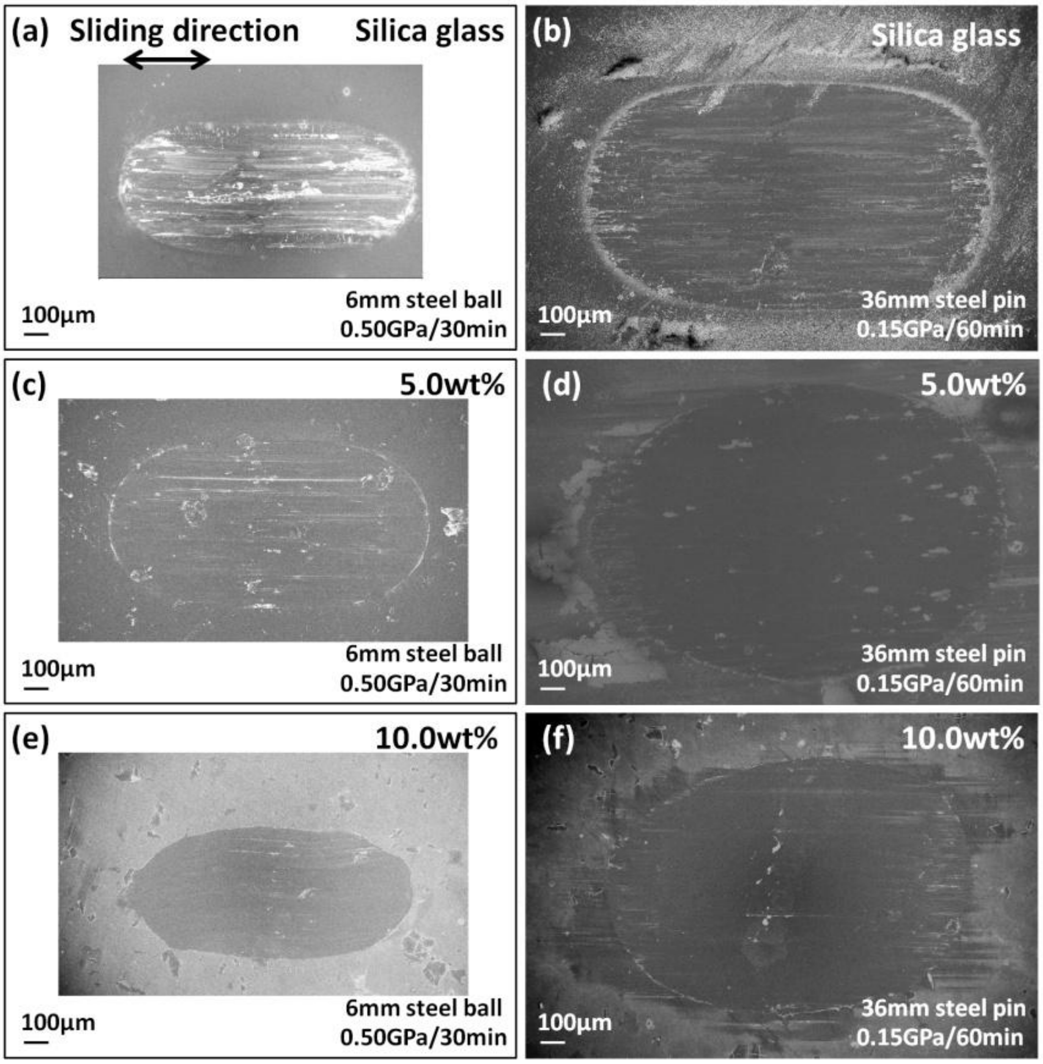

Figure 6.58: SEI-SEM images of wear scars produced on (a-b) silica glass, (c-d) 5.0wt% and (e-f) 10.0wt% MWCNT-SiO_2 glass composites at two different sliding loads of 0.50GPa (a,c&e) and 0.15GPa (b,d&f). Wear scars increased in size on 5.0wt% MWCNT-SiO_2 glass composites but decreased on 10.0wt% MWCNT-SiO_2 glass composites.

Apart from the hardness of composites affecting the wear properties, the fracture toughness can also have an important influence on wear behaviour; especially, the hardness to fracture toughness ratio (H/K_{IC}), also called the brittleness index [255], is considered useful in characterising the wear resistance [256]. A new brittleness index [257] also incorporates the elastic modulus along with hardness and fracture toughness (HE/K_{IC}^2); the low brittleness index values show improved machinability and wear resistance. As the addition of MWCNTs continuously increases the fracture toughness of the composites and decreases their hardness and elastic modulus, the low brittleness index values are obtained, which indicate increased wear resistance. However, the current results show that the wear resistance was first decreased up to 7.5wt% MWCNT loading and then suddenly increased at 10wt% loading. The hardness to elastic modulus ratio (H/E) has also been suggested as a suitable parameter for predicting wear resistance [258]. However, this parameter is not significant here as both the hardness and elastic modulus of composites decrease on adding MWCNTs in silica glass and the H/E ratio of composites remains relatively similar.

The wear scars on silica glass and composite specimens produced by sliding against the ball and the pin are shown in Figure 6.58; three different types of specimens were examined, i.e. pure silica glass, 5.0wt% and 10.0wt% MWCNT-SiO_2 glass composites. The size of scars increased on 5.0wt% MWCNT-SiO_2 glass composites at both of the applied loads compared to that on silica glass specimens, while it reduced on 10.0wt% MWCNT-SiO_2 glass composites. Also, the scar surfaces on composites get smoother and indicate the lubricating effect due to the presence of MWCNTs.

A magnified SEM image of the scar edge produced on silica glass at 0.15GPa load using a steel pin of 36mm diameter is shown in Figure 6.59(a). Wear debris can be seen inside and outside the scar surface (Figure 6.59(b)), which consists of silica glass particles. The wear debris act as a third body between the two sliding bodies and increase the wear and friction of the sliding surfaces. An unusual feature is the conversion of silica particles into rod-like features under the applied load and the sliding action of the steel pin against the specimen surface

(Figure 6.59(c-d)). Although the entire scar surface was not filled with these features, they were found at different places within the scar. It can be expected that these silica rods contain metallic wear debris coming from the steel pin. It is also to be noted that these features may not be confused with the MWCNTs, as the specimens were made of CNT-free silica glass. The presence of these silica rods might have helped in reducing the friction by providing a rolling action between the counter bodies, as these were oriented along the sliding direction.

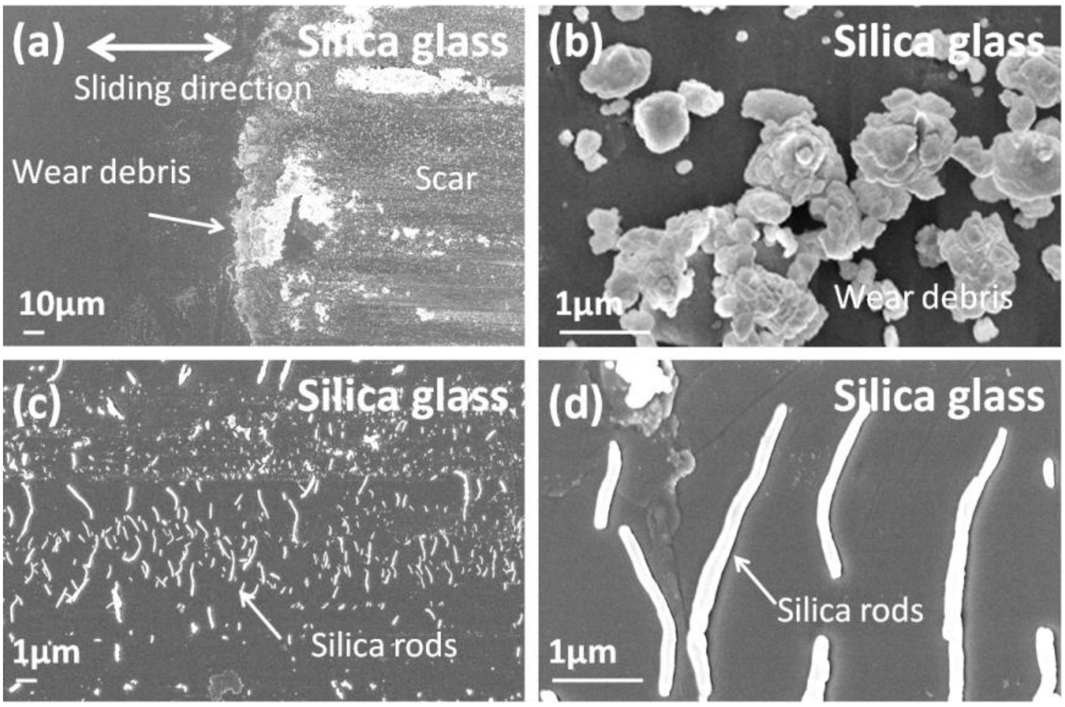

Figure 6.59: SEI-SEM images of (a) the edge of wear scar produced on silica glass specimen by sliding the steel pin at 0.15GPa load showing the presence of wear debris consisted of silica particles within and (b) outside the scar. (c-d) Transformation of silica glass particles into rod-like shapes, i.e. silica rods, facilitates easy sliding of steel pin against the glass surface by providing rolling action between the counter bodies.

The complementary steel pin and the wear debris transferred to it from the silica glass specimen were also examined (Figure 6.60(a-b)); wear debris consisted of silica glass particles (Figure 6.60(c)). Plastic deformation of the steel pin was observed at the contact area due to the application of a high load (Figure 6.60(d)); also the silica particles were found to be entrapped into the cavities developed due to the plastic deformation of the contact area.

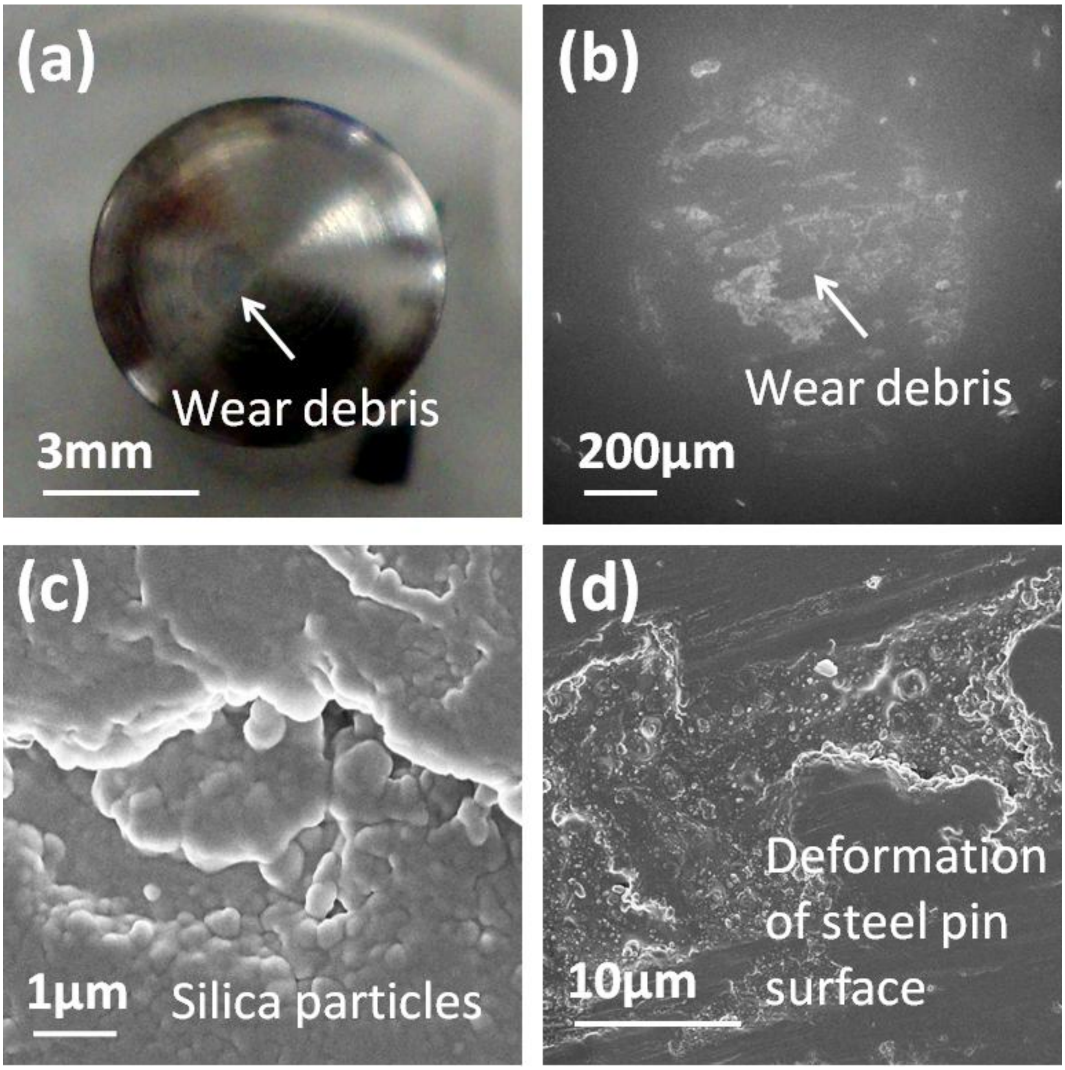

Figure 6.60: (a) Photograph of the steel pin slid against the silica glass specimen. SEI-SEM images showing (b) the contact area of the pin, (c) transferred silica glass particles from the specimen and (d) the plastic deformation of the contact area of the steel pin.

A similar comprehensive microstructural characterisation was performed on the 5.0wt% MWCNT-SiO_2 glass composites and the complementary steel pins slid against them. Figure 6.61(a) shows the edge of the wear scar produced on 5.0wt% MWCNT-SiO_2 glass composite specimen after sliding against the steel pin of diameter 36mm at 0.15GPa load. Wear debris is evident within and outside the scar (Figure 6.61(b)). The transformation of silica particles into rod-like shapes was also observed in these specimens; however, the size of these silica rods was small and there were fewer of them, as compared to that in pure silica glass specimens (Figure 6.61(c-d)). Another feature is the size of the wear debris that was larger than in silica glass specimens (compare Figure 6.59(a) with Figure 6.61(a)). MWCNTs may have provided a "gluing effect" to bind the debris of silica glass particles. The smearing of MWCNTs under the sliding action of the pin may be the reason. Severe deformation of MWCNTs under a high load is expected to distort their shape due to their exposure during the abrasion process, as shown in the magnified image (Figure 6.62) of Figure 6.61(d).

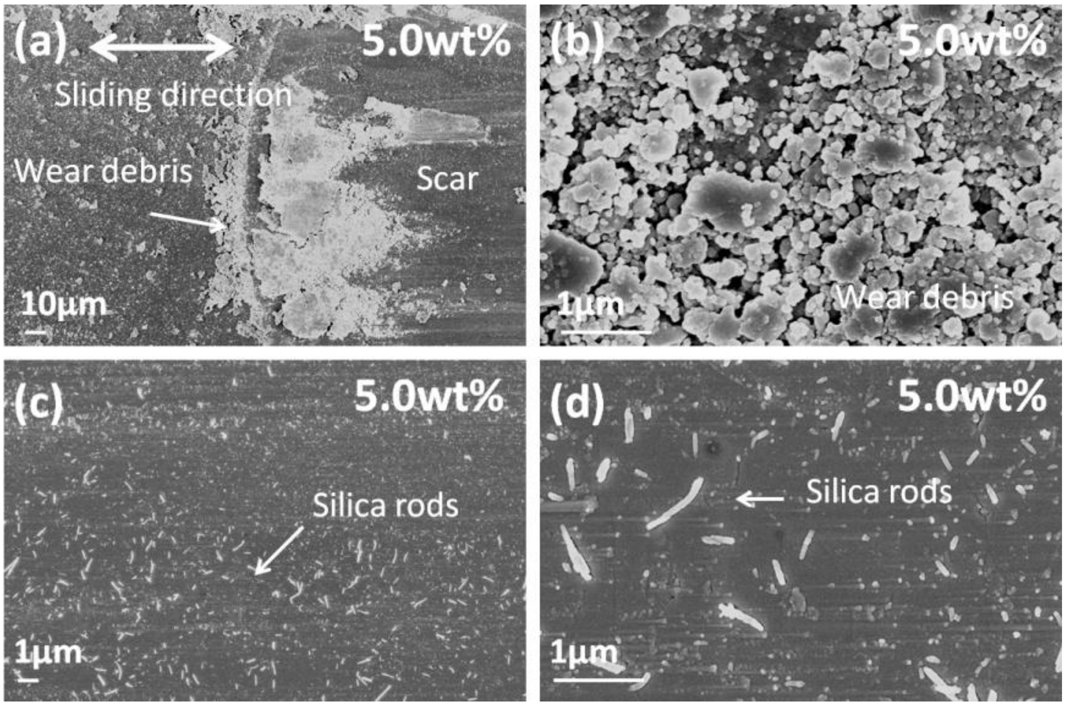

Figure 6.61: SEI-SEM images of (a) the edge of the wear scar produced on 5.0wt% MWCNT-SiO$_2$ glass composite specimen by sliding against the steel pin at 0.15GPa load, showing the presence of wear debris, consisting of silica particles and smeared MWCNTs within and (b) outside the scar. (c-d) Transformation of silica glass particles into rod-like shapes, i.e. silica rods, is also witnessed.

It is important to mention here that some of the published data insists on the survival of the morphology of CNTs at the sliding surface [194], and it is believed that CNTs remain undamaged under the harsh wear test conditions due to their high stiffness and strength, and only the ceramic matrix abrades. Moreover, a rolling action of CNTs has been suggested to improve the wear resistance [194] and lower the friction coefficient [198]. However, in the present study, the MWCNTs did not survive the sliding action of steel pin/ball, nor was there any evidence of MWCNT rolling. In fact, MWCNTs could not maintain their tubular morphology under severe conditions and produced a graphitic film, as discussed below.

The images of the steel pin slid against 5.0wt% MWCNT-SiO_2 glass composite specimen reveal the presence of wear debris transferred from the worn specimen surface (Figure 6.63(a-b)). The wear debris consisted of silica glass particles and a discontinuous graphitic layer (Figure 6.63(c-d)), which is expected to form due to the smearing of MWCNTs. It can be argued that this film may be formed from the carbon present in the steel pin but it should be noted that such a layer was not formed on the pin slid against the CNT-free silica glass specimen. Moreover, no evidence is available wherein a graphitic film is formed by sliding the steel against a counter body.

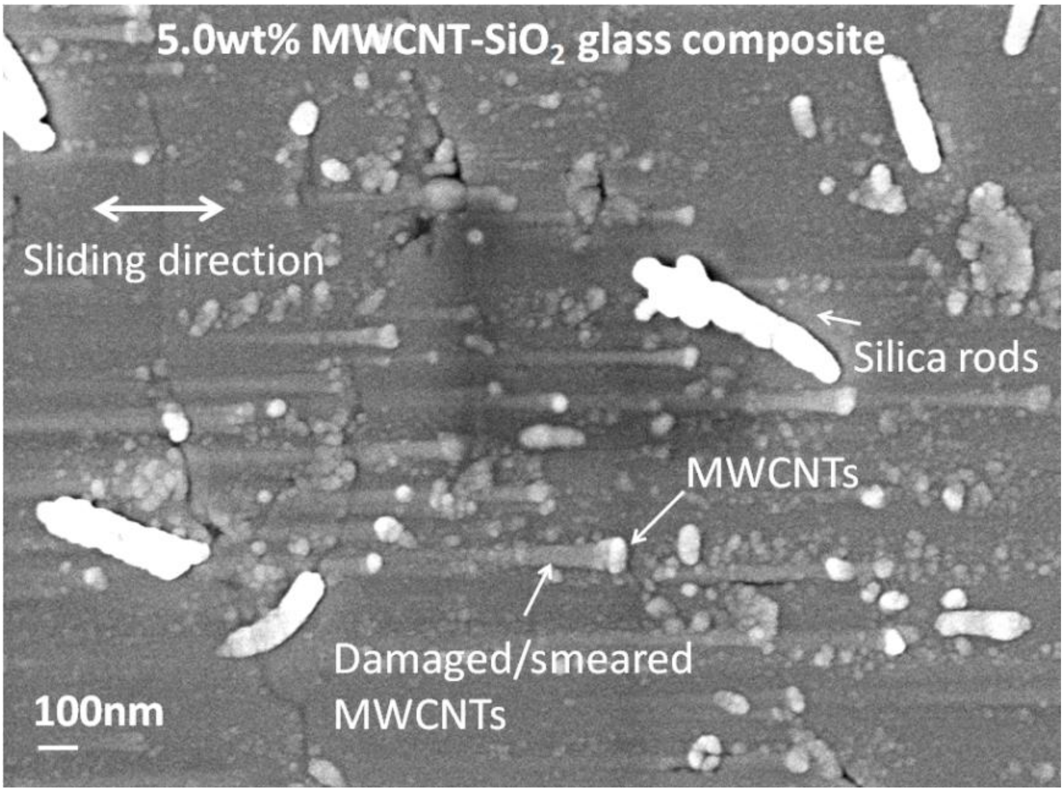

Figure 6.62: SEI-SEM image of the wear scar surface of 5.0wt% MWCNT-SiO_2 glass composite specimen after the sliding of steel pin at 0.15GPa load, showing the smearing of the exposed MWCNTs (from right to left). Silica rods are also present.

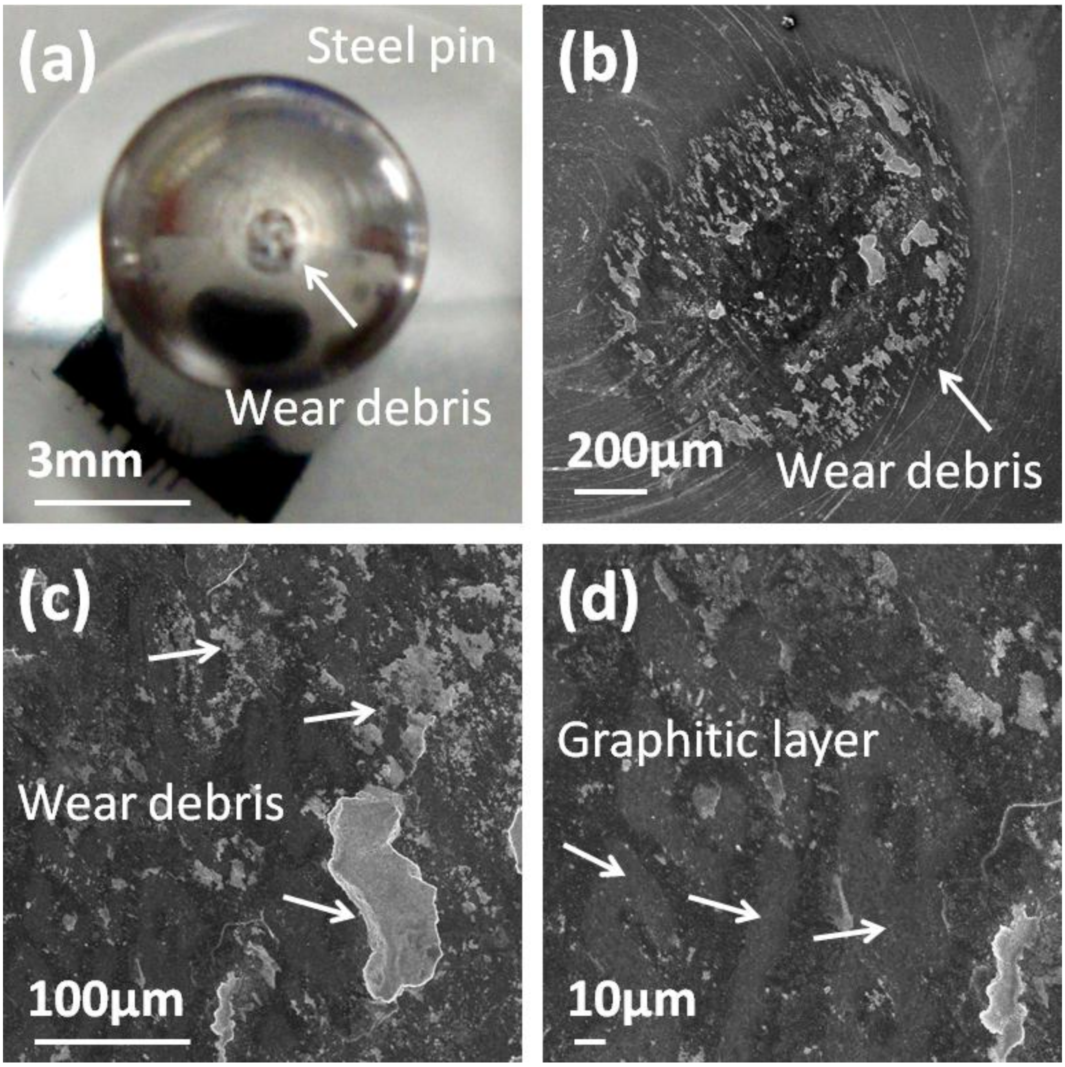

Figure 6.63: (a) Photograph of the steel pin slid against 5.0wt% MWCNT-SiO_2 glass composite specimen. SEI-SEM images show (b) the pin contact area with the specimen, (c) the presence of wear debris, consisting of the silica glass particles from the specimen and (d) a discontinuous graphitic layer from the smeared MWCNTs.

To observe the morphology of the wear debris and the graphitic film, the image in Figure 6.63(d) was inspected at a high magnification (Figure 6.64). Three distinct regions of the debris were identified, which were transferred from the specimen to the steel pin. The region "X" confirms the presence of silica glass particles (Figure 6.64(b)); region "Y" shows the islands of graphite layer (Figure 6.64(c)) and region "Z" shows a continuous graphitic layer with pores inside (Figure 6.64(d)). It seems that the islands of graphite grew into a continuous graphitic layer by the provision of more MWCNTs from the worn specimen surface. A few of the MWCNTs can also be identified in the graphite layer, yet to be smeared. This graphitic layer contributes to lowering the friction coefficient but wear rate increases due to the presence of hard silica glass particles, as the graphitic layer could not develop to a sufficiently large area to cover the entire contact surface of the pin.

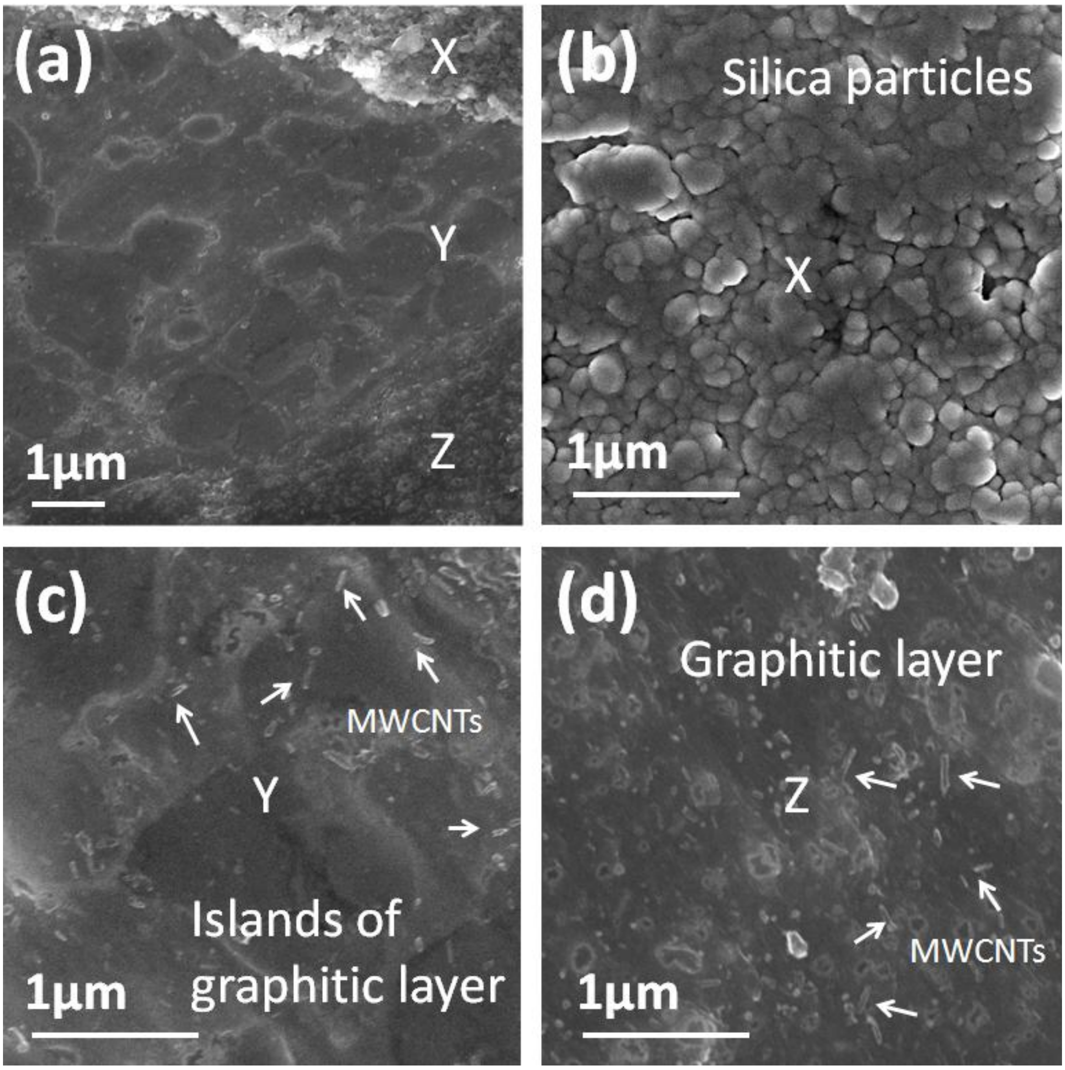

Figure 6.64: SEI-SEM images of (a) the contact area of the steel pin slid against 5.0wt% MWCNT-SiO_2 glass composite specimen, showing three distinct regions of transferred wear debris containing (b) silica glass particles (c) islands of graphitic layer and (d) continuous but porous graphitic layer. Isolated MWCNTs can also be seen (arrowed) on the graphitic layer.

Microstructural characterisation of 10wt% MWCNT-SiO_2 glass composites and their complementary sliding pins was also performed to explore the reasons for a decrease in the wear rate and friction coefficient in these composites. Figure 6.65(a) shows the edge of the wear scar produced on 10wt% MWCNT-SiO_2 glass composites by sliding against a steel pin of diameter 36mm under a load of 0.15GPa. A smooth scar surface is evident due to the lubricating effect of the smeared MWCNTs. Wear debris also seems to be glued together due to distorted MWCNTs (Figure 6.65(b)), although MWCNTs could not be identified in the wear debris. The wear scar surface did not show the presence of rod-like features; instead, the exposed MWCNTs are evident (Figure 6.65(c)), which are yet to be smeared because they are still present in their slots under the worn surface (Figure 6.65(d)).

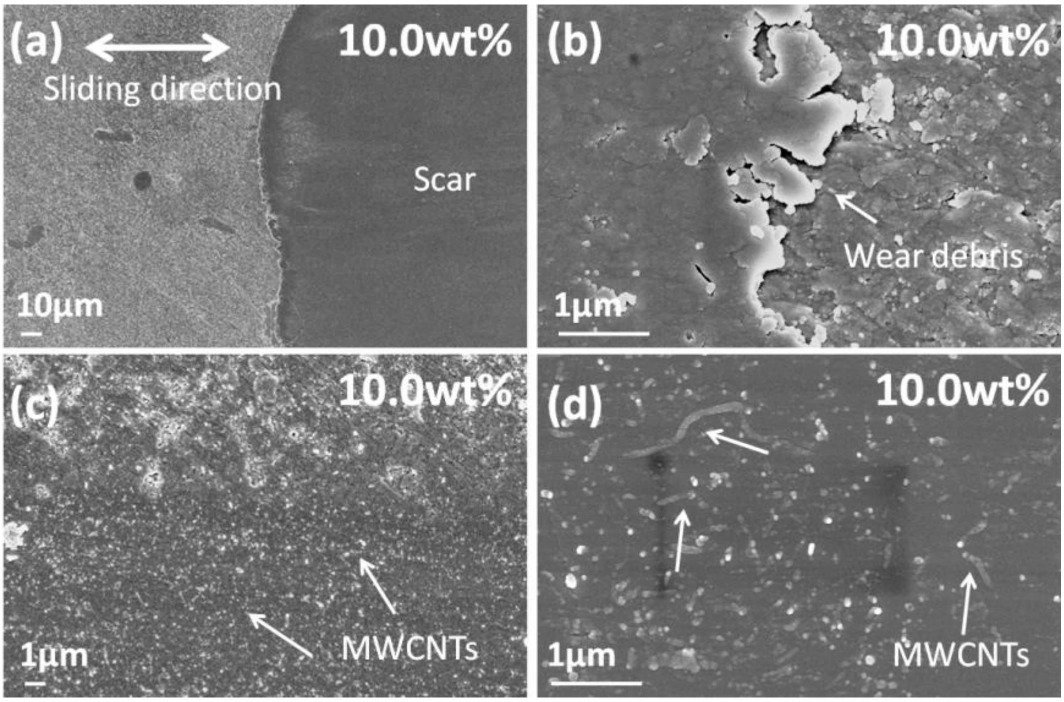

Figure 6.65: SEI-SEM images of (a) the edge of the wear scar produced on 10.0wt% MWCNT-SiO_2 glass composite specimen by sliding against the steel pin at 0.15GPa load, (b) wear debris and (c) another edge of the scar shows the exposed MWCNTs (d) still retained in their slots.

A graphitic layer was observed (Figure 6.66(a)) on the steel pin slid against the 10wt% MWCNT-SiO_2 glass composite, which was also observed in the SEM (Figure 6.66(b)). Although, it contains porosity, the graphitic layer seems to be well-established over the contact area of the pin (Figure 6.66(c-d)). High magnification images reveal the morphology of this porous graphitic film, which is likely to act as a soft third body between the two counter hard bodies and cause a significant reduction in both friction coefficient and wear rate. In a previous study on carbon fibre GMCs [190], the presence of an isle-shaped discontinuous film was claimed to be present at the counterbody, which was supposed to become continuous in some areas but no microstructural evidence was provided.

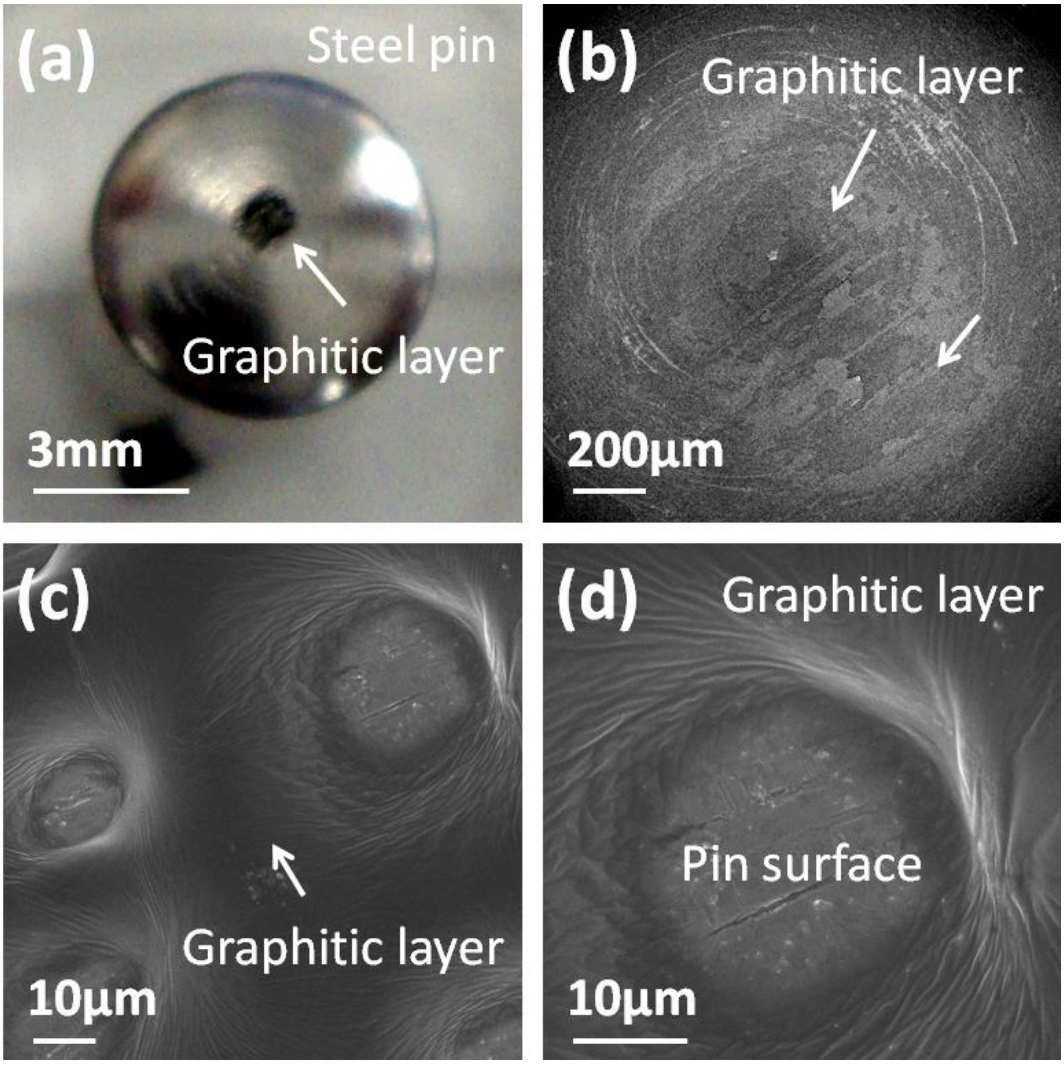

Figure 6.66: (a) Photograph of the steel pin slid against 10.0wt% MWCNT-SiO_2 glass composite specimen. SEI-SEM images show (b) the contact area with the specimen revealing the (c-d) graphitic layer produced due to the smearing of MWCNTs.

To further verify if the developed layer is graphite, EDS was performed on areas of the steel pin with and without the graphitic layer. EDS revealed the presence of carbon in the graphitic layer, while the pin surface without graphitic layer displayed the typical elements present in the steel of the sliding pin (Figure 6.67(a-b)).

Another interesting feature, leading to decreased wear and friction coefficient, is the good adhesion of smeared MWCNTs to the deformed steel pin/ball surfaces. The cavities/scars generated at the steel pin surface due to the plastic deformation are likely to be filled with the smeared MWCNTs until they grow and form a layer composed of MWCNT-converted graphite. A good adhesion of CNTs on the porous specimen surfaces is reported to develop during sliding, leading to a reduced friction coefficient; in contrast, a high friction coefficient is observed in dense composites with low wear rates [191,197]. In the present study, the gradual increase in the porosity in composites containing 2.5wt% to 10wt% MWCNTs can have an effect on the adhesion of MWCNTs with the sliding surfaces but the decreased hardness and elastic modulus increases the wear rate until the establishment of a permanent graphitic layer between the two sliding surfaces. The possibility of the development of a graphitic layer has been discussed previously on CNT-ceramic composites [196,202] but MWCNT-derived graphitic layer is shown for the first time in the present study.

Similar to the present study, a continuous decrease in the friction coefficient has been reported in CNT-reinforced polymeric [8] and metallic [72] matrix composites; however, contrary to the present result, a continuous decrease in the wear rate has been shown, which increases at high CNT contents due to the formation of CNT-agglomerates.

It can be inferred from the above results that abrasion is the likely wear mechanism in the present silica glass and composite specimens and that the low MWCNT contents in composites generate a discontinuous graphitic layer, which decreases the friction coefficient but does not assist in decreasing the wear rate. However, at a critical MWCNT content, their supply becomes sufficient to establish a distinct graphitic layer between the sliding surfaces, which almost completely covers the contact area of the steel pin. At this stage, the graphitic layer acts as a solid lubricant; the behaviour for which graphite is known.

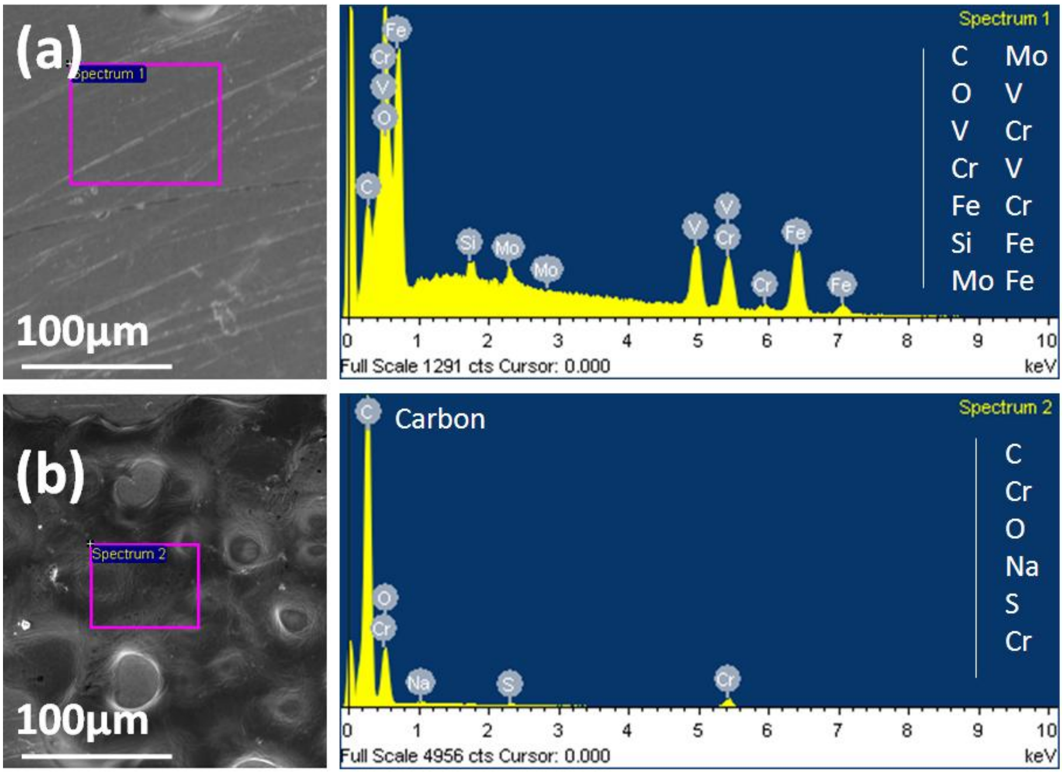

Figure 6.67: EDS results of the steel pin used for the wear test of 10wt% MWCNT-SiO$_2$ glass composites; (a) area without the graphitic layer indicates the elements present in steel while (b) the graphitic layer clearly indicates the presence of carbon.

6.3 Summary

A model MWCNT-SiO$_2$ glass composite system was developed with different MWCNT aspect ratios (~31-65) and loadings (2.5-10wt%). It was confirmed that the colloidal mixing process by heterocoagulation provided a uniform dispersion of MWCNTs in silica glass powder without the presence of agglomerates. PLS provided dense (96-99%) and amorphous matrices. MWCNTs were retained after sintering; neither a significant graphitisation of MWCNTs nor deterioration was observed after sintering.

The composites were characterised for physical, microstructural, mechanical, functional and technological properties. A flexible MWCNT structure was observed by SEM/TEM along with their random dispersion in an amorphous matrix without the grain size and boundary effects. A mechanical interface was observed in HRTEM without any chemical reaction between MWCNTs and silica glass. However, good bonding was detected showing the physical attachment of MWCNTs with the matrix without any gaps in between, which may be due to the residual stresses in MWCNTs after consolidation at high pressure and temperature.

The mechanical properties of composites showed different trends, depending upon the structural features of MWCNTs and their bonding with the matrix. The nature of MWCNTs similar to graphite, along with the structural flexibility, adversely affected the hardness of the composites (~21-38%). The presence of a mechanical interface and the low (but unknown) effective modulus of MWCNTs decreased the composites stiffness (~20-37%). It was estimated that for an increased composite stiffness with three-dimensional random MWCNT orientation, a high intrinsic MWCNT elastic modulus is required, i.e. >350GPa, which is higher than the value of most CVD-grown CNTs. It was found that the uniformly dispersed porosity coming from the MWCNT hollow core may also have contributed to reduced hardness and stiffness. As expected, the weak but reasonably good (not strong) interface improved the fracture toughness of composites (~100%) by encouraging the emergence of known energy dissipating (toughening) mechanisms, such as crack deflection, bridging and pullout. However, the extent of improvement was insufficient to transform the brittle glass into a structurally reliable material. The quantification of energy absorbing mechanisms showed results comparable to experimental data. It was also estimated that the decrease in the diameter of MWCNTs could not provide increased fracture toughness unless MWCNTs of significantly increased strength were used.

The electrical and thermal conductivity of composites increased with MWCNTs. A modest increase was observed in thermal conductivity, i.e. 41-48%, due to a difference of only three orders of magnitude between the thermal conductivities of the two composite phases, and the large interfacial thermal resistance. The development of a percolation network tremendously increased the electrical conductivity, i.e. >11 orders of magnitude.

The effect of different MWCNT sizes could not be detected on the mechanical properties, as high aspect ratio MWCNTs impeded the densification of composites, thereby reducing the mechanical properties. However, composites containing high aspect ratio MWCNTs showed comparatively higher electrical and thermal conductivities. A systematic decrease in the electrical percolation threshold of the composites was also observed with MWCNTs of increasing aspect ratios.

Incorporating MWCNTs in the composites retained the known high thermal shock resistance of the silica glass matrix when quenching from 1200°C to 20°C without thermal cracking. Likewise, repeated thermal shocks from 1000°C to 20°C, up to 20 times, could not damage the composites except for the appearance of glass matrix devitrification. A range of ageing temperatures (500-1200°C) and durations (6-96h) were employed to observe the thermal stability of composites. No significant composite deterioration was observed after thermal ageing the composites at 500°C except for limited MWCNT surface oxidation. However, at 750°C and 1000°C, significant MWCNT oxidation was observed, which started from the surface and progressed into the specimen bulk producing a decarburised and porous surface region. No indication of crystallisation was noted in the glass matrix until 750°C but cristobalite was formed at ≥1000°C producing surface cracking on cooling. At the selected temperatures, the decarburisation depth in 2.5wt% MWCNT composites showed a parabolic increase as a function of ageing time. Increasing the MWCNT content in composites to 5.0wt%, 7.5wt% and 10wt% provided completely porous composites at ≥750°C after 48h of ageing. The stiffness and hardness of porous composites decreased continuously with increasing porosity content, as the composites with higher MWCNT contents produced high porosity levels after oxidation. In short, MWCNT-SiO_2 glass composites can be used until ~500°C without significant degradation, while at ≥1000°C, composites were damaged due to both the surface cracking and CNT oxidation. However, amorphous glass with tailorable volume, concentration and shape of nanoporosity can be achieved at 750°C.

The friction coefficient of composites continuously decreased with an increase in the MWCNT content in silica glass matrix up to 10wt%, i.e. 0.81-0.91 to 0.29-0.39, respectively. However, the wear rate was first increased at low contents (≤7.5wt%) but dropped by the establishment of a permanent graphitic layer between the counter sliding bodies and the composites containing higher content (10wt%).

7. MWCNT-borosilicate glass composites

Manufacture and characterisation of 2.5-10wt% (4.2-17.0vol%) MWCNT-borosilicate glass composites are described. Manufacture includes the preparation of composite powders by mixing the suspensions of MWCNTs and borosilicate glass particles to promote heterocoagulation, and subsequent densification by pressureless sintering. Characterisation comprises the physical, microstructural, mechanical and functional property evaluation by measuring density, hardness, elastic modulus, fracture toughness, thermal and electrical conductivity, X-ray diffraction and scanning electron microscopy. These composites were manufactured to ascertain the applicability of the model composite system (Chapter 6) to other inorganic matrices.

7.1 Manufacture

7.1.1 Materials

MWCNTs synthesised by using 3wt% ferrocene in toluene in ICCVD setup (Figure 5.1) were used as reinforcement in composites based on commercially-available borosilicate (BS) glass powder (SCHOTT, Nanofine NF180) of chemical composition, i.e. 55%SiO_2, 25%BaO, 10%B_2O_3 and 10%Al_2O_3 (Figure 7.1). The BS glass family is extraordinarily broad and possesses a high resistance to chemical corrosion and temperature change. As a result, BS glasses are used extensively in the chemical and pharmaceutical industries, process plants and laboratories [75]. SCHOTT Nanofine NF180 BS glass powder is typically used for dental applications and was chosen for the present investigation due to its reproducible chemical composition, ready availability and average nanometer particle size of ~180nm. A large particle size distribution of 50nm to >1000nm (Figure 7.2) was selected to investigate the effect of different particle sizes on the MWCNT distribution quality in the matrix, as discussed further below (Section 7.2.2(b)).

7.1.2 Composite powder preparation

To prepare MWCNT-BS glass composite powders, the technique of heterocoagulation upon colloidal mixing was utilised, as already established for MWCNT-SiO_2 glass composites (Section 6.1.2). Stable aqueous suspensions of MWCNTs were again obtained by treating MWCNTs with a mixture of sulphuric and nitric acids, i.e. 40 ml acid for 1g of MWCNTs (Section 5.2.1), while BS glass particle suspension was obtained by following the same recipe as adopted for silica glass powder (Section 6.1.2). Subsequent mixing and drying of the two suspensions, in selected volumes, produced composite powders of different MWCNT concentrations, i.e. 2.5-10wt%. To obtain reference specimens, a BS glass powder suspension was dried without mixing MWCNTs but processed following a similar treatment as applied to the composite powders.

Unlike MWCNT-SiO_2 glass composites, where silica nanoparticles of ~20nm were completely coated to the surface of larger diameter MWCNTs (~37-57nm), BS glass particles, due to their large size (~180nm) and variation (~50-1000nm) in diameter, could not completely coat the surface of MWCNTs; only smaller particles partially coated MWCNTs. Conversely, BS glass particles were not large enough to be coated entirely with MWCNTs. Nevertheless, the repulsive forces among MWCNTs, due to the presence of negative surface charges, avoided the formation of agglomerates and a good dispersion of MWCNTs in BS glass particles was obtained, as shown in the green body of 2.5wt% MWCNT-BS glass composites (Figure 7.3).

7.1.3 Composite powder compaction

PLS was employed for the consolidation of BS glass and MWCNT-BS glass composite powders. Green bodies were prepared by uniaxial (120MPa) and cold isostatic (400MPa) pressing into the discs of diameter ~10mm and thickness ~2.0mm, which were subsequently sintered under ambient pressure in a tube furnace under an inert atmosphere of argon to avoid the oxidation of MWCNTs. A temperature range of 700°C to 800°C was chosen for the sintering of BS glass and composite specimens. The reasons for selecting these temperatures are discussed in the next section. The other sintering parameters include the heating rate of 10°C/min and a holding time of 3h, followed by normal furnace cooling.

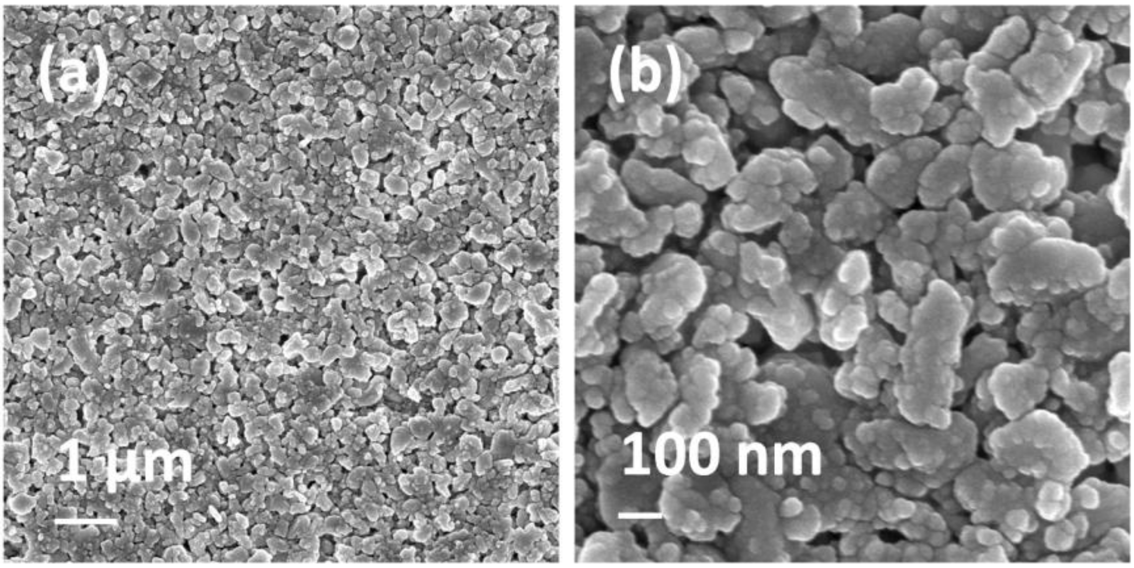

Figure 7.1: SEI-SEM images of BS glass powder (SCHOTT, Nanofine NF180) used for the manufacturing of MWCNT-BS glass composites.

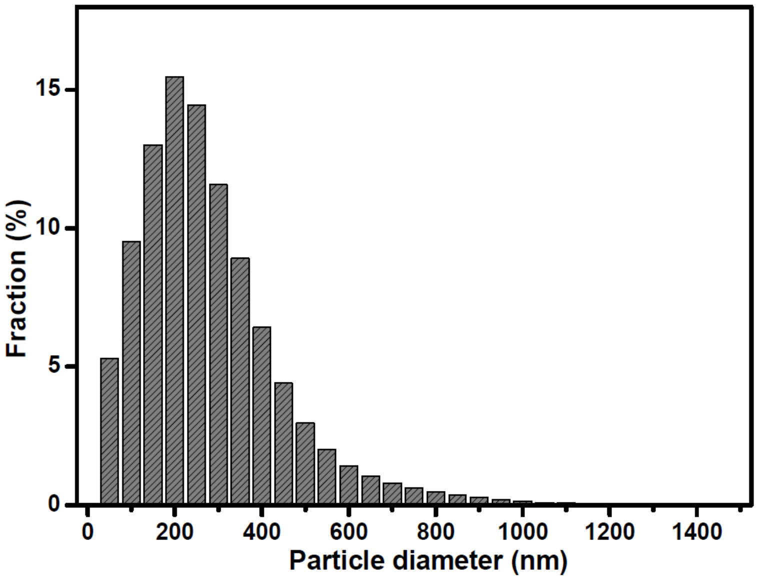

Figure 7.2: Particle size distribution of BS glass powder (SCHOTT, Nanofine NF180).

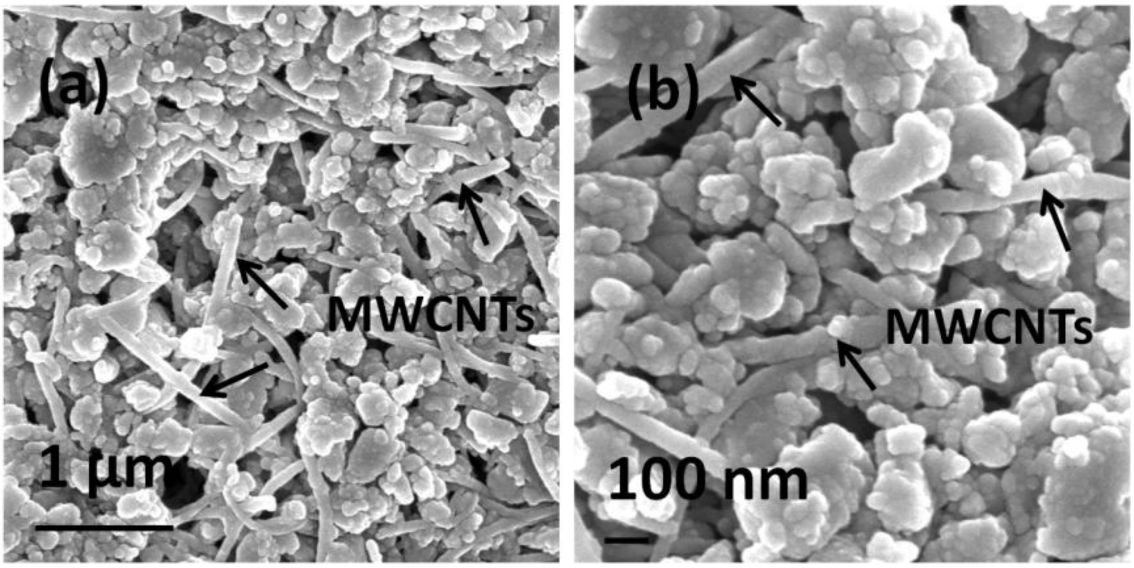

Figure 7.3: (a-b) SEI-SEM images showing the dispersion of 2.5wt% MWCNTs in BS glass particles; agglomerates were not observed although MWCNTs were not completely coated with glass particles.

7.2 Characterisation

7.2.1 Physical characterisation

a. Density

PLS provided dense BS glass and 2.5wt% MWCNT-BS glass composite specimens. The relative densities (actual/theoretical) are shown by taking a typical value of 2.8g/cm^3 for SCHOTT Nanofine NF180 BS glass and 1.65g/cm^3 for MWCNTs [91] (Figure 7.4). BS glass sintered at 700°C showed a relative density of ~94%, which increased to ~99% at 775°C; a further increase in temperature to 800°C gave similar density results. Hence, the sintering of BS glass specimens was optimised at 775°C. In contrast, the composite specimens showed comparatively lower densities after sintering at 700°C and 775°C, i.e. ~87% and ~94%, respectively. An increase in the effective viscosity of the composite system due to the presence of MWCNTs may be the reason [231]. However, the composite density increased with temperature and reached 97%

at 800°C; a further increase in temperature to 810°C did not improve the density of the composites. Hence, the sintering of composite specimens was optimised at 800°C.

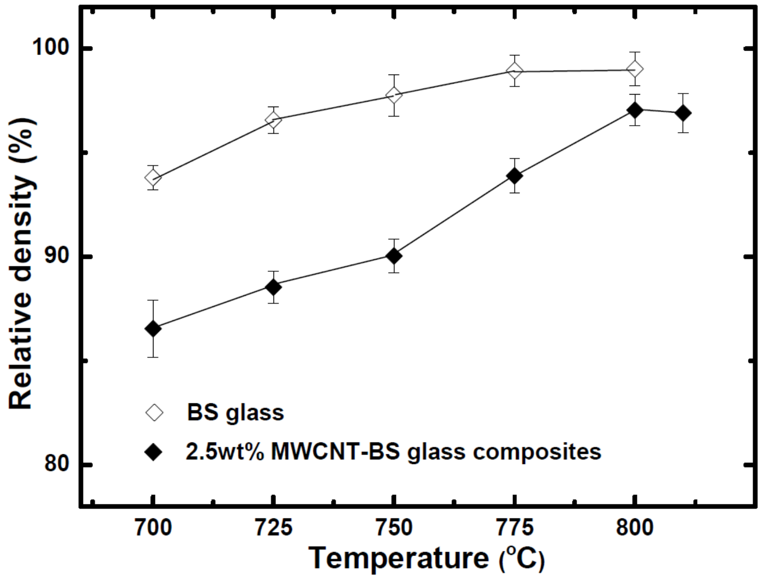

Figure 7.4: Relative densities (actual/theoretical) of sintered BS glass and 2.5wt% MWCNT-BS glass composites at different sintering temperatures.

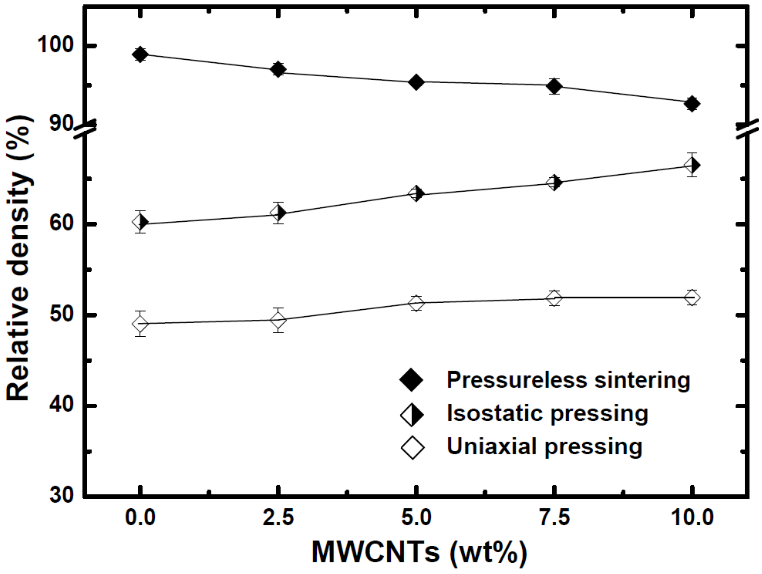

Figure 7.5: Relative densities (actual/theoretical) of BS glass and 2.5wt% to 10wt% MWCNT-BS glass composites in green and sintered states.

The sintering of MWCNT-BS glass composites containing 5.0wt%, 7.5wt% and 10wt% MWCNTs was also performed at 800°C. A systematic decrease in the sintered density of the composites was observed with increasing the amount of MWCNTs (Figure 7.5). BS glass showed the highest density and 10wt% MWCNT-SiO_2 composite the lowest. The gradual decrease in sintered densities with increasing content of MWCNTs is consistent with the observation that MWCNTs hinder the viscous flow densification [231]. A reverse trend (increase) in the green densities of the composites was seen on adding more MWCNTs, as already observed in MWCNT-SiO_2 glass composites (Figure 6.6), which may be related to the compressed state of flexible MWCNTs after uniaxial and isostatic pressing during the green state, and to their partial recovery after PLS.

7.2.2 Microstructural characterisation

a. X-ray diffraction

XRD data of BS glass and 2.5wt% MWCNT-BS glass composites, obtained during the optimisation of their sintering temperatures (Figure 7.6), show the presence of an amorphous matrix in both the glass and the composite specimens. As a reference, XRD of the green bodies is also displayed to confirm the amorphous nature of powders before sintering. XRD of the composites containing 2.5wt% to 10wt% MWCNTs (Figure 7.7) similarly showed a predominantly amorphous matrix without the indication of the presence of crystalline phases as a result of any chemical reaction between glass matrix and MWCNTs; cristobalite was reported to form in a previous study on hot-press sintered CNT-BS glass composites [105]. The graphitic peak (002) corresponding to MWCNTs ($2\theta=26.20$) emerged above the characteristic bump of the amorphous glass, the intensity of which increased with the quantity of MWCNTs in composites and became evident in composites containing ≥7.5wt% MWCNTs.

b. Scanning electron microscopy

SEM was performed to observe the level of porosity in glass and composite specimens, the retention of MWCNTs after sintering and their dispersion quality. Porosity was observed in BS glass specimens sintered at 700°C (Figure 7.8) while a completely dense glass was obtained at 775°C in agreement with the density measurement results (Figure 7.4).

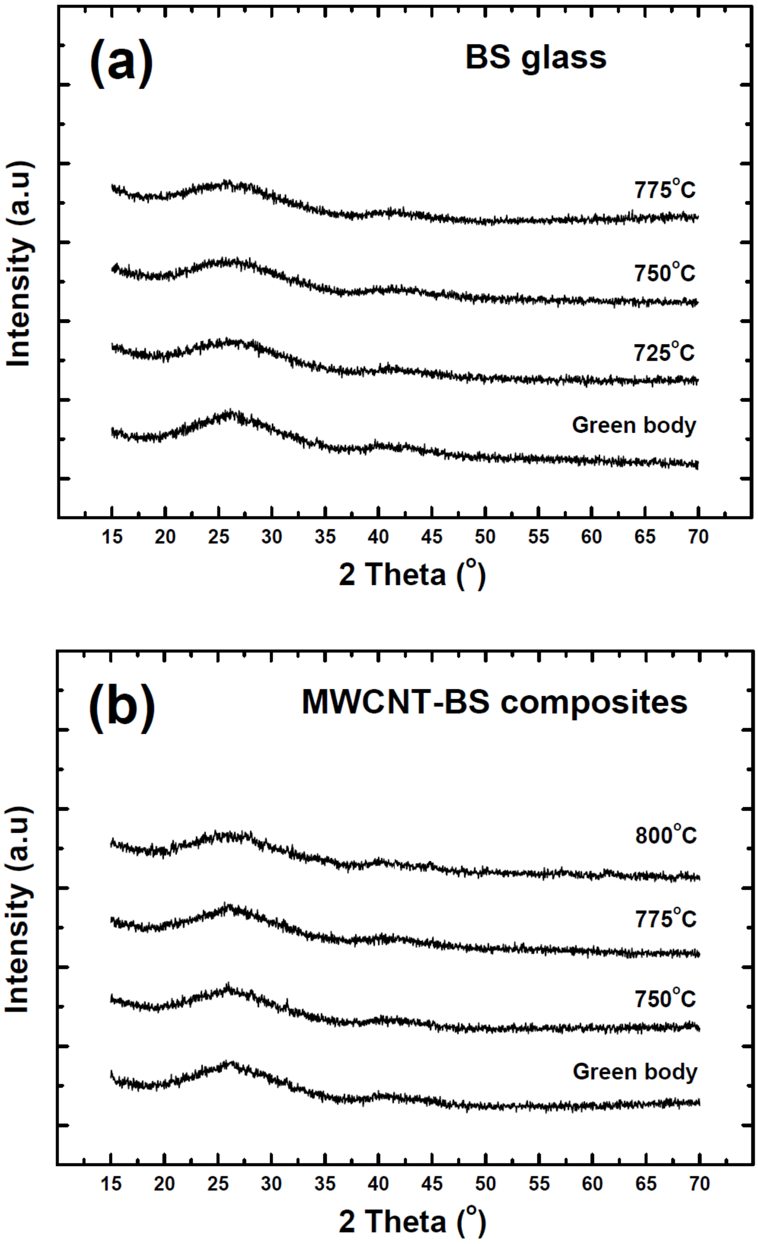

Figure 7.6: XRD of (a) BS glass and (b) 2.5wt% MWCNT-BS glass composites during the sintering temperature optimisation; XRD of green bodies are shown to confirm the amorphous state of specimens before sintering.

The images in Figure 7.9 compare the porosity content of 2.5wt% MWCNT-BS glass composite specimens at the three different sintering temperatures. Clearly, the SEM images support the density measurement results (Figure 7.4). Even at best sintering conditions, the inter-particle porosity remains (~3%), while no such evidence was recorded in 2.5wt% MWCNT-SiO_2 glass composites (Section 6.2.1(a)), which showed <1% porosity. The particle size difference of the two glass powders (silica and BS) may be the reason for the different densification results of the composites. MWCNTs were completely coated with small silica glass particles, which subsequently sintered to make a continuous glass body. In contrast, large BS glass particles only partially coated the MWCNTs, which might have hindered the viscous flow of large BS glass particles; for example, by lying in between the particles.

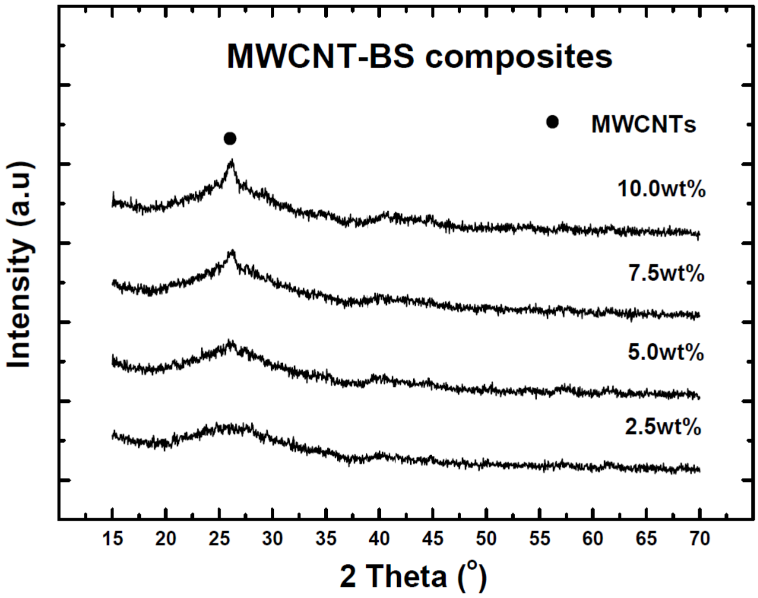

Figure 7.7: XRD of 2.5wt% to 10wt% MWCNT-BS glass composites showing amorphous matrix. The presence of MWCNTs is indicated by the graphitic peaks, the intensity of which increases in relation to MWCNT content in composites.

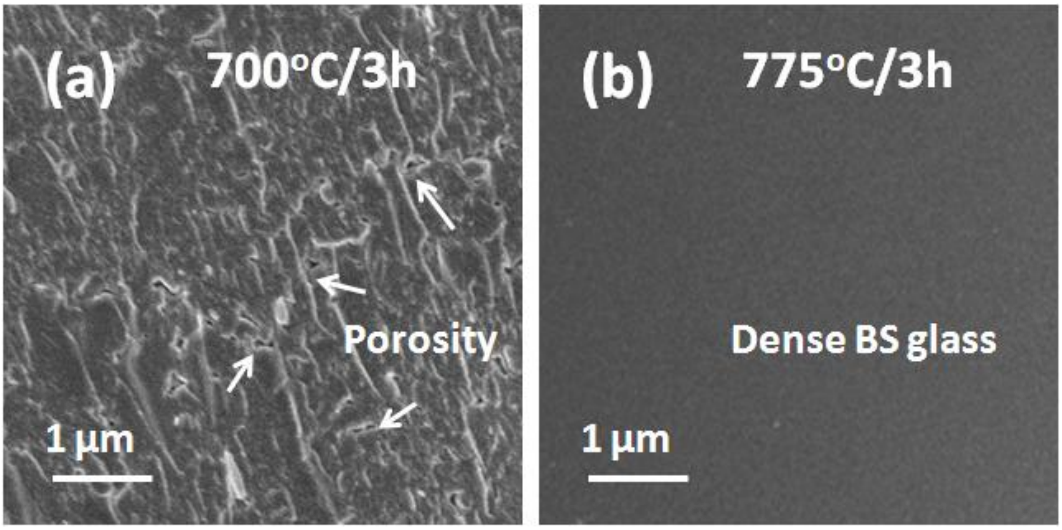

Figure 7.8: SEI-SEM images of BS glass sintered at (a) 700°C and (b) 775°C with and without the presence of porosity, respectively.

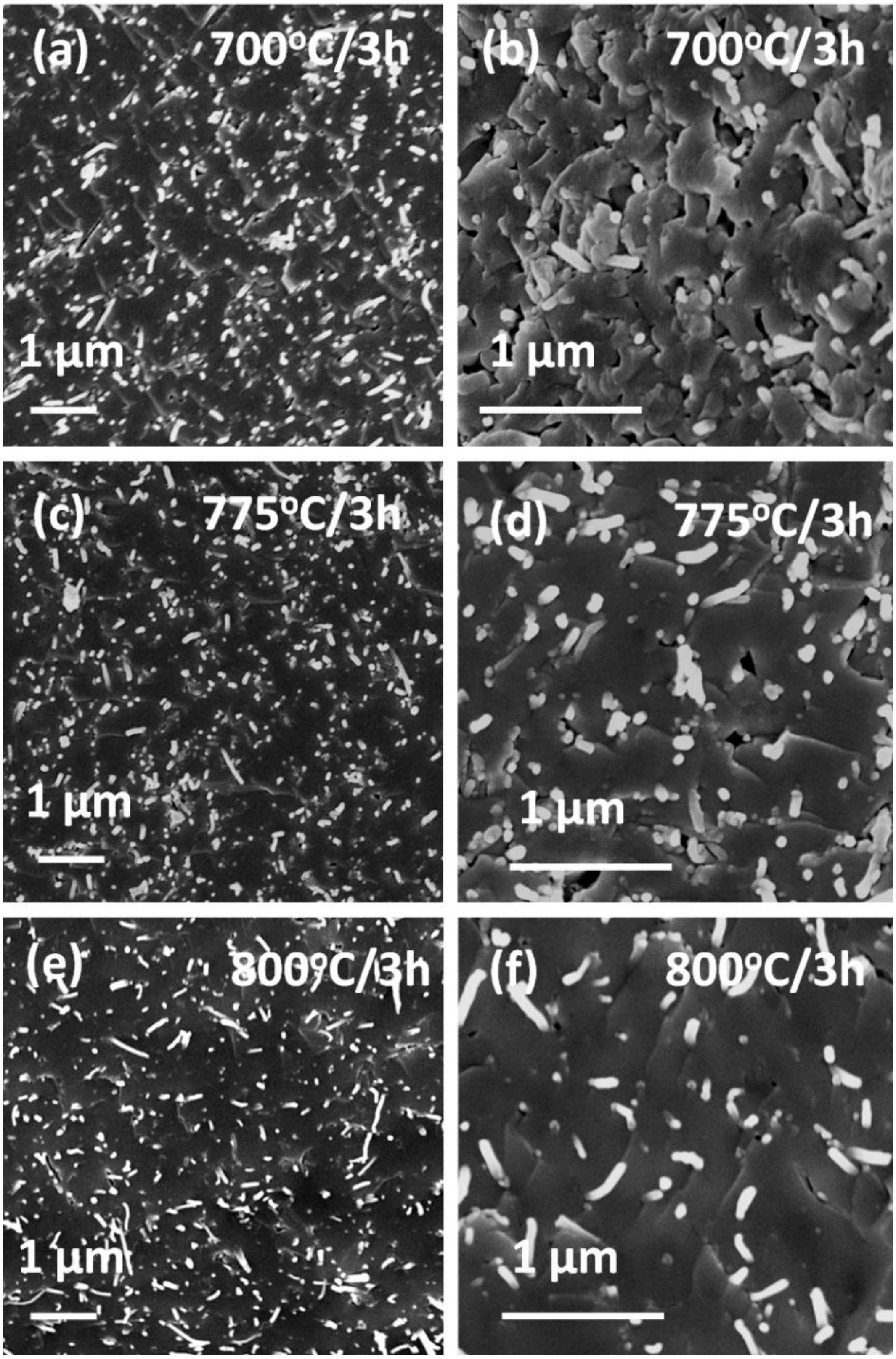

Figure 7.9: SEI-SEM images of 2.5wt% MWCNT-BS glass composites sintered at (a-b) 700ºC, (c-d) 775ºC and (e-f) 800ºC, showing the level of porosity at different magnifications. MWCNT dispersion quality was maintained at all sintering temperatures.

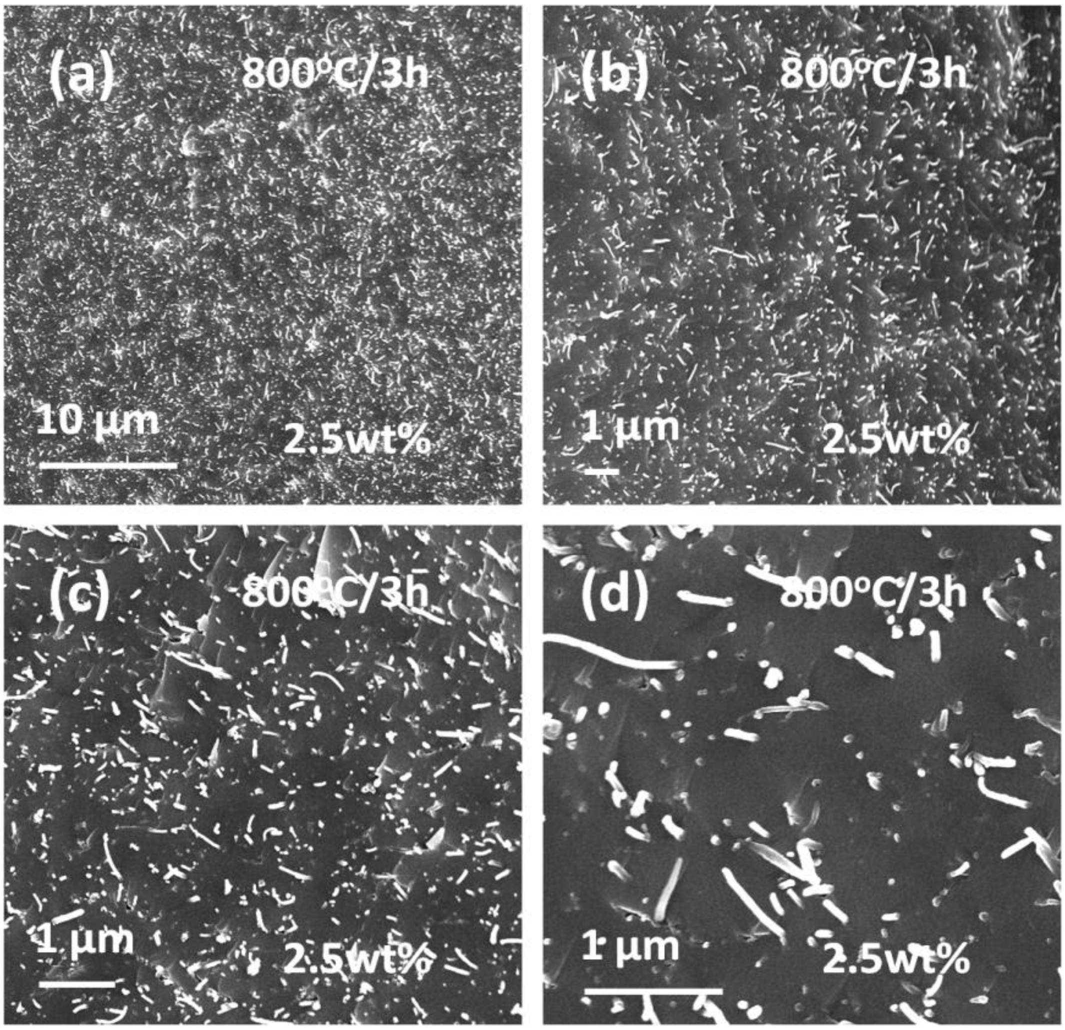

Figure 7.10: SEI-SEM images of (a-d) 2.5wt% (4.25vol%) MWCNT-BS glass composites showing the MWCNT dispersion quality at different magnifications.

Nevertheless, a good MWCNT dispersion was observed (Figure 7.9) without the formation of agglomerates. The same dispersion quality was observed at different magnifications, i.e. over local and large areas of the specimens (Figure 7.10) and also at different MWCNT loadings, i.e. 2.5wt% to 10wt% (Figure 7.11). This MWCNT dispersion quality is better than that reported on CNT-BS glass matrix composites using mechanical mixing [105] and sol-gel processing [106] as CNT dispersion techniques.

Although a good dispersion of MWCNTs was achieved in composites, the distribution was not perfect, in comparison to MWCNT-SiO_2 glass composites (Figure 6.14 and Figure 6.15). Some areas were observed deprived of MWCNTs. This effect is not due to the problem with the dispersion technique but due to the presence of some large BS glass particles (up to 1000nm).

The larger glass particles restrict CNTs on their peripheries and an increase in the concentration of CNTs is observed there, while the body of the particles remains devoid of CNTs. Nevertheless, no area >1µm^2 was seen without MCWNTs in composites. It can be inferred that the selection of a uniform and small matrix particles (less than the diameter of CNTs) has several advantages in colloidal mixing technique: they completely coat the CNTs to avoid their unwanted interactions, improve CNT distribution quality by avoiding the particle boundary effects, and minimise the inter-MWCNT distance to accommodate greater amounts of CNTs in composites.

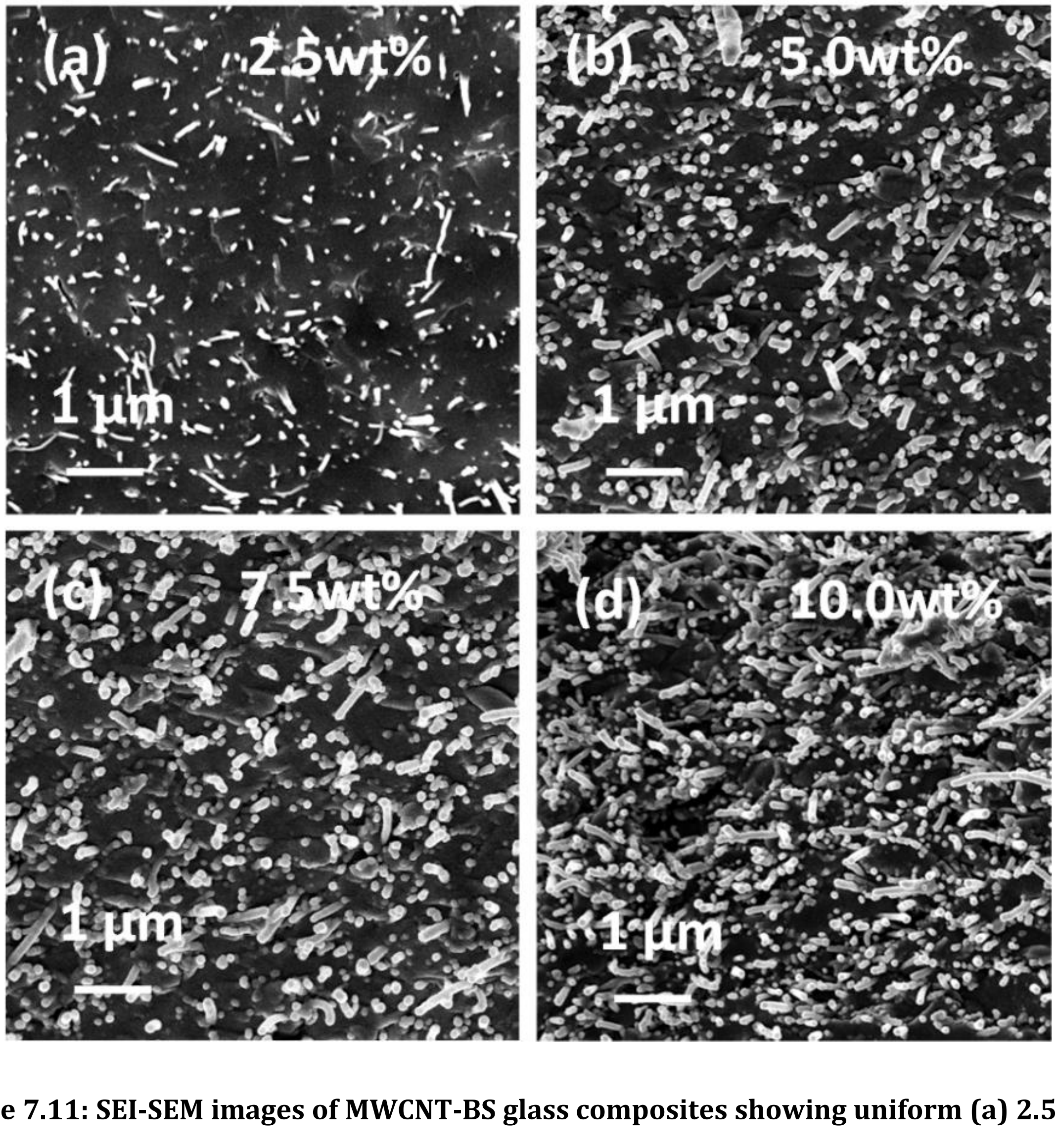

Figure 7.11: SEI-SEM images of MWCNT-BS glass composites showing uniform (a) 2.5wt%, (b) 5.0wt%, (c) 7.5wt% and (d) 10wt% MWCNT dispersion at the same magnification.

7.2.3 Mechanical characterisation

Mechanical properties of MWCNT-BS glass composites showed a similar trend as already observed in MWCNT-SiO_2 glass composites (Section 6.2.3); hardness and elastic modulus decreased, while indentation fracture toughness increased with the addition of MWCNTs.

a. Hardness

The hardness of glass and composite specimens was measured by manual Vickers micro-indentation and instrumented Berkovich nano-indentation techniques. Both of the hardness results showed similar trends, although different values were observed at the two different loads, i.e. 0.50N and 4.90N (Figure 7.12). The hardness values measured for the BS glass matrix are similar to those already published [106,111].

BS glass showed the maximum hardness, which decreased continuously with the addition of MWCNTs. The similarity of the current results with those on MWCNT-SiO_2 glass composites (Section 6.2.3(a)) verifies the decreasing hardness trend in MWCNT reinforced glass composites. The non-uniform CNT dispersion, which often leads to low hardness in composites, was also absent in the current work, which thus enabled to explore the real trend of hardness in a brittle matrix containing CNTs.

b. Elastic modulus

The Berkovich indentation technique was used to measure the elastic modulus of the glass and composite specimens. A similar declining trend of the elastic modulus was observed with the addition of MWCNTs (Figure 7.13) as found for the hardness. BS glass showed the elastic modulus values comparable to those previously found [75,111]. The addition of MWCNTs continuously decreased the elastic modulus of the composites; the composites containing 10wt% MWCNTs showed the lowest values. The possible reasons of a drop in elastic modulus have been comprehensively discussed in Section 6.2.3(b) and the present results simply verify the drop in elastic modulus, as previously observed in the model MWCNT-SiO_2 glass composite system.

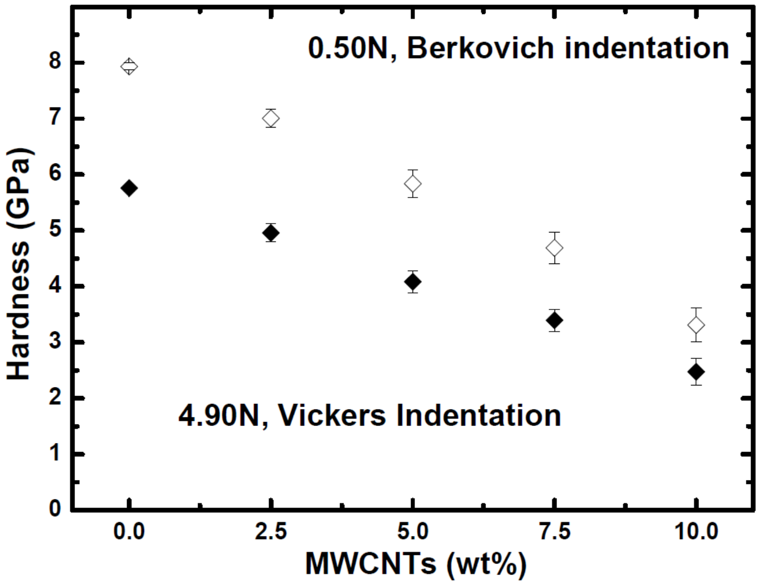

Figure 7.12: Berkovich and Vickers indentation hardness measurements of BS glass and 2.5wt% to 10wt% MWCNT-BS glass composites.

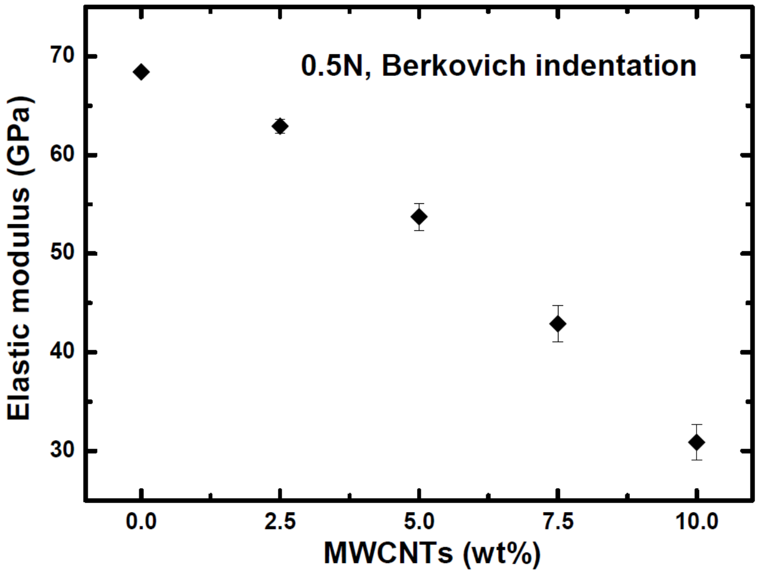

Figure 7.13: Elastic moduli of BS glass and 2.5wt% to 10wt% MWCNT-BS glass composites measured by Berkovich indentation technique.

b. Indentation fracture toughness

The fracture toughness results (Figure 7.14) of glass and composite specimens were obtained by Vickers indentation technique using Anstis et al's. expression [211]. The fracture toughness of BS glass is similar to that reported earlier [111]. A rise in the fracture toughness of composites was observed with an increase in MWCNT content; BS glass showed a value of ~0.65MPam$^{1/2}$ that increased to ~1.25MPam$^{1/2}$ in 10wt% MWCNT composites.

The indentation fracture toughness results achieved in the present study on both the glass systems (silica and BS) together with the available published data [91] indicate the achievable degree of toughening in amorphous/brittle matrices with 10wt% MWCNT loading, i.e. ~100%, which is significant but is not high enough to transform the brittle glass matrix into a structurally reliable material.

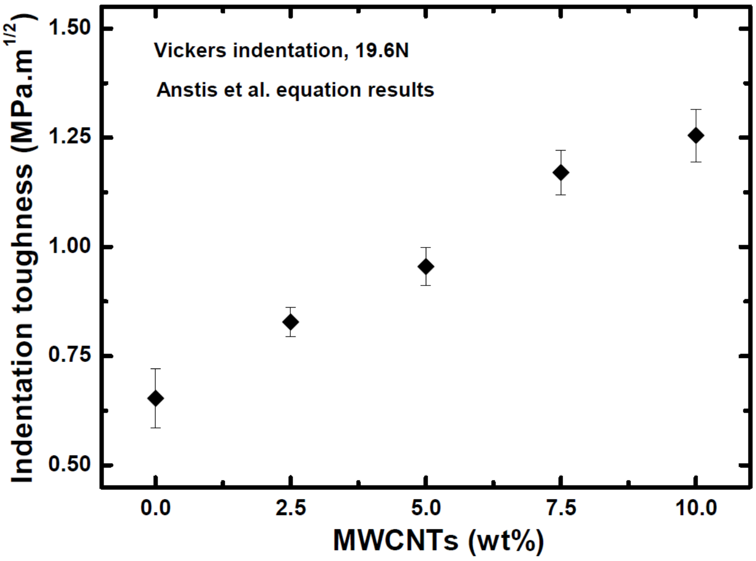

Figure 7.14: Indentation fracture toughness of BS glass and 2.5wt% to 10wt% MWCNT-BS glass composites measured by Vickers indentation technique.

7.2.4 Functional characterisation

a. Electrical conductivity

The addition of MWCNTs significantly increased the electrical conductivity of the insulating BS glass, which otherwise showed a low value, i.e. 1.8x10^{-9}S/cm. The composites showed a typical percolation behaviour (Figure 7.15).

Following the percolation theory [247], the increment in the electrical conductivity of composites obeyed the scaling law (Equation 6.11); the inserted plots in log-log scale display the electrical conductivity (σ) values as a function of $p-p_c$, expressed in MWCNT volume fraction showing well fitted data. The exponent (t) of 1.01 and a percolation threshold (p_c) of 1.26wt% (2.1vol%) were obtained, which are similar to the values previously obtained in CNT-BS glass composites [106]. This percolation threshold value indicates a uniform dispersion of MWCNTs, as observed in SEM images (Figure 7.10 and Figure 7.11) and already discussed in Section 6.2.4(a).

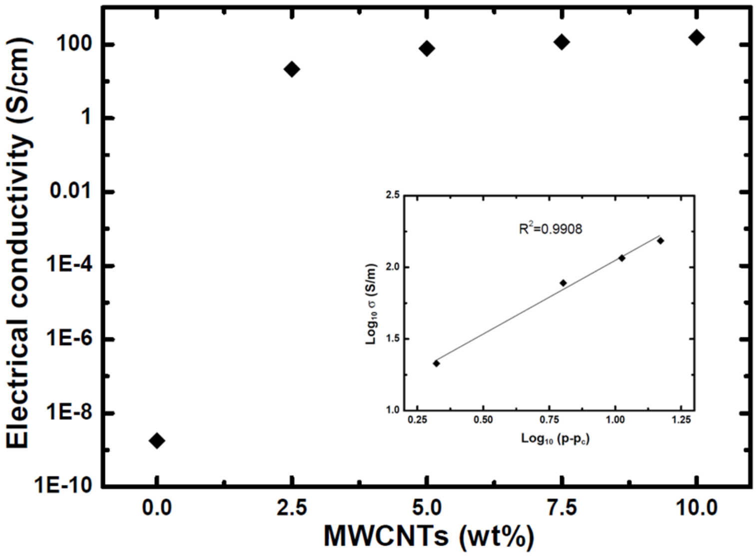

Figure 7.15: Experimental electrical conductivity data of BS glass and 2.5wt% to 10wt% MWCNT-BS glass composites as a function of MWCNT content. Inserted plot shows a fit to percolation theory.

b. Thermal conductivity

The room temperature thermal conductivities of the glass and composite specimens were calculated from their thermal diffusivity, specific heat capacity and density values using Equation 4.12. A linear increase in the thermal conductivity was observed in BS glass after the incorporation of MWCNTs (Figure 7.16). However, like in MWCNT-SiO_2 glass composites (Section 6.2.4(b)), the improvement was modest due to a difference of only three orders of magnitude between the two phases (BS glass and MWCNTs). The presence of a large interfacial surface area is the other reason for relatively small increase in thermal conductivity of the composites, as discussed in Section 6.2.4(b).

By inserting the Equation 6.13 with the measured thermal conductivity (K_m) of BS glass: 0.96W/m.K, published thermal conductivity (K_f) of MWCNTs: 3000W/m.K [66], the volume fraction of MWCNTs (V_f) in 10wt% MWCNT-BS composites: 0.17, the assumed random orientation ($\cos^2\theta$) of MWCNTs: 1/3, length of MWCNTs (L): 2.21μm, and the interfacial thermal resistance (R_i): $8 \times 10^{-8} m^2/KW$ [250], the thermal conductivity (K_c) of 10wt% MWCNT-BS glass composites was found to be 1.73W/m.K, which is close to the measured value of 1.72W/m.K. The values for composites at other MWCNT loadings (2.5wt% to 7.5wt%) also provided good matches with the calculated values (Figure 7.16), which indicate the applicability of Equation 6.13 to calculate the actual thermal conductivity values by incorporating the thermal resistance as a parameter in the equation due to the large interfacial area in MWCNT-BS glass composites.

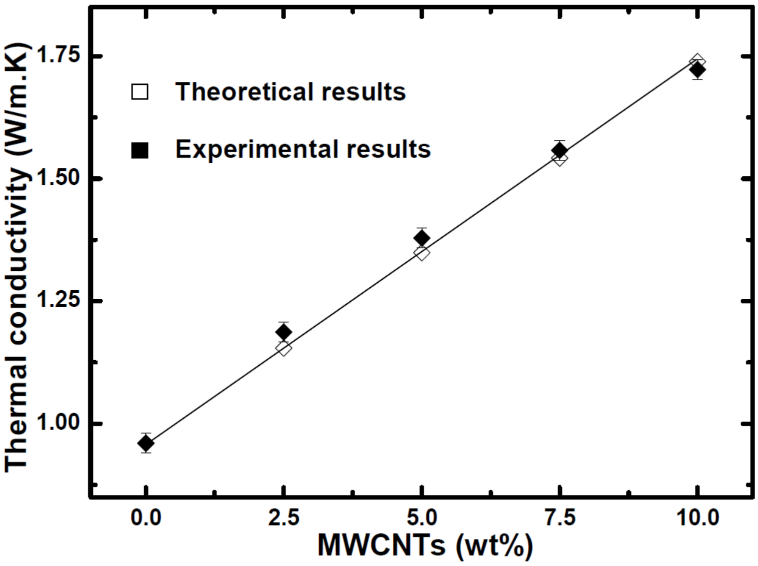

Figure 7.16: Room temperature thermal conductivity of BS glass and 2.5wt% to 10wt% MWCNT-SiO_2 glass composites; theoretically predicted values (using Equation 6.13) of the composites are also shown.

7.3 Summary

MWCNT-BS glass composites were manufactured and characterised for physical, microstructural, mechanical and functional properties. The technique of heterocoagulation upon colloidal mixing was successfully applied to prepare composite powders. PLS provided ~99% dense BS glass specimens, while the densities of 2.5wt% to 10wt% MWCNTs-BS glass composites were found to range between ~97% and ~93%, respectively. A predominantly amorphous glass matrix was obtained with a homogeneous dispersion of MWCNTs up to 10wt%

(17vol%) without the formation of agglomerates. Although the large variation in the size of BS glass particles slightly impaired the MWCNT distribution quality when compared to the MWCNT-SiO_2 glass composites, the obtained dispersion results are still significantly better than available in literature [105]. Hardness and stiffness values decreased with MWCNT addition, i.e. ~58% and ~54%, respectively, in 10wt% MWCNT-BS glass composites, while a ~90% increase in the indentation fracture toughness was observed. In similarly loaded MWCNT-BS glass composites, the electrical conductivity increased >11 orders of magnitude, while thermal conductivity displayed a linear improvement up to ~80%. In short, the applicability of the developed MWCNT-SiO_2 glass composite model (Section 6.1) was successfully demonstrated on a commercial BS glass system. The approach developed for the model system should thus be relevant to other technically similar inorganic matrix composite systems and provide a route to produce composites containing uniformly dispersed CNTs, at relatively high loadings.

8. Conclusions and future work

8.1 Conclusions

Good quality MWCNTs were synthesised by injection catalytic chemical vapour deposition and subsequently acid-treated to improve their dispersion quality in order to be used as the nano-reinforcement in glass matrix composites. The detailed microstructural, thermal and dimensional characterisation of MWCNTs assisted in understanding their role in dictating the composite properties. During MWCNT synthesis, the catalyst particles were found at their base showing a base-growth mechanism. The round tip and gradually increasing base structure of MWCNTs was observed originating from the growing catalyst particles. MWCNTs showed a high crystallinity level although a variety of structural defects and impurities were also identified, along with the characteristic MWCNT hollow core. The acid-treatment effectively reduced the MWCNT impurities, significantly shortened their lengths and efficiently attached functional groups to their surfaces for better dispersion. However, the process also introduced oxidation debris on MWCNT surfaces, which increased surface roughness and reduced the crystallinity and thermal stability of MWCNTs. Surface roughness assisted in developing the mechanical interlocking between the MWCNTs and the matrix and resulted in a good bonding. In short, the acid-treatment provided purified, fragmented, and functionalised MWCNTs in different aspect ratios, for subsequent use in composite manufacturing.

A model MWCNT-SiO_2 glass composite system was successfully developed with different MWCNT aspect ratios (~31-65) and loadings (2.5-10wt%). It was shown that the colloidal processing by heterocoagulation provided homogeneous dispersion of MWCNTs in composite powders, which was retained even after densification. Pressureless sintering provided dense (96-99%) and essentially amorphous matrix composites without significant MWCNT degradation or graphitisation. A random orientation of MWCNTs was observed in the amorphous silica matrix without grain size or boundary effects. A mechanical MWCNT/glass interface was formed without any chemical reaction between the filler and the matrix, as evidenced by XRD and HRTEM. The physical attachment of MWCNTs was also ascribed to residual stresses developed after consolidation at high pressure and temperature, thus producing a good bonding.

The hardness and stiffness of composites decreased with the addition of MWCNTs by 21-38% and 20-37%, respectively. The lateral flexibility of MWCNTs and the absence of a strong (chemical) interface were the possible reasons for a decrease in hardness and stiffness of composites, respectively. It was found that the porosity due to MWCNT hollow core may also have contributed to decreased hardness and stiffness. In contrast, an increase in the indentation fracture toughness was noted by 100%, due to a good but weak interface. The toughening mechanisms due to the presence of MWCNTs are likely to be the crack-bridging, crack deflection and pullout, as observed by SEM/TEM.

The development of MWCNT percolating network tremendously increased the electrical conductivity of composites, as expected for randomly dispersed high aspect ratio MWCNTs. The thermal conductivity increased linearly but the magnitude of the effect was limited (~41-48%) due to the thermal resistance of a large interfacial surface area.

The effect of different MWCNT sizes on the mechanical properties of composites could not be identified due to the MWCNT effect on the composite density; an increase in the MWCNT aspect ratio inversely affected the densification of composites. As a result, higher aspect ratio MWCNT composites showed lower densities and hence lower mechanical properties. However, the functional properties reflected the opposite effect by providing increased values in composites containing higher aspect ratio MWCNTs.

Well-dispersed MWCNT-SiO_2 glass composites did not produce cracks due to the thermal shock (quenching in water) from 1200°C to 20°C or even after twenty cycles from 1000°C. However, heating at 1200°C for a single thermal shock cycle and at 1000°C for repeated cycles encouraged surface crystallisation, which produced cracking after cooling. Thermal ageing of composites was performed up to 1000°C for up to 96h; at 500°C, MWCNTs were partially oxidised from the specimen surfaces while increased ageing temperature and holding time showed a parabolic increase in the MWCNT oxidation of composites containing 2.5wt% MWCNTs. An increase in the MWCNT contents (5-10wt%) showed complete MWCNT oxidation, leaving behind nanoporous silica glass.

A continuous decrease in the friction coefficient of composites was observed with the increase in MWCNT contents, up to 10wt%. However, the wear rate increased with increasing MWCNT content until a stable graphitic layer was formed in 10wt% MWCNT-SiO_2 glass composites, which reversed the otherwise increasing trend.

After manufacturing the model MWCNT-SiO_2 glass composites, the developed powder processing and sintering skill was successfully applied to fabricate commercial borosilicate glass matrix composites containing MWCNTs, in order to confirm the suitability of this technology to other relevant inorganic matrices. The extent of mechanical and functional property improvement in MWCNT-BS glass composites was evaluated to further verify the already observed MWCNT influence in silica glass matrix in order to assess the true effect of the incorporation of MWCNTs in inorganic matrices. The consistent results of both the composite systems prove the reliability of the methods and conclusions.

8.2 Future work

CNTs produced by different techniques offer varying characteristics in their purity, crystallinity, straightness, diameter and aspect ratio; therefore, the optimum type, quality and size of the CNTs, for composite manufacturing, is still an open question. The selection of SWCNTs, DWCNTs or MWCNTs for reinforcement in inorganic matrices may have a strong influence on mechanical and functional properties, particularly on toughening mechanisms. The flexibility of CNTs and their high axial stiffness are contrasting characteristics. It remains to be seen whether thin flexible SWCNTs or comparatively stiff, straight MWCNTs are most effective as filler materials.

The interface in nanocomposites occupies a large surface area. It might be possible to develop *in-situ* interphases by the chemical reaction between CNTs and the surrounding matrix, which may provide better and adaptable mechanical properties by controlling the interface.

The effect of CNTs on the thermal shock properties of inorganic materials prone to thermal cracking, especially soda-lime-silica glasses, is another area of potential research. The coating of CNTs with high temperature resistant materials may provide oxidation-resistant filler for composites developed for high temperature applications. The process of developing a nanoporous glass after burning the incorporated CNTs may be used for certain applications where controlled nanoporosity is required, such as filters, catalyst supports, or sorbents. The recipe of producing porous glasses can also be applied to other ceramic matrices to develop porous materials. Moreover, increased CNT contents and different CNT sizes can provide the materials with tailorable porosity volume, type and morphology.

The wear and friction testing of the composite containing higher CNT contents (>10wt%) is another research area, as higher filler contents in glass matrix composites may provide even better friction/wear resistant materials.

In future, CNTs may also be used in combinations with other fillers to fabricate hybrid composites for desired properties. The combination of CNTs with conventional fibre reinforcements has already been demonstrated in polymer matrix systems [259].

Finally, “carbon” enjoys a special place as a raw material for the manufacturing of refractories [260] and high temperature ceramics (HTCs) [261-262]. The uniformly dispersed CNTs may, therefore, be utilized as a carbon source to develop and characterise a new class of refractories and HTCs [263], and novel ceramic nano-structures [264].

9. Appendix

Table 9.1: Experimental elastic modulus values of CNTs grown by high and low temperatures synthesis techniques.

CNTs type	Method	Elastic modulus (GPa)	Year (Ref)
MWCNTs*	Tension	270-950	2000 ([37])
MWCNTs*	Tension	620-1200	2007 ([38])
MWCNTs*	Tension	590-1105	2008 ([39])
MWCNTs*	Bending	~900	2002 ([265])
MWCNTs*	Bending	670-1100	1999 ([26])
MWCNTs*	Bending	1280±550	1997 ([266])
MWCNTs*	Bending	~1060	2006 ([267])
MWCNTs*	Bending	~3300	2006 ([268])
MWCNTs*	Compression	920-1550	2006 ([267])
MWCNTs*	Thermal vibration	420-4150	1996 ([269])
MWCNTs*	Electric vibration	100-1000	1999 ([32])
MWCNT ropes^	Tension	~450	2000 ([270])
MWCNT ropes^	Tension	450±230	1999 ([42])
MWCNTs^	Bending	12-50	1999 ([26])
MWCNTs^	Bending	350±110	2007 ([271])
MWCNTs^	Compression	~130	2011 ([28])
MWCNTs^	Electric vibration	23-32 2-3 (Highly defective)	2000 ([272])
MWCNTs^	Electric vibration	100-300 ~3 (Highly defective)	2005 ([27])
MWCNTs^	Bending	1-100	2005 ([29])
DWCNT Bundles^	Bending	10-1000	2005 ([33])
MWCNTs^	Electric vibration	393±201	2008 ([30])
MWCNTs^	Radial Shear	1.4±0.3	2007 ([271])
MWCNTs^	Shear/Electric vibration	0.1-0.8	2008 ([30])

SWCNTs	Thermal vibration	1250±450	1998 (22)
SWCNTs	Electric vibration	320-1470	2000 (24)
SWCNTs	Bending	67-1310	1999 (23)
SWCNTs^	Thermal vibration	~10	2003 (25)
SWCNT ropes	Radial Shear	0.7-6.5	1999 (23)

* High temperature (EAD and LAE) grown ^ Low temperature (CVD) grown

Table 9.2: Experimental fracture strength values of CNTs grown by high and low temperatures synthesis techniques.

CNTs type	Method	Strength (GPa)	Year (Ref)
SWCNTs	Tension	3.6-22.2	2000 (35)
SWCNTs	Tension	13-52	2000 (24)
SWCNTs	Tension	25-100	2010 (36)
SWCNT strands	Tension	~1.0	2002 (40)
DWCNT strands^	Tension	~1.2	2005 (41)
MWCNT ropes^	Tension	~1.7	1999 (42)
MWCNTs^	Compression	~2.0	2011 (28)
MWCNTs*	Tension	11-63	2000 (37)
MWCNTs*	Tension	10-66	2007 (38)
MWCNTs*	Tension	35-110	2008 (39)

* High temperature (EAD and LAE) grown ^ Low temperature (CVD) grown

10. References

1 H. W. Kroto, J. R. Heath, S. C. Obrien, R. F. Curl, and R. E. Smalley, "C-60 - buckminsterfullerene", Nature, 318 [6042] 162-63 (1985).

2 S. Iijima, "Helical microtubules of graphitic carbon", Nature, 354 [6348] 56-58 (1991).

3 L. V. Radushkevich and V. M. Lukyanovich, "O strukture ugleroda obrazujucegosja pri termiceskom razlozenii okisi ugleroda na zeleznom kontakte", Zurn Fisic Chim, 26 [1] 8 (1952).

4 C. P. Poole and F. J. Owens, "Introduction to nanotechnology", John Wiley, (2003).

5 M. Meyyappan, "Carbon nanotubes: science and applications", CRC Press, (2005).

6 M. Terrones, "Science and technology of the twenty-first century: synthesis, properties and applications of carbon nanotubes", Annual Review of Materials Research, 33 [1] 419-501 (2003).

7 T. W. Ebbesen, H. J. Lezec, H. Hiura, J. W. Bennett, H. F. Ghaemi, and T. Thio, "Electrical conductivity of individual carbon nanotubes", Nature, 382 [6586] 54-56 (1996).

8 M. S. P. Shaffer and J. Sandler, "Carbon nanotube/nanofibre polymer composites", in "Processing and properties of nanocomposites", World Scientific Publishing, (2007).

9 M. Wilson, K. Kannangara, G. Smith, M. Simmons, and B. Raguse, "Nanotechnology: basic science and emerging technologies", Chapman and Hall / CRC, (2002).

10 M. S. Dresselhaus, "Nanotubes - burn and interrogate", Science, 292 [5517] 650-51 (2001).

11 P. M. Ajayan, P. Redlich, and M. Ruhle, "Balance of graphite deposition and multishell carbon nanotube growth in the carbon arc discharge", Journal of Materials Research, 12 [1] 244-52 (1997).

12 E. G. Gamaly and T. W. Ebbesen, "Mechanism of carbon nanotube formation in the arc-discharge", Physical Review B, 52 [3] 2083-89 (1995).

13 T. Guo, P. Nikolaev, A. Thess, D. T. Colbert, and R. E. Smalley, "Catalytic growth of single-walled nanotubes by laser vaporization", Chemical Physics Letters, 243 [1-2] 49-54 (1995).

14 Z. F. Ren, Z. P. Huang, J. W. Xu, J. H. Wang, P. Bush, M. P. Siegal, and P. N. Provencio, "Synthesis of large arrays of well-aligned carbon nanotubes on glass", Science, 282 [5391] 1105-07 (1998).

15 J. Kong, H. T. Soh, A. M. Cassell, C. F. Quate, and H. J. Dai, "Synthesis of individual single-walled carbon nanotubes on patterned silicon wafers", Nature, 395 [6705] 878-81 (1998).

16 Z. W. Pan, S. S. Xie, B. H. Chang, C. Y. Wang, L. Lu, W. Liu, M. Y. Zhou, and W. Z. Li, "Very long carbon nanotubes", Nature, 394 [6694] 631-32 (1998).

17 E. Dervishi, Z. R. Li, Y. Xu, V. Saini, A. R. Biris, D. Lupu, and A. S. Biris, "Carbon nanotubes: synthesis, properties, and applications", Particulate Science and Technology, 27 [2] 107-25 (2009).

18 S. Hofmann, C. Ducati, J. Robertson, and B. Kleinsorge, "Low-temperature growth of carbon nanotubes by plasma-enhanced chemical vapor deposition", Applied Physics Letters, 83 [1] 135-37 (2003).

19 E. Raymundo-Pinero, A. Cazorla-Amoros, S. Delpeux, E. Frackowiak, K. Szostak, and F. Beguin, "High surface area carbon nanotubes prepared by chemical activation", Carbon, 40 [9] 1614-17 (2002).

20 B. T. Kelly, "Physics of graphite", Applied Science Publishers, (1981).

21 G. Overney, W. Zhong, and D. Tomanek, "Structural rigidity and low-frequency vibrational-modes of long carbon tubules", Zeitschrift Fur Physik D - Atoms Molecules and Clusters, 27 [1] 93-96 (1993).

22 A. Krishnan, E. Dujardin, T. W. Ebbesen, P. N. Yianilos, and M. M. J. Treacy, "Young's modulus of single-walled nanotubes", Physical Review B, 58 [20] 14013-19 (1998).

23 J. P. Salvetat, G. A. D. Briggs, J. M. Bonard, R. R. Bacsa, A. J. Kulik, T. Stockli, N. A. Burnham, and L. Forro, "Elastic and shear moduli of single-walled carbon nanotube ropes", Physical Review Letters, 82 [5] 944-47 (1999).

24 M. F. Yu, B. S. Files, S. Arepalli, and R. S. Ruoff, "Tensile loading of ropes of single wall carbon nanotubes and their mechanical properties", Physical Review Letters, 84 [24] 5552-55 (2000).

25 B. Babic, J. Furer, S. Sahoo, S. Farhangfar, and C. Schonenberger, "Intrinsic thermal vibrations of suspended doubly clamped single-wall carbon nanotubes", Nano Letters, 3 [11] 1577-80 (2003).

26 J. P. Salvetat, A. J. Kulik, J. M. Bonard, G. A. D. Briggs, T. Stockli, K. Metenier, S. Bonnamy, F. Beguin, N. A. Burnham, and L. Forro, "Elastic modulus of ordered and disordered multiwalled carbon nanotubes", Advanced Materials, 11 [2] 161-65 (1999).

27 J. Gaillard, M. Skove, and A. M. Rao, "Mechanical properties of chemical vapor deposition-grown multiwalled carbon nanotubes", Applied Physics Letters, 86 [23] 233109-3 (2005).

28 J. O. Zhao, M. R. He, S. Dai, J. Q. Huang, F. Wei, and J. Zhu, "TEM observations of buckling and fracture modes for compressed thick multiwall carbon nanotubes", Carbon, 49 [1] 206-13 (2011).

29 B. Lukic, J. W. Seo, E. Couteau, K. Lee, S. Gradecak, R. Berkecz, K. Hernadi, S. Delpeux, T. Cacciaguerra, F. Beguin, A. Fonseca, J. B. Nagy, G. Csanyi, A. Kis, A. J. Kulik, and L. Forro, "Elastic modulus of multi-walled carbon nanotubes produced by catalytic chemical vapour deposition", Applied Physics A - Materials Science and Processing, 80 [4] 695-700 (2005).

30 X. L. Wei, Y. Liu, Q. Chen, M. S. Wang, and L. M. Peng, "The very low shear modulus of multi-walled carbon nanotubes determined simultaneously with the axial Young's modulus via in situ experiments", Advanced Functional Materials, 18 [10] 1555-62 (2008).

31 N. Yao and V. Lordi, "Young's modulus of single-walled carbon nanotubes", Journal of Applied Physics, 84 [4] 1939-43 (1998).

32 P. Poncharal, Z. L. Wang, D. Ugarte, and W. A. de Heer, "Electrostatic deflections and electromechanical resonances of carbon nanotubes", Science, 283 [5407] 1513-16 (1999).

33 B. Lukic, J. W. Seo, R. R. Bacsa, S. Delpeux, F. Beguin, G. Bister, A. Fonseca, J. B. Nagy, A. Kis, S. Jeney, A. J. Kulik, and L. Forro, "Catalytically grown carbon nanotubes of small diameter have a high Young's modulus", Nano Letters, 5 [10] 2074-77 (2005).

34 J. Zhao and J. Zhu, "Electron microscopy and in situ testing of mechanical deformation of carbon nanotubes", Micron, 42 [7] 663-79 (2011).

35 F. Li, H. M. Cheng, S. Bai, G. Su, and M. S. Dresselhaus, "Tensile strength of single-walled carbon nanotubes directly measured from their macroscopic ropes", Applied Physics Letters, 77 [20] 3161-63 (2000).

36 M. S. Wang, D. Golberg, and Y. Bando, "Tensile tests on individual single-walled carbon nanotubes: linking nanotube strength with its defects", Advanced Materials, 22 [36] 4071-75 (2010).

37 M. F. Yu, O. Lourie, M. J. Dyer, K. Moloni, T. F. Kelly, and R. S. Ruoff, "Strength and breaking mechanism of multiwalled carbon nanotubes under tensile load", Science, 287 [5453] 637-40 (2000).

38 W. Ding, L. Calabri, K. M. Kohlhaas, X. Chen, D. A. Dikin, and R. S. Ruoff, "Modulus, fracture strength, and brittle versus plastic response of the outer shell of arc-grown multi-walled carbon nanotubes", Experimental Mechanics, 47 [1] 25-36 (2007).

39 B. Peng, M. Locascio, P. Zapol, S. Y. Li, S. L. Mielke, G. C. Schatz, and H. D. Espinosa, "Measurements of near-ultimate strength for multiwalled carbon nanotubes and irradiation-induced crosslinking improvements", Nature Nanotechnology, 3 [10] 626-31 (2008).

40 H. W. Zhu, C. L. Xu, D. H. Wu, B. Q. Wei, R. Vajtai, and P. M. Ajayan, "Direct synthesis of long single-walled carbon nanotube strands", Science, 296 [5569] 884-86 (2002).

41 Y. J. Li, K. L. Wang, J. Q. Wei, Z. Y. Gu, Z. C. Wang, J. B. Luo, and D. H. Wu, "Tensile properties of long aligned double-walled carbon nanotube strands", Carbon, 43 [1] 31-35 (2005).

42 Z. W. Pan, S. S. Xie, L. Lu, B. H. Chang, L. F. Sun, W. Y. Zhou, G. Wang, and D. L. Zhang, "Tensile tests of ropes of very long aligned multiwall carbon nanotubes", Applied Physics Letters, 74 [21] 3152-54 (1999).

43 H. Shima, "Buckling of carbon nanotubes: a state of the art review", Materials, 5 [1] 47-84 (2012).

44 M. B. Nardelli, B. I. Yakobson, and J. Bernholc, "Mechanism of strain release in carbon nanotubes", Physical Review B, 57 [8] R4277-R80 (1998).

45 J. Y. Huang, S. Chen, Z. Q. Wang, K. Kempa, Y. M. Wang, S. H. Jo, G. Chen, M. S. Dresselhaus, and Z. F. Ren, "Superplastic carbon nanotubes - conditions have been discovered that allow extensive deformation of rigid single-walled nanotubes", Nature, 439 [7074] 281-81 (2006).

46 S. Iijima, C. Brabec, A. Maiti, and J. Bernholc, "Structural flexibility of carbon nanotubes", Journal of Chemical Physics, 104 [5] 2089-92 (1996).

47 J. F. Despres, E. Daguerre, and K. Lafdi, "Flexibility of graphene layers in carbon nanotubes", Carbon, 33 [1] 87-89 (1995).

48 M. R. Falvo, G. J. Clary, R. M. Taylor, V. Chi, F. P. Brooks, S. Washburn, and R. Superfine, "Bending and buckling of carbon nanotubes under large strain", Nature, 389 [6651] 582-84 (1997).

49 H. Y. Liang and M. Upmanyu, "Axial-strain-induced torsion in single-walled carbon nanotubes", Physical Review Letters, 96 [16] (2006).

50 M. F. Yu, T. Kowalewski, and R. S. Ruoff, "Investigation of the radial deformability of individual carbon nanotubes under controlled indentation force", Physical Review Letters, 85 [7] 1456-59 (2000).

51 S. J. Tans, M. H. Devoret, H. J. Dai, A. Thess, R. E. Smalley, L. J. Geerligs, and C. Dekker, "Individual single-wall carbon nanotubes as quantum wires", Nature, 386 [6624] 474-77 (1997).

52 A. D. Bozhko, D. E. Sklovsky, V. A. Nalimova, A. G. Rinzler, R. E. Smalley, and J. E. Fischer, "Resistance versus pressure of single-wall carbon nanotubes", Applied Physics A - Materials Science and Processing, 67 [1] 75-77 (1998).

53 J. E. Fischer, H. Dai, A. Thess, R. Lee, N. M. Hanjani, D. L. Dehaas, and R. E. Smalley, "Metallic resistivity in crystalline ropes of single-wall carbon nanotubes", Physical Review B, 55 [8] R4921-R24 (1997).

54 G. T. Kim, E. S. Choi, D. C. Kim, D. S. Suh, Y. W. Park, K. Liu, G. Duesberg, and S. Roth, "Magnetoresistance of an entangled single-wall carbon-nanotube network", Physical Review B, 58 [24] 16064-69 (1998).

55 J. C. Charlier and J. P. Issi, "Electrical conductivity of novel forms of carbon", 8th International Symposium on Intercalation Compounds, (1995).

56 J. O. Lee, C. Park, J. J. Kim, J. Kim, J. W. Park, and K. H. Yoo, "Formation of low-resistance ohmic contacts between carbon nanotube and metal electrodes by a rapid thermal annealing method", Journal of Physics D - Applied Physics, 33 [16] 1953-56 (2000).

57 O. Breuer and U. Sundararaj, "Big returns from small fibers: a review of polymer/carbon nanotube composites", Polymer Composites, 25 [6] 630-45 (2004).

58 H. J. Dai, E. W. Wong, and C. M. Lieber, "Probing electrical transport in nanomaterials: conductivity of individual carbon nanotubes", Science, 272 [5261] 523-26 (1996).

59 M. Ouyang, J. L. Huang, and C. M. Lieber, "Fundamental electronic properties and applications of single-walled carbon nanotubes", Accounts of Chemical Research, 35 [12] 1018-25 (2002).

60 B. Q. Wei, R. Vajtai, and P. M. Ajayan, "Reliability and current carrying capacity of carbon nanotubes", Applied Physics Letters, 79 [8] 1172-74 (2001).

61 J. Hone, M. Whitney, and A. Zettl, "Thermal conductivity of single-walled carbon nanotubes", International Conference on Science and Technology of Synthetic Metals, (1998).

62 J. W. Che, T. Cagin, and W. A. Goddard, "Thermal conductivity of carbon nanotubes", 7th Annual Foresight Conference on Molecular Nanotechnology, (1999).

63 S. Berber, Y. K. Kwon, and D. Tomanek, "Unusually high thermal conductivity of carbon nanotubes", Physical Review Letters, 84 [20] 4613-16 (2000).

64 J. Hone, M. C. Llaguno, N. M. Nemes, A. T. Johnson, J. E. Fischer, D. A. Walters, M. J. Casavant, J. Schmidt, and R. E. Smalley, "Electrical and thermal transport properties of magnetically aligned single wall carbon nanotube films", Applied Physics Letters, 77 [5] 666-68 (2000).

65 R. Q. Pan, "Diameter and temperature dependence of thermal conductivity of single walled carbon nanotubes", Chinese Physics Letters, 28 [6] (2011).

66 P. Kim, L. Shi, A. Majumdar, and P. L. McEuen, "Thermal transport measurements of individual multiwalled nanotubes", Physical Review Letters, 87 [21] 215502 (2001).

67 W. Yi, L. Lu, D. L. Zhang, Z. W. Pan, and S. S. Xie, "Linear specific heat of carbon nanotubes", Physical Review B, 59 [14] R9015-R18 (1999).

68 D. J. Yang, Q. Zhang, G. Chen, S. F. Yoon, J. Ahn, S. G. Wang, Q. Zhou, Q. Wang, and J. Q. Li, "Thermal conductivity of multiwalled carbon nanotubes", Physical Review B, 66 [16] (2002).

69 H. L. Zhang, J. F. Li, K. F. Yao, and L. D. Chen, "Spark plasma sintering and thermal conductivity of carbon nanotube bulk materials", Journal of Applied Physics, 97 [11] (2005).

70 J. M. Schnorr and T. M. Swager, "Emerging applications of carbon nanotubes", Chemistry of Materials, 23 [3] 646-57 (2011).

71 T. Nishino, S. Kanata, and Y. Umezawa, "Selective visualization of point defects in carbon nanotubes at the atomic scale by an electron-donating molecular tip", Chemical Communications, 47 [26] 7467-69 (2011).

72 S. R. Bakshi, D. Lahiri, and A. Agarwal, "Carbon nanotube reinforced metal matrix composites - a review", International Materials Reviews, 55 [1] 41-64 (2010).

[73] J. Cho, A. R. Boccaccini, and M. S. P. Shaffer, "Ceramic matrix composites containing carbon nanotubes", Journal of Materials Science, 44 [8] 1934-51 (2009).

[74] K. K. Chawla, "Ceramic matrix composites", Kluwer Academic Publishers, (2003).

[75] H. G. Pfaender, "Schott guide to glass", Van Nostrand Reinhold Company, (1983).

[76] F. L. Matthews and R. D. Rawlings, "Composite materials: engineering and science", Woodhead Publishing, (1999).

[77] M.Bengisu, "Engineering Ceramics", Springer, (2001).

[78] M. Sternitzke, "Structural ceramic nanocomposites", Journal of the European Ceramic Society, 17 [9] 1061-82 (1997).

[79] S. Y. Fu and B. Lauke, "The fibre pull-out energy of misaligned short fibre composites", Journal of Materials Science, 32 [8] 1985-93 (1997).

[80] A. G. Evans and F. W. Zok, "The physics and mechanics of fiber-reinforced brittle-matrix composites", Journal of Materials Science, 29 [15] 3857-96 (1994).

[81] A. R. Boccaccini, "Glass and glass ceramic matrix composite materials: a review", Interceram, 51 [1] 24-34 (2002).

[82] I. Crivelli-Visconti and G. A. Cooper, "Mechanical properties of a new carbon fibre material", Nature, 221 [5182] 754-55 (1969).

[83] R. A. J. Sambell, A. Briggs, D. C. Phillips, and D. H. Bowen, "Carbon fibre composites with ceramic and glass matrices. Part 2: continuous fibres", Journal of Materials Science, 7 [6] 676-81 (1972).

[84] R. A. J. Sambell, D. C. Phillips, and D. H. Bowen, "Carbon fiber composites with ceramic and glass matrices. Part 1: discontinuous fibers", Journal of Materials Science, 7 [6] 663-75 (1972).

[85] J. Aveston, "Strength and toughness in fibre reinforced ceramics", Conference on Properties of Fiber Composites, (1971).

[86] N. P. Bansal, "Mechanical behavior of silicon carbide fiber-reinforced strontium aluminosilicate glass-ceramic composites", Materials Science and Engineering A - Structural Materials Properties Microstructure and Processing, 231 [1-2] 117-27 (1997).

[87] K. M. Prewo and J. J. Brennan, "High strength silicon carbide fiber-reinforced glass-matrix composites", Journal of Materials Science, 15 [2] 463-68 (1980).

[88] K. M. Prewo and J. J. Brennan, "Silicon carbide yarn reinforced glass matrix composites", Journal of Materials Science, 17 [4] 1201-06 (1982).

[89] J. J. Brennan and K. M. Prewo, "Silicon carbide fiber reinforced glass-ceramic matrix composites exhibiting high-strength and toughness", Journal of Materials Science, 17 [8] 2371-83 (1982).

90 G. Otieno, A. A. Koos, F. Dillon, A. Wallwork, N. Grobert, and R. I. Todd, "Processing and properties of aligned multi-walled carbon nanotube/aluminoborosilicate glass composites made by sol-gel processing", Carbon, 48 [8] 2212-17 (2010).

91 J. Cho, F. Inam, M. J. Reece, Z. Chlup, I. Dlouhy, M. S. P. Shaffer, and A. R. Boccaccini, "Carbon nanotubes: do they toughen brittle matrices?", Journal of Materials Science, 46 [14] 4770-79 (2011).

92 C. B. Mo, S. I. Cha, K. T. Kim, K. H. Lee, and S. H. Hong, "Fabrication of carbon nanotube reinforced alumina matrix nanocomposite by sol-gel process", Materials Science and Engineering A - Structural Materials Properties Microstructure and Processing, 395 [1-2] 124-28 (2005).

93 J. Sun and L. Gao, "Development of a dispersion process for carbon nanotubes in ceramic matrix by heterocoagulation", Carbon, 41 [5] 1063-68 (2003).

94 S. L. Shi and J. Liang, "Effect of multiwall carbon nanotubes on electrical and dielectric properties of yttria-stabilized zirconia ceramic", Journal of the American Ceramic Society, 89 [11] 3533-35 (2006).

95 E. Flahaut, A. Peigney, C. Laurent, C. Marliere, F. Chastel, and A. Rousset, "Carbon nanotube-metal-oxide nanocomposites: microstructure, electrical conductivity and mechanical properties", Acta Materialia, 48 [14] 3803-12 (2000).

96 X. P. Huang, C. X. Pan, and X. T. Huang, "Preparation and characterization of gamma-MnO_2/CNTs nanocomposite", Materials Letters, 61 [4-5] 934-36 (2007).

97 S. Rul, F. Lefevre-schlick, E. Capria, C. Laurent, and A. Peigney, "Percolation of single-walled carbon nanotubes in ceramic matrix nanocomposites", Acta Materialia, 52 [4] 1061-67 (2004).

98 A. Peigney, S. Rul, F. Lefevre-Schlick, and C. Laurent, "Densification during hot-pressing of carbon nanotube-metal-magnesium aluminate spinel nanocomposites", Journal of the European Ceramic Society, 27 [5] 2183-93 (2007).

99 Q. Huang and L. Gao, "Manufacture and electrical properties of multiwalled carbon nanotube/$BaTiO_3$ nanocomposite ceramics", Journal of Materials Chemistry, 14 [16] 2536-41 (2004).

100 C. Balazsi, Z. Konya, F. Weber, L. P. Biro, and P. Arato, "Preparation and characterization of carbon nanotube reinforced silicon nitride composites", Materials Science and Engineering C - Biomimetic and Supramolecular Systems, 23 [6-8] 1133-37 (2003).

101 Y. Katsuda, P. Gerstel, J. Narayanan, J. Bill, and F. Aldinger, "Reinforcement of precursor-derived Si-C-N ceramics with carbon nanotubes", Journal of the European Ceramic Society, 26 [15] 3399-405 (2006).

102 L. Q. Jiang and L. Gao, "Carbon nanotubes-metal nitride composites: a new class of nanocomposites with enhanced electrical properties", Journal of Materials Chemistry, 15 [2] 260-66 (2005).

103 E. T. Thostenson, P. G. Karandikar, and T. W. Chou, "Fabrication and characterization of reaction bonded silicon carbide/carbon nanotube composites", Journal of Physics D - Applied Physics, 38 [21] 3962-65 (2005).

104 X. L. Shi, H. Yang, S. Wang, G. Q. Shao, and X. L. Duan, "Fabrication and properties of WC-10Co cemented carbide reinforced by multi-walled carbon nanotubes", Materials Science and Engineering A - Structural Materials Properties Microstructure and Processing, 486 [1-2] 489-95 (2008).

105 A. R. Boccaccini, D. R. Acevedo, G. Brusatin, and P. Colombo, "Borosilicate glass matrix composites containing multi-wall carbon nanotubes", Journal of the European Ceramic Society, 25 [9] 1515-23 (2005).

106 B. J. C. Thomas, M. S. P. Shaffer, and A. R. Boccaccini, "Sol-gel route to carbon nanotube borosilicate glass composites", Composites. Part A - Applied Science and Manufacturing, 40 [6-7] 837-45 (2009).

107 J. Wang, H. M. Kou, X. J. Liu, Y. B. Pan, and J. K. Guo, "Reinforcement of mullite matrix with multi-walled carbon nanotubes", Ceramics International, 33 [5] 719-22 (2007).

108 F. Ye, L. M. Liu, Y. J. Wang, Y. Zhou, B. Peng, and Q. C. Meng, "Preparation and mechanical properties of carbon nanotube reinforced barium aluminosilicate glass-ceramic composites", Scripta Materialia, 55 [10] 911-14 (2006).

109 A. Mukhopadhyay, B. T. T. Chu, M. L. H. Green, and R. I. Todd, "Understanding the mechanical reinforcement of uniformly dispersed multiwalled carbon nanotubes in alumino-borosilicate glass ceramic", Acta Materialia, 58 [7] 2685-97 (2010).

110 R. Giovanardi, M. Montorsi, G. Ori, J. Cho, T. Subhani, A. R. Boccaccini, and C. Siligardi, "Microstructural characterisation and electrical properties of multiwalled carbon nanotubes/glass-ceramic nanocomposites", Journal of Materials Chemistry, 20 [2] 308-13 (2010).

111 A. R. Boccaccini, B. J. C. Thomas, G. Brusatin, and P. Colombo, "Mechanical and electrical properties of hot-pressed borosilicate glass matrix composites containing multi-wall carbon nanotubes", Journal of Materials Science, 42 [6] 2030-36 (2007).

112 A. Peigney, C. Laurent, O. Dumortier, and A. Rousset, "Carbon nanotubes Fe alumina nanocomposites. Part I: influence of the Fe content on the synthesis of powders", Journal of the European Ceramic Society, 18 [14] 1995-2004 (1998).

113 J. W. Ning, J. J. Zhang, Y. B. Pan, and J. K. Guo, "Fabrication and mechanical properties of SiO_2 matrix composites reinforced by carbon nanotube", Materials Science and

Engineering A - Structural Materials Properties Microstructure and Processing, 357 [1-2] 392-96 (2003).

114 G. D. Zhan, J. D. Kuntz, J. L. Wan, and A. K. Mukherjee, "Single-wall carbon nanotubes as attractive toughening agents in alumina-based nanocomposites", Nature Materials, 2 [1] 38-42 (2003).

115 C. Balazsi, K. Konya, F. Weber, L. P. Biro, and P. Arato, "Preparation and characterization of carbon nanotube reinforced silicon nitride composites", Symposium on Current Trends in Nanoscience: From Materials to Application, (2003).

116 M. J. de Andrade, M. D. Lima, L. Stein, C. P. Bergmann, and S. Roth, "Single-walled carbon nanotube silica composites obtained by an inorganic sol-gel route", Physica Status Solidi B - Basic Solid State Physics, 244 [11] 4218-22 (2007).

117 J. W. Ning, J. J. Zhang, Y. B. Pan, and J. K. Guo, "Fabrication and thermal property of carbon nanotube/SiO_2 composites", Journal of Materials Science Letters, 22 [14] 1019-21 (2003).

118 J. W. Ning, J. J. Zhang, Y. B. Pan, and J. K. Guo, "Surfactants assisted processing of carbon nanotube-reinforced SiO_2 matrix composites", Ceramics International, 30 [1] 63-67 (2004).

119 K. Babooram and R. Narain, "Fabrication of SWNT/silica composites by the sol-gel process", ACS Applied Materials and Interfaces, 1 [1] 181-86 (2009).

120 B. T. T. Chu, G. Tobias, C. G. Salzmann, B. Ballesteros, N. Grobert, R. I. Todd, and M. L. H. Green, "Fabrication of carbon-nanotube-reinforced glass-ceramic nanocomposites by ultrasonic in situ sol-gel processing", Journal of Materials Chemistry, 18 [44] 5344-49 (2008).

121 M. J. de Andrede, M. D. Lima, C. P. Bergmann, G. D. Ramminger, N. M. Balzaretti, T. M. H. Costa, and M. R. Gallas, "Carbon nanotube/silica composites obtained by sol-gel and high-pressure techniques", Nanotechnology, 19 [26] 1-7 (2008).

122 M. J. de Andrade, A. Weibel, C. Laurent, S. Roth, C. P. Bergmann, C. Estournes, and A. Peigney, "Electrical conductive double-walled carbon nanotubes - silica glass nanocomposites prepared by the sol-gel process and spark plasma sintering", Scripta Materialia, 61 [10] 988-91 (2009).

123 T. Seeger, P. Redlich, N. Grobert, M. Terrones, D. R. M. Walton, H. W. Kroto, and M. Ruhle, "SiO_x-coating of carbon nanotubes at room temperature", Chemical Physics Letters, 339 [1-2] 41-46 (2001).

124 T. Seeger, T. Kohler, T. Frauenheim, N. Grobert, M. Ruhle, M. Terrones, and G. Seifert, "Nanotube composites: novel SiO_2 coated carbon nanotubes", Chemical Communications [1] 34-35 (2002).

125 T. Seeger, G. de la Fuente, W. K. Maser, A. M. Benito, M. A. Callejas, and M. T. Martinez, "Evolution of multiwalled carbon-nanotube/SiO_2 composites via laser treatment", Nanotechnology, 14 [2] 184-87 (2003).

126 V. G. Gavalas, R. Andrews, D. Bhattacharyya, and L. G. Bachas, "Carbon nanotube sol-gel composite materials", Nano Letters, 1 [12] 719-21 (2001).

127 K. Hernadi, E. Ljubovic, J. W. Seo, and L. Forro, "Synthesis of MWNT-based composite materials with inorganic coating", Acta Materialia, 51 [5] 1447-52 (2003).

128 L. Berguiga, J. Bellessa, F. Vocanson, E. Bernstein, and J. C. Plenet, "Carbon nanotube silica glass composites in thin films by the sol-gel technique", Optical Materials, 28 [3] 167-71 (2006).

129 J. DiMaio, S. Rhyne, J. Ballato, R. Czerw, J. Xu, S. Webster, D. L. Carroll, K. Fu, and Y. P. Sun, "Transparent silica glasses containing single walled carbon nanotubes", Conference on Inorganic Optical Materials III, (2001).

130 H. B. Zhan, W. Z. Chen, M. Q. Wang, Zhengchan, and C. L. Zou, "Optical limiting effects of multi-walled carbon nanotubes suspension and silica xerogel composite", Chemical Physics Letters, 382 [3-4] 313-17 (2003).

131 Y. J. Zhang, Y. F. Shen, D. X. Han, Z. J. Wang, J. X. Song, and L. Niu, "Reinforcement of silica with single-walled carbon nanotubes through covalent functionalization", Journal of Materials Chemistry, 16 [47] 4592-97 (2006).

132 C. Zheng, M. Feng, X. Zhen, J. Huang, and H. B. Zhan, "Effect of doping levels on the pore structure of carbon nanotube/silica xerogel composites", Materials Letters, 61 [3] 644-47 (2007).

133 C. Zheng, M. Feng, X. Zhen, J. Huang, and H. B. Zhan, "Materials investigation of multi-walled carbon nanotubes doped silica gel glass composites", Journal of Non-Crystalline Solids, 354 [12-13] 1327-30 (2008).

134 H. Xu, Y. B. Pan, Y. Zhu, H. M. Kou, and J. K. Guo, "Transparent multi-walled carbon nanotube-silica composite prepared by hot-pressed sintering and its nonlinear optical properties", Journal of Alloys and Compounds, 481 [1-2] L4-L7 (2009).

135 H. B. Zhan, C. Zheng, W. Z. Chen, and M. Q. Wang, "Characterization and nonlinear optical property of a multi-walled carbon nanotube/silica xerogel composite", Chemical Physics Letters, 411 [4-6] 373-77 (2005).

136 C. S. Xiang, Y. B. Pan, X. J. Liu, X. W. Sun, X. M. Shi, and J. K. Guo, "Microwave attenuation of multiwalled carbon nanotube-fused silica composites", Applied Physics Letters, 87 [12] (2005).

137 C. S. Xiang, Y. Pan, and J. K. Guo, "Electromagnetic interference shielding effectiveness of multiwalled carbon nanotube reinforced fused silica composites", Ceramics International, 33 [7] 1293-97 (2007).

138 S. Loo, S. Idapalapati, S. Wang, L. Shen, and S. G. Mhaisalkar, "Effect of surfactants on MWCNT-reinforced sol-gel silica dielectric composites", Scripta Materialia, 57 [12] 1157-60 (2007).

139 A. J. Lopez, A. Urena, and J. Rams, "Fabrication of novel sol-gel silica coatings reinforced with multi-walled carbon nanotubes", Materials Letters, 64 [8] 924-27 (2010).

140 M. Vila, J. L. Hueso, M. Manzano, I. Izquierdo-Barba, A. de Andres, J. Sanchez-Marcos, C. Prieto, and M. Vallet-Regi, "Carbon nanotubes-mesoporous silica composites as controllable biomaterials", Journal of Materials Chemistry, 19 [41] 7745-52 (2009).

141 J. Sun, L. Gao, and W. Li, "Colloidal processing of carbon nanotube/alumina composites", Chemistry of Materials, 14 [12] 5169-72 (2002).

142 J. Sun, M. Iwasa, L. Gao, and Q. H. Zhang, "Single-walled carbon nanotubes coated with titania nanoparticles", Carbon, 42 [4] 895-99 (2004).

143 C. Balazsi, B. Fenyi, N. Hegman, Z. Kover, F. Weber, Z. Vertesy, Z. Konya, I. Kiricsi, L. P. Biro, and P. Arato, "Development of CNT/Si_3N_4 composites with improved mechanical and electrical properties", Composites. Part B - Engineering, 37 [6] 418-24 (2006).

144 S. Q. Guo, R. Sivakumar, and Y. Kagawa, "Multiwall carbon nanotube-SiO_2 nanocomposites: sintering, elastic properties, and fracture toughness", Advanced Engineering Materials, 9 [1-2] 84-87 (2007).

145 S. Q. Guo, R. Sivakumar, H. Kitazawa, and Y. Kagawa, "Electrical properties of silica-based nanocomposites with multiwall carbon nanotubes", Journal of the American Ceramic Society, 90 [5] 1667-70 (2007).

146 R. Sivakumar, S. Q. Guo, T. Nishimura, and Y. Kagawa, "Thermal conductivity in multi-wall carbon nanotube/silica-based nanocomposites", Scripta Materialia, 56 [4] 265-68 (2007).

147 C. Arvanitelis, D. D. Jayaseelan, J. Cho, and A. R. Boccaccini, "Carbon nanotube-SiO_2 composites by colloidal processing", Advances in Applied Ceramics, 107 [3] 155-58 (2008).

148 M. S. P. Shaffer, X. Fan, and A. H. Windle, "Dispersion and packing of carbon nanotubes", Carbon, 36 [11] 1603-12 (1998).

149 Y. Morisada, Y. Miyamoto, Y. Takaura, K. Hirota, and N. Tamari, "Mechanical properties of SiC composites incorporating SiC-coated multi-walled carbon nanotubes", International Journal of Refractory Metals and Hard Materials, 25 [4] 322-27 (2007).

150 L. Q. Jiang and L. Gao, "Fabrication and characterization of carbon nanotube-titanium nitride composites with enhanced electrical and electrochemical properties", Journal of the American Ceramic Society, 89 [1] 156-61 (2006).

151 Q. Huang and L. Gao, "Multiwalled carbon nanotube/$BaTiO_3$ nanocomposites: electrical and rectification properties", Applied Physics Letters, 86 [12] 3 (2005).

152 Z. Xia, W. A. Curtin, and B. W. Sheldon, "Fracture toughness of highly ordered carbon nanotube/alumina nanocomposites", Journal of Engineering Materials and Technology - Transactions of the ASME, 126 [3] 238-44 (2004).

153 A. Peigney, E. Flahaut, C. Laurent, F. Chastel, and A. Rousset, "Aligned carbon nanotubes in ceramic-matrix nanocomposites prepared by high-temperature extrusion", Chemical Physics Letters, 352 [1-2] 20-25 (2002).

154 M. H. Bocanegra-Bernal, J. Echeberria, J. Ollo, A. Garcia-Reyes, C. Dominguez-Rios, A. Reyes-Rojas, and A. Aguilar-Elguezabal, "A comparison of the effects of multi-wall and single-wall carbon nanotube additions on the properties of zirconia toughened alumina composites", Carbon, 49 [5] 1599-607 (2011).

155 J. Echeberria, J. Ollo, M. H. Bocanegra-Bernal, A. Garcia-Reyes, C. Dominguez-Rios, A. Aguilar-Elguezabal, and A. Reyes-Rojas, "Sinter and hot isostatic pressing (HIP) of multi-wall carbon nanotubes (MWCNTs) reinforced ZTA nanocomposite: microstructure and fracture toughness", International Journal of Refractory Metals and Hard Materials, 28 [3] 399-406 (2010).

156 S. C. Zhang, W. G. Fahrenholtz, G. E. Hilmas, and E. J. Yadlowsky, "Pressureless sintering of carbon nanotube-Al_2O_3 composites", Journal of the European Ceramic Society, 30 [6] 1373-80 (2010).

157 S. W. Kim, W. S. Chung, K. S. Sohn, C. Y. Son, and S. Lee, "Improvement of wear resistance in alumina matrix composites reinforced with carbon nanotubes", Metallurgical and Materials Transactions A - Physical Metallurgy and Materials Science, 41A [2] 380-88 (2010).

158 R. S. Dobedoe, G. D. West, and M. H. Lewis, "Spark plasma sintering of ceramics: understanding temperature distribution enables more realistic comparison with conventional processing", Advances in Applied Ceramics, 104 [3] 110-16 (2005).

159 J. Cho, "Processing and characterisation of inorganic matrix composites containing carbon nanotubes", PhD Thesis, Imperial College London, (2010).

160 D. S. Lim, D. H. You, H. J. Choi, S. H. Lim, and H. Jang, "Effect of CNT distribution on tribological behavior of alumina-CNT composites", 15th International Conference on Wear of Materials, (2005).

161 M. J. de Andrade, M. D. Lima, L. Stein, C. P. Bergmann, and S. Roth, "Single-walled carbon nanotube silica composites obtained by an inorganic sol-gel route", 21st International Winterschool on Electronic Properties of Novel Materials, (2007).

162 G. D. Quinn and R. C. Bradt, "On the Vickers indentation fracture toughness test", Journal of the American Ceramic Society, 90 [3] 673-80 (2007).

163 A. Mukhopadhyay, G. Otieno, B. T. T. Chu, A. Wallwork, M. L. H. Green, and R. I. Todd, "Thermal and electrical properties of aluminoborosilicate glass-ceramics containing multiwalled carbon nanotubes", Scripta Materialia, 65 [5] 408-11 (2011).

164 W. Bauhofer and J. Z. Kovacs, "A review and analysis of electrical percolation in carbon nanotube polymer composites", Composites Science and Technology, 69 [10] 1486-98 (2009).

165 W. E. Lee and W. M. Rainforth, "Ceramic microstuctures: property control by processing", Kluwer Academic Publishers, (1994).

166 M. Arnold, A. R. Boccaccini, and G. Ondracek, "Theoretical and experimental considerations on the thermal shock resistance of sintered glasses and ceramics using modelled microstructure-property correlations", Journal of Materials Science, 31 [2] 463-69 (1996).

167 A. R. Boccaccini, D. H. Pearce, J. Janczak, W. Beier, and C. B. Ponton, "Investigation of cyclic thermal shock behaviour of fibre reinforced glass matrix composites using non-destructive forced resonance technique", Materials Science and Technology, 13 [10] 852-58 (1997).

168 A. R. Boccaccini, K. Pfeiffer, and H. Kern, "Thermal shock resistant Al_2TiO_5-glass matrix composite", Journal of Materials Science Letters, 18 [23] 1907-09 (1999).

169 A. R. Boccaccini, A. J. Strutt, K. S. Vecchio, D. Mendoza, and K. K. Chawla, "Behavior of Nicalon (TM) fiber-reinforced glass-matrix composites under thermal cycling conditions", Composites. Part A - Applied Science and Manufacturing, 29 [11] 1343-52 (1998).

170 A. R. Boccaccini, R. Liebald, W. Beier, and K. K. Chawla, "Fabrication, mechanical properties and thermal stability of a novel glass matrix composite material reinforced by short oxycarbide fibres", Journal of Materials Science, 37 [20] 4379-84 (2002).

171 M. H. Chen, S. L. Zhu, M. L. Shen, F. H. Wang, and Y. Niu, "Effect of NiCrAlY platelets inclusion on the mechanical and thermal shock properties of glass matrix composites", Materials Science and Engineering A - Structural Materials Properties Microstructure and Processing, 528 [3] 1360-66 (2011).

172 D. P. H. Hasselman, "Thermal stress resistance of engineering ceramics", Materials Science and Engineering, 71 [0] 251-64 (1985).

173 A. R. Boccaccini, J. Janczak Rusch, and I. Dlouhy, "Thermal aging behavior of an SiC-fiber reinforced glass matrix composite in a non-oxidizing atmosphere", Materials Chemistry and Physics, 53 [2] 155-64 (1998).

174 I. Dlouhy, Z. Chlup, D. N. Boccaccini, S. Atiq, and A. R. Boccaccini, "Fracture behaviour of hybrid glass matrix composites: thermal ageing effects", Composites Part A - Applied Science and Manufacturing, 34 [11] 1177-85 (2003).

175 K. M. Prewo and J. A. Batt, "The oxidative stability of carbon-fiber reinforced glass-matrix composites", Journal of Materials Science, 23 [2] 523-27 (1988).

176 R. G. Iacocca and D. J. Duquette, "The effects of matrix microcracking on the oxidation behavior of carbon-fiber glass-matrix composites", Journal of Materials Science, 28 [17] 4749-61 (1993).

177 K. L. Page and D. J. Duquette, "The oxidation behaviour of carbon reinforced glass matrix composites", Ceramics International, 23 [3] 209-13 (1997).

178 G. Hackl, H. Gerhard, and N. Popovska, "Coating of carbon short fibers with thin ceramic layers by chemical vapor deposition", Thin Solid Films, 513 [1-2] 217-22 (2006).

179 X. K. Li, Z. J. Dong, A. Westwood, A. Brown, S. W. Zhang, R. Brydson, N. Li, and B. Rand, "Preparation of a titanium carbide coating on carbon fibre using a molten salt method", Carbon, 46 [2] 305-09 (2008).

180 A. Kovalcikova, T. Orsolya, C. Balazsi, and J. Dusza, "Indentation thermal shock resistance of Si_3N_4/CNT composites", Chemicke Listy, 105 [1] S824-S25 (2011).

181 R. H. Savage, "Graphite lubrication", Journal of Applied Physics, 19 [1] 1-7 (1948).

182 M. Mangalic, "Frictional behavior of commercial graphites", Carbon, 12 [5] 573-76 (1974).

183 E. Minford and K. Prewo, "Friction and wear of graphite-fiber-reinforced glass matrix composites", Wear, 102 [3] 253-64 (1985).

184 Z. Lu, K. Friedrich, W. Pannhorst, and J. Heinz, "Sliding wear of a unidirectional carbon fiber-reinforced glass composite against steel", Journal of Materials Science Letters, 12 [3] 173-75 (1993).

185 Z. Lu, K. Friedrich, W. Pannhorst, and J. Heinz, "Wear and friction of a unidirectional carbon-fiber glass matrix composite against various counterparts", Wear, 162 [2] 1103-13 (1993).

186 R. Reinicke, K. Friedrich, W. Beier, and R. Liebald, "Tribological properties of SiC and C-fiber reinforced glass matrix composites", Wear, 225 [2] 1315-21 (1999).

187 V. Bianchi, P. Fournier, F. Platon, and P. Reynaud, "Carbon fibre-reinforced (YMAS) glass-ceramic matrix composites: dry friction behaviour", Journal of the European Ceramic Society, 19 [5] 581-89 (1999).

188 J. M. McKittrick, N. S. Sridharan, and M. F. Amateau, "Wear behavior of graphite-fiber-reinforced glass", Wear, 96 [3] 285-99 (1984).

189 A. Skopp, M. Woydt, K. H. Habig, T. Klug, and R. Bruckner, "Friction and wear behavior of C-fiber-reinforced and SiC-fiber-reinforced glass composites against ceramic materials", Wear, 169 [2] 243-50 (1993).

190 G. Gevorkian, H. J. Schorcht, H. Kern, and A. R. Boccaccini, "Preliminary investigation of the wear behaviour of self-lubricating carbon fibre reinforced glass matrix composites in vacuum", Applied Composite Materials, 9 [3] 169-77 (2002).

191 A. Hirata and N. Yoshioka, "Sliding friction properties of carbon nanotube coatings deposited by microwave plasma chemical vapor deposition", Tribology International, 37 [11-12] 893-98 (2004).

192 A. K. Keshri, J. Huang, V. Singh, W. B. Choi, S. Seal, and A. Agarwal, "Synthesis of aluminum oxide coating with carbon nanotube reinforcement produced by chemical vapor deposition for improved fracture and wear resistance", Carbon, 48 [2] 431-42 (2010).

193 K. Balani, S. P. Harimkar, A. Keshri, Y. Chen, N. B. Dahotre, and A. Agarwal, "Multiscale wear of plasma-sprayed carbon-nanotube-reinforced aluminum oxide nanocomposite coating", Acta Materialia, 56 [20] 5984-94 (2008).

194 I. Ahmad, A. Kennedy, and Y. Q. Zhu, "Wear resistant properties of multi-walled carbon nanotubes reinforced Al_2O_3 nanocomposites", Wear, 269 [1-2] 71-78 (2010).

195 Z. H. Xia, J. Lou, and W. A. Curtin, "A multiscale experiment on the tribological behavior of aligned carbon nanotube/ceramic composites", Scripta Materialia, 58 [3] 223-26 (2008).

196 G. Yamamoto, M. Omori, K. Yokomizo, T. Hashida, and K. Adachi, "Structural characterization and frictional properties of carbon nanotube/alumina composites prepared by precursor method", Materials Science and Engineering B - Advanced Functional Solid State Materials, 148 [1-3] 265-69 (2008).

197 D. S. Lim, D. H. You, H. J. Choi, S. H. Lim, and H. Jang, "Effect of CNT distribution on tribological behavior of alumina-CNT composites", Wear, 259 [1-6] 539-44 (2005).

198 J. W. An, D. H. You, and D. S. Lim, "Tribological properties of hot-pressed alumina-CNT composites", Wear, 255 [1] 677-81 (2003).

199 J. Gonzalez-Julian, J. Schneider, P. Miranzo, M. I. Osendi, and M. Belmonte, "Enhanced tribological performance of silicon nitride-based materials by adding carbon nanotubes", Journal of the American Ceramic Society, 94 [8] 2542-48 (2011).

200 O. Koszor, A. Lindemann, F. Davin, and C. Balazsi, "Observation of thermophysical and tribological properties of CNT reinforced Si_3N_4", in "Fractography of Advanced Ceramics", Trans Tech Publications, (2009).

201 Q. M. Gong, Z. Li, Z. Y. Zhang, B. Wu, X. W. Zhou, Q. Z. Huang, and J. Liang, "Tribological properties of carbon nanotube-doped carbon/carbon composites", Tribology International, 39 [9] 937-44 (2006).

202 G. Yamamoto, T. Hashida, K. Adachi, and T. Takagj, "Tribological properties of single-walled carbon nanotube solids", Journal of Nanoscience and Nanotechnology, 8 [5] 2665-70 (2008).

203 B. Thomas, "Processing and characterisation of inorganic matrix composites containing carbon nanotubes", PhD Thesis, Imperial College London, (2007).

204 M. S. Dresselhaus, A. Jorio, and R. Saito, "Characterizing graphene, graphite, and carbon nanotubes by Raman spectroscopy", in "Condensed Matter Physics", Annual Reviews, (2010).

205 F. Tuinstra and J. L. Koenig, "Raman spectrum of graphite", Journal of Chemical Physics, 53 [3] 1126-30 (1970).

206 H. Hiura, T. W. Ebbesen, K. Tanigaki, and H. Takahashi, "Raman studies of carbon nanotubes", Chemical Physics Letters, 202 [6] 509-12 (1993).

207 R. M. Langford and C. Clinton, "In situ lift-out using a FIB-SEM system", Micron, 35 [7] 607-11 (2004).

208 J. B. Wachtman, "Mechanical properties of ceramics", John Wiley, (2008).

209 W. C. Oliver and G. M. Pharr, "An improved technique for determining hardness and elastic-modulus using load and displacament sensing indentation experiments", Journal of Materials Research, 7 [6] 1564-83 (1992).

210 W. C. Oliver and G. M. Pharr, "Measurement of hardness and elastic modulus by instrumented indentation: advances in understanding and refinements to methodology", Journal of Materials Research, 19 [1] 3-20 (2004).

211 G. R. Anstis, P. Chantikul, B. R. Lawn, and D. B. Marshall, "A critical evaluation of indentation techniques for measuring fracture toughness - 1: direct crack measurements", Journal of the American Ceramic Society, 64 [9] 533-38 (1981).

212 J. A. Roether, D. J. Daniel, D. A. Rani, D. E. Deegan, C. R. Cheeseman, and A. R. Boccaccini, "Properties of sintered glass-ceramics prepared from plasma vitrified air pollution control residues", Journal of Hazardous Materials, 173 [1-3] 563-69 (2010).

213 J. K. W. Sandler, J. E. Kirk, I. A. Kinloch, M. S. P. Shaffer, and A. H. Windle, "Ultra-low electrical percolation threshold in carbon-nanotube-epoxy composites", Polymer, 44 [19] 5893-99 (2003).

214 A. Boccaccini, "Assessment of damage induced by thermal shock in SiC- fiber-reinforced borosilicate glass composites", Composites Science and Technology, 59 [1] 105-12 (1999).

215 C. Singh, M. S. Shaffer, and A. H. Windle, "Production of controlled architectures of aligned carbon nanotubes by an injection chemical vapour deposition method", Carbon, 41 [2] 359-68 (2003).

216 M. Mayne, N. Grobert, M. Terrones, R. Kamalakaran, M. Ruhle, H. W. Kroto, and D. R. M. Walton, "Pyrolytic production of aligned carbon nanotubes from homogeneously dispersed benzene-based aerosols", Chemical Physics Letters, 338 [2-3] 101-07 (2001).

217 L. S. K. Pang, J. D. Saxby, and S. P. Chatfield, "Thermogravimetric analysis of carbon nanotubes and nanoparticles", Journal of Physical Chemistry, 97 [27] 6941-42 (1993).

218 D. Bom, R. Andrews, D. Jacques, J. Anthony, B. L. Chen, M. S. Meier, and J. P. Selegue, "Thermogravimetric analysis of the oxidation of multiwalled carbon nanotubes: evidence

for the role of defect sites in carbon nanotube chemistry", Nano Letters, 2 [6] 615-19 (2002).

219 P. M. Ajayan, T. Ichihashi, and S. Iijima, "Distribution of pentagons and shapes in carbon nanotubes and nanoparticles", Chemical Physics Letters, 202 [5] 384-88 (1993).

220 K. Esumi, M. Ishigami, A. Nakajima, K. Sawada, and H. Honda, "Chemical treatment of carbon nanotubes", Carbon, 34 [2] 279-81 (1996).

221 J. Hilding, E. A. Grulke, Z. G. Zhang, and F. Lockwood, "Dispersion of carbon nanotubes in liquids", Journal of Dispersion Science and Technology, 24 [1] 1-41 (2003).

222 I. D. Rosca, F. Watari, M. Uo, and T. Akaska, "Oxidation of multiwalled carbon nanotubes by nitric acid", Carbon, 43 [15] 3124-31 (2005).

223 R. Verdejo, S. Lamoriniere, B. Cottam, A. Bismarck, and M. Shaffer, "Removal of oxidation debris from multi-walled carbon nanotubes", Chemical Communications [5] 513-15 (2007).

224 S. Nagasawa, M. Yudasaka, K. Hirahara, T. Ichihashi, and S. Iijima, "Effect of oxidation on single-wall carbon nanotubes", Chemical Physics Letters, 328 [4-6] 374-80 (2000).

225 G. Ovejero, J. L. Sotelo, M. D. Romero, A. Rodriguez, M. A. Ocana, G. Rodriguez, and J. Garcia, "Multiwalled carbon nanotubes for liquid-phase oxidation: functionalization, characterization, and catalytic activity", Industrial and Engineering Chemistry Research, 45 [7] 2206-12 (2006).

226 S. C. Tsang, P. J. F. Harris, and M. L. H. Green, "Thinning and opening of carbon nanotubes by oxidation using carbon dioxide", Nature, 362 [6420] 520-22 (1993).

227 N. Yao, V. Lordi, S. X. C. Ma, E. Dujardin, A. Krishnan, M. M. J. Treacy, and T. W. Ebbesen, "Structure and oxidation patterns of carbon nanotubes", Journal of Materials Research, 13 [9] 2432-37 (1998).

228 V. Datsyuk, M. Kalyva, K. Papagelis, J. Parthenios, D. Tasis, A. Siokou, I. Kallitsis, and C. Galiotis, "Chemical oxidation of multiwalled carbon nanotubes", Carbon, 46 [6] 833-40 (2008).

229 Z. H. Wu, C. U. Pittman, and S. D. Gardner, "Nitric acid oxidation of carbon fibers and the effects of subsequent treatment in refluxing aqueous sodium hydroxide", Carbon, 33 [5] 597-605 (1995).

230 J. F. Zhang, R. Tu, and T. Goto, "Fabrication of transparent SiO_2 glass by pressureless sintering and spark plasma sintering", Ceramics International, 38 [4] 2673-78 (2012).

231 A. R. Boccaccini, "On the viscosity of glass composites containing rigid inclusions", Materials Letters, 34 [3-6] 285-89 (1998).

232 M. Estili and A. Kawasaki, "An approach to mass-producing individually alumina-decorated multi-walled carbon nanotubes with optimized and controlled compositions", Scripta Materialia, 58 [10] 906-09 (2008).

233 F. Inam, H. Yan, M. J. Reece, and T. Peijs, "Dimethylformamide: an effective dispersant for making ceramic-carbon nanotube composites", Nanotechnology, 19 [19] 5 (2008).

234 V. C. Moore, M. S. Strano, E. H. Haroz, R. H. Hauge, R. E. Smalley, J. Schmidt, and Y. Talmon, "Individually suspended single-walled carbon nanotubes in various surfactants", Nano Letters, 3 [10] 1379-82 (2003).

235 R. Andrews, D. Jacques, D. Qian, and E. C. Dickey, "Purification and structural annealing of multiwalled carbon nanotubes at graphitization temperatures", Carbon, 39 [11] 1681-87 (2001).

236 C. J. McConville, W. E. Lee, and J. H. Sharp, "Microstructural evolution in fired kaolinite", British Ceramic Transactions, 97 [4] 162-68 (1998).

237 H. Lemmens, M. Czank, G. Van Tendeloo, and S. Amelinckx, "Defect structure of the low temperature alpha-cristobalite phase and the cristobalite-tridymite transformation in (Si-Ge)O_2", Physics and Chemistry of Minerals, 27 [6] 386-97 (2000).

238 G. Yamamoto, M. Omori, T. Hashida, and H. Kimura, "A novel structure for carbon nanotube reinforced alumina composites with improved mechanical properties", Nanotechnology, 19 [31] 7 (2008).

239 G. D. Quinn, P. Green, and K. Xu, "Cracking and the indentation size effect for Knoop hardness of glasses", Journal of the American Ceramic Society, 86 [3] 441-48 (2003).

240 H. Krenchel, "Fibre reinforcement", Akademisk Forlag, Denmark (1964).

241 D. Hull and T. W. Clyne, "An intriduction to composite materials", Cambridge University Press, (2001).

242 T. Klug, "Preparation of C-fiber borosilicate glass composites: influence of the fiber type on mechanical properties", Journal of Materials Science, 29 [15] 4013-21 (1994).

243 D. H. Grande, J. F. Mandell, and K. C. C. Hong, "Fiber matrix bond strength studies of glass, ceramic, and metal matrix composites", Journal of Materials Science, 23 [1] 311-28 (1988).

244 K. M. Prewo, "Carbon-fiber reinforced glass matrix composite tension and flexure properties", Journal of Materials Science, 23 [8] 2745-52 (1988).

245 B. Derby, D. Hills, and C. Ruiz, "Materials for engineering: a fandamental design approach", Longman Scientific and Technical, (1992).

246 M. H. G. Wichmann, K. Schulte, and H. D. Wagner, "On nanocomposite toughness", Composites Science and Technology, 68 [1] 329-31 (2008).

247 D. Stauffer, "Introduction to the Percolation Theory", Taylor and Francis, London, (1985).

248 G. D. Zhan, J. D. Kuntz, J. E. Garay, and A. K. Mukherjee, "Electrical properties of nanoceramics reinforced with ropes of single-walled carbon nanotubes", Applied Physics Letters, 83 [6] 1228-30 (2003).

249 C. W. Nan, Z. Shi, and Y. Lin, "A simple model for thermal conductivity of carbon nanotube-based composites", Chemical Physics Letters, 375 [5-6] 666-69 (2003).

250 C. W. Nan, G. Liu, Y. H. Lin, and M. Li, "Interface effect on thermal conductivity of carbon nanotube composites", Applied Physics Letters, 85 [16] 3549-51 (2004).

251 M. K. Fahad, "Stresses and failure in the diametral compression test", Journal of Materials Science, 31 [14] 3723-29 (1996).

252 I. Fanderlik, "Silica glass and its applications: glass science and technology", Elsevier, (1996).

253 N. G. Ainslie, J. D. Mackenzie, and D. Turnbull, "Melting kinetics of quartz and cristobalite", Journal of Physical Chemistry B, 65 [10] 1718-24 (1961).

254 M. D. Sacks and T. Y. Tseng, "Preparation of SiO_2 glass from model powder compacts. Part 2: sintering", Journal of the American Ceramic Society, 67 [8] 532-37 (1984).

255 B. R. Lawn and D. B. Marshall, "Hardness, toughness, and brittleness: an indentation analysis", Journal of the American Ceramic Society, 62 [7-8] 347-50 (1979).

256 A. R. Boccaccini, "The relationship between wear behaviour and brittleness index in engineering ceramics and dispersion-reinforced ceramic composites", Interceram, 48 [3] 176-86 (1999).

257 J. B. Quinn and G. D. Quinn, "Indentation brittleness of ceramics: a fresh approach", Journal of Materials Science, 32 [16] 4331-46 (1997).

258 A. Leyland and A. Matthews, "On the significance of the H/E ratio in wear control: a nanocomposite coating approach to optimised tribological behaviour", Wear, 246 [1–2] 1-11 (2000).

259 H. Qian, E. S. Greenhalgh, M. S. P. Shaffer, and A. Bismarck, "Carbon nanotube-based hierarchical composites: a review", Journal of Materials Chemistry, 20 [23] 4751-62 (2010).

260 S. Zhang and W. E. Lee, "Carbon containing castables: current status and future prospects", British Ceramic Transactions, 101 [1] 1-8 (2002).

261 A. Paul, D. D. Jayaseelan, S. Venugopal, E. Zapata-Solvas, J. Binner, B. Vaidhyanathan, A. Heaton, P. Brown, and W. E. Lee, "UHTC composites for hypersonic applications", American Ceramic Society Bulletin, 91 [1] 22-28 (2012).

262 E. Wuchina, M. Opeka, S. Causey, K. Buesking, J. Spain, A. Cull, J. Routbort, and F. Guitierrez-Mora, "Designing for ultrahigh-temperature applications: the mechanical and thermal properties of HfB_2, HfC_x, HfN_x, and alpha HfN", Journal of Materials Science, 39 [19] 5939-49 (2004).

263 E. Khaleghi, Y. S. Lin, M. A. Meyers, and E. A. Olevsky, "Spark plasma sintering of tantalum carbide", Scripta Materialia, 63 [6] 577-80 (2010).

264 J. K. Ye, S. W. Zhang, and W. E. Lee, "Novel low temperature synthesis and characterisation of hollow silicon carbide spheres", Microporous and Mesoporous Materials, 152 25-30 (2012).

265 B. G. Demczyk, Y. M. Wang, J. Cumings, M. Hetman, W. Han, A. Zettl, and R. O. Ritchie, "Direct mechanical measurement of the tensile strength and elastic modulus of multiwalled carbon nanotubes", Materials Science and Engineering A - Structural Materials Properties Microstructure and Processing, 334 [1-2] 173-78 (2002).

266 E. W. Wong, P. E. Sheehan, and C. M. Lieber, "Nanobeam mechanics: elasticity, strength, and toughness of nanorods and nanotubes", Science, 277 [5334] 1971-75 (1997).

267 T. Kuzumaki and Y. Mitsuda, "Nanoscale mechanics of carbon nanotube evaluated by nanoprobe manipulation in transmission electron microscope", Japanese Journal of Applied Physics. Part 1 - Regular Papers Brief Communications and Review Papers, 45 [1A] 364-68 (2006).

268 K. Enomoto, S. Kitakata, T. Yasuhara, N. Ohtake, T. Kuzumaki, and Y. Mitsuda, "Measurement of Young's modulus of carbon nanotubes by nanoprobe manipulation in a transmission electron microscope", Applied Physics Letters, 88 [15] (2006).

269 M. M. J. Treacy, T. W. Ebbesen, and J. M. Gibson, "Exceptionally high Young's modulus observed for individual carbon nanotubes", Nature, 381 [6584] 678-80 (1996).

270 S. S. Xie, W. Z. Li, Z. W. Pan, B. H. Chang, and L. F. Sun, "Mechanical and physical properties on carbon nanotube", Journal of Physics and Chemistry of Solids, 61 [7] 1153-58 (2000).

271 G. Guhados, W. K. Wan, X. L. Sun, and J. L. Hutter, "Simultaneous measurement of Young's and shear moduli of multiwalled carbon nanotubes using atomic force microscopy", Journal of Applied Physics, 101 [3] 1-5 (2007).

272 R. P. Gao, Z. L. Wang, Z. G. Bai, W. A. de Heer, L. M. Dai, and M. Gao, "Nanomechanics of individual carbon nanotubes from pyrolytically grown arrays", Physical Review Letters, 85 [3] 622-25 (2000).

Presentations / Conference talks

1. T. Subhani, M. S. P. Shaffer, A. R. Boccaccini and W. E. Lee, “Glass matrix composites containing carbon nanotubes: fabrication and characterisation”, Oral Presentation on 24th February 2010 at the 2nd Year Seminar, Department of Materials, Imperial College London, UK.
2. T. Subhani, M. S. P. Shaffer, A. R. Boccaccini and W. E. Lee, “Fabrication of glass matrix composites containing carbon nanotubes by pressureless sintering”, Poster Presentation on 22nd March 2010 at the Post Graduate Research Day, Department of Materials, Imperial College London, UK.
3. T. Subhani, J. Cho, M. S. P. Shaffer, A. R. Boccaccini and W. E. Lee, “Nanotube-filled glass composites: processing, characterization and prospects for toughening”, Oral Presentation on 3rd September 2010 at the Nanotechnology in Carbon and Related Materials (NANOTEC10), Oxford, UK.
4. T. Subhani, M. S. P. Shaffer, A. R. Boccaccini and W. E. Lee, “Glass matrix composites containing carbon nanotubes”, Oral Presentation on 21st October 2010 at the Institute of Biomaterials, University of Erlangen Nuremberg, Germany.
5. T. Subhani, J. Cho, F. Inam, M. J. Reece, M. S. P. Shaffer, A. R. Boccaccini and W. E. Lee, “Glass composites containing carbon nanotubes: processing, characterisation and prospects for toughening”, Poster Presentation on 25th January 2011 at the 35th International Conference and Exposition on Advanced Ceramics and Composites, Hilton Daytona Beach Resort and Ocean Centre, FL, USA.
6. T. Subhani, M. S. P. Shaffer, A. R. Boccaccini and W. E. Lee, “Processing of glass matrix composites containing carbon nanotubes by spark plasma and pressureless sintering”, Oral Presentation on 21st March 2011 at the Post Graduate Research Day, Department of Materials, Imperial College London, UK.
7. T. Subhani, M. S. P. Shaffer, A. R. Boccaccini and W. E. Lee, “Fabrication and characterization of glass matrix composites containing carbon nanotubes”, Oral

Presentation on 13th April 2011 at the One Day Research Meeting on Advanced Ceramics, Centre for Advanced Structural Ceramics (CASC), Imperial College London.

8. T. Subhani, M. S. P. Shaffer, A. R. Boccaccini and W. E. Lee, "Carbon nanotube reinforced glass matrix composites", Poster Presentation on 17th May 2011 at the Centre for Advanced Structural ceramics (CASC) Industrial Day, Imperial College London, UK.
9. T. Subhani, M. S. P. Shaffer, A. R. Boccaccini and W. E. Lee, "Thermal ageing of carbon nanotube reinforced glass matrix composites", Oral Presentation on 10th September 2012 at the 5th International Workshop on Advanced Ceramics (IWAC05), Imperial College London, UK.

Journal publications

1. T. Subhani, M. S. P. Shaffer, A. R. Boccaccini and W. E. Lee, "Densification of carbon nanotube reinforced glass matrix composites using pressureless sintering", has been submitted to the Journal of the European Ceramic Society.
2. T. Subhani, C. Ciurea, F. M. Mackovic, Giuliani, E. Spiecker, M. S. P. Shaffer, A. R. Boccaccini and W. E. Lee, "Microstructural and interfacial characterization of carbon nanotube reinforced glass matrix composites", will be submitted to the Journal of the European Ceramic Society.
3. R. Giovanardi, M. Montorsi, G. Ori, J. Cho, T. Subhani, A. R. Boccaccini and C. Siligardi, "Microstructural characterisation and electrical properties of multiwalled carbon nanotubes/glass-ceramic nanocomposites", Journal of Materials Chemistry, 20 308–313 (2010).
4. A. R. Boccaccini, J. Cho, T. Subhani, C. Kaya and F. Kaya, "Electrophoretic deposition of carbon nanotube-ceramic nanocomposites", Journal of the European Ceramic Society, 30 1115-1129 (2010).
5. S. Seuss, T. Subhani, M. Kang, K. Okudaira, I. E. Aguilar-Ventura and A. R. Boccaccini, "Electrophoretic deposition of PEEK-TiO_2 composite coatings on stainless steel", Key Engineering Materials, 507 127-133 (2012).

Research papers under preparation

1. T. Subhani, V. Bhakhri, C. Ciurea, F. Giuliani, M. S. P. Shaffer, A. R. Boccaccini and W. E. Lee, "Mechanical, electrical and thermal property characterisation of carbon nanotube reinforced inorganic matrix composites."
2. T. Subhani, V. Bhakhri, F. Giuliani, M. S. P. Shaffer, A. R. Boccaccini and W. E. Lee, "An attempt to investigate the size effect of different aspect ratio carbon nanotubes in inorganic matrix composites."
3. T. Subhani, M. S. P. Shaffer, A. R. Boccaccini and W. E. Lee, "Lubricating effect of carbon nanotubes on wear and friction properties of glass matrix composites."
4. T. Subhani, M. S. P. Shaffer, A. R. Boccaccini and W. E. Lee, "Thermal shock, cycling and ageing behaviour of carbon nanotube reinforced silica glass matrix composites.
5. T. Subhani, M. S. P. Shaffer, A. R. Boccaccini and W. E. Lee, "Tailorable porous silica glass using carbon nanotubes as sacrificial reinforcements."
6. T. Subhani, N. Ur-rehman, M. S. P. Shaffer, A. R. Boccaccini and W. E. Lee, "Borosilicate glass matrix composites containing well dispersed carbon nanotubes: manufacturing and characterization."

Book chapter

1. T. Subhani, M. S. P. Shaffer and A. R. Boccaccini, "Carbon nanotube reinforced glass and glass-ceramic matrix composites", accepted for the book "Ceramic Nanocomposites: Properties and Applications." Woodhead Publishing.

Prize

1. First prize of best poster awards at the 35th International Conference and Exposition on Advanced Ceramics and Composites (2011), Hilton Daytona Beach Resort, FL, USA.